Studying large-scale structures and polarization of the Northern sky facilitating single-station data of the Low Frequency Array (LOFAR)

Dissertation

zur
Erlangung des Doktorgrades (Dr.rer.nat.)
der Mathematisch-Naturwissenschaftlichen Fakultät
der Rheinischen Friedrich-Wilhelms-Universität Bonn

vorgelegt von

Jana Köhler
aus Luckau, Deutschland

Bonn 2015

Angefertigt mit Genehmigung der Mathematisch-Naturwissenschaftlichen Fakultät der
Rheinischen Friedrich-Wilhelms-Universität Bonn

1. Gutachter: Prof. Dr. Michael Kramer

2. Gutachter: Prof. Dr. Pavel Kroupa

Erscheinungsjahr: 2016

Tag der Promotion: 31. Mai 2016

Contents

Preface

All-sky surveys help to gather a deep knowledge about the nature of large-scale structures in the Universe, the Milky Way and extragalactic galaxies. In the context of that, observations in the radio domain are important, as they provide information which cannot be archived from any other observing frequency. This thesis will present a new northern sky survey at radio frequencies below 200 MHz, made with one of the new generation of radio telescopes-the Low Frequency Array (LOFAR; van Haarlem et al., 2013). Using data of a single station of this array a novel approach has developed to produce a northern sky survey. The necessary steps are described on how to generate a scientific usable sky map from the raw voltages. The scientific analysis of these maps will be discussed and used for further studies.

An overview of the general properties of the LOFAR array will be given in Chapter 2. In this array a single station will have a physical diameter of around 60 m and therefore it allows to study large-scale emission in the northern sky at 30 to 240 MHz. Even more, with its wide frequency range and the ability to observe in polarization, LOFAR allows polarization studies at frequencies below 240 MHz. In this way it is an important instrument to study the Milky Way at low frequencies. In case of Galactic and extra-galactic emission this was never possible before. Unfortunately with existing LOFAR software it was not possible to perform all-sky imaging with a frequency resolution better than 200 kHz. Due to physical limitation, in particular the strong Faraday Rotation at low frequencies, this spectral resolution is not sufficient enough. To solve this problem, this thesis will present a way how to use raw voltages from the Transient Buffer Boards (TBBs) for all-sky imaging at sufficiently high frequency resolution. In particular for all necessary steps new software tools and algorithm had to be developed. The correlation of the data will be described in Chapter 3, as well as all the technical challenges of the further data reduction. This includes the data inspection, the calibration and dealing with the antenna pattern and ionospheric effects. Especially the self-calibration will become an important method, to calibrate strong unknown structures and individual sources, to improve the image quality. Some of the strong unknown source can be an active Sun, a bursting Jupiter or even just strong men made radio frequency interference (RFI). As all observations presented in this thesis were done with the LOFAR station in Effelsberg dealing with the strong RFI is one of the main challenge in the calibration process.

The developed software is afterwards used to produce single all-sky images of a LOFAR station. In Chapter 4 the procedure is explained how a high number of single all-sky ob-

servations were combined to map out the entire northern sky down to a declination of 0°. The detected large-scale structures in this new map will be studied and compared to earlier surveys.

In Chapter 5 a spectral analysis using the LOFAR survey at various frequencies is discussed. As part of this analysis the spectral index maps between frequencies below 50 MHz and the high frequency surveys at 408 MHz (Haslam et al., 1982), 820 MHz (Berkhuijsen, 1972) and 1400 MHz (Reich et al., 1981) will be investigated. This allows to study physical nature of the continuum emission and a possible flattening of the spectrum toward lower frequency due to thermal absorption. Furthermore the spectral index data will be used to estimate turn-overs at low frequencies and high frequency breaks and indicate a possible transition from thermal to non-thermal emission. In Chapter 6 a short analysis of the spectral properties of the strong radio source Cas A is investigated. In general measurements of this source during the last years show that the flux density is decreasing. The LOFAR measurements do confirm the predicted intensities of the Cas A model and also indicates similar flux densities for the strong radio source Cyg A.

In order to determine the influence of the ionosphere on the polarization measurements pulsar observation are used. Chapter 7 will discuss the variations of the Rotation Measure (RM) values of the pulsars with time due to ionospheric fluctuations.

Taking all corrections into account the polarization properties of Jupiter bursts can now be studied. The measurements show that the burst are highly linear- and circular-polarized and that the RM values per burst are frequency depended (Chapter 8).

In Chapter 9 the polarization properties of the large-scale emission from the Milky Way will be discussed. For this linear polarization intensity maps are created and RM Synthesis will be used to determine the generally weak polarization emission.

Chapter 1

Introduction

As this work has the aim to study the sky at frequencies below 300 MHz, an overview of the most important physical processes at these frequencies is given in this chapter. It starts with an explanation of the origin of the observed emission, which is mainly due to free-free radiation and synchrotron radiation. This radiation allows to study magnetic fields in the Universe. Afterwards an overview of polarization and depolarization properties is given. Especially the considerations of the depolarization effects are important for the further data handling of this work. Furthermore the Rotation Measure Synthesis method will be introduced, which became prominent during the last years and allows to study magnetic fields in a more detailed way. At the end a short overlook of recently studies of the Milky Way in total and polarized intensity is given. This will later be used for a comparison with the observations of this work and will be compared with theoretical modeling.

The theory of radiation processes and polarization, as introduced in the following, is discussed widely in the literature. This chapter mainly follows the deviations found in Rybicki and Lightman (1985) and the teaching script by Klein[1].

1.1 Continuum radiation processes

1.1.1 Synchrotron radiation

Observations at radio frequencies are one of the most important tool to study the magnetic fields in the Universe, as the observed radiation is mainly caused by synchrotron radiation. Synchrotron radiation originates from relativistic electrons that are accelerated in a magnetic field by the Lorentz force

$$\mathbf{F} = -e\left(\mathbf{E} + \mathbf{v} \times \mathbf{B}\right) \tag{1.1}$$

$$\frac{d}{dt}\gamma m_e \mathbf{v} = \frac{q}{c}\,\mathbf{v} \times \mathbf{B}\,. \tag{1.2}$$

[1]The script 'Galactic & Intergalactic Magnetic Fields' is available at `http://www.astro.uni-bonn.de/~uklein/teaching/B_Fields/MagneticFields.pdf`

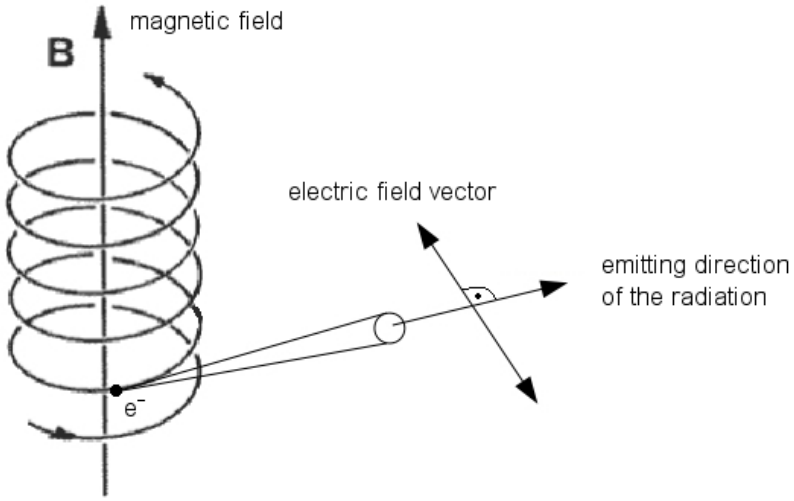

Figure 1.1: Origin of synchrotron radiation. **B**-vector, **E**-vector and the radiation direction are perpendicular to each other as described in Eq. (1.1).

Thereby the electrons are moving on a helical path around the field vector **B** are radiating due to there acceleration. The emission is radiated perpendicular to the moving direction of the particle. The energy of these electrons can be described by the Einstein relation:

$$E = \gamma m_e c^2 \tag{1.3}$$

with γ being the Lorentz-factor:

$$\gamma = \frac{1}{\sqrt{1-(\mathrm{v/c})^2}}\,. \tag{1.4}$$

Here v is the velocity of the particle and c the speed of light. A particle in a magnetic field B at a given energy E emits most of its radiation at a characteristic frequency ν_c:

$$\nu_c\,[\mathrm{Hz}] = \frac{3\gamma^2 \mathrm{eB}_\perp}{4\pi \mathrm{m_0 c}} \approx 4.2 \cdot 10^6 \gamma^2 \mathrm{B[G]}\,. \tag{1.5}$$

In case of an ensemble of electrons the radiation spectra provides information about the energy distribution of the electrons. Hereby is the total synchrotron spectrum is the superposition of the single electron spectra and follows in general a power-law:

$$P(\omega) \propto \omega^{-\alpha}\,, \tag{1.6}$$

where α is defined as the spectral index. For the total spectrum of the radiation a sum over the distribution from all electrons is needed, as plotted in the left image of Fig. 1.2. For this we use the number density N(E) of the electrons with energies ranging from E to dE:

$$\mathrm{N(E)dE} = \mathrm{CE}^{-\mathrm{g}}\mathrm{dE}\,. \tag{1.7}$$

C is a constant and g is the electron distribution index. The total power radiation per unit volume and per unit frequency is the integral over the number density (Eq. (1.7)) times the single electron energy:

$$P_{\rm total}(\omega) = C \int_{E_1}^{E_2} P(\omega) E^{-g} \mathrm{d}E \,, \tag{1.8}$$

where

$$P(\omega) = \frac{\sqrt{3} q^3 B \sin\alpha}{2\pi m_e c^2} F\left(\frac{\omega}{\omega_c}\right) . \tag{1.9}$$

Solving Eq. (1.8) (for details see Rybicki and Lightman, 1985) leads to

$$P_{\rm total}(\omega) \propto \omega^{-(g-1)/2} \,. \tag{1.10}$$

As a result the spectral index α and the particle distribution index g are related with each other by:

$$\alpha = \frac{g-1}{2} \,. \tag{1.11}$$

From the study of cosmic ray events a power-law with g = 2.4 (e.g. Cronin et al., 1997) was found that leads to a spectral index of $\alpha = 0.7$. This value is the most frequently found spectral index for synchrotron emission. A similar calculation for the brightness

$$I_\nu = \frac{1}{4\pi} \int_0^{s_0} \int_0^{\infty} P(\nu) N(E) \mathrm{d}E \mathrm{d}s \tag{1.12}$$

shows the dependence of the synchrotron radiation as a function of the magnetic field component perpendicular to the line of sight, with s_0 being the total path length:

$$I_\nu \sim B_\perp^{1+\alpha} \nu^{-\alpha} \,. \tag{1.13}$$

1.1.2 Free-free radiation

An other important contribution to the spectral energy distribution is the free-free radiation or Bremsstrahlung, originating from particles accelerated by Coulomb fields. It can be found in ionized (HII) regions, where free electrons moving on orbits close to the protons. This causes the emission of photons by the electrons.

In case of local thermo-dynamical equilibrium the brightness temperature of the radiation follows the Planck's law

$$B_\nu(T) = \frac{2h\nu^3}{c^2} \cdot \frac{1}{\exp(\frac{h\nu}{kT}) - 1} \,, \tag{1.14}$$

which can be approximated by the Rayleigh-Jeans law in the radio domain, where $h\nu/kT \ll 1$:

$$B_\nu(T) \approx \frac{2h\nu^2}{c^2} \cdot kT \,. \tag{1.15}$$

For the following calculations the optical depth is needed:

$$\tau_\nu = \int_0^{s_0} \kappa_\nu \mathsf{d}s \,, \tag{1.16}$$

which is defined as the integral over the absorption coefficient

$$\kappa_\nu = \sqrt{\frac{2}{\pi}} \frac{4e^6 Z^2 n_{ion} n_e}{3c(m_e kT)^{3/2}\nu^2} \cdot g_{ff} \tag{1.17}$$

over the line of sight. From solving the integral we arrive at

$$\tau_\nu = 8.77 \cdot 10^{-3} \nu[\mathrm{Hz}]^{-2} T[K]^{-3/2} g_{ff} \cdot \int_0^{s_0} n_{ion}[cm^{-3}] n_e[cm^{-3}] \mathsf{d}s \,. \tag{1.18}$$

As the plasma is in general neutral, the electron density n_e is equal to the density of the ions n_{ion}. The integral over the electron density is defined as the emission measure EM:

$$EM = \int_0^{s_0} n_e^2 \, \mathsf{d}s \,. \tag{1.19}$$

Using this the optical depth can be expressed as

$$\tau_\nu = 3.01 \cdot 10^{-2} \cdot EM[pc/cm^6] \cdot \nu[\mathrm{GHz}]^{-2} \cdot T[K]^{-3/2} \cdot g_{ff} \,. \tag{1.20}$$

The Gaunt factor for the free-free radiation is defined by

$$g_{ff} = \ln\left(\frac{3kT}{2Ze^2\pi\nu} \cdot \sqrt{\frac{8kT}{\pi m_e}}\right) \tag{1.21}$$

$$= 12.5 + \ln\left(Z^{-1} \cdot T[10^4 K]^{3/2} \cdot \nu[\mathrm{GHz}]^{-1}\right) \,. \tag{1.22}$$

The observed intensity of a source depends on the optical thickness:

$$I_\nu = B_\nu(T_e) \cdot (1 - e^{-\tau_\nu}) \,. \tag{1.23}$$

There are two extreme cases of the optical depth, which are discussed in the following. In the case of high optical thickness, which means $\tau_\nu \gg 1$, the exponential function becomes negligible and the intensity

$$I_\nu = B_\nu(T_e) = \frac{2hk\nu^2 T_e}{c^2} \tag{1.24}$$

follows the Rayleigh-Jeans law, which behaves like a power law with a spectral index of 2. This spectrum only depends on the electron temperature.

For low optical thickness and $\tau_\nu \ll 1$ we get:

$$I_\nu = \tau_\nu \cdot B_\nu(T_e) = 8.29 \cdot 10^{-23} \cdot g_{ff} \cdot \left(\frac{EM}{\mathrm{pc\ cm^{-6}}}\right) \cdot \left(\frac{T_e}{10^4 \mathrm{K}}\right)^{-0.5} \,. \tag{1.25}$$

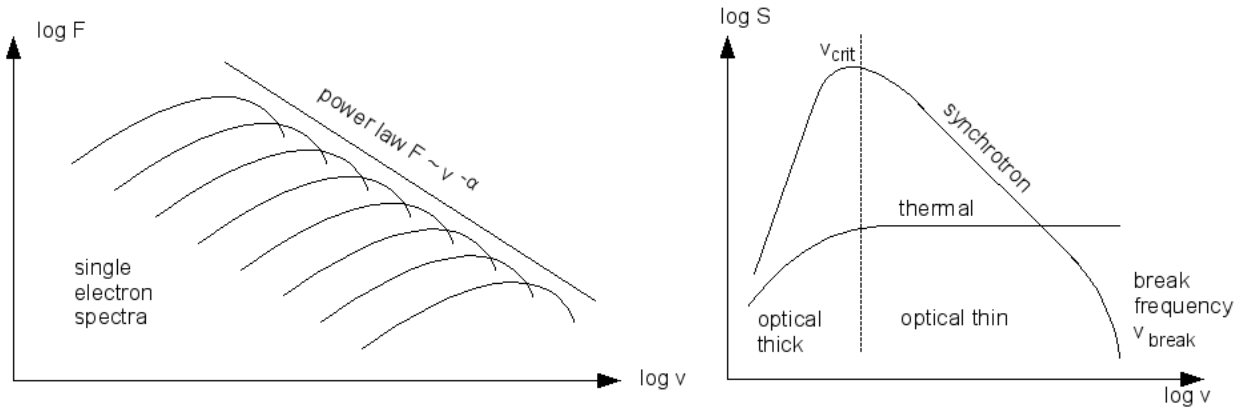

Figure 1.2: Left: Superposition of single electron spectra to a total energy spectrum (Credits: Adapted from Schneider, 2006). Right: Comparison of synchrotron and thermal spectrum.

The spectrum varies slowly with frequency caused by the Gaunt factor. The resulting spectral index is of the order of 0.1. As this value is much lower than the spectral index of 0.7 expected by the synchrotron radiation, the spectral index analysis helps to clarify the underlying process which causes the observed radiation. In the right hand side image of Fig. 1.2 the spectral behavior of thermal (free-free) and non-thermal(synchrotron) radiation is plotted depending of its optical thickness. In the Universe both processes are present and the observed emission spectrum is a superposition of both. Due to the high spectral index value of 0.7 for the synchrotron radiation, compared to the low value of 0.1 for the free-free radiation, the observed emission at low frequencies is dominated by synchrotron radiation.

1.2 Polarization

1.2.1 Polarization of synchrotron radiation

Generally the radiated emission is unpolarized. However in the presence of a mechanism that affects a certain wave, the resulting emission will be polarized. This effect can be caused by e.g. magnetic fields or dust grains.

The polarization of transverse waves describes the orientation of the oscillation from an electromagnetic wave. The electric field vector, which is perpendicular to the magnetic field vector (see Fig. 1.3 left), can be separated into its two components:

$$E_x = A_x \cos(kz - \omega t) \cdot x \tag{1.26}$$

$$E_y = A_y \cos(kz - \omega t + \delta) \cdot y \tag{1.27}$$

with A being the amplitude and the wavenumber $k = 2\pi n/\lambda$ with the wavelength λ. $\omega = 2\pi f$ is the angular frequency and z the direction. δ is the phase which affects the type of polarization. If $\delta = 0$ one speaks of linear polarization, whereas for $\delta = \pi/2$ one speaks of

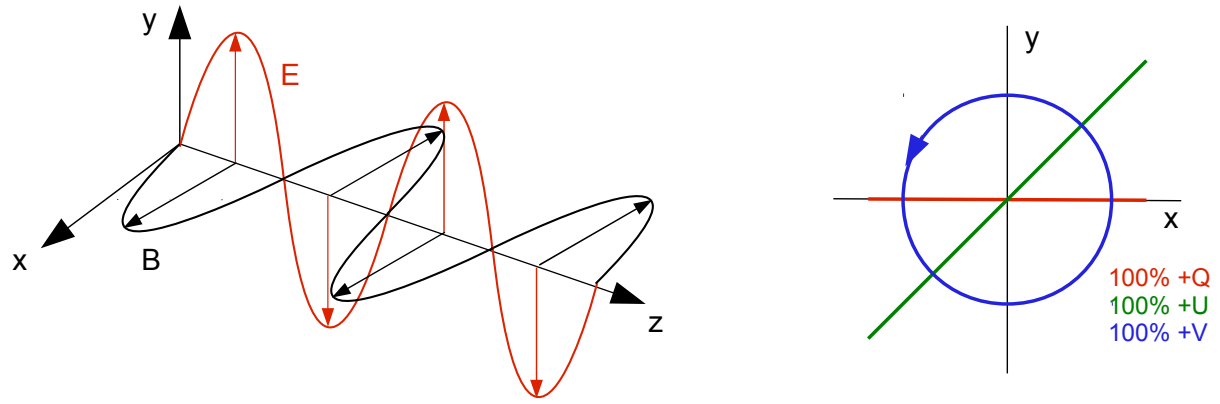

Figure 1.3: Left: B and E field vectors of an electromagnetic wave. Right: Projection of 100% linear, orthogonal linear and circular polarization.

circular polarization. Every other value leads to elliptical polarization, where a distinction into right-handed ($0 < \delta < \pi$) and left-handed ($\pi < \delta < 2\pi$) polarization is made.

Stokes (Stokes, 1952) used a set of four parameters to describe the polarization state of an electromagnetic wave

$$\mathrm{I} = \left\langle \mathrm{E_y^* E_y} + \mathrm{E_x E_x^*} \right\rangle \tag{1.28}$$

$$\mathrm{Q} = \left\langle \mathrm{E_y^* E_y} - \mathrm{E_x E_x^*} \right\rangle \tag{1.29}$$

$$\mathrm{U} = \left\langle \mathrm{E_y^* E_x} + \mathrm{E_y E_x^*} \right\rangle \tag{1.30}$$

$$\mathrm{V} = \left\langle \mathrm{E_y^* E_x} - \mathrm{E_y E_x^*} \right\rangle . \tag{1.31}$$

Here E_x and E_y are the electric field vectors measured with a single antenna dipole, which are perpendicular to each other. The * donates the complex conjugated and the brackets stands for averaging in time. Stokes I describes the total intensity, where Q represent the linear, U the orthogonal linear and V the circular polarized intensity (see Fig. 1.3 right). The degree of polarization is determined via:

$$\mathrm{m} = \frac{\sqrt{\mathrm{Q}^2 + \mathrm{U}^2 + \mathrm{V}^2}}{\mathrm{I}} . \tag{1.32}$$

If an electromagnetic wave propagates through a magnetic field it gets rotated by

$$\Delta\psi = \frac{1}{2} \arctan\left(\frac{\mathrm{U}}{\mathrm{Q}}\right) = \mathrm{RM} \cdot \lambda^2 . \tag{1.33}$$

This effect is called Faraday rotation and depends on the strength of the magnetic field $\mathrm{B}_\parallel$, the electron density n_e and the path length of the passed medium. The rotation measure (RM) is defined as the differential

$$RM = \frac{\mathrm{d}\psi(\lambda^2)}{\mathrm{d}\lambda^2} . \tag{1.34}$$

Sometimes it is equated to the Faraday depth

$$\phi(\mathbf{r}) = \frac{e^3}{2\pi m^2 c^4} \int_{observer}^{source} n_e \mathbf{B}_{\parallel} \cdot \mathrm{d}\mathbf{r} \tag{1.35}$$

even though RM and ϕ are only the same in very simple sources (uniform amount of Faraday rotation across the source). If the RM value is positive the observed magnetic field is pointing toward the observer, whereas a negative value means the magnetic fields points away from the observer. Figure 1.4 shows how an electromagnetic wave gets rotated while passing a magnetized medium.

The maximum expected degree of polarization can be calculated from

$$m = \frac{1+\alpha}{\frac{5}{3}+\alpha} \tag{1.36}$$

with α being the spectral index as introduced in Eq. (5.4). Using $\alpha = 0.7$ for synchrotron radiation leads to a maximum degree of linear polarization of around 72 %. Due to different depolarization effects, which will be discussed in the following, the observed degree of polarization is much smaller than this maximum value.

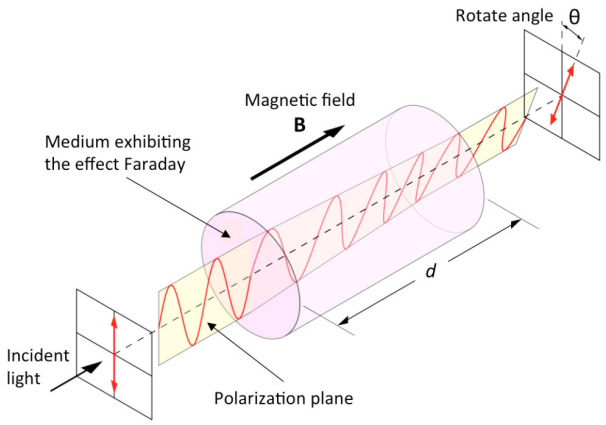

Figure 1.4: Faraday rotation of the polarization angle of a wave which is passing a magnetized medium (Credits: Adapted from Wikipedia).

1.2.2 Depolarization

Depolarization is a reduction in the degree of polarization of a source, which is produced by the summing of polarization vectors that are not aligned. One has to distinguish between instrumental effects (e.g., beam and bandwidth depolarization) and physical mechanisms that lead to depolarization (see below). A detailed discussion of effects of the wavelength-dependent depolarization can be found in Arshakian and Beck (2011). They showed that all of the following effects can lead total depolarization at frequencies below 100 MHz.

1.2.2.1 Instrumental depolarization

Beam depolarization

The line-of-sight length of the magnetic field vector can change on very small spatial scales. If these structures in the magnetic field can not be resolved by our telescope then polarization vectors with different orientations are added, leading to beam depolarization. Since the

angular resolution of a single LOFAR station is on the order of several degrees, only large-scale structures in the magnetic field will not be beam depolarized.

Bandwidth depolarization
As the polarization angle (Eq. (1.33)) depends on the square of the wavelength, it is changing between two frequencies

$$\Delta\psi = \mathsf{RM}\left(\lambda_1^2 - \lambda_2^2\right) . \tag{1.37}$$

The rotation of the angle increases with increasing wavelength, meaning with decreasing frequency. If the bandwidth between two observing channels is too large and the polarization angle is rotating fast within one band, the result is bandwidth depolarization. This effect gets stronger toward longer wavelength, which means at lower frequencies. To solve for this a good frequency resolution is needed.

1.2.2.2 Physical depolarization

Differential Faraday rotation
Faraday rotation changes the polarization angle of an electromagnetic wave when this wave travels through a plasma with an embedded magnetic field. When observing a source which extends along the line of sight the emission coming from the near side of the source will undergo less Faraday rotation than emission from the far side of the source. If the source emits uniformly along the line of sight, and the Faraday depth increases linearly with physical depth, then the amount of depolarization is given by

$$\mathrm{DP} = \frac{|\sin\left(2\mathrm{RM}\lambda^2\right)|}{|2\mathrm{RM}\lambda^2|} . \tag{1.38}$$

As Faraday rotation not just happen within the source, but in every magnetized medium along the line-of-sight of the observer and the source, these inter-median medium can be other galaxies, the Milky Way or the earth ionosphere. Rotation measure synthesis can help to some extent, as it allows to image the intensity at different Faraday depth.

Faraday dispersion
Faraday dispersion occurs in regions with turbulent magnetic fields and causes wavelength-dependent depolarization. Internal Faraday rotation appears in emitting and Faraday-rotating regions and the depolarization is given by

$$\mathrm{DP} = \frac{1 - \mathrm{e}^{-S}}{S} , \tag{1.39}$$

where $S = 2\sigma_R M^2 \lambda^4$ with σ_{RM} being the RM dispersion. If a turbulent foreground screen lies in front of a uniformly emitting source (and the angular scale of the fluctuations is much smaller than the size of the background source) then

$$DP = \mathrm{e}^{-S} \tag{1.40}$$

with S as defined above.

1.2.3 Reconstructing the magnetic field

To obtain RM values, polarization measurements at different frequencies are needed. By plotting the polarization angle over the square of the wavelength, the slope provides the value of the RM. The nπ ambiguity of the polarization angle can lead to several possible solutions for the RM values. To solve for this problem the RM Synthesis method can be used. The main principal of the RM Synthesis is some kind of Fourier transformation on the polarization angle over the square of the wavelength, which produces a so called Faraday spectrum of Faraday depth values. This allows to obtain the polarized intensity for different Faraday depths. In this way the instrumental polarization can be better identified, which occurs at a Faraday depth of zero. Furthermore the different RM layers within sources become visible which gives a better opportunity to study the 3D polarization properties of a source. In the same way it can be used to study the foreground medium, which shows up at a given depth (Burn, 1966).

The complex Faraday dispersion function F(ϕ) was first introduced by Burn (1966):

$$P(\lambda^2) = \int_{-\infty}^{\infty} F(\phi) \mathrm{e}^{2i\phi\lambda^2} \mathrm{d}\phi \,, \tag{1.41}$$

which is the complex polarized surface brightness per unit Faraday depth. All the further considerations are based on Brentjens et al. (2005). P can be written as

$$P = Q + iU = |P| \, \mathrm{e}^{2i\psi} \,, \tag{1.42}$$

where Q and U are the Stokes values of the linear polarization and ψ the polarization angle (Eq. (1.33)) as defined above. The connectedness is imaged in the right handed panel of Fig. 1.5. What distinguish Eq. (1.41) from a Fourier transformation is that $P(\lambda^2)$ only has a physical meaning for positive wavelength. For the inversion some assumptions for negative wavelength have to be done. To solve for the problem a window function is introduced

$$\tilde{P}(\lambda^2) = W(\lambda^2) P(\lambda^2) \,, \tag{1.43}$$

which is zero at negative wavelength and everywhere else in the spectrum for which no measurements are available. Such tricks allow to calculate the inverse Fourier transformation to obtain the Faraday dispersion function

$$\tilde{F}(\phi) = F(\phi) * R(\phi) = K \int_{-\infty}^{\infty} \tilde{P}(\lambda^2) \mathrm{e}^{-2\pi\phi\lambda^2} \mathrm{d}\lambda^2 \,, \tag{1.44}$$

where $R(\phi)$ is called the rotation measure transfer function (RMTF), which is used to normalize to unity at a Faraday depth of zero:

$$R(\phi) = \frac{\int_{-\infty}^{\infty} W(\lambda^2) \mathrm{e}^{-2i\phi\lambda^2} \mathrm{d}\lambda^2}{\int_{-\infty}^{\infty} W(\lambda^2) \mathrm{d}\lambda^2} = K \int_{-\infty}^{\infty} W(\lambda^2) \mathrm{e}^{-2\pi\phi\lambda^2} \mathrm{d}\lambda^2 \tag{1.45}$$

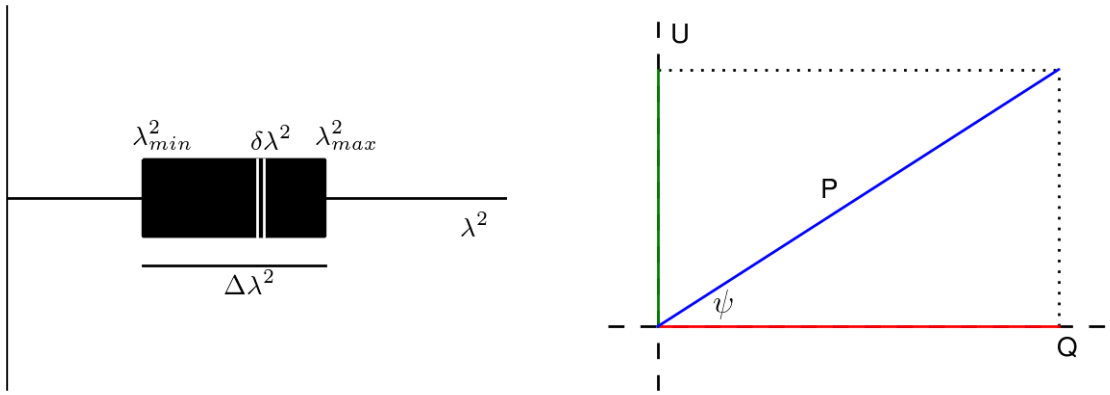

Figure 1.5: Left: Illustration of the total bandwidth $\Delta\lambda^2$, the channel width $\delta\lambda^2$ and the minimum and maximum of the observed spectrum in the λ^2 space. Right: Illustration of the Q and U value with the corresponding polarization P and polarization angle ψ.

with K being

$$K = \left(\int_{-\infty}^{\infty} W(\lambda^2) \mathrm{d}\lambda^2 \right)^{-1} . \tag{1.46}$$

The $*$ denotes the convolution between the functions.

The quality of the reconstruction depends on the coverage in λ^2 space and can be explained by the theory of the Fourier transformation. In case of numerous gaps in the frequency spectrum, stronger side lobes will appear in the Faraday spectrum. A large covering in λ^2 space increases the resolution in the Faraday space.

The behavior of the RM spectrum depends on the input parameters like the channel width $\delta\lambda^2$, the total bandwidth $\Delta\lambda^2 = \lambda^2_{max} - \lambda^2_{min}$ and the shortest wavelength λ^2_{min}. For illustration, these parameters are imaged in the left handed panel of Fig. 1.5. These parameters lead to the resolution in the RM space

$$\delta\phi \approx \frac{2\sqrt{3}}{\Delta\lambda^2} , \tag{1.47}$$

the max-scale in RM space to which one is sensitive

$$\mathrm{max-scale} \approx \frac{\pi}{\lambda^2_{min}} \tag{1.48}$$

and the maximum observable Faraday depth:

$$\|\phi_{max}\| \approx \frac{\sqrt{3}}{\delta\lambda^2} . \tag{1.49}$$

Following these properties large RM values can be better measured at higher frequencies, whereas small RM values and nearby RM peaks can better be resolved at lower frequencies. To measure large RM values at low frequencies a high frequency resolution down to a few kHz is needed.

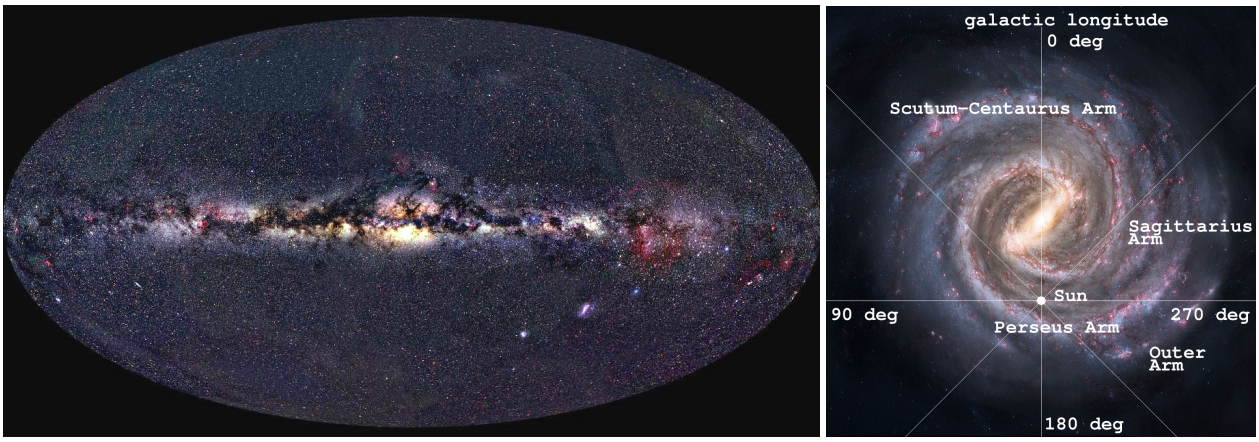

Figure 1.6: Left: Optical image of the Milky Way from combined photographs (Axel Meltinger, 2000). Right: Artistic impression of the Milky Way as seen from above (Nick Risinger). Star-forming regions appear red in the image.

1.3 The Milky Way

Sitting inside the Milky way makes it partly hard to study it. Nevertheless, observations at various frequencies (radio, infrared, optical, X-ray etc.) provided information to reconstruct structures of the Milky Way. From our current knowledge the Milky Way is a spiral galaxy as imaged in the right-handed picture of Fig. 1.6. This image is just one artistic reconstruction. By now scientist were not able to prove, if the Milky Way has two, four or even more spiral arms. The Milky Way is assumed to have a diameter of around 30 kpc with the Sun sitting inside a local bubble at a distance of around 8 kpc away from the Galactic center. The Galaxy is surrounded by a Galactic halo with a diameter around 50 kpc. An optical image of the entire sky is shown in the left-handed picture of Fig. 1.6. Most of the visible stars appear along the Galactic disc, but also interstellar dust can be observed, which absorbs the optical light lying behind. Therefore observations in the radio, infrared and X-ray are important, because this emission is much less affected by dust absorption.

1.3.1 Total intensity

All-sky surveys in total intensity have been obtained in the past at radio frequencies even down to 10 MHz (Caswell, 1976). The oldest of these surveys result from single dish observations, whereas newer surveys are produced from interferometric data. Such antenna arrays have the benefit to provide a better resolution even at low frequencies. In all cases the measurements were done by observing small patches or strips on the sky, which were combined afterwards. In this way the entire sky was mapped. Due to this mosaicking scanning artefacts are seen in the maps. By using data from a single LOFAR station it is now for the first time possible to combine all-sky maps. This allows to remove to some extent

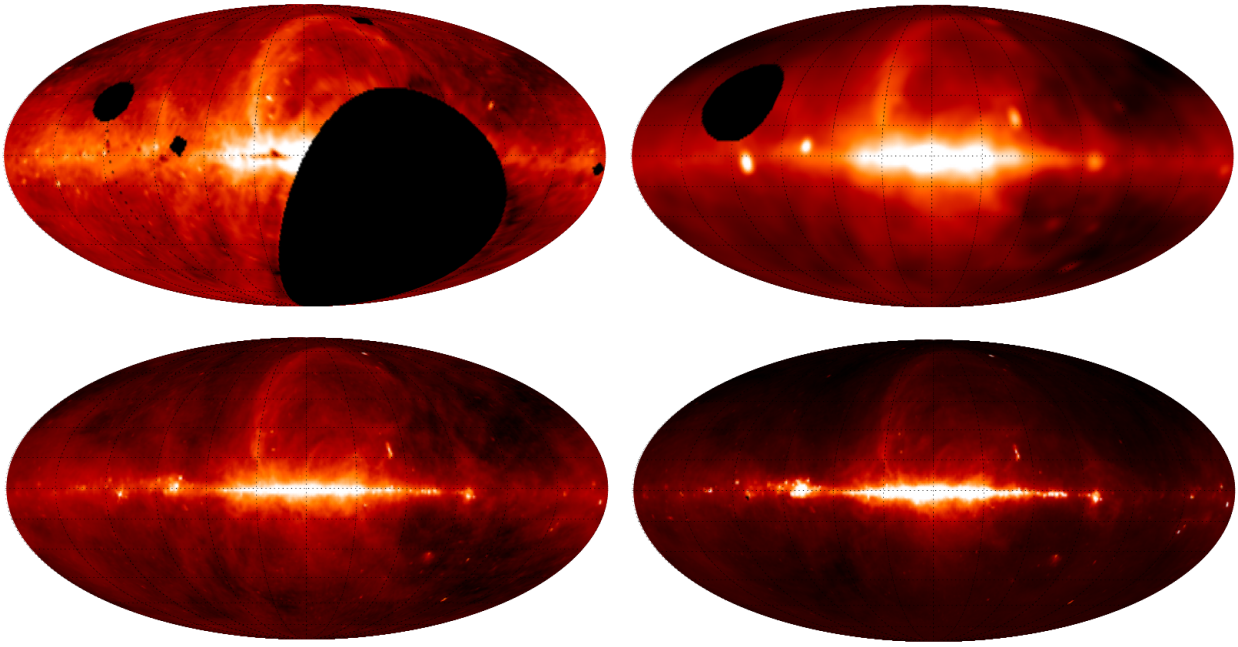

Figure 1.7: All-sky surveys of total intensity in Galactic coordinates. Top left: 22 MHz survey by Roger et al. (1998). Top right: 45 MHz survey by Guzmán et al. (2010). Bottom left: 408 MHz survey by Haslam et al. (1982). Bottom right: 1420 MHz survey by Reich & Reich (1986).

Table 1.1: Summary of used surveys

frequency	telescope	resolution	coverage	reference
22 MHz	DRAO	1.1° x 1.7°	$-28° \leq \delta \leq 80°$	Roger et al. (1999)
45 MHz	Maipu, MUradar	5° x 5°	$-90° \leq \delta \leq 65°$	Guzmán et al. (2009)
408 MHz	Jodrell, Effelsb., Parks	0.51'	$-90° \leq \delta \leq 90°$	Haslam et al. (1982)
820 MHz	Dwingeloo	1.2°	$-70° \leq \delta \leq 85°$	Berkhuijsen (1972)
1400 MHz	Stockert	35.4'	$-90° \leq \delta \leq 90°$	Reich et al. (1981)

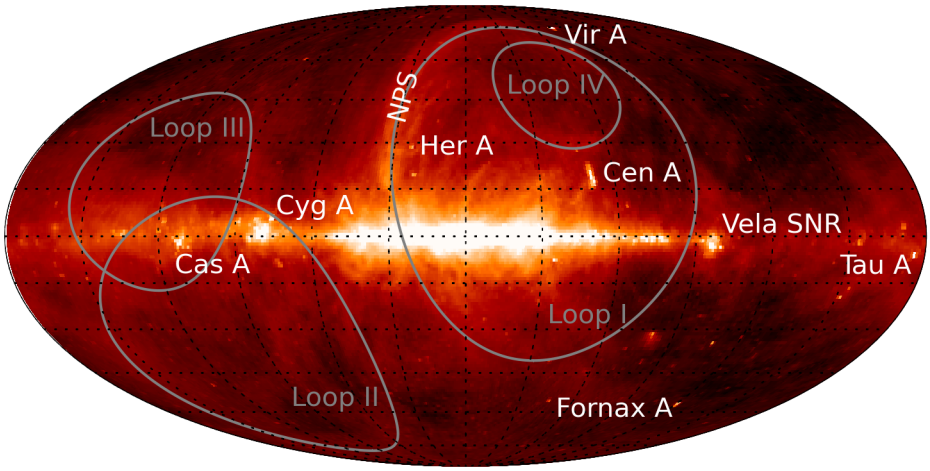

Figure 1.8: 408 MHz map by Haslam et al. (1982) including a description of the brightest sources visible, as well as the three most prominent loops.

the scanning effects as seen in the older surveys.

Four prominent low frequency surveys at 22[2], 45[3], 408[2] and 1400 MHz[2] are shown in Fig. 1.7. All information (telescope used for the observations, the beam resolution of the telescope, the declination coverage of the sky and the references) about the surveys can be found in Table 1.1. Mainly large scale structures are visible, as well as some strong radio sources. Strong emission shows up along the Galactic plane of the Milky Way, which is becoming weaker toward the outer disc and the halo and stronger toward the Galactic center. Other strong features of the Milky Way can be seen, like the famous North Polar Spur and some other weaker loops. These structures are expected to originate from old Supernova remnants (Berkhuijsen et al., 1971). Beside of that strong radio sources, like Cyg A, Cas A, Vir A, Tau A in the northern sky and in the southern sky also Cen A, For A and others are visible (Fig. 1.8).

At high frequency most of the emission is picked up along the inner disc, whereas at the lower frequencies the emission is more extended toward the outer disc and the halo. In the halo of the Galaxy the magnetic fields are weaker (below 1 μG), than inside the disc (around 10 μG) and therefore the emission from the halo is picked up at lower frequencies. Besides at the lowest frequencies thermal absorption along the Galactic plane becomes visible, as seen in the 22 MHz map. Especially in the region close to the Galactic center a band of strong absorption is detected within the strong Galactic emission, caused by the HII gas.

[2]Data available at `http://www3.mpifr-bonn.mpg.de/survey.html`
[3]Data available at `http://cdsarc.u-strasbg.fr/viz-bin/qcat?J/A+A/525/A138`

1.3.2 Polarized intensity

Although there are a few existing total intensity all-sky surveys at several frequencies, there are just a small number of large scale polarization observations. The ones at 22 GHz (WMAP, Page et al., 2007) and 1.4 GHz (Reich et al., 1986) will be discussed in the following. The measured linear polarization from the synchrotron radiation contains information about the total magnetic field strength and orientation of the ordered component of the magnetic field perpendicular to the line of sight.

As seen in the left image of Fig. 1.9 at 22 GHz strong linear polarization is detected in the inner disc and the center of the Galaxy. Besides of that, strong features show up along the North Polar Spur (NPS) and at the so called Fan Region (at a galactic longitude of 140° and a galactic latitude of 8°). Up to now it is not clear, what causes the strong polarization in the Fan region. Polarization also can be observed along the other loops, even as it is not as strong as in the region of the NPS.

Toward 1.4 GHz (right image of Fig. 1.9) strong depolarization is coming up along the Galactic plane for galactic latitudes below 30°, which leaves a patchy structure. Nevertheless, strong polarization toward the North Polar Spur and Fan region is still visible.

Some measurements from smaller regions of the sky are existing even at lower frequencies, like at 240 MHz (Wilkinson, 1973). Most of them were observing the strong polarization of the Fan region, which is still visible even at the lowest frequencies. In most of the other parts the depolarization is so strong that no more polarization is visible.

The problem of the depolarization at low frequencies was already discussed in Sect. 1.2.2. Especially the lower resolution of telescopes at low frequencies is a problem, as well as the need of a high frequency resolution. New antenna arrays provide better beam resolution, but unfortunately have problems of missing spacings, therefore some of the large-scale emission cannot be detected.

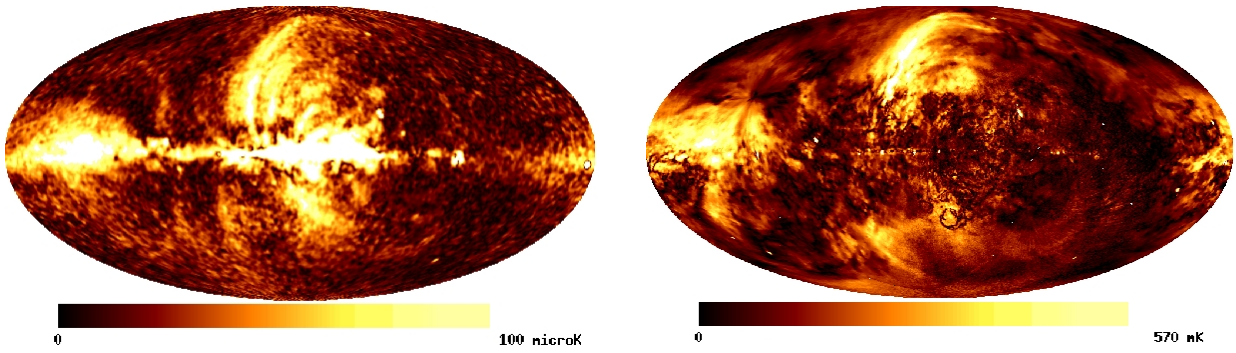

Figure 1.9: All-sky surveys of the linear polarized intensity ($\sqrt{Q^2 + U^2}$) in Galactic coordinates. Left: 22 GHz map from WMAP (Page et al., 2007). Right: 1420 MHz map by Reich & Reich (1986).

1.3.3 The Faraday sky

As the radiation from extra-galactic sources gets rotated by passing the magnetized medium of the Milky Way, these sources can be used to model the RM structures in the Milky Way. In the same way pulsar measurements can be used, as pulsars have no intrinsic polarization and all of the observed polarization is caused by the Milky Way foreground. Measurements of the Faraday rotation give information about the strength and direction of the line of sight component of the magnetic field. One of the most prominent all-sky RM map was produced by Taylor et al. (2009) using more than 37,000 measurements of polarized sources provided by the NRAO VLA Sky Survey (NVSS (Condon et al., 1998)). These data cover the sky down to a declination of $-40°$. With the high number of data on average more than one data point per square degree is available. For the calculation of the RM value two frequency measurements at 1364.9 MHz and 1435.1 MHz were available.

A new reconstruction using the NVSS data plus a number of other catalogs, Oppermann et al. (2012) created an updated version of the RM sky as seen in Fig. 1.10. They introduced a weighting to the data depending how reliable they were. The judgment was done by using information of the position and the number of frequencies for the calculation of the RM values. Whereas the RM values obtained from the NVSS were calculated just with two frequencies, other catalogs provided RM values from a higher number of frequency measurements.

The RM maps show an antisymmetric large scale structure. At positive galactic latitudes four quadrants can be recognized with a change from negative to positive and again from negative to positive RM values. At negative galactic latitudes the structure is divided into negative RM values at longitudes from 0 to 180° and positive RM values at longitudes from 180 to 360°. Beside of that, the largest RM values of a several 100 rad/m^2 can be

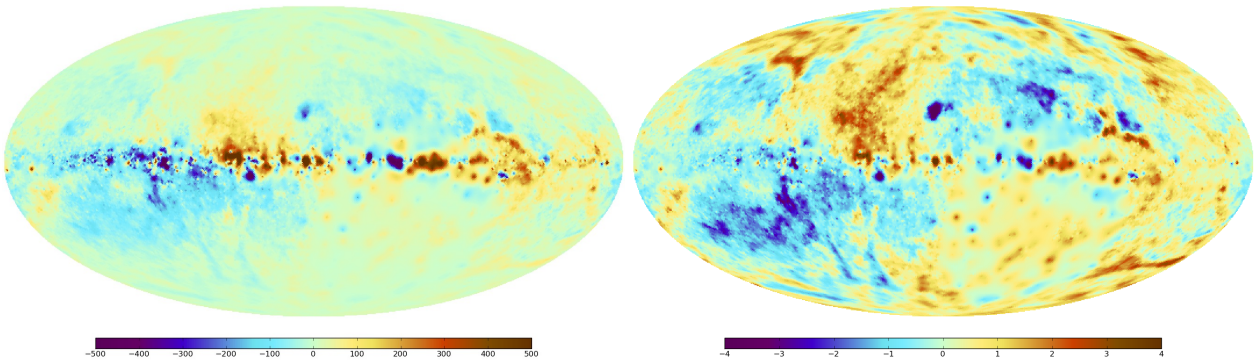

Figure 1.10: RM all-sky map from Oppermann et al. (2012). The maps are based on interpolation of RM measurements. In the right handed image (RM values ranging from -4 to 4 rad/m^2) the Galactic disc is subtracted from the left handed image (RM values ranging from -500 to 500 rad/m^2), wherefore the Galactic halo with smaller RM values becomes better visible.

found along the Galactic plane, where a high electron density and strong magnetic fields are present. Lower values of a few 10 rad/m^2 can be found in the halo of our Galaxy (Fig. 1.10 right handed). As the plotted RM values are giving an information about the magnetic field pointing toward (RM>0) or away (RM<0) from us, a magnetic field model for the Milky Way can be obtained. One model to explain the antisymmetric pattern is given by the AO dynamo from Han et al. (1997).

Chapter 2

The Low Frequency Array (LOFAR)

The Low Frequency Array (LOFAR) (van Haarlem et al., 2013) is an radio aperture synthesis array, with a frequency coverage between 10 to 240 MHz. It is part of a new generation of arrays and a pathfinder project of the Square Kilometer Array (SKA). Whereas in the old telescopes the mechanics have priority, LOFAR is known to be a software telescope. The observations are not anymore done by pointing the telescope into one direction on the sky, but by observing the entire sky and calculating a direction in the sky afterwards. The number of pointing directions is mainly limited due to computer performance. LOFAR currently consists of 49 stations, 36 core and remote stations in the Netherlands and 9 international stations located in Germany (6), France, Sweden and the UK. For experiments for which long baselines are not needed, the international stations can be used separately as single stations.

A LOFAR station contains two arrays with different antenna types. Observations from 10 to 90 MHz are performed with the Low Band Antennas (LBA), frequencies from 120 to 240 MHz are observed with the High Band Antennas (HBA). A LBA consists of two linear dipoles that are perpendicular to each other (Fig. 2.1 left handed). The dipoles in all

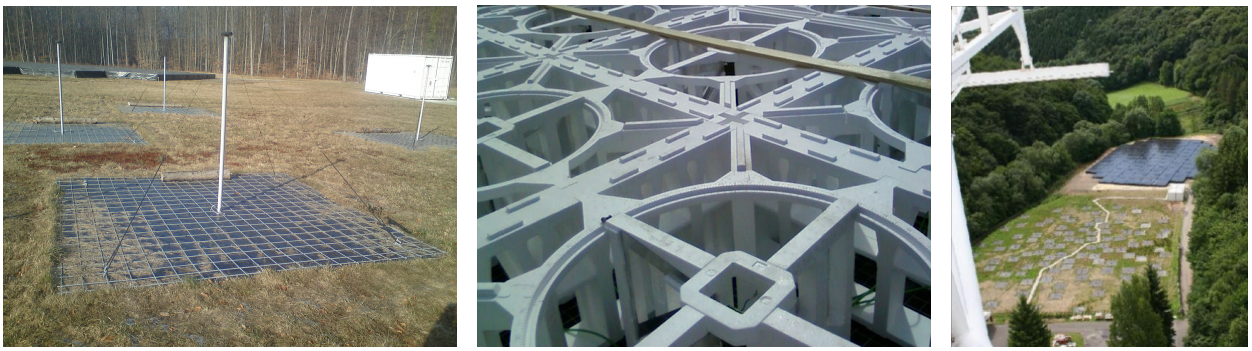

Figure 2.1: Left: The LBA antenna field in Tautenburg with a single antenna in the front. Middle: HBA antennas within a tile (Credits: ASTRON). Right: The Effelsberg LOFAR station as seen from the top of the 100 meter dish (Credits: J.Anderson).

LOFAR antennas are oriented in the north-east to south-west direction called the X dipoles, and the Y dipoles in north-west to south-east direction as shown in right plot of Fig. 3.15. HBAs have elements of two perpendicular, bow-tie dipoles. 16 of the elements arranged in a quadratic 4×4 pattern form a HBA tile (Fig. 2.1 middle). The signals from the X and the Y dipoles within a tile are combined in two analog beam-formers. The LBAs of the LOFAR stations are placed in a quasi-random pattern to reduce the side-lobes of the station beam. The HBA tiles are placed close to each other to reduce the space requirements, unfortunately this causes strong side-lobes.

2.1 LOFAR Single Station

Instead of using several LOFAR stations as an aperture synthesis array for high resolution imaging, it is possible to use just a single station as a phased array. In this case only short baselines within one station are used, what allows to study large scale emission, which is solved out by using the long baselines between distant stations. The motivation of using a single station for scientific reasons will be discussed in the following section. Furthermore the data handling of single station observations will be described.

Table 2.1: Parameters of an international LOFAR station (van Haarlem et al., 2013).

frequency [MHz]	λ [m]	D [m]	Θ_{res} [deg]	A_{eff} [m^2]
30	10.0	65.0	9.7	2516.0
45	6.67	65.0	6.46	1378.0
60	5.0	65.0	4.85	800.0
75	4.0	65.0	3.88	512.0
120	2.5	56.5	2.59	2400.0
150	2.0	56.5	2.07	2048.0
180	1.67	56.5	1.73	1422.0
200	1.5	56.5	1.55	1152.0
210	1.43	56.5	1.48	1045.0
240	1.25	56.5	1.29	800.0

In an international station the LBA field contains 96 antennas and the HBA field is made of 96 tiles. The beam resolution of the array is defined by:

$$\Theta_{res} = \alpha \frac{\lambda}{D} \tag{2.1}$$

with λ being the wavelength of the observation and D being the longest distant between two antennas in the array. The factor α depends on the telescope properties and is taken as 1.1 for the LBA antennas and 1.02 for the HBA antennas (van Haarlem et al., 2013). The LBA field has a diameter of 65 m, which leads to beamwidths from around 10° at 30 MHz to around 4° at 80 MHz. The HBA field has a diameter of 56.5 m, the resolution at 120 MHz is around 2.6° and around 1.3° at 240 MHz. A summary of important parameters for a single international station at several frequencies is given in Table 2.1. The given effective area A_{eff} is contained from numerical simulations, accounting for overlaps of the dipoles. The full table with all information for the core, remote and international stations is available in the LOFAR paper by Haarlem et al. (2013). The design of the LOFAR station located in Effelsberg is shown in Fig. 2.2. The black points denote the antenna positions. As for the all-sky imaging with the HBAs just one antenna per tile is

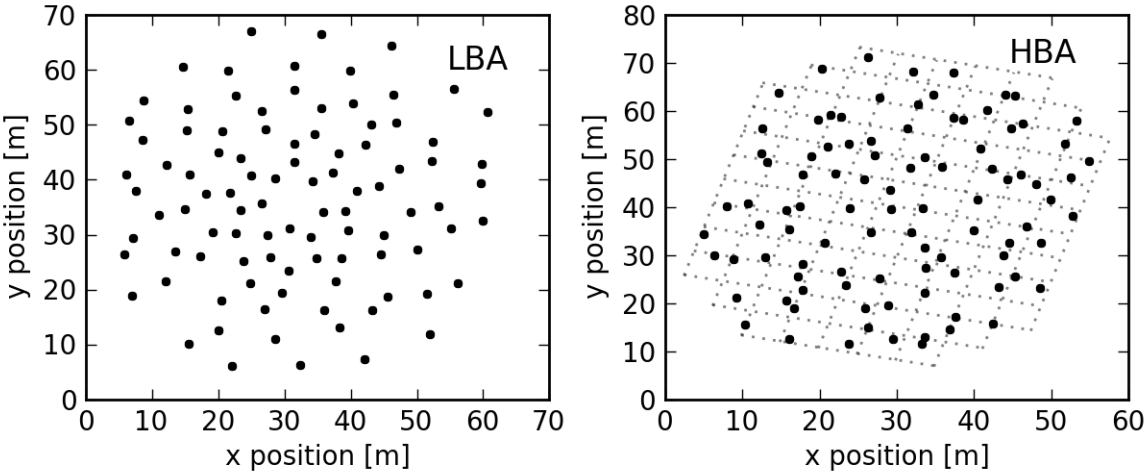

Figure 2.2: Positions of the LBAs (left handed) and HBAs (right handed) for the international station in Effelsberg. For the HBA field the squares show the structure of the tiles. Each of these tiles contain 16 antennas. The black point denote the position of the single antennas used for the all-sky imaging.

used for the observations (will be discussed in Sect. 3.7), the black points show the position of the chosen antenna within one tile.

There are three different data-products from the station: a data stream from the station beam-former, cross-correlation matrices from the station correlator, and dipole data from the Transient Buffer Boards (TBBs).

When the radio signal enters the antenna already a first amplification is performed. Afterwards the signal is transported to the processing cabinet via coaxial cables, where it enters first the digital ReCeiver Units (RCUs). In case of an international station each dipole of the antenna field contains one RCU in the cabinet. The RCUs contains an analog filter to suppress the strong terrestrial radiation, showing up at low frequencies. Then the signal gets digitized by a 12 bit analogue to digital converter (ADC) at a sampling frequency of 200 MHz (for 100 MHz total bandwidth) or 160 MHz (for 80 MHz total bandwidth- just for RCU mode 6). A summary of the RCU modes with related frequency filters and clock properties can be found in Table 2.2. The frequency spectrum, for the RCU modes used for the observations of this work, is plotted in Fig. 2.3. The behavior of the spectrum follows mainly the bandpass (sensitivity) of the antennas. Peaks in the spectrum

Table 2.2: Summary of the RCU modes available at an international station.

RCU mode	antenna field	frequency range [MHz]	sampling frequency [MHz]
3	LBA	10 - 90	200
4	LBA	30 - 90	200
5	HBA	110 - 190	200
6	HBA	170 - 230	160
7	HBA	210 - 240	200

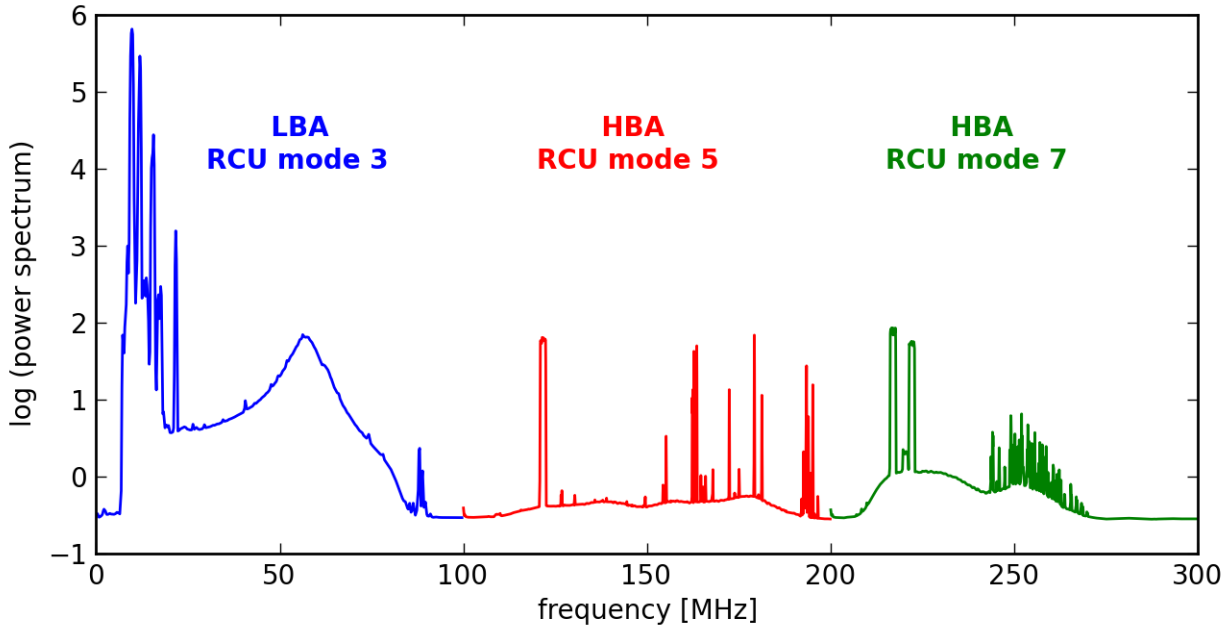

Figure 2.3: Combined LOFAR spectrum from RCU modes 3, 5 and 7. Due to strong RFI, filters in the LOFAR software are used to suppress frequencies below 10 and above 240 MHz.

indicate strong Radio Frequency Interference (RFI) at the given frequency.

Afterwards there are two main options to continue with the signal- whether using the TBBs or the Remote Station Processing (RSP) boards. The RSP is used for all beam-formed observations, including pulsar observations, and correlation for the all-sky imaging. For this, the signal coming from the RCUs is splitted into 512 subbands (frequency channels) via a polyphase filter, following a fast Fourier transformation (FFT). In case of the beam-forming into one direction in the sky a geometrical delay is applied during the correlation of the data (for more information have a look at Sect. 3.2). The correlation between all RCU can be performed without any delay correction, wherefore the entire visible sky can be imaged. In this case an integration time of multiples of seconds per single sub-band is possible. This is good enough for calibrating the station (the original aim of the station correlator) or simple all sky maps, but not for polarization studies.

Beside the RSP boards, every LOFAR station contains ring buffers, so called Transient Buffer Boards (TBBs). These boards can store data from all receiver units of the station, i.e. from a single LBA dipole or from a single HBA tile. The data to be stored is either the raw ADC data from the receivers or a selection of subbands. In subband mode a maximum of 487 out of the 512 possible subbands can be used at the same time. In their original configuration the TBBs have enough memory to store 0.5 GByte from each receiver, which corresponds to an observation time of 1.3 s. A memory upgrade to a storage depth of 2 GByte or 5 s has been done in the meantime.

The data on the TBBs are stored in a ring-buffer, with new data overwriting the oldest data once the buffer is fully filled. Writing of new data is stopped by a software command which can be given by an internal[1] or external trigger or at a freely chosen time. The TBBs are not stopped at exactly the same time by the control software, but the data is stored in packets with a full time-stamp in the header, which allows to align the data afterwards. When the TBBs are stopped a chosen amount of data can be transferred to the recording computers. The data taking time is dominated by the time it takes to transfer the data from the TBBs. With the setup at Effelsberg the transfer of the full dataset for 1.3 s of data (96 GByte) takes about 15 minutes. Using the full memory after the upgrade of the TBBs would have increased this to about 1 hour. The data are written out in a HDF5 format. The LOFAR data access library contains routines for reading in these files.

2.2 The advantage of using TBB data for imaging

Using the raw voltages from the TBBs and a software correlator brings along two main advantages. One is getting a higher frequency resolution than given by the station correlator. The other is being able to observe the full sky in a more efficient way, compared to the small sky patches as observed with the station beam-former. Especially the advantages of the high frequency resolution will be discussed in the following.

To study polarization at low frequencies a higher frequency resolution is needed, to avoid bandwidth depolarization effects. The given resolution of 200 kHz from the station correlator would not be sufficient. To measure RM values up to around 200 rad/m^2 at 30 MHz, a frequency resolution down to around 5 kHz is needed. Using instead a bandwidth of 200 kHz, as given by the station correlator, will cause depolarization within the channel, as the measurable difference of the polarization angle is given by:

$$\Delta\phi = \mathrm{RM}(\lambda_1^2 - \lambda_2^2) \approx 2\lambda_0 \Delta\lambda \mathrm{RM} \tag{2.2}$$

with λ_0 being the center of the frequency band between λ_1 and λ_2.

If enough recording computers are available, the observations with the TBBs allows additional quasi-simultaneous pulsar observations. These can be used at a later point for the polarization calibration of the Faraday Rotation due to the ionosphere. In this case the pulsar will be observed for several minutes, while the TBB data are written to disc, which needs a few minutes because of the large data volume. This allows a more accurate Faraday rotation correction, when using just the theoretical models which are produced just every second hour.

By using correlated TBB data, all frequencies are observed simultaneously. This is not the case for data from the station correlator, where always just one frequency channel can be observed at a given time. By observing with the station correlator all channels from 30 MHz

[1]The TBBs have a system to detect peaks in raw data and report them to the control computer, which was not used for this work.

to 80 MHz, the time difference between the first and the last channels amounts to more than 4 minutes. Therefore using TBB data is useful to study spectral behavior of sources, which strongly change even on short time scales of seconds or less, like it is the case for bursts from Jupiter or the Sun. And even the polarization study benefits from simultaneous frequency observations, as the ionosphere is partly strongly varying even on short time scales of seconds.

Beside of the scientific motivation, an other important point comes up with the data reduction. As described in the further Chapters, by observing the sky not just astronomical sources are detected, but also signals from terrestrial sources, so called Radio Frequency Interference (RFI). Most of these signals appear in the narrow band and are therefore better resolved at a higher frequency resolution and are smeared over a larger frequency range otherwise. In this way a higher frequency resolution is helpful to remove the RFI in a more effective way. This is especially important for studies at the lower part of the LBA spectrum where a lot of RFI is present. The Effelsberg station is an example where more RFI than at most of the other stations is present. An example for a spectrum from the Effelsberg Station with strong RFI peaks over the entire frequency range can be seen in Fig. 3.9.

Chapter 3

Data Reduction

In the following Chapter the data reduction of the LOFAR Single-Station data will be described. The reduction scheme will start with the raw data as observed with the single antennas and ends with the final images, which can be used for scientific studies. Furthermore this includes the transformation from raw voltages to visibilities, the data inspection and removal of bad data, and the calibration of the data. The calibration procedure includes all corrections caused by the instrumental- and the atmospheric-effects. Furthermore the essential steps of the self-calibration method and the HBA all-sky imaging will be explained. General information for all the further discussion on the data reduction can be found in the literature, e.g. in Thompson et al. (2001).

The entire software for the data reduction presented in the following chapter is developed as part of this thesis. A summary of the most important software tools can be found in the Appendix.

3.1 Relation between coordinate systems

All single station observations are obtained in the Horizon system. After calibration, at which directional cosines have been applied, the data has been transformed into Equatorial coordinates. For the final imaging step the transformation into Galactic coordinates is needed. This enables us to combine single observations and to map out the entire visible sky. Furthermore, the large-scale structures of the Milky Way are better defined for further analysis by using Galactic coordinates, e.g. the range of the Galactic plane can be describe by the galactic latitude only.

3.1.1 Relation between ground and sky based coordinate systems

The measurements of a telescope on the earth surface correspond to intensities in the sky. By using an interferometer, the observation is done with a high number of antennas. These antennas are spread over a large area, whereby the incoming signal from the sky varies for each antenna. To combine all these various signals a conversion between the coordinate

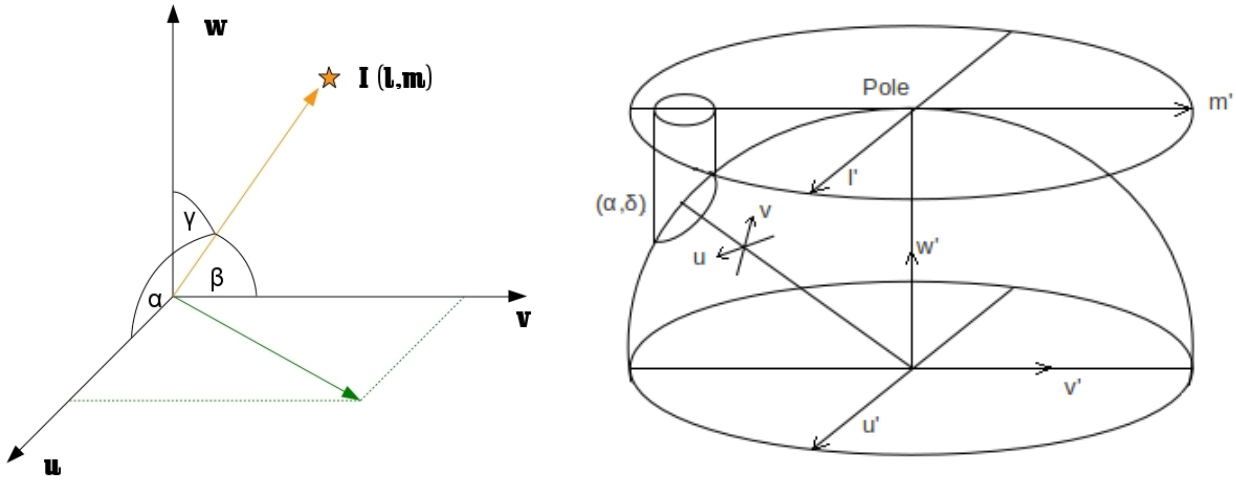

Figure 3.1: Left: Relation between ground and sky based coordinate systems. Right: Projection of sky coordinates into the lm-plane (Adapted from Thompson et al., 2001).

system on the ground into the coordinate system on the sky is needed. The coordinate system on the ground, which describes the antennas positions, is defined by (u,v,w) coordinates, whereby v is pointing toward south, u points toward east, and w points into the sky toward the direction of the center of the observed field. For a plane array, like a single LOFAR station, the w component can set to zero. For the coordinate system on the sky (l,m,n) coordinates are used, which are called direction cosines:

$$l = \cos\alpha \tag{3.1}$$
$$m = \cos\beta \tag{3.2}$$
$$n = \cos\gamma \tag{3.3}$$

with the following relation:

$$l^2 + m^2 + n^2 = 1\,. \tag{3.4}$$

The coordinate system is defined in such a way that the coordinate l corresponds to the east-west direction and m to the north-south direction. The coordinate n can be set to one, if just a small region in the sky is observed. Figure 3.1 illustrate the relation between the earth and sky coordinate systems and provide a definition of the angles α, β and γ. The relation between the different coordinate systems is a two-dimensional Fourier transformation, converting the measurements of an interferometer in the (u,v) domain into sky intensities measured in (l,m) coordinates (see Sect. 3.3). In practice imaging the entire visible sky can be done by plotting the direction cosines l and m from -1 to 1.

In order to combine observations obtained at different locations the direction cosines need to be converted into the Horizon coordinate system. The azimuth (A) and the elevation (h)

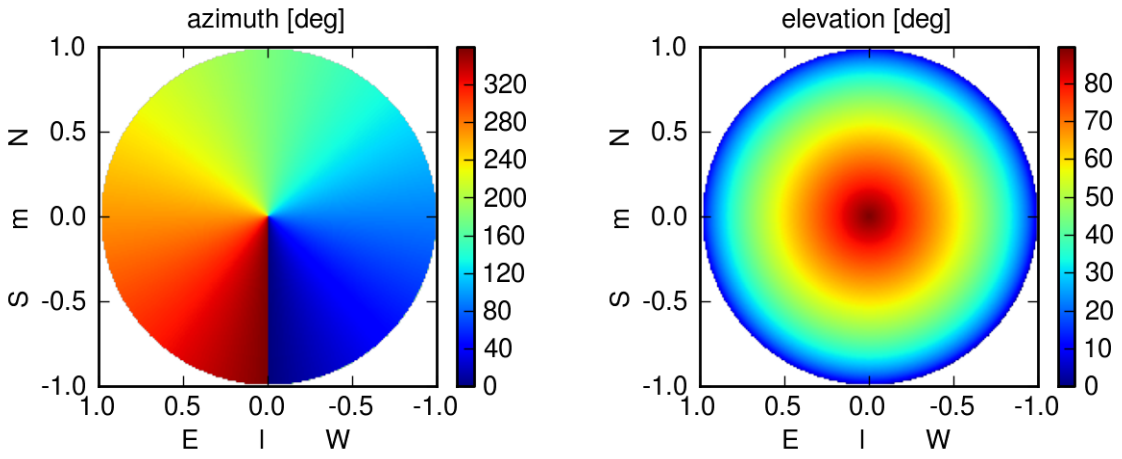

Figure 3.2: The azimuth (left) and elevation (right) in the (l,m) coordinate frame following the Eqs. (3.5) and (3.6). An elevation of 90° correspond to the zenith and the horizon is at an elevation of 0°. The azimuth counting starts in the south and goes anti clock wise around.

of the Horizon system can be related to the direction cosines using trigonometry. Hereby is the azimuth A described by

$$A = \arctan\left(\frac{m}{l}\right) \tag{3.5}$$

that runs from south (0°) to north via west. The elevation h is the angle starting at the horizon running toward the zenith and is defined by

$$h = \arccos\left(\sqrt{m^2 + l^2}\right). \tag{3.6}$$

The elevation range from 0° at the horizon to 90° in the zenith. Figure 3.2 displays the relation between the individual coordinates of both systems.

3.1.2 Coordinate transformation between the Horizon, Equatorial and Galactic system

In order to combine all sky maps from different dates, times or stations, a common coordinate system is needed. The most suitable ones for this purpose would be the fixed Equatorial or the Galactic coordinate system.

The Equatorial system uses a projection of the Earth's equator into the celestial sphere. In this way the sky is divided into a northern and a southern sky, whereby the declination is positive toward the north pole and negative toward the south pole. The conversion between the Horizon system and the Equatorial system can be done by using the following transformations. Hereby is the declination δ is defined as:

$$\sin\delta = \sin h \sin\varphi - \cos h \cos\varphi \cos A\,. \tag{3.7}$$

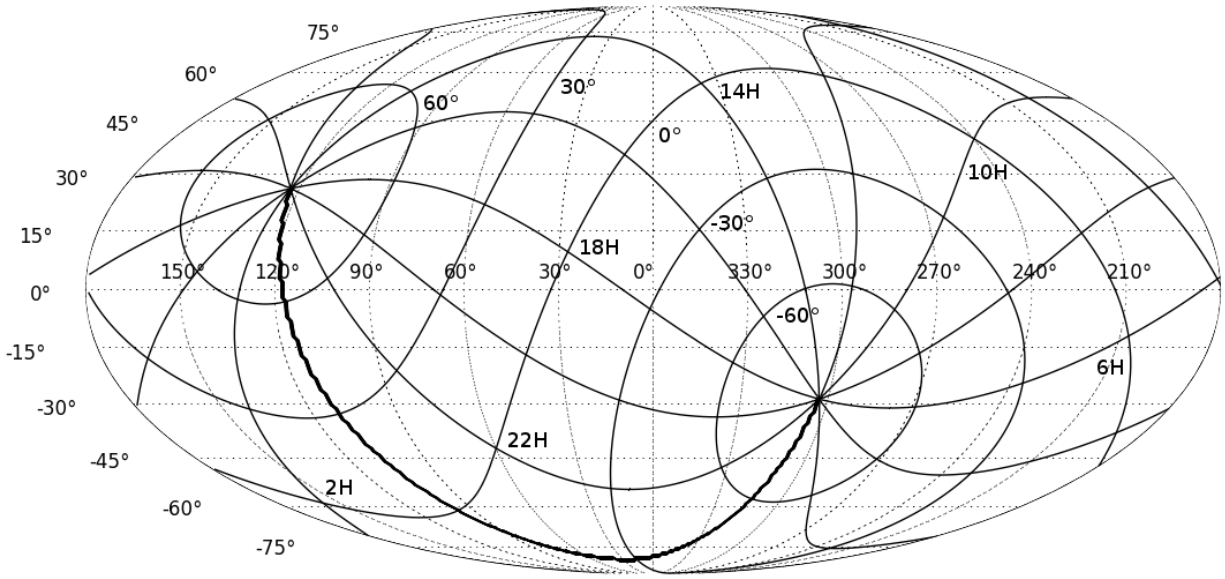

Figure 3.3: Relation between Equatorial (solid lines) and Galactic (dash lines) coordinates.

The hour angle of the vernal equinox can be calculated as

$$\tan\tau = \frac{\sin A}{\cos A \sin\varphi + \tan h \cos\varphi} \tag{3.8}$$

and by knowing the Greenwich time θ_0, the longitude λ, and the latitude ϕ of the telescope position, the right ascension α can be calculated via

$$\alpha = \theta_0 + \lambda - \tau\,. \tag{3.9}$$

For the final imaging process the galactic latitude (b) and longitude (l) is used. The galactic longitude l = 0 is defined as the center of the Milky Way and counts right-to-left up to 360°. The galactic latitude divides the Galactic sphere in a northern and southern sky, which is different to the Equatorial sphere see Figure 3.3. The transformation between the Equatorial system and the Galactic system is described by:

$$\sin b = \sin\delta \sin 27.13^\circ + \cos\delta \cos 27.13^\circ \cos(192.86^\circ - \alpha) \tag{3.10}$$

$$\tan x = \frac{\sin(192.86^\circ - \alpha)}{\cos(192.86^\circ - \alpha)\sin 27.13^\circ - \tan\delta \cos 27.13^\circ} \tag{3.11}$$

$$l = 303^\circ - x\,. \tag{3.12}$$

These formulas assuming that the Equatorial coordinates are at the epoch J2000, where the Galactic North Pole has the coordinates $\alpha = 12^h51^{min} = 192.86^\circ$ and $\delta = 27.13^\circ$, as

defined by the IAU. In this coordinate system the Galactic plane is located at the galactic latitude of b = 0° - 30°. The region at b = 0° and l = 180° is called the anticenter. The relation between Equatorial (solid lines) and Galactic coordinates (dashed lines) is displayed in Fig. 3.3. Known problems in the transformation between both systems are strongest at the poles.

3.2 The TBB correlator

The data of the TBB system needs to be correlated to be used for all sky imaging. In the correlation two equivalent ways can be employed to convert the raw voltages to visibilities, by using the Fourier transformation (F) and the cross-correlation (X). Depending on which calculation is done first, the correlator is called XF (Lag correlator) or FX correlator (see for example Thompson et al., 2001). The XF correlator is just useful if the observations are obtained with a small number of antennas. In the case of high number of antennas, like for a LOFAR antenna field, is it more practical to use a FX correlator (see Fig. 3.4) instead, as the computing time is much lower.

In this light we introduce the Fourier transformation as:

$$\mathrm{V}(\nu) = \int_{-\infty}^{\infty} \mathrm{E(t)}\, \mathsf{e}^{-2\pi \mathrm{i}\nu \mathrm{t}}\, \mathrm{dt}\,. \tag{3.13}$$

The raw voltages are time dependent measurements of each dipole that are converted via the Fourier transformation into the frequency domain and therefore it results in a frequency spectrum of each dipole (Fig: 3.5).

The cross correlation of the individual spectra of each dipole will generate the so called visibilities:

$$\mathrm{V_{ij}} = \left\langle\, \mathrm{E_i E_j^*}\, \right\rangle \tag{3.14}$$

where the brackets indicate averaging over time and * donates the complex conjugated. In practice the correlation introduces a geometrical delay between each dipole (τ) that is illustrated in the convolution theorem[1]

$$\mathrm{V_i}(\nu)\mathrm{V_j}(\nu) = \mathcal{F}\left(\int_{-\infty}^{\infty} \mathrm{E_i(t)E_i(t-\tau)dt}\right)\,. \tag{3.15}$$

This geometric delay depends on the observed direction in the sky, as the arrival time for the signal depends on the antenna positions. The LOFAR antenna are fixed on the ground and are not able to steer toward an observing direction, generally a LOFAR dipole always observe the entire sky. In case of observing a single source in the sky one would specify a certain delay correction to introduce a beam forming mode. However, for the all-sky imaging the

[1]Note that the convolution theorem also indicates that the FX- and the XF correlation will produce the same results.

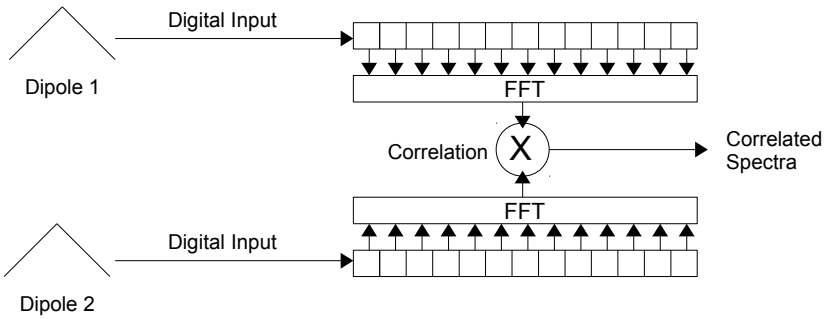

Figure 3.4: Schematic diagram of an FX correlator for two dipoles.

beam-forming mode is not used. The zenith is chosen as the phase center of the correlation, and therefore no geometric delay correction has been applied ($\tau = 0$).

After this step the resulting visibilities can be used for further data processing and imaging described in Sect. 3.3

3.2.1 Handling the TBB data

In developing the correlator software problems had to be addressed and solutions developed. In the following practical solutions and approaches are discussed.

The software is entirely developed in house and written in Python and is running on normal desktop machines. Some of the procedures make use of a library written by the group in Nijmegen (pycrtools) apart from this no specific library is needed. The total running time depends on the IO-qualities of the computing machine. Using a 3.1 GHz Intel Core i5 processor with 4 cores and 8 GB of RAM on the entire 100 GB dataset for 1.3 sec integration time and all dipoles of an international LOFAR station needs around 200 min computing time. This is mostly independent of the chosen frequency resolution. The maximum frequency resolution that can be performed depends on the available memory of the computer. For the study of cosmic ray events the observation lasted mostly just 1 msec. In this case the correlation is done within 2 min and is therefore a fast opportunity to map these events and obtain the direction of the measured signal. The default data output format of this software correlator is an ascii file, which contains the visibilities for all dipoles, as well as information about the observation date and time, the station which was used for the observation and a frequency list. These information are necessary for the further data processing as sketched in Fig. 3.7 and described in detail in the next sections. It should be mentioned that the software for the further data processing, which consists mainly of data inspection, calibration and imaging, cannot just be used by the correlated TBB data as described above. The code runs in the same way for output data from the station correlator. Just the reading in of the

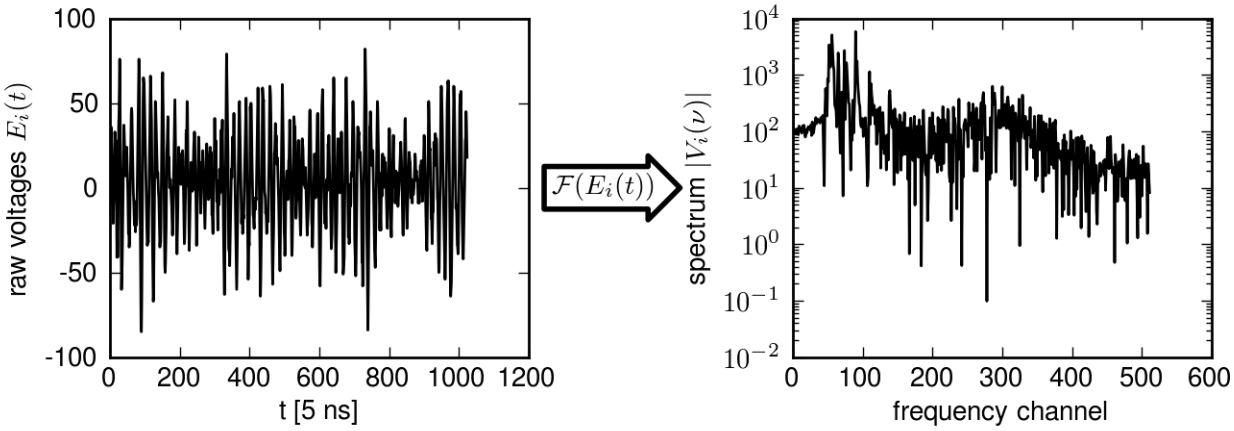

Figure 3.5: Left: Input of a single dipole for 1024 time stamps (every 5 ns). Right: LBA frequency spectrum of the same dipole after the Fourier transformation. Channel 0 corresponds to 0 MHz and channel 512 to 100 MHz.

data has to be varied.

The code allows to read in a several datasets in parallel, in case that the data from one observation are distributed over different data files. This is e.g. the case for the LOFAR station in Effelsberg where the measurements were spread over four data files. Furthermore, this allows to perform a correlation between different stations, e.g. for all Core Stations. This has been developed and tested successfully in collaboration with colleagues from Nijmegen.

In the Fourier transformation process sidelobe effects need to be suppressed, therefore a Window Function has been used on time blocks of raw voltages. There are different window functions existing and the most commonly used ones are the Blackman, Barlett, Boxcar, Hanning, Hamming, and Kaiser windows. For the TBB correlation a Blackmann window has been chosen, which is defined by:

$$\mathrm{w(n)} = 0.42 - 0.5\cos\left(\frac{2\mathrm{n}}{\mathrm{N}}\pi\right) + 0.08\cos\left(\frac{4\mathrm{n}}{\mathrm{N}}\pi\right) \tag{3.16}$$

with n = 0 to N-1 (N is the blocksize; Faint and Read, 2003). This filter was chosen as default choice after several tests with different filter functions, as it produces the best results. Nevertheless, it is possible to choose manually any other filter for the correlation. In the same way the frequency resolution and integration time of the data can be chosen manually.

One of the most challenging parts for the development of the correlator was to keep the computing time as short as possible. For speeding up the code parallelization and matrix multiplication are used. The time consuming part comes mainly from the reading in of the data, especially when the entire 1.3 sec data of all 192 dipoles are used, which is corresponding to a data volume of 100 GB. Due to this large size, the data file cannot be read in at once.

Instead a smaller fraction of the time Δt is read in for all the dipoles, which is split into $\Delta t = m \cdot t_{bz}$, where t_{bz} is the needed time block size to get the wanted frequency resolution. The reading in of the larger time block as needed for the FFT, helps to reduce the total read in time. During the FFT and correlation of the small part of data, already the next time slot is read in in parallel. The factor m is chosen in a way that reading in of the data and FFT and correlation takes nearly the same computing time to optimize the entire process. The FFT is done for each RCU on each time block t_{bz}, which leads to $t_{bz}/2 + 1$ channels in the frequency spectrum. An example for the Fourier transformation from raw voltages of a single dipole to the frequency spectrum is plotted in Fig. 3.5. The left image shows 1024 time stamp measurements made every 5 ns for an individual dipole. After the Fourier transformation 513 frequency channels from 0 MHz to 100 MHz are available. In the right image just the amplitude of the complex values from the Fourier transformation are plotted. The peak area at around 58 MHz (channel 300) is already visible just like the strong RFI at low frequencies. After the integration over the entire observation time the structures are becoming more clear. After the FFT, the correlation between all dipoles and an integration over the m time slots are performed. To chose the most efficient way this is done by using a matrix product

$$\sum_{i=1}^{m} \begin{bmatrix} V_{rcu1}V^*_{rcu1}(t_i) & V_{rcu1}V^*_{rcu2}(t_i) & \cdots & V_{rcu1}V^*_{rcun}(t_i) \\ V_{rcu2}V^*_{rcu1}(t_i) & V_{rcu2}V^*_{rcu2}(t_i) & \cdots & V_{rcu2}V^*_{rcun}(t_i) \\ \vdots & \vdots & \ddots & \vdots \\ V_{rcun}V^*_{rcu1}(t_i) & V_{rcun}V^*_{rcu2}(t_i) & \cdots & V_{rcun}V^*_{rcun}(t_i) \end{bmatrix} = \mathbf{V_{rcu}(t)V_{rcu}(t)}^H \tag{3.17}$$

with

$$\mathbf{V_{rcu}(t)} = \begin{bmatrix} V_{rcu1}(t_1) & V_{rcu1}(t_2) & \cdots & V_{rcu1}(t_m) \\ V_{rcu2}(t_1) & V_{rcu2}(t_2) & \cdots & V_{rcu2}(t_m) \\ \vdots & \vdots & \ddots & \vdots \\ V_{rcun}(t_1) & V_{rcun}(t_2) & \cdots & V_{rcun}(t_m) \end{bmatrix} \tag{3.18}$$

where H represents the conjugate transpose operation. Eq. (3.17) gives the correlation matrix of the visibilities, which is used for the further data reduction. The whole procedure is repeated for each time slot of the entire dataset. Summing up all the correlation matrices leads to the final integration time of 1.3 sec. Of cause it is also possible to correlate just a fraction of the entire dataset.

3.3 From visibilities to calibrated skymaps

The intensities in the sky I are related to visibilities V via a Fourier transformation:

$$\mathbf{V}_{ij}(u,v,w) = \iint \mathbf{J}_i \mathbf{I}(l,m) \mathbf{J}_j^H e^{-2\pi i[lu+mv+w(\sqrt{1-l^2-m^2}-1)]} \frac{\mathrm{d}l\,\mathrm{d}m}{\sqrt{1-l^2-m^2}} \tag{3.19}$$

where u,v,w are the antenna positions on the ground measured in wavelength and l,m are the direction cosines in the sky, and H represents the conjugate transpose operation. If all antennas are build on a flat ground, like it is the case for a single LOFAR station, w = 0 and Eq. (3.19) results in a 2D Fourier transformation simplifying the imaging process:

$$\mathbf{V}_{ij}(u,v) = \iint \mathbf{J}_i \mathbf{I}(l,m) \mathbf{J}_j^H e^{-2\pi i[lu+mv]} \frac{\mathrm{d}l\,\mathrm{d}m}{\sqrt{1-l^2-m^2}}\,. \tag{3.20}$$

In the two equations above **J** is the Jones term, which describes various instrumental and atmospheric effects caused along the physical path of the real signal in the sky to the antennas. The Jones term can be split in a direction depended part **D** and a direction independent part **K**, which can be taken out of the integral of Eq. (3.20) and leads to:

$$\mathbf{V}_{ij}(u,v) = \mathbf{K}_i \left(\iint \mathbf{D}_i \mathbf{I}(l,m) \mathbf{D}_j^H e^{-2\pi i[lu+mv]}\,\mathrm{d}l\,\mathrm{d}m \right) \mathbf{K}_j^H \quad . \tag{3.21}$$

The **D** term includes the square root $\sqrt{1-l^2-m^2}$, because of its direction dependence. The inverse Fourier transformation of Eq. (3.21) is the intensity in the sky:

$$\mathbf{D}_i \mathbf{I}(l,m) \mathbf{D}_j^H = \iint \mathbf{K}_i \mathbf{V}(u,v) \mathbf{K}_j^H e^{2\pi i(ul+vm)} \mathrm{d}u\mathrm{d}v\,. \tag{3.22}$$

Doing the Fourier transformation of the visibilities in Eq. (3.22), not taking any correction into account, gives an uncalibrated image of the sky as seen by the instrument. To illustrate the relation between visibilities and sky intensities, and the influence of the calibration on the data Fig. 3.6 is used. The left-hand side show the "uv-plots" displaying the amplitudes and phases of the visibilities of each antenna pair in the uv-plane. The coordinates are calculated with $u = (x_i - x_j)/\lambda$ and $v = (y_i - y_j)/\lambda$, hereby are x and y the positions of the antennas and λ is the observing wavelength. The right-hand side of the figure shows the observed sky intensity. This image is produced by a Fourier transformation on the visibilities following Eq. (3.22). Hereby are the intensities in sky coordinates l and m. Note that the synthesized beam (Fig. 3.8) is calculated via a Fourier transformation of the data coverage in the uv-plane. The color coding of the visibilities shows stronger amplitudes on short uv distances. This is expected as the large-scale structures of the observed emission are detected on short baselines. The phases shows irregular pattern indicating that calibration needs to be applied. After the calibration process the phases of the visibilities show stripes, which confirms that the calibration was successful. The stripes are caused by the two strong point sources Cyg A and Cas A, which are tar away from the pointing direction in the zenith.

The figure showed the improvement of the image quality before and after the calibration process. The aim in the calibration is to determine the measured intensities as close as possible to the real signal in the sky, therefore the correction **K** and **D** has to be determined. The direction independent part **K** is determined in the calibration process, including a complex antenna gain **G** and the bandpass correction **B**. These correction are applied to the visibilities only as described in Sect. 3.5. Similar to this **D** can be broken into the Faraday

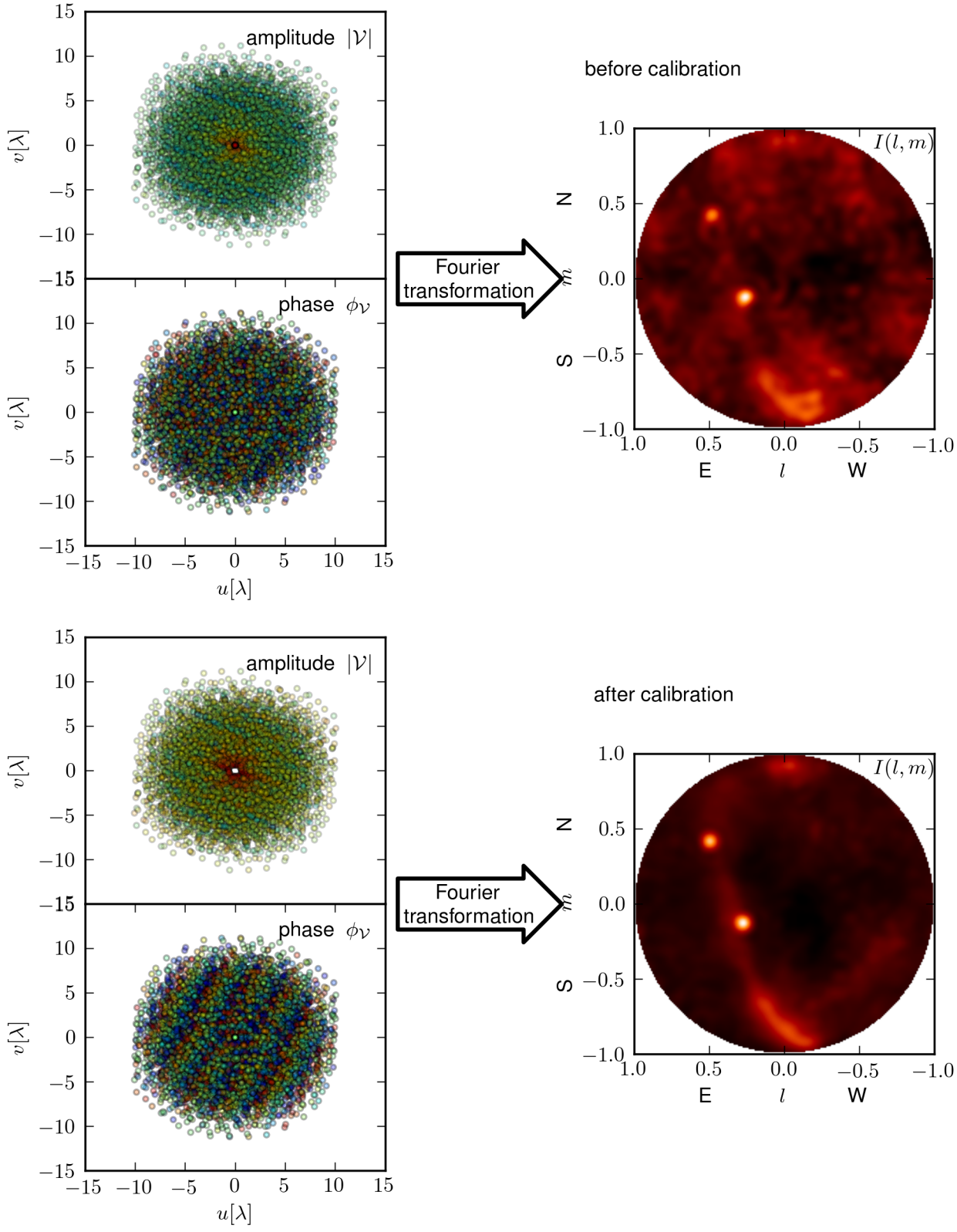

Figure 3.6: From visibilities (left) to intensities (right) for uncalibrated (top) and calibrated data (bottom).

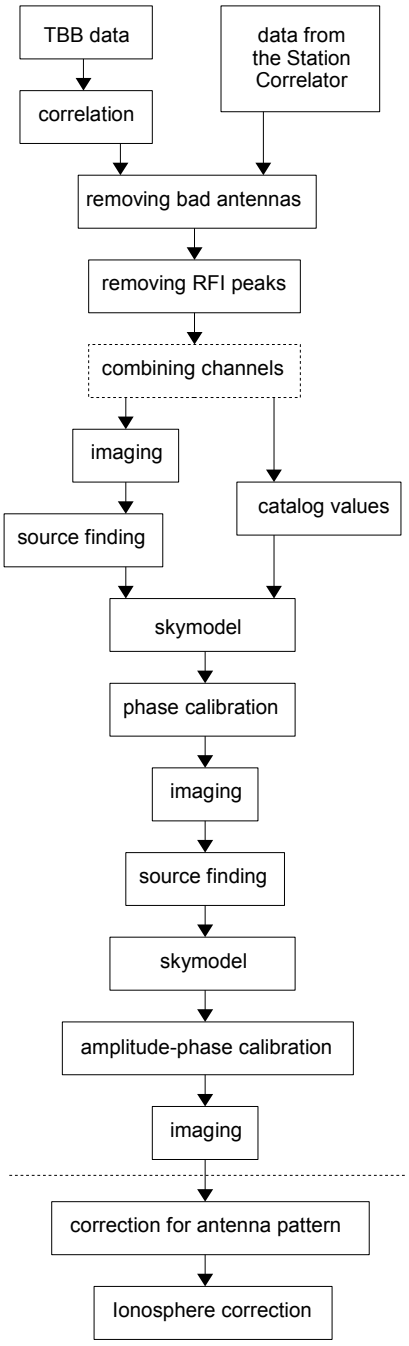

Figure 3.7: The calibration pipeline as described in detail in this Chapter.

Rotation **F** and the antenna response pattern **E** (primary beam) term. The Faraday Rotation as well as the antenna primary beam are direction depending changing with the position in the sky. Therefore these corrections are applied in the imaging plane and are in our case the most important effects. Generally the Eq. (3.21) can now be rewritten in direction independent and direction dependent components like:

$$\mathbf{V}_{ij}(u,v) = \mathbf{G}_i\mathbf{B}_i\mathcal{F}\left(\mathbf{E}_i\mathbf{F}_i\mathbf{I}(l,m)\mathbf{F}_j^H\mathbf{E}_j^H\right)\mathbf{B}_j^H\mathbf{G}_j^H \tag{3.23}$$

with $\mathcal{F}$ denoting the Fourier Transformation and the indices i and j the antenna pair.

The Fig. 3.7 provides an overview of the individual levels of the calibration procedure starting from antenna measurements to calibrated skymaps. In particular, the necessary steps are described in the following sections. Removing bad antennas and RFI will be discussed in Sect. 3.4. The phase and amplitude-phase calibration is explained in Sect. 3.5, these are based on the measurements of reference sources and therefore the source finding algorithm is illustrated in Sect. 3.6. The imaging in the self-calibration process and the final imaging is explained in the last section see Eq. (3.22). The correction of the antenna pattern is discussed in Sect. 4.8 and the ionospheric corrections are discussed in Sect. 3.10.

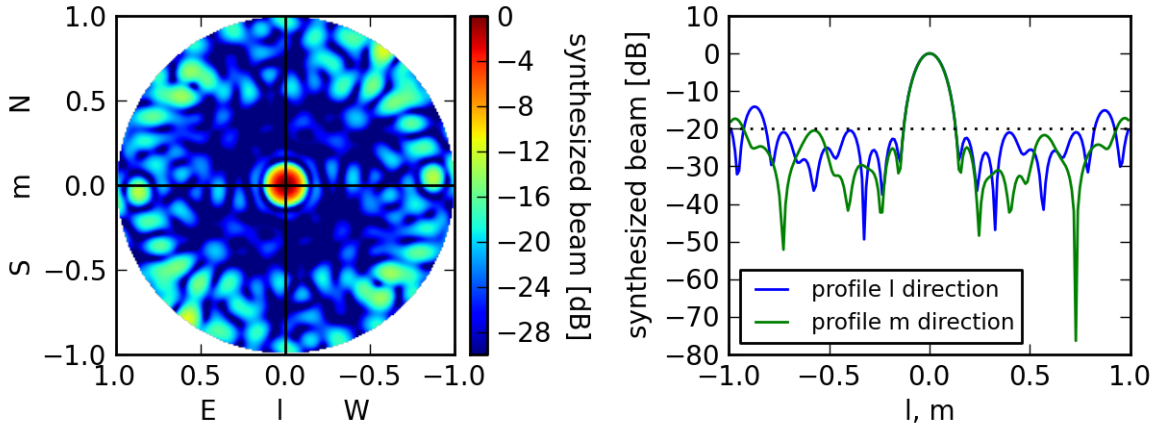

Figure 3.8: The synthesized beam of the LBA field at 45 MHz. The right hand plot shows the profile through the synthesized beam in l and m direction. The sidelobes are for most parts of the skymap below 1% of the main lobe. The edge of the skymap, where the sidelobe level is above 1%, is blanked later in the creation of the sky survey (Chapter 4).

3.4 Data inspection and preparation

The first step in the data processing of the visibilities is to identify and delete Radio Frequency Interference (RFI) and bad antennas from the data. Such data will cause problems in the calibration and will limit the quality of the sky image.

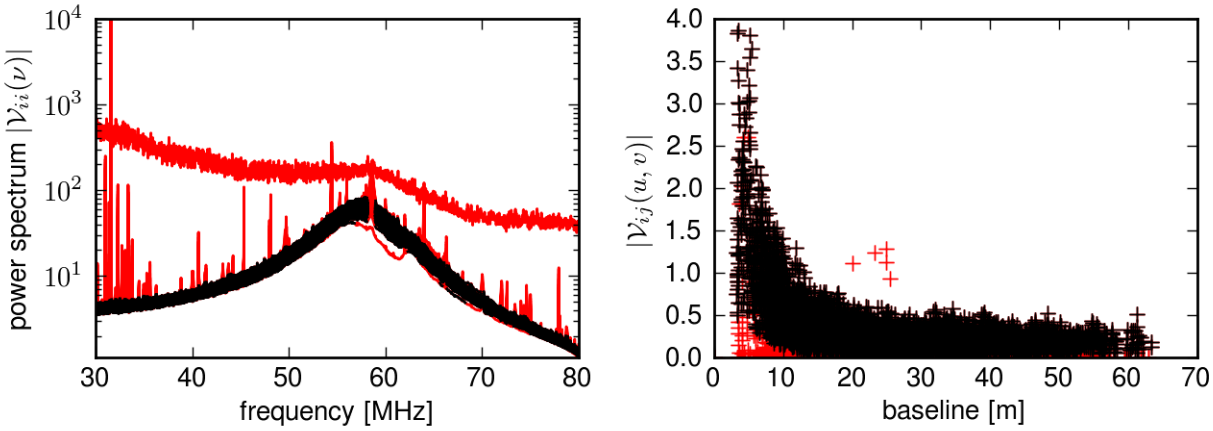

Figure 3.9: Observation done with the TBBs from the Effelsberg station. Left: Autocorrelation spectra over the frequency range from 30 to 80 MHz with 6400 channels. One dipole with too high signal over the entire frequency range and one with too low intensities at a certain frequency range is visible. Beside of that, a lot of RFI peaks are seen. The flagged dipole and frequency channels are marked red. Right: Amplitudes of the cross-correlation visibilities over baseline length at 65 MHz. Flagged baselines are marked red.

The data from the TBB system have the advantage that one can generate datasets with high frequency resolution in the spectral domain. Such high frequency resolution can be useful to resolve and remove narrow band RFI, which is otherwise smeared over a wider frequency range. The RFI can have different reasons and origins, and varies between all LOFAR stations one having bigger problems than others. For the station in Effelsberg the strongest RFI is coming from the direction of the nearby 100 m telescope. Different tests let assume that this is mainly caused by reflection on the surface of the 100 m dish. Just a minor fraction of the RFI is expected to origin from the telescope mechanics. This RFI is time- and frequency-depending due to the different positions of the dish and the varying sky emission. The RFI signal is not only strong in total intensity it is also strongly polarized. Generally the quality of the visibilities is estimated in the time domain, but in this special case of the TBB datasets of using only short observations times flagging in the time domain is not possible and an other solution has been developed. The search for bad data is done in two ways.

The first one is by looking at the power spectrum over the entire frequency range, the other by looking at the amplitudes of the visibilities of a single frequency channel. In practice the power spectrum is used to identify bad antennas with too low or too high amplitudes. This is done by comparing the power spectrum of each dipole with the mean value of all dipoles. An example of this is shown in the left-hand image of Fig. 3.9, where a dipole with a too high amplitude is clearly visible. After that, the power spectrum is used to identify strong RFI peaks. Most of the peaks are narrow band RFI and therefore easy to identify.

The second way is flagging within a single frequency channel, the amplitudes from the cross correlations of the visibilities are plotted over the baselines like done in the right-hand image of Fig. 3.9. Visibilities with a similar baseline distance have comparable amplitudes, as they pick up the same signal from the sky. Extended emission is detected by shorter baselines, whereas point sources better show up in longer baselines. Outliers that differ to much from the mean value at a given baseline distance, will be removed by flagging the corresponding baseline.
Even as the search for RFI is done separately for both dipole orientations, in the end always both dipoles of one antenna will be flagged, to make sure that the out coming polarization signal is right. As described in Sect. 1.2 the total and polarized intensity is always a combination of the single dipole signals. All the flagging is done automatically without manual impact. Nevertheless, the flagging options can be verified inside the code. Unfortunately even flagging carefully in the spectral domain some strong RFI may remain and will appear as sources in the skymap. This is the case if the brightness of the RFI source is in the order of the strongest astronomical sources or slightly higher. Unfortunately strong unknown sources can also cause problems in the calibration of the data and therefore cannot be ignored. The method dealing with such RFI signals is described in the calibration process in Sect. 3.6.
Generally the RFI situation in Effelsberg is such that at least around 10% of the frequency channels in the range from 30 to 80 MHz need to be deleted.

3.5 Gain calibration

The calibration of the visibilities is necessary to correct for atmospheric or instrumental effects. For the observing system this can be errors caused by the cable delays and varying system noise temperature. At frequencies observed with LOFAR the atmospheric problems are mainly caused within the ionosphere. Errors in position and intensity of the data are generally caused by different origins, wherefore the visibilities are separated in an amplitude- and a phase-part

$$\mathcal{V} = |\mathcal{V}|\, e^{\phi_v i} \tag{3.24}$$

such that the calibration can be done independently. Errors in the phases ϕ_v causes errors in the source positions, whereas errors in the amplitude $|\mathcal{V}|$ will affect the measured sky intensities.

In order to correct the visibilities one observe a calibrator sources with known positions and intensities. These calibrators should be unresolved and for the amplitude calibration its intensities should not be variable. In addition, the amplitudes need to be strong enough to have a good signal to noise ratio on each baseline between antenna pairs. The calibrated visibility is

$$\mathcal{V}_{cal} = \frac{\mathcal{V}_{uncal}}{G_{ij}} = \mathcal{V}_{uncal} \left(\frac{S_c}{\mathcal{V}_c} \right) \tag{3.25}$$

with S_c being the flux density and $\mathcal{V}_c$ the visibilities of the calibrator source. $G_{ij} = G_i G_j^*$ is the complex antenna gain as introduced in Sect. 3.3. As ionospheric fluctuation causes phase

shifts, observing a calibration source with known position helps to determine the difference of the calibrator and the observed source position. The subtraction of both phases will lead to the correction of the visibility phases. Generally the more calibrator sources are used for the creation of the calibration model, which is used to generate model visibilities, the more likely the calibration is expected to be successful.

The complex gain calibration of LOFAR single-station observations is based on the algorithm of the program GCALC1 from the Astronomical Image Processing System (AIPS). With the low angular resolution of a single LOFAR station most sources in the sky cannot be resolved or are too weak to be able to detect. The only point like sources that are detectable and usable for the calibration of all-sky data are strong sources like Cyg A, Cas A, Vir A and Tau A, which properties are summarized in Table 3.1. Especially Cyg A and Cas A are, due to there strong intensities and high declination, good candidates for the calibration. These sources are not strongly variable on time scales shorter than a year. However Cas A shows a decreasing intensity of around 1% per year (Baars et al., 1977; Vinyaikin, 2014), depending on the observing frequency. Note that this has no influence on the position of Cas A and therefore it is usable for the phase calibration. Another problem is caused by the short integration time of a few seconds that leads to a low signal to noise ratio. Even more, the sensitivity is decreasing by decreasing the channel width as needed for a high frequency resolution. To estimate reliable complex gains these effects need to be taken into account in the calibration process.

In practice the calibration routine starts with a local sky model of visible sources and generates model visibilities. The first phase gains are determined by comparing the model to the observed visibilities. These solutions are applied to the uncalibrated visibilities and a new and better sky model can be created from the calibrated image. Afterwards a second calibration run determine the amplitudes and phases is done. Iterating these steps will lead to the so called self-calibration process. Using more calibration steps for the typical LOFAR observation used here would not improve the quality of the data. In any case the calibration is done for both dipoles independently, as due to instrumental and source polarization effects, the measured intensities varies, as they depend on the position of the sources toward the orientation of the dipoles. Especially RFI is in most cases strongly polarized. The calibration of the polarization is discussed in Sect. 1.2.

Directional dependent calibration have been shown to improve the quality of LOFAR data sets in general. Hereby a gain value is produced for some directions in the sky. However there are not enough strong sources in the observed field of view that could be used for the calibration and therefore no direction depended calibration is applied. To investigate a practical scheme of directional dependent calibration for the here used single LOFAR station data would go beyond the scope of this project. However this will lead only to small phase errors as the ionospheric fluctuations are varying with position in the sky.

Table 3.1: Positions and intensities at 38 MHz and 178 MHz of the brightest sources. Beside of Cas A, all intensities are taken from Kellermann et al. (1969). The intensity from Cas A at 38 MHz is taken from Hales et al. (1995), at 178 MHz from Gower et al. (1967) an at 1400 MHz from Findlay et al. (1965).

source	RA [^{h} ^{m} ^{s}]	DEC [° ' "]	S_{38} [Jy]	S_{178} [Jy]	S_{1400} [Jy]
Cas A	23 23 27.9	58 48 42	25000	12000	2335
Cyg A	19 59 28.3	40 44 02	22000	8700	1590
Vir A (M87)	12 30 49.4	12 23 28	3570	1050	214
Tau A (M1)	05 34 32.0	22 00 52	2430	1534	930
Her A (3C348)	16 51 08.1	04 59 33	1690	351	45

3.6 Source finding and self-calibration

In the LOFAR frequency range Cas A and Cyg A are the strongest observed radio galaxy. Due to their strong intensities they are even detectable with the low beam resolution of a single LOFAR station and therefore useful for the calibration of the data. However Cas A and Cyg A are not always be the strongest sources in the field of view. In some cases RFI sources or other variable astronomical sources, like the Sun or Jupiter, appear even stronger. The origins of RFI sources for LOFAR stations have been discussed earlier in Sect. 3.4. The Sun is particularly becoming a problem at higher frequencies, due to an inverted spectrum. In the LOFAR high band, above 100 MHz, the intensity of the Sun is of the order of Cas A and Cyg A or even higher. The measured intensity of the Sun even more depends on the Sun activity. From time to time Sun bursts are observed, which are also observed at frequencies below 100 MHz. Strong bursts from Jupiter are just observable at frequencies below 38 MHz. An example of an observation with a strong RFI source appearing in the field of view is shown in the left-hand image of Fig. 3.11. The right-hand image of Fig. 3.11 shows a daytime observation performed with the HBAs including a bright Sun. In both cases Cas A and Cyg A are not anymore the only strong guessed sources in the sky. As RFI, the Sun and Jupiter bursts are strongly changing with frequency and time and even on short time scales, it is not possible to create a theoretical model of their emission. Nevertheless, for a successful calibration these sources have to be part of the calibration model.

The use of the so called self-calibration method allows to do the calibration even on unknown fields. For the self-calibration method the skymap is used for the calibration itself instead of theoretical predictions of the observed field. In the iterative calibration process the aim is to minimize

$$\left| \frac{\mathcal{V}_{ij}^{meas}}{\mathcal{V}_{ij}^{model}} - G_{ij} \right| \tag{3.26}$$

which means to find antenna gain corrections G_{ij} for which the measured visibilities is fitted best by the model. Afterwards the calibration model can be improved by using the corrected visibilities.The loop of generating a calibration model out of the skymap and determine gain

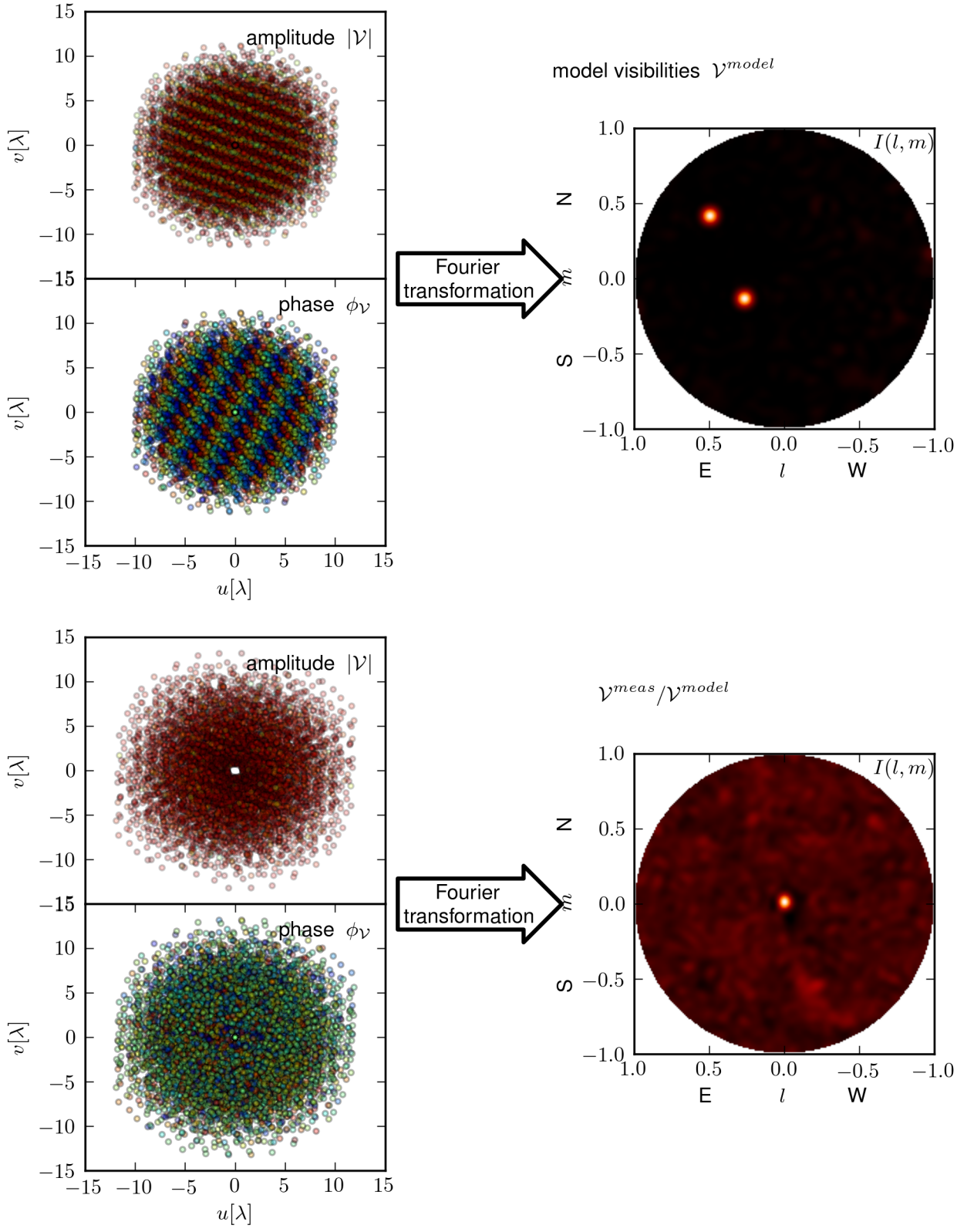

Figure 3.10: Visibilities (left) and intensities (right) for the model data of Cas A and Cyg A.

factors is repeated until convergence is reached (in e.g. the noise floor does not improve). Of course this method implies that the uncalibrated data are already sufficiently good with a high signal to noise ratio. For the creation of the calibration model a Fourier transformation of the observed visibilities is performed to obtain a skymap as described in Sect. 3.3. The strongest sources appearing in the skymap are identified and the positions and relative intensities are stored in the calibration model. The source finding is done independently for both dipoles of one antenna as they measure different signals in case the observed source or emission is polarized. This is especially the case for Jupiter bursts and RFI sources. The positions of the detected sources are compared with known positions of bright astronomical sources, like the Sun or the radio galaxies tabeled in Table 3.1. If the difference between obtained and theoretical source position is within the size of the beam resolution, the theoretical source position is used to generate the calibration model. For the amplitude calibration the relative flux densities of the sources are taken. The absolute flux density correction is done at a later stage in the calibration procedure, in correcting the bandpass. Visibilities and skymaps for a calibration model which is just using the point sources Cas A and Cyg A is shown in Fig. 3.10, hereby are two strong point sources visible in the map. In the amplitudes of the visibility stripes are visible as expected of the Fourier transformation of two point sources. Stripes are also visible in the phases of the visibilities. This corresponds to the two point sources being several degrees away from the phase center, which is located at the zenith. The plots in the bottom of Fig. 3.10 illustrate the ratio of measured and modeled visibilities. In case the model visibilities do properly describe the real visibilities a single point source will appear in the center of the skymap and the phases of the visibilities in the figure do not show any stripes due to a phase offset. This set of visibilities will be used to estimate the complex gain to calibrate the original dataset. Testing the self-calibration process, using a LSM generated within the process, with the calibration using a fixed LSM of known cataloged sources is discussed in Sect. 3.8.

The self-calibration method does improve greatly the image quality of the observations and is used in the developed calibration process.

3.7 Specifics in all-sky imaging with the HBA

For the all-sky imaging with the high band antennas (HBAs) of a single LOFAR station some additional restrictions need to be considered. The HBA field consists of several tiles whereas each of these tiles contains 4x4 dipole antennas. In general, the HBA observation of a LOFAR station is done in beam-formed mode for which all antennas within one tile are used and correlated with each other.

In order to use the HBA field for all-sky imaging this mode is not the optimal solution, because of the reduced field of view of the HBA tiles. Therefore the best way to observe the entire sky is by using just one antenna per tile and switch off the rest of the antennas. To get a reasonable good uv-coverage for instantaneous imaging not the same antenna in every

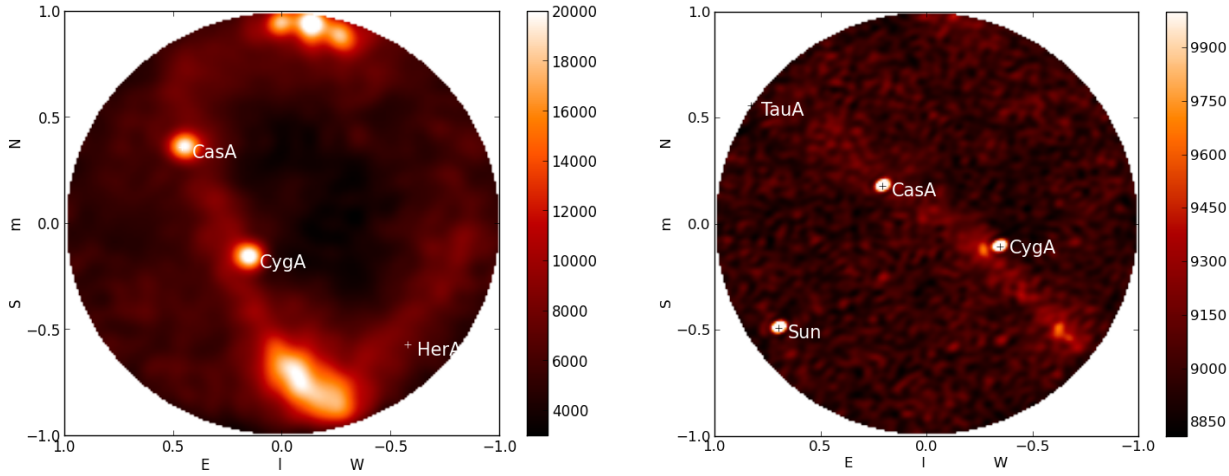

Figure 3.11: Self-calibrated images with correlated data from the TBBs. Left: LBA observation at 47 MHz with strong RFI in the north, which is coming from the direction of the 100 m telescope in Effelsberg. The channel width is just 5 kHz. Right: HBA observation at 120 MHz, where the intensity of the Sun is stronger than of the A-team sources. The channel width is just 50 kHz. Both observations are done with the TBBs of the Effelsberg station and have an integration time of 1.3 sec. But even the short observation time and the high frequency resolution provides enough signal for the calibration. In both images no primary beam correction is applied.

tile should be used (see Fig. 2.2). Unfortunately following this approach only one antenna out of 16 is used and the sensitivity is decreased by a factor of one over 16. To compensate this effect several frequency channels have to be combined to get a reasonable good signal to noise ratio. A longer observation time would be helpful as well, but in the TBB system the observing time is limited to 1.3 sec. For the calibration of day time observations with the HBA, the self-calibration mode is unavoidable. As the Sun has an inverted spectrum, the intensity is much stronger than in the LBA observations. Therefore the Sun cannot be ignored in the calibration process of the data. An example for an observation at 120 MHz is shown in the right-hand image of Fig. 3.11. In this observation the Sun already shows a stronger intensity than Cas A and Cyg A. This effect becomes even stronger toward higher frequencies.

Due to grating loops in the antenna pattern sources can appear more than ones in the skymaps. Such ghost sources are shown in Fig. 3.12. At 123 MHz Cyg A, Cas A and some extended emission of the Milky Way is visible. At 144 MHz Cas A appears a second time in the bottom of the map. In the same way the strong RFI source in the north shows up a second time in the south and also the emission from the Milky Way appears again in the west. At 177 MHz the ghost sources move more and more into the center of the map. Now

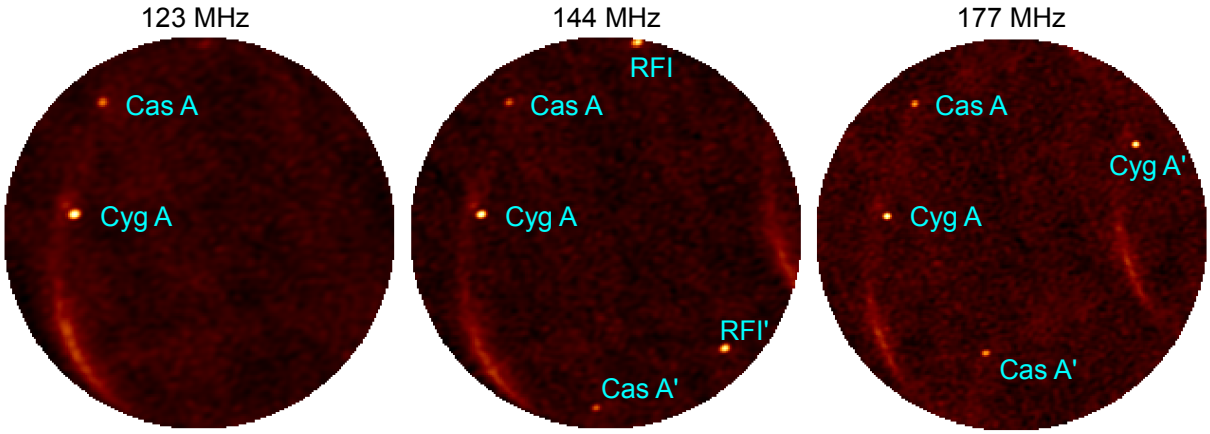

Figure 3.12: Snapshot observation using the HBA. Depending on the frequency sources appear a second time in the image (marked with a ').

Cyg A is visible a second time beside Cas A and the Milky Way emission as well. All ghost sources are marked with a ', whereas the real sources are just marked by their name.

In the calibration process using the self calibration method it is taken care of the double appearance of the sources. By calculating the location of the ghost sources, it is ensured that each source appears just once in the calibration model. In the combination of the snapshot images the ghost sources are blanked. For the large scale emission of the Milky Way the situation is more complicated as it is difficult to model the location of these large scale structures. Nevertheless, as the ghost structures will always appear at a different positions on the sky they should averaged out by combining a high number of single snapshot images. In order to properly exclude the extended- and individual ghost sources in the field of view one need to take the following equations into account:

$$\Delta \mathrm{x} = \pm\, hbpw \cdot \sin(\phi) \tag{3.27}$$

$$\Delta \mathrm{y} = \pm\, hbpw \cdot \cos(\phi)\,. \tag{3.28}$$

Hereby:

$$hbpw = 1.057\,\frac{\lambda}{\mathrm{D}} \tag{3.29}$$

with λ being the wavelength and D the dipole length (D = 1.38 m for the HBAs). The angle ϕ is the rotation of the LOFAR field in relation to the North Celestial Pole. Adding the values of Δx and Δy to the source position results in the position of the ghost sources. If the distance of source and ghost source position is smaller than the field of view, the ghost sources appear above the horizon.

3.8 Testing the calibration software

The quality of the self-calibration process will rely on the quality of how good the local sky model (LSM) can be determined. In the following section the developed self-calibration method is tested against the calibration routine that relies only on known cataloged calibrator sources. In particular, this step is crucial in the phase-calibration step only.

3.8.1 Self-calibration vs calibrator based calibration of a known field

The particular TBB dataset for this test has been observed in August 2011 in Effelsberg and was correlated with a frequency resolution of 100 kHz. These known field will show no RFI or other strong unknown source and Cas A and Cyg A are at a high elevation. Even with such low frequency resolution and short integration time interval the signal to noise ratio is good enough to detect Cas A and Cyg A already in the uncalibrated image (left of the figure). Before producing the images in the middle- and at the right-hand side of the figure, bad antennas have been removed from the dataset.

Images are produced by a single frequency of the snapshot dataset with an integration time of 1.3 sec and are shown in Fig. 3.13 for a comparison between the non-calibrated images (left) and the calibrated images in the middle and right hand side of the figure.

The difference of both calibration approaches is in the initial step of generating the LSM and the impact of the phase-calibration that will lead into an improved LSM for the amplitude-phase calibration. In case of the middle image the theoretical models for Cas A and Cyg A has been used for the phase calibration. Due to the low sensitivity there are no other strong sources visible in the field of view which could be used for the following calibration step. In case of the right-hand images the source finding was applied on the uncalibrated skymaps to create the model visibilities. After using this model for the phase calibration, a new image was made to create a new local sky model including also the extended radio emission. In the final phase-amplitude-self-calibration step this LSM is used to produce the resulting images as seen in Fig. 3.13.

There is no significant discrepancy in the total intensity (Stokes I) between both calibration techniques. In polarization the differences are more pronounces, such that small differences can be recognized in Stokes Q and Stokes U and strong differences become more visible in Stokes V.

The good agreement in Stokes I and also in Stokes Q and Stokes U indicates that both methods will lead to a reliable calibration. As not much is known about the polarization property, which is in this example anyhow dominated by noise, it is impossible to conclude which calibrating method lead to a better result. In order to evaluate the quality of the calibration of the polarized intensities a strong polarized source is needed. This will be discussed for a Jupiter burst in the next subsection.

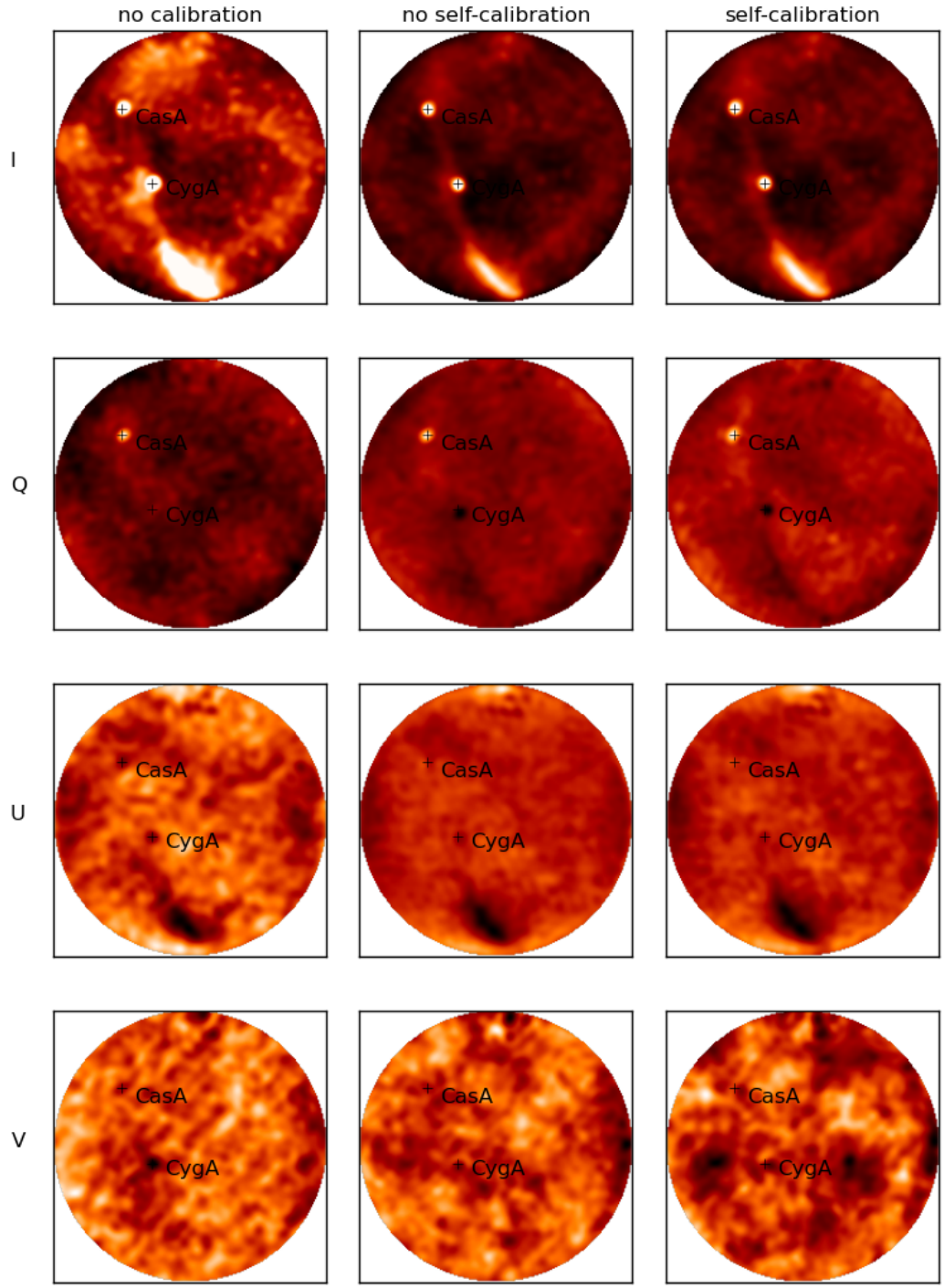

Figure 3.13: Observation at 65 MHz from August 2011 done with the TBBs in Effelsberg. From top to bottom the four Stokes values are imaged. The left four images are non calibrated, the middle ones are done by using Cyg A and Cas A as calibrators and the right ones are done using self-calibration. No beam correction is applied.

3.8.2 Self-calibration vs calibrator based calibration of an unknown field

After showing that the self-calibration code is working fine for a field with known sources, the same testing is performed on an observation with a strong unknown source, which is moreover strongly polarized. In this example the 'unknown' source is Jupiter and its spectral intensity cannot be modeled theoretically, as it is variable in time and in frequency. The observation of Jupiter as shown in Fig. 3.14 was done in August 2013 using the TBBs from the LOFAR station in Effelsberg. The data were afterwards correlated with a frequency resolution of 20 kHz and an integration of 1.3 sec. Similar to the discussion above the left-hand side shows the uncalibrated images.

The images in the middle are produced by using Cas A as a calibrator as it is the only visible strong and known source in the field of view. On the right-hand side the full self-calibration method in generating the LSM was used as described in Sect. 3.6. For both calibration routines the skymaps for all four Stokes values are produced. As Jupiter is 100% elliptical polarized, it is detectable in Stokes I, Q, U and V and is therefore useful to study the quality of the code for polarized intensities. At this point no correction for the instrumental polarization (Sect. 4.8) has been applied and will not have any influence in the comparison of both methods to generate the LSM.

If Cas A is used as calibrator only (middle) it appears after the calibration as the strongest source in the skymap, as by the software the strongest intensity is expected to be at the position of Cas A. If the self-calibration method is used instead, the measured total intensity of Jupiter is stronger than the one of Cas A. The difference between both calibration techniques is becoming even more obvious by comparing the polarized intensities. Here especially the problems in the calibration in Stokes U and Stokes V are nicely demonstrated. It clearly can be seen that the phase calibration is not successful, if no self-calibration is applied (middle), and the position and polarized intensity of Jupiter is smeared out. Furthermore, Cas A is theoretical unpolarized but due to the calibration errors it shows up in all Stokes images. Also for Stokes Q the sign for the polarization of Cas A and Jupiter is swapped in comparison to the self-calibrated images. Beside of that, most of the intensity ends up in Cas A, instead of Jupiter.

In case of the self-calibration (right) the phases are calibrated correctly and all of the intensity occurs at the right position. Nevertheless, Cas A also appears slightly polarized in the self-calibrated images, as it is close to the horizon for which strong instrumental polarization is expected. After the antenna beam correction this strong polarization should mostly disappear.

The example clearly shows the need of generating the local sky model using the self-calibration method, as otherwise no reliable calibration of the data is possible.

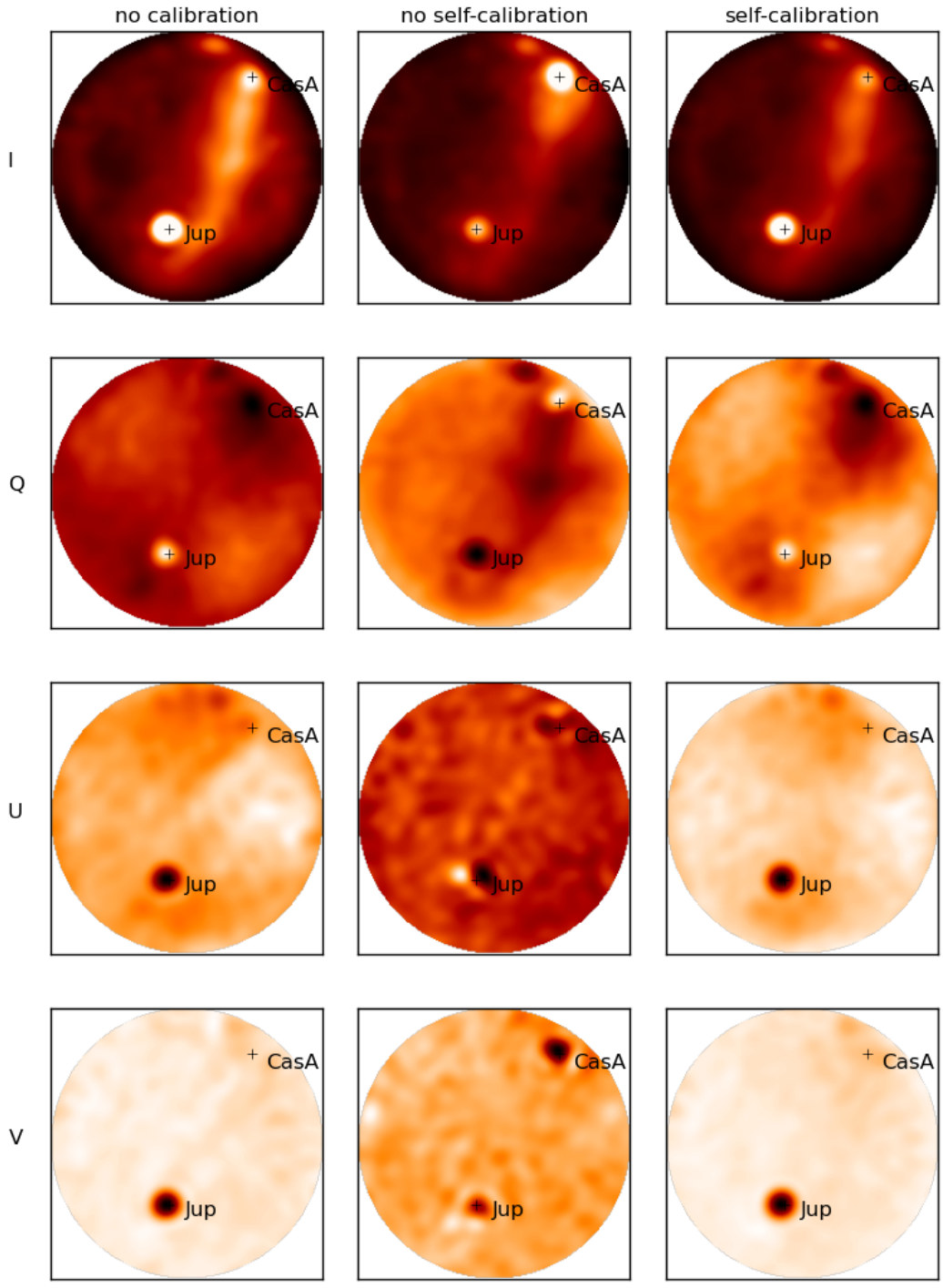

Figure 3.14: Jupiter observation at 34 MHz from August 2013 done with the TBBs in Effelsberg. From top to bottom the four Stokes values are imaged. The left four images are the uncalibrated skymaps, the middle ones are calibrated using no self-calibration, the right ones are using self-calibration. No beam correction is applied.

3.9 Correction of the dipole beam pattern

Archiving real sky intensity images the beam correction for all dipoles toward various positions in the sky is needed, because of the direction dependent sensitivities of the dipoles. For the LOFAR dipoles a model by Hamaker is used to correct for the beam pattern of the individual dipoles (van Haarlem et al., 2013). This model is based on electromagnetic (EM) simulations and shows a dependence in azimuth and elevation for every frequency. The left hand image of Fig. 3.15 shows both dipole orientations of a single LOFAR antenna. The right hand image shows the beam pattern at 50 MHz for the Y-dipole orientation.

In order to determine directional dependent corrections of the LOFAR data the measurement equation method is used employing specific matrices for various effects. In case of the dipoles the notation from Eq. (3.23) **E** describes the Jones matrix for the dipole beam pattern. The Jones matrix is applied to the individual visibility correlations XX, XY, YX, YY:

$$\begin{bmatrix} XX & XY \\ YX & YY \end{bmatrix}_{corr} = \mathbf{E} \begin{bmatrix} XX & XY \\ YX & YY \end{bmatrix}_{meas} \mathbf{E}^H \tag{3.30}$$

whereby

$$\mathbf{E} = \begin{bmatrix} E_{x\Theta} & E_{x\Phi} \\ E_{y\Theta} & E_{y\Phi} \end{bmatrix} \tag{3.31}$$

$E_{x\Theta}$, $E_{x\Phi}$, $E_{y\Theta}$ and $E_{y\Phi}$ are the complex field components in cylindrical polar coordinates and H represents the conjugate transpose operation.

3.9.1 Parallactic angle correction

The electric field vectors, on which the beam correction is applied, are sensitive to geometric rotations. Depending on the telescope mount this rotation will take place and one needs to correct for this effects in the process of converting the data from one coordinate frame into another. This is done by using the parallactic angle, which depends on the observing direction. It is defined as the angle between the zenith and the North Celestial Pole as seen from the direction of the source position. The correction for the parallactic angle is particular important for the polarization calibration, as the positive Stokes Q is defined to point toward the Pole. In practice the parallactic angle, which represent the angle between Equatorial basis and Horizon basis into one direction in the sky, can now be calculated by

$$\chi = \arctan\left(\frac{-\sin H \cos\lambda}{\cos\delta\sin\lambda - \sin\delta\cos\lambda\cos H}\right) \tag{3.32}$$

By knowing the latitude λ and longitude ϕ of the station a relation between elevation h and the declination δ and hour angle H can be given:

$$h = \arcsin\left(\sin\delta\sin\lambda + \cos\delta\cos\lambda\cos H\right) \tag{3.33}$$

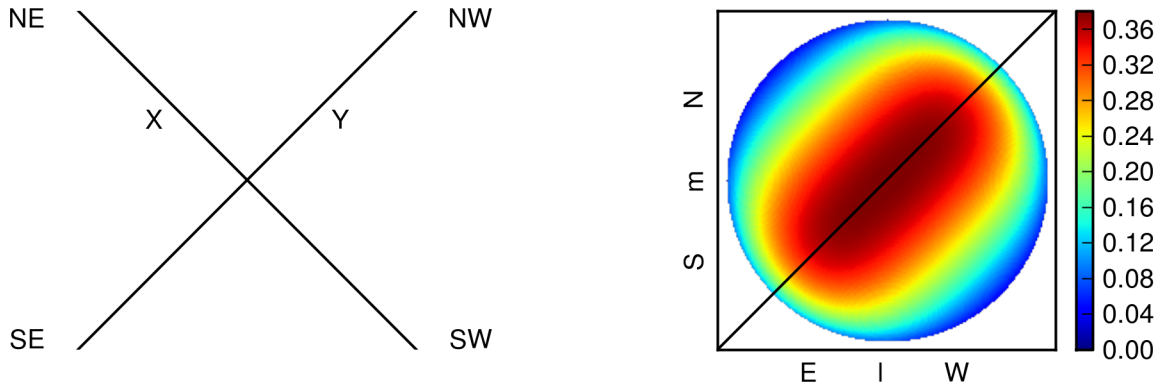

Figure 3.15: Left: A single antenna with the definition of the orientation of the two dipoles, which are named with X and Y. Right: Antenna pattern for a single X-dipole at 50 MHz calculated by using EM simulations done with a code from Tobia Carozzi (priv. comm.). The black line shows the orientation of the dipole. As expected the sensitivity is lowest at the horizon and strongest around the zenith. Beside of that the azimuthal direction dependence is visible. Sources which are perpendicular to the dipole orientation appear stronger than sources, which are parallel to the dipole orientation.

And in the same way for the azimuth A:

$$A = \arctan\left(\frac{-\sin H \cos\delta}{\sin\phi\sin\delta - \sin\phi\cos\delta\cos H}\right) \tag{3.34}$$

Note that transformation between the Equatorial and the Horizon system has been introduced earlier in Sect. 3.1.

In the case of the LOFAR antenna fields some special assumptions are needed, as it does not work in the standard Horizon system, where the azimuth is relative to the astronomical North Pole (NP). As each LOFAR station is oriented independently an angle with the North pole is introduced. The LOFAR station "north" pole (LP) is defined by its latitude $\lambda_{LP} = 0$ and its longitude $\phi_{LP} = -83.12983°$. Now the offset between the astronomical and LOFAR North pole can be calculated:

$$\epsilon_{station} = \frac{\pi}{2} - \arctan\left(\frac{\sin\left(\phi_{LP} - \phi_{station}\right)}{\sin\lambda\cos\left(\phi_{LP} - \phi_{station}\right)}\right) \tag{3.35}$$

This value is constant for each LOFAR station. For the stations in the 'Superterp' as part of the LOFAR Core in the Netherlands its value is zero. For the station in Effelsberg one get $\epsilon_{DE601} = 0.0897°$ (Hamaker at al., 2011). Now the relation between the coordinate system as seen by the antennas of the station (Θ, Φ) and the astronomical system can be transformed via

$$\Theta = \frac{\pi}{2} - h \tag{3.36}$$

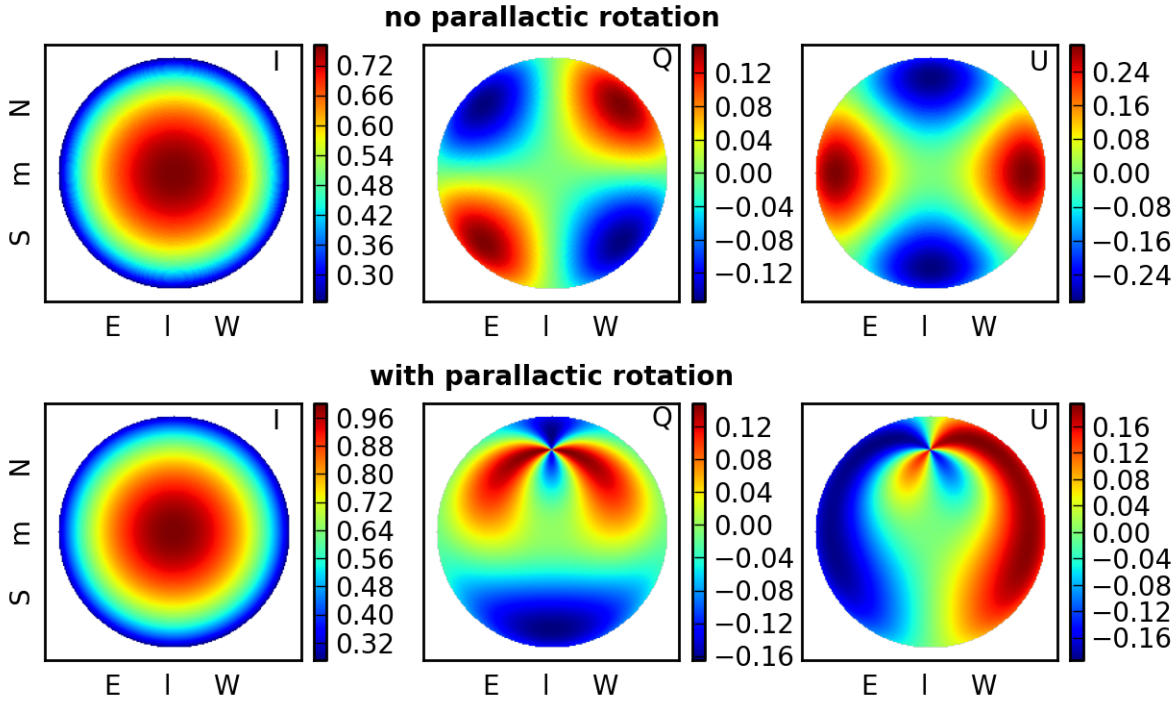

Figure 3.16: Antenna beam pattern for Stokes I, Q and U at 50 MHz calculated based on EM simulations from Hamaker done with a code from Tobia Carozzi (priv. comm.). Top: No parallactic rotation is applied. Bottom: Applying the parallactic rotation to the antenna pattern.

and

$$\Phi = A + \epsilon_{station} - \frac{\pi}{4} \tag{3.37}$$

After applying these specific station corrections, the parallactic angle can be calculated and applied to the electric field vectors using a rotation matrix:

$$\mathbf{R_{parallac}} = \begin{pmatrix} \cos\chi & -\sin\chi \\ \sin\chi & \cos\chi \end{pmatrix} \tag{3.38}$$

The effect of the parallactic rotation is illustrated in Fig. 3.16. The top images shows the antenna beam pattern of Stokes I, Q and U at 50 MHz with no parallactic corrections applied. The bottom images shows the beam model with the parallactic rotation applied. For Stokes I there is no difference visible. The difference is clearly visible in the linear polarized emission and demonstrates the need for polarization corrections. Note that toward the North Celestial Pole, with its asymmetric structure in polarization, the applied corrections will be most critical.

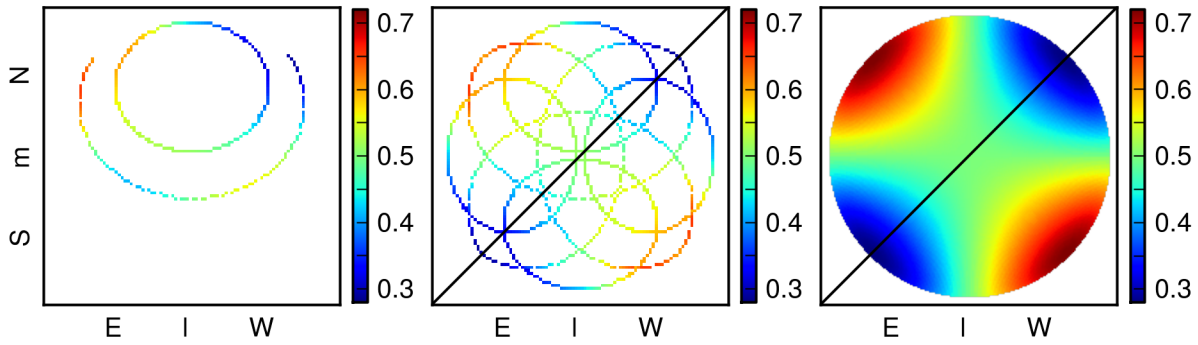

Figure 3.17: Left: Relative intensities of Cas A and Cyg A depending on the sky position. Middle: Using symmetry properties of the dipole on the left image. Right: Beam pattern as obtained from the Hamaker model. All measurements are at 50 MHz. The black line indicates the dipole orientation.

3.9.2 Probing the dipole beam model by tracking Cas A and Cyg A

The direction depending sensitivities of the dipole can be measured and illustrated by tracing the path of unpolarized sources on the sky. In doing so, the measured source intensity will vary with the position on the sky if no beam correction is applied. For this procedure and using single station observations Cas A and Cyg A are the best candidates, due to their strong intensities and high declinations. The polarization of both sources can be neglected in the short duration of the observations (integration time 1 sec) and all measured polarization are caused by instrumental effect. In the following the azimuth-depending variation and the elevation dependent part of the beam model will be determined separately.

In Fig. 3.17 a comparison of observations and theoretical model is shown. In the left hand image the relative intensities I_{YY}/I_{total} of Cas A (small cycle) and Cyg A (large cycle) are plotted as position on the sky. Using the relative intensities no information of the absolute intensity is needed and also eliminates the elevation dependent part of the beam model. As Cas A is a circumpolar source for middle and northern Europe, it is observable for 24 hours, whereas Cyg A disappears at at some time behind the horizon. Nevertheless, measurements were used, if the elevation of the source is above 20°. As expected the relative intensities follow a clear trend and shows regions of stronger and weaker intensity. In order to describe the full properties on the sky, symmetry properties of the dipole have been used to generate the middle image by mirroring the measured points. Hereby the black line shows the orientation of the dipole. The relative intensities appear strongest if the observed source is perpendicular to the dipole orientation and weakest if it situated parallel to it. Close to the zenith no direction depending effects are detected. For comparison the right hand image shows the direction depended part $(E_{y\Theta}^2 + E_{y\Phi}^2)/\left\|\mathbf{E}\right\|_2$ of the Hamaker model at the same frequency of 50 MHz (Note this part is not elevational dependent). The measurements and

the theoretical model are in good agreement with each other and the structures as well as the relative intensities do show a similar behavior. The same study can be done for the elevation depending part of the model.

The left hand plot of Fig. 3.18 shows now the elevation dependent part as well as the azimuth dependent part of the antenna beam and an interpolation on the measured points was performed to generate a final dipole model. For comparison the Hamaker model for the same frequency is plotted in the middle. At first glance both models look similar however for a quantitative understanding the difference of the here generated beam model and the Hamker model is plotted in the right-hand side of the image. Negative values means that the Hamaker model contains higher values at this position. It can be seen that especially at high elevations both models are comparable and just show small differences. The largest difference is visible at low elevations, especially along the dipole orientation. At this locations both models differ by around 30%. It cannot clearly be said, if this difference is due to an overestimation in the Hamaker model or due to mismatches in the interpolation process of the source tracking data. Even if a model for the X and Y dipoles was created, it is generally not possible to calculate directly the four complex values of the Jones matrix. Nevertheless, these here generated models can help to test the quality of existing models and can be used for further improvements.

At a later stage the differences of both beam corrections applied to the final galactic maps will be discussed in Sec. 4.8.

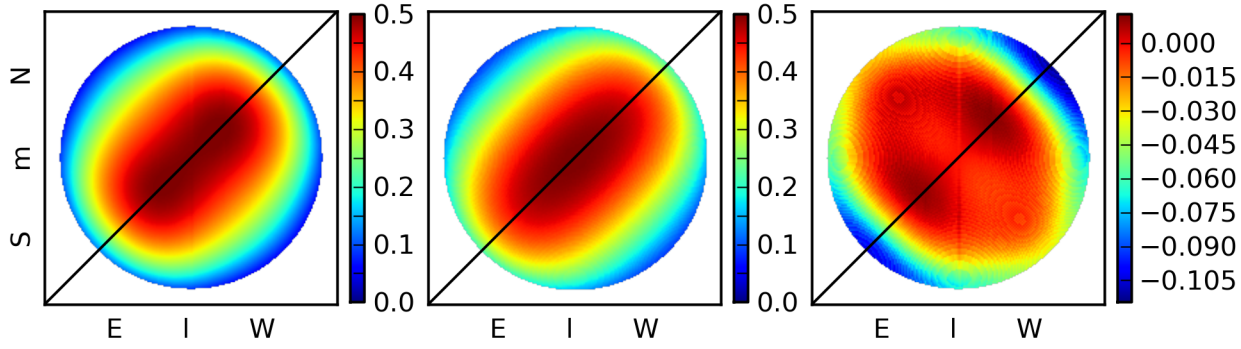

Figure 3.18: Comparison of the Hamaker beam model and the beam model as obtained from the Cas A and Cyg A measurements at 45 MHz for one dipole orientation (marked with the black line). Left: My generated beam model from the source tracking. Middle: Hamaker beam model. Right: Difference of my beam model and the Hamaker model.

3.10 Correction of the ionospheric Faraday rotation

For all kind of astronomical observations, the atmosphere has a strong influence on the quality of the data. At the lowest frequencies, at which LOFAR is observing, the ionosphere has the strongest impact. The ionosphere is located at an altitude of 85 km above the Earth surface and is therefore lying in the upper part of the atmosphere. It is ionized by the UV and X-ray radiation from the Sun and contains free electrons and electrically charged atoms and molecules. Electromagnetic radiation at low frequencies interacts with these particles and a rotation of the oscillation direction of the wave is introduced, the so called Faraday rotation (see Sect. 1.2.1). The number of free electrons in the ionosphere depends on the Sun activity. The electron density is higher during the day time (in the order of 10^6 cm^{-3}) and lower during the night time (in the order of 10^4 cm^{-3}). On short timescales variations in the ionosphere will show up strongest during sunset and sunrise. The electron density is on average strongest during summer time and also varies for different regions on Earth, whereby he highest values are found around the equator.

The electron density in the ionosphere can be described by the total electron content (TEC). It describes the number of electrons integrated along the line-of-sight with a cross section of one-by-one meter:

$$TEC = \int_{receiver}^{satellite} n_e(s)\,\mathrm{d}s\,. \tag{3.39}$$

In addition, the TEC unit (TECU) is defined as TECU = 10^{16} m^{-2}. As an example the ionosphere on a quiet day will show TECU value between 5 and 25. During Sun flares this value can go up to values of 200.

Different ways of measuring the TEC values in the ionosphere have been developed in the past. During the last decade measurements of the dual-frequency transmission from the Global Position System (GPS) became the most prominent. This method uses two waves at different frequencies send through the ionosphere. The travel time of the waves depends on the frequency and the difference can be used to obtain the TEC value along the path. GPS receivers are located at various places around the world. Data are available for different time periods measuring a scatter of directions on the sky. Various existing models are performing an interpolation for inter media times and positions.

The Earth's magnetic field is modeled every five years by the International Association of Geomagnetism and Aeronomy (IAGA) and is available to download. In the end of 2009 the eleventh generation of the International Geomagnetic Reference Field (IFRF11; Finlay et al., 2010) was released and is used for this work. With the knowledge of the magnetic field strength and electron content, the Faraday rotation due to the ionosphere of the Earth can be calculated and applied to the skymaps by using a rotation matrix

$$\mathbf{F} = \mathsf{Rot}\varphi = \begin{bmatrix} \cos\varphi & -\sin\varphi \\ \sin\varphi & \cos\varphi \end{bmatrix} \tag{3.40}$$

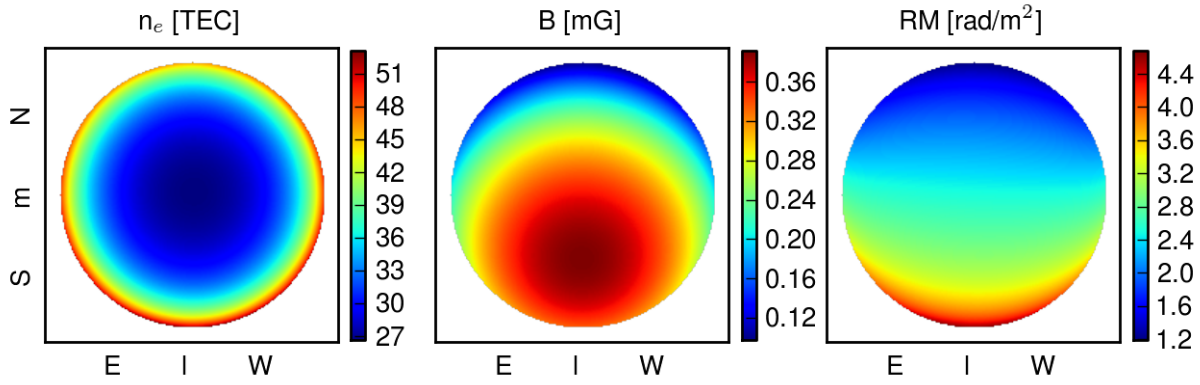

Figure 3.19: TEC map, magnetic field map and the corresponding RM map for a given time.

with

$$\varphi = \mathrm{RM}\lambda^2 \tag{3.41}$$

The Faraday rotations just shows up in the linear polarization of Stokes Q and U and has no influence on Stokes I and V.

An example of the TEC layer, the magnetic field, and the corresponding RM map for one observation is shown in Fig. 3.19. The TEC values are highest along the horizon due to geometric effects and therefore the ionospheric layer is thicker toward this pointing direction.

As seen in pulsar measurements, the fluctuations in the ionosphere are on short time scales, down too a few seconds. Unfortunately the existing models and measurements are just able to provide predictions of the TEC values every second hour. Modeling the ionosphere in the intermediate time steps is possible by interpolation only. A more accurate correction of the intermediate times steps can be achieved by using RM measurements of pulsars. Such measurements are discussed in Chapter 7. This correction would not change the relative values within a single RM map as it just provides a single line-of-sight RM value per time slot. However it is used to determine the relative RM values between the different observation times.

3.11 Summary of the data reduction

In this Chapter the data reduction software for the LOFAR single station data is introduced. The software correlator and the calibration code was written as part of this thesis. Nevertheless it is possible to use both software suits independently for other purposes. The Fig. 3.20 shows an overview of all data reduction steps necessary to transform raw voltages, as measured by the antennas, to a final skymap.

The correlator (sub-images a - c) converts the raw voltages, from the TBBs, into visibilities by performing a Fourier transformation on the time data (a) in order to create a

frequency spectrum (b) for each dipole. Afterwards the correlation between the individual dipoles is calculated in addition to a time integration over 1.3 sec (c) of the observation. The resulting visibilities are described via:

$$V_{ij}(\nu) = \int_0^{1.3sec} (\mathcal{F}(E_i(t)) \cdot \mathcal{F}(E_j(t))) \, \mathrm{dt} \tag{3.42}$$

These visibilities are further processed by the calibration software (plots d - e). The first step is the identification of bad antennas and frequency channels (d), which otherwise would causes problems in the further reduction of the data. In order to produce a reliable skymap out of the visibilities various corrections have to be applied and a further Fourier transformation is needed:

$$\mathbf{V}_{\mathrm{ij}}(u,v) = \mathbf{G}_{\mathrm{i}}\mathbf{B}_{\mathrm{i}}\mathcal{F}\left(\mathbf{E}_{\mathrm{i}}\mathbf{F}_{\mathrm{i}}\mathbf{I}(l,m)\mathbf{F}_{\mathrm{j}}^{\mathrm{H}}\mathbf{E}_{\mathrm{j}}^{\mathrm{H}}\right)\mathbf{B}_{\mathrm{j}}^{\mathrm{H}}\mathbf{G}_{\mathrm{j}}^{\mathrm{H}} \tag{3.43}$$

Here

$$\mathbf{G} = \mathbf{G}_{phase} \cdot \mathbf{G}_{amp-phase} = \begin{bmatrix} G_x & 0 \\ 0 & G_y \end{bmatrix} \tag{3.44}$$

is the gain, which is calculated for both dipole orientations (X and Y) for each antenna by a phase self-calibration (g), followed by a second phase-amplitude-self-calibration (h). In the amplitude calibration, the G matrix includes also correction for the bandpass B.

The correction of the dipole beam pattern, including the parallactic angle correction

$$\mathbf{E} = \mathbf{E}_{beam} \cdot \mathrm{R}_{parallac} = \begin{bmatrix} E_{x\Theta} & E_{x\Phi} \\ E_{y\Theta} & E_{y\Phi} \end{bmatrix} \cdot \begin{bmatrix} \cos\chi & -\sin\chi \\ \sin\chi & \cos\chi \end{bmatrix} \tag{3.45}$$

is applied afterwards (i) using a script separated from the calibration routine. The beam model is explicitly separated from the general calibration routines because the actual LOFAR beam model is known to be not perfect. Therefore separating both steps will allow testing of new and upcoming beam models in the future of already calibrated skymaps without repeating the entire calibration procedure.

The correction of the Faraday rotation is described by

$$\mathbf{F} = \mathsf{Rot}\varphi = \begin{bmatrix} \cos\varphi & -\sin\varphi \\ \sin\varphi & \cos\varphi \end{bmatrix} \tag{3.46}$$

with

$$\varphi = \mathsf{RM}\lambda^2 \tag{3.47}$$

and has to be applied on the linear polarization maps (Q and U) and is performed in the end on the final maps.

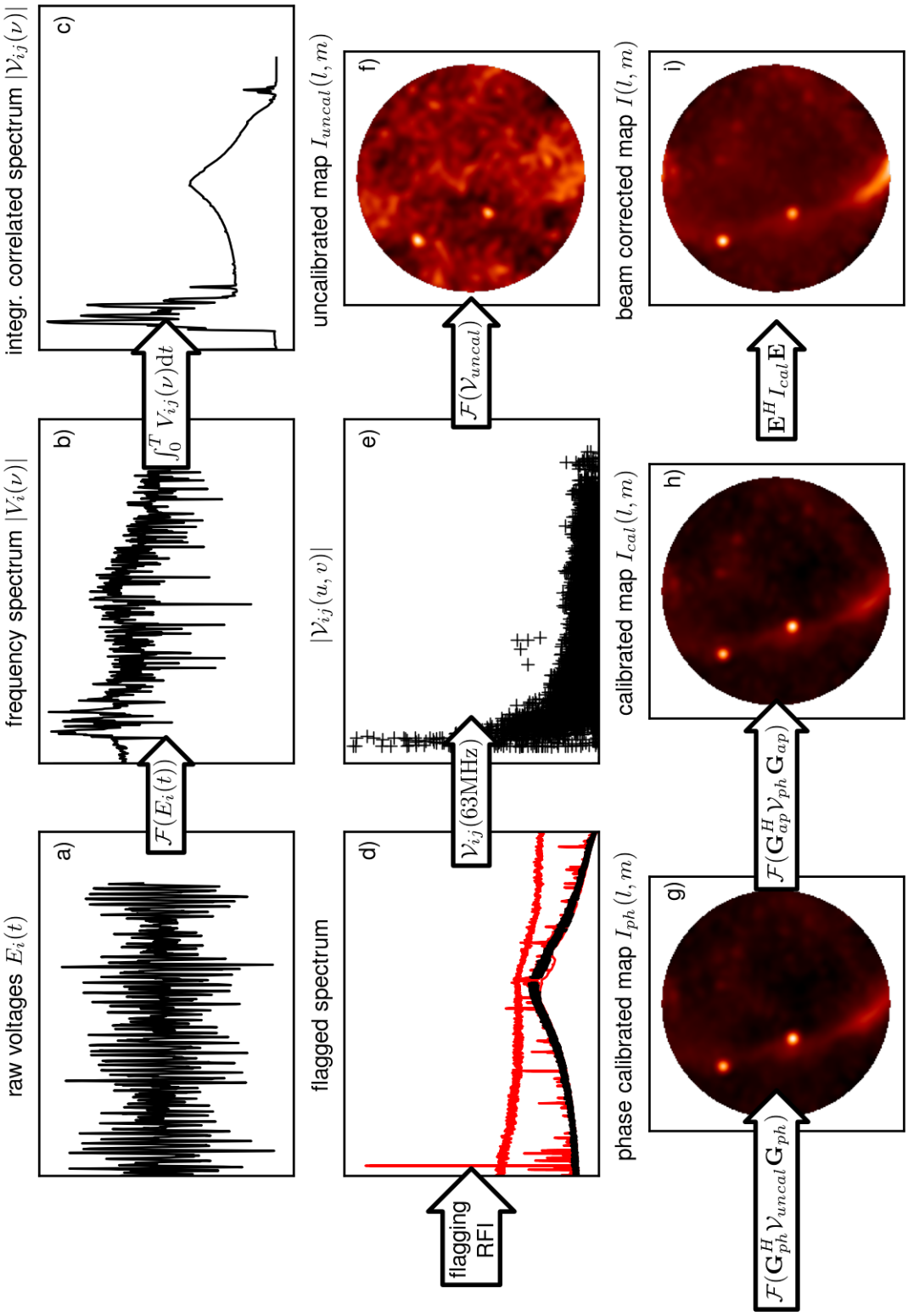

Figure 3.20: Summary of the data reduction.

Chapter 4

LOFAR Single Station Continuum Survey

By combining several snapshort images the entire northern sky can be mapped. This chapter presents the results of the galactic maps in total intensity. At the beginning an overview of the observation performance and the stacking of single observations is given, which leads to the skymaps shown at different frequencies. A comparison of the LOFAR maps with other known surveys is done to study structures in the sky which may vary for the individual surveys. This is done by using profiles at various latitudes and longitudes.

4.1 The observations

The observations performed for the presented survey were done as part of the LOFAR cycle 0 (LC0) observations at the first half of 2013. A proposal (LC0_044) for 288 hours observation time with the single station in Effelsberg (DE601) was written and accepted at the end of 2012. These 288 hours corresponds to 12 observation runs of 24-hour each. The observations were spread over several month, so that on average every part of the sky appeared at least once at day and once at night time. By combining all the data in the end, ionospheric effects due to the Sun should be more or less averaged out. This is just a rough assumption, as the ionosphere behaves differently at summer and winter time and strongly depends on the Sun

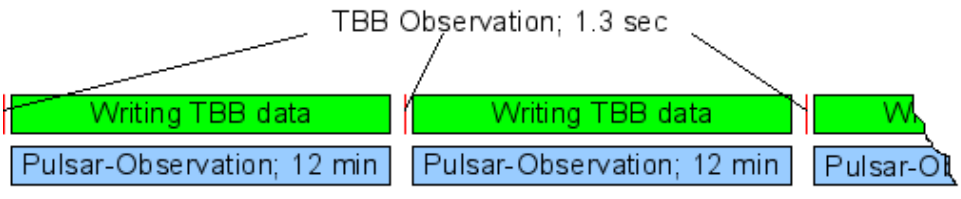

Figure 4.1: Schematic diagram of observations.

Table 4.1: Overview of the performed observations.

date	RCU mode	
2013-01-09	LBA 3	just 12 hours; pulsars in RCU 3
2013-01-14	LBA 3	pulsars in RCU 3
2013-02-05	HBA 5	
2013-02-22	HBA 7	just 12 hours
2013-03-11	LBA 3	
2013-03-26	HBA 7	just 12 hours
2013-04-01	HBA 5	
2013-04-15	LBA 3	strong RFI; Sun burst
2013-05-03	HBA 7	
2013-05-28	LBA 3	not usable because of RFI
2013-06-04	LBA 3	just 6 hours
2013-06-10	HBA 5	
2013-06-24	HBA 7	
2013-07-08	HBA 5	
2013-08-05	HBA 7	
2013-09-16	LBA 3	

activity.

From January 2013 to September 2013 observations were performed every second week if possible. The time between two observation runs was needed for the data processing to guarantee free disc space, as the total amount of raw data after 24 hours was in the order of 32 TB. The observations were performed in the low band (RCU mode 3 - from 0 MHz to 100 MHz), high band low (RCU mode 5 - from 100 MHz to 200 MHz) and high band high (RCU mode 7 - from 200 MHz to 240 MHz), in a way that four observation runs were done for every single frequency range. No observations in high band middle (RCU mode 6 - from 160 MHz to 240 MHz) were performed to avoid problems (especially for the pulsar observations and data reduction) coming up by using the 160 MHz station clock. During a 24-hour run several snapshot observations were done, starting with a TBB measurement of the entire sky. As the data from the TBBs are raw voltages, an observation of 1.3 sec produces a data volume of around 100 GB, which leads to a writing time to disc up to around 15 minutes for the system set up in Effelsberg. Meanwhile this writing process, a pulsar was observed in RCU mode 5 with 12 minutes integration time. At the beginning of the observations in January 2013 two observation runs were done by performing the pulsar measurements using LBAs instead of the HBAs. This was done to test if pulsar observations with the LBAs are possible and if usable RM values could be obtained. Due to a bad RFI situation for the station in Effelsberg, which is also mentioned in other parts of this thesis, it is not possible to get an RM value for the pulsar, even if the pulsar can be detected in the dataset. All the following observations were done using RCU mode 5 for the pulsar

measurements. This combination of TBB and pulsar observation, as described above and sketched in Fig. 4.1, was done over 24 hours. This leads to 90 single snapshot observations over 24 hours which correspond to a total integration time of around 2 minutes. Due to the facilities of eight recording machines at the Effelsberg station (four used for the TBB measurements, four for the pulsar observations), this kind of simultaneous observation was possible.

At least one 24-hour run would be needed to map out the entire sky. To increase the sensitivity in the final maps several of these observation runs were necessary. This is crucial especially for the higher frequencies, where the system temperatures noise becomes higher than the sky noise, as well as for the measurement of the weak polarization. More observations are also needed for the HBA data as for the all-sky imaging just one antenna per tile can be used. Therefore the sensitivity is decreased by a factor of one over 16 (as already discussed in Sect. 3.7). Unfortunately not all of the HBA observations were usable for the final data reduction, as the Sun was close to a solar maximum in 2013 and daytime observations are occupied by the strong input of the Sun intensity. An overview of the performed observations is given in Table 4.1. The observations in different RCU modes have been done alternating so that every part of the sky at least once show up during day and night time for each frequency band. Larger time breaks during different observation runs are mainly caused by technical problems showing up at this time. This could have been for example problems in the hardware of the system or an even stronger RFI environment as normal. Some observations were not usable, due to a strong RFI situation, which was not recognized during the set up of the observation.

4.2 Combination of the data sets

After all snapshot observations were calibrated separately, the single skymaps were combined to map the entire northern sky and to increase the sensitivity of the final map. To combine all observations an accurate weighting of the single measurements is necessary. This is done by using the amplitudes of the gain values as output from the calibration of the data. The weighting for every single snapshot is done by using the median of the gain amplitudes from all dipoles. This works fine for an 24-hour run, as the properties of the system are expected to be stable over this time period. Unfortunately, it turned out that the systems is not stable over the nine month where the observations were performed. To deal with this situation all datasets within a 24-hour run are combined to a galactic map. Afterwards T-T plots (temperature-temperature plots) between the different observation runs are used to scale the data of various runs. In Fig. 4.2 the T-T plot at 45 MHz for the observation from March and September is shown. The data follow a straight line as expected, although some variations are seen for lower temperatures, where the noise and errors are expected to be higher. The slope m and offset n of the data is used for the scaling

$$\mathrm{T}_{20130311} = m\,\mathrm{T}_{20130916} + n \tag{4.1}$$

between both observations. In Fig. 4.2 the scaling value is m = 1.47 and the offset n = 144.5 K. This scaling is done for every dataset and every frequency channel.

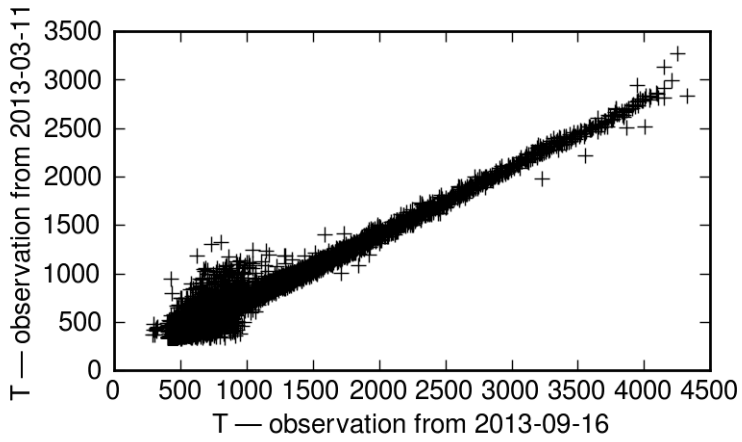

Figure 4.2: T-T plot at 45 MHz before the absolute amplitude calibration for the observations performed at March 11th and September 16th in 2013. Here the scaling value is m = 1.47 and the offset n = 144.5 K.

In the final skymaps the Sun and Jupiter are blanked out before the combination, as they are always appearing at different positions in the sky. RFI sources are already blanked in the single snapshot images. Furthermore, elevations below 30° were not used for the generating of the survey as well. An example for the combination of two single snapshot observations is shown in Fig. 4.3. Both belong to the same 24-hour run from March 2013, made with the TBBs at the Effelsberg station. The integration time for the snapshots is 1.3 sec and the bandwidth is 5 kHz. Both observations are separated by around 17 hours. In the map mainly Cas A, Cyg A and some part of the strong Galactic emission is visible. The signal to noise ratio in the overlapping region is already slightly better, than in the single snapshots. The result of all combined observations is shown in the following sections.

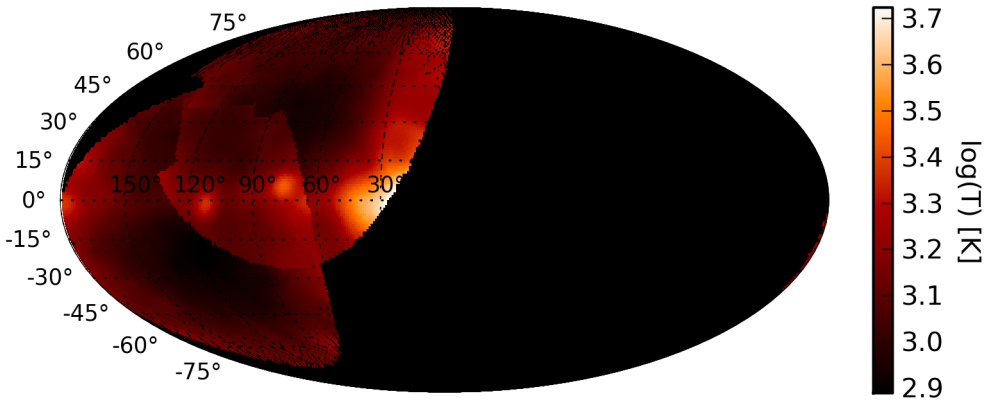

Figure 4.3: Combination of two snapshot images with 1.3 sec integration time and 5 kHz bandwidth at 40 MHz. Both observation were done with the TBBs in Effelsberg during the same 24-hour run in March 2013.

Table 4.2: Temperatures for the used calibrator sources from different surveys.

ν [MHz]	min. north [K]	anticenter [K]	Calpoint [K]	resolution	reference
10	130000 ± 10000	290000 ± 20000	-	2° x 2°	Caswell (1976)
13.1	80000 ± 8000	150000 ± 15000	-	53° x 12°	Bridle (1966)
17.5	35500 ± 3500	78000 ± 7800	-	12° x 17°	Bridle (1966)
22	-	44500 ± 4000	140000 ± 10000	1.1° x 1.7°	Roger et al. (1999)
26.3	12800 ± 400	27000 ± 840	-	15° x 44°	Turtle et al. (1962)
38	4800 ± 300	13000 ± 700	40500 ± 2000	7.5°	Milogradov-Turin et al. (1972)
45	3310 ± 300	9140 ± 900	30900 ± 3000	3.6°	Maeda et al. (1999)
81	680 ± 50	1800 ± 130	-	12° x 17°	Bridle (1966)
85	-	-	7000 ± 500	3.8° x 3.5°	Landecker et al. (1970)
102.5	-	-	5500 ± 500	1° x 0.5°	Ariskin (1981)
150	-	-	2000 ± 140	2.2°	Landecker et al. (1970)
151	160 ± 20	420 ± 40	-	17° x 12°	Sironi (1973)
177	120 ± 10	280 ± 20	-	15° x 44°	Turtle et al. (1962)
178	80 ± 10	310 ± 20	1700 ± 80	13'4 x 4.6 °	Turtle et al. (1962)

4.3 Absolute brightness temperature calibration

The absolute calibration of the brightness temperatures is done after the combination of all data, to get a reasonable good signal to noise ratio. For all studies of the Galactic emission the brightness temperature is used, which is related to the flux density by

$$B_\nu(T) = \frac{2h\nu^3}{c^2} \cdot \frac{1}{\exp(\frac{h\nu}{kT}) - 1} \tag{4.2}$$

following Rayleigh-Jeans at low frequencies (see Sect. 1.1.1). Just for the study of individual sources, like for Cas A and Cyg A demonstrated in Chapter 6, and for Jupiter discussed in Chapter 8, the flux density is used instead. To get the real brightness temperatures in the sky a correction for the bandpass and for the zero-level is needed. For the LOFAR survey this is done by correcting for a multiplicative factor b and an additive factor n:

$$\mathrm{T_{obs}} = b\mathrm{T_{theo}} + n \tag{4.3}$$

It is assumed that b and n stay mainly constant for most positions in the sky. This is just partly true, as it is known that the noise increases toward low declination. Nevertheless this assumption is needed, as it is not possible to perform an independent correction for all positions in the sky. By using at least two calibration sources b can be obtained via:

$$b = \frac{\mathrm{T^1_{obs}} - \mathrm{T^2_{obs}}}{\mathrm{T^1_{theo}} - \mathrm{T^2_{theo}}} \tag{4.4}$$

where 1 and 2 indicates the two calibration sources. Afterwards b can be used to calculate n. T_{theo} denotes a theoretical model, which is expected to be as close as possible to the real brightness temperatures of the source. It is an advantage to use sources or regions in the sky which are known best, meaning a high number of observations are available at various frequencies.

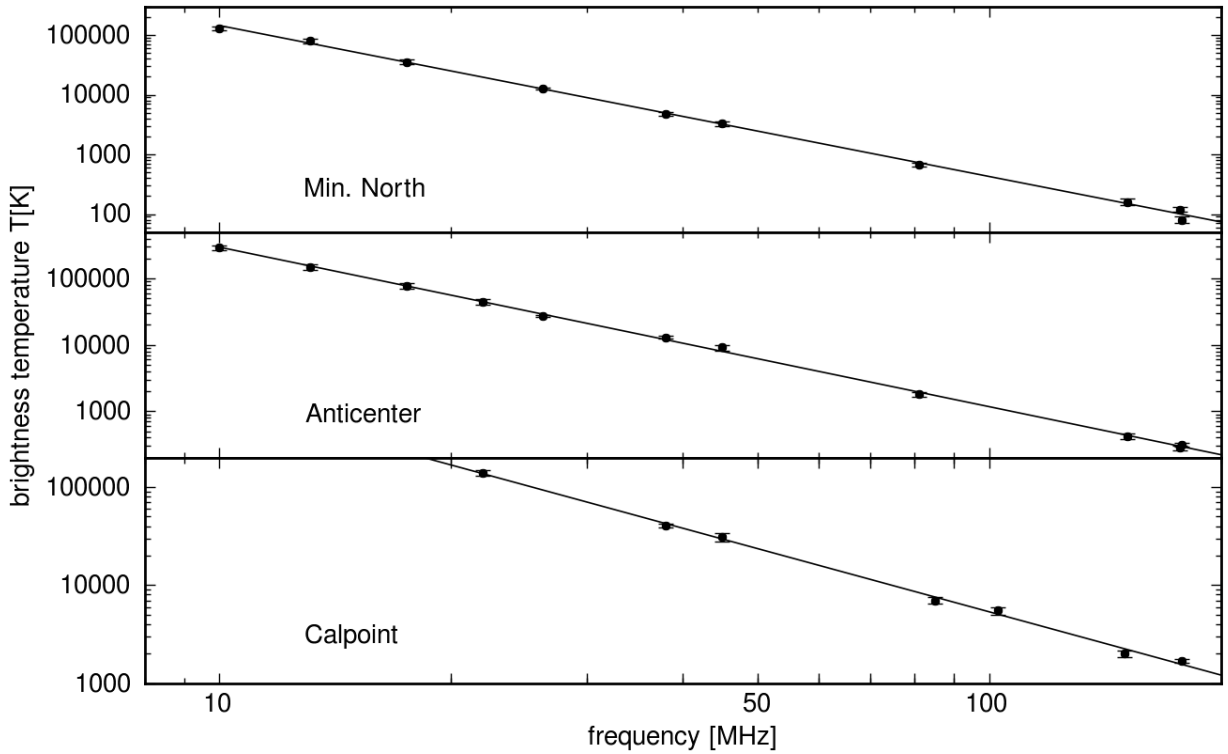

Figure 4.4: Spectrum of the calibration sources from Table 4.2.

Three regions in the sky have been chosen for the amplitude calibration of the data: the minimum temperature zone (l = 192°, b = 48°), the anticenter (l = 180°, b = 0°) and a region in the inner disk of the Milky Way, the so called Calpoint (l = 38°, b = -1°)(Guzmán et al., 2010). These regions already were used for the calibration of the 45 MHz survey from Meada et at. (1999) and Guzmán et al. (2010), wherefore measurements at various frequencies are available. A summary of the positions of these regions is given in Table 5.2. After testing also other regions in the sky for the calibration of the data, it turned out that the mentioned regions lead to the best results. Especially the use of a strong and a weak region is useful. The area with strong emission is less affected by errors. The area with weak emission is sensitive to errors and therefore useful to correct for systematic effects and to get a right zero-level correction. The brightness temperatures for the three calibration zones as measured by other surveys is summarized in Table 4.2. In Fig. 4.4 the spectra are plotted including a fitted line through these data. For all points the fitted lines clearly follow a single power law. It seems that this good agreement is also not affected by the different resolutions of the surveys, for which normally a correction is needed. If the varying resolutions causes an error, it is not significantly strong and does not show a deviation from the fitted power law. The slope of the fitted line is defined as the spectral index of the source. A summary of the achieved spectral indices are listed in Table 5.2.

4.4 Brightness temperature maps at 30 MHz, 45 MHz and 60 MHz (LBA)

The final galactic maps at 30 MHz, 45 MHz and 60 MHz, with an integration over 1 MHz bandwidth, are shown in Fig. 4.5. All of the maps were produced by using observations from the TBB system made with the single LOFAR station located Effelsberg. The observation time of the surveys, as shown in the top image of Fig. 4.6, depends on the sky position. A maximum of the observation time is found around the North Celestial Pole (410 seconds) as this region is circumpolar for the station in Effelsberg and therefore visible in all of the snapshot images. In addition, the observation time decreases toward lower declinations. In average an observation time of 250 seconds to 300 seconds is achieved. Note that the signal to noise ratio of the skymaps is related to the observation time ($S \propto 1/\sqrt{t}$) and the therefore also varies with the sky position.

As the beam resolution at 30 MHz is around 10° only large-scale structures are visible. No weak structures and sources can not be resolved. At 60 MHz the beam resolution is around 5° and therefore already some small-scale structures can be resolved. In all the maps mainly Galactic emission from the Milky Way and a few strong sources can be detected. Most of the emission originates in the Galactic inner disc and is visible at latitudes from -10 to 10°. Along the Galactic plane the emission gets stronger toward the Galactic center becomes weaker toward the anticenter. Another strong large-scale feature, along a galactic longitude of 30°, is the famous North Polar Spur (NPS) as part of Loop I, which is expected to be an old supernova remnant shell (Berkhuijsen et al., 1971). In addition, Loop III near the North Celestial Pole (NCP) can be detected, as well as some other weaker filaments. Aside from the large-scale structures especially two strong point sources become visible- Cas A (l = 111.5°, b = -2.3°) and Cyg A (l = 76.2°, b = 5.8°). At higher frequencies some other strong point sources can be resolved as well, like Vir A (l = 285°, b = 74.3°), Tau A (l = 184.6°, b = -5.8°) and Her A (l = 23.0°, b = 28.9°).

By comparing the maps it becomes obvious that the noise is increasing with frequency. This is due to decreasing sky temperatures and increasing system temperatures toward the higher frequencies. At 65 MHz the system temperatures is dominating over the sky temperatures (van Haarlem et al., 2013). Besides of that, the noise increases at lower declinations as the sensitivity of the antennas is lowest at the horizon. Apart from that, errors in the beam corrections are expected to show off at the horizon as well.

4.5 Brightness temperature map at 130 MHz (HBA)

The combination of the HBA data was performed in the same way as described for the LBA observations. The only difference came by dealing with the ghost sources. If the strongest sources in the field appeared due to grating loops a second time in the snapshot image (see Sect. 3.7) the region was blanked. For the extended emission this was not done, as the

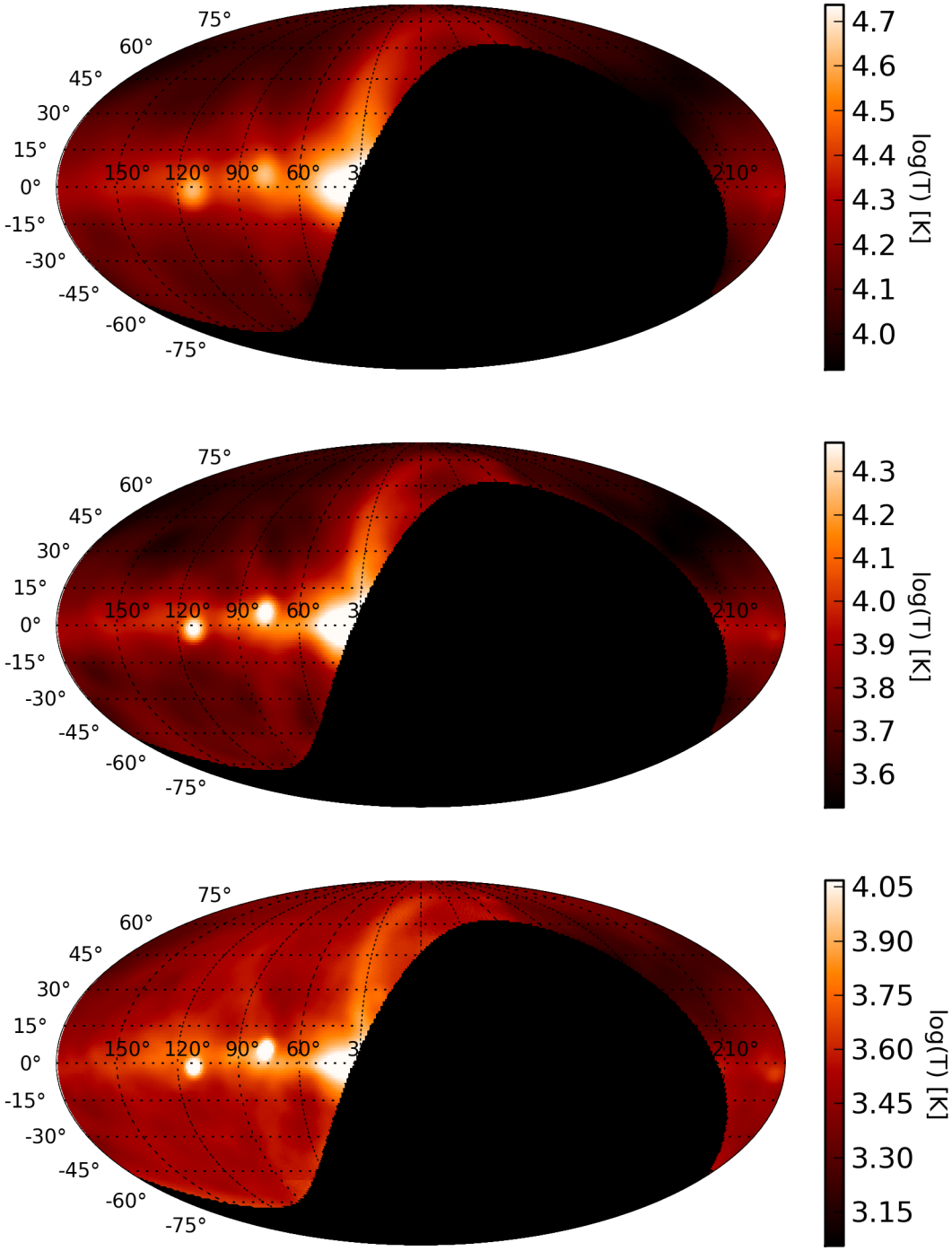

Figure 4.5: Northern sky surveys observed with the LOFAR station in Effelsberg down to an elevation of 90° at 30 MHz (top), 45 MHz (middle) and 60 MHz (bottom). The bandwidth is 1 MHz.

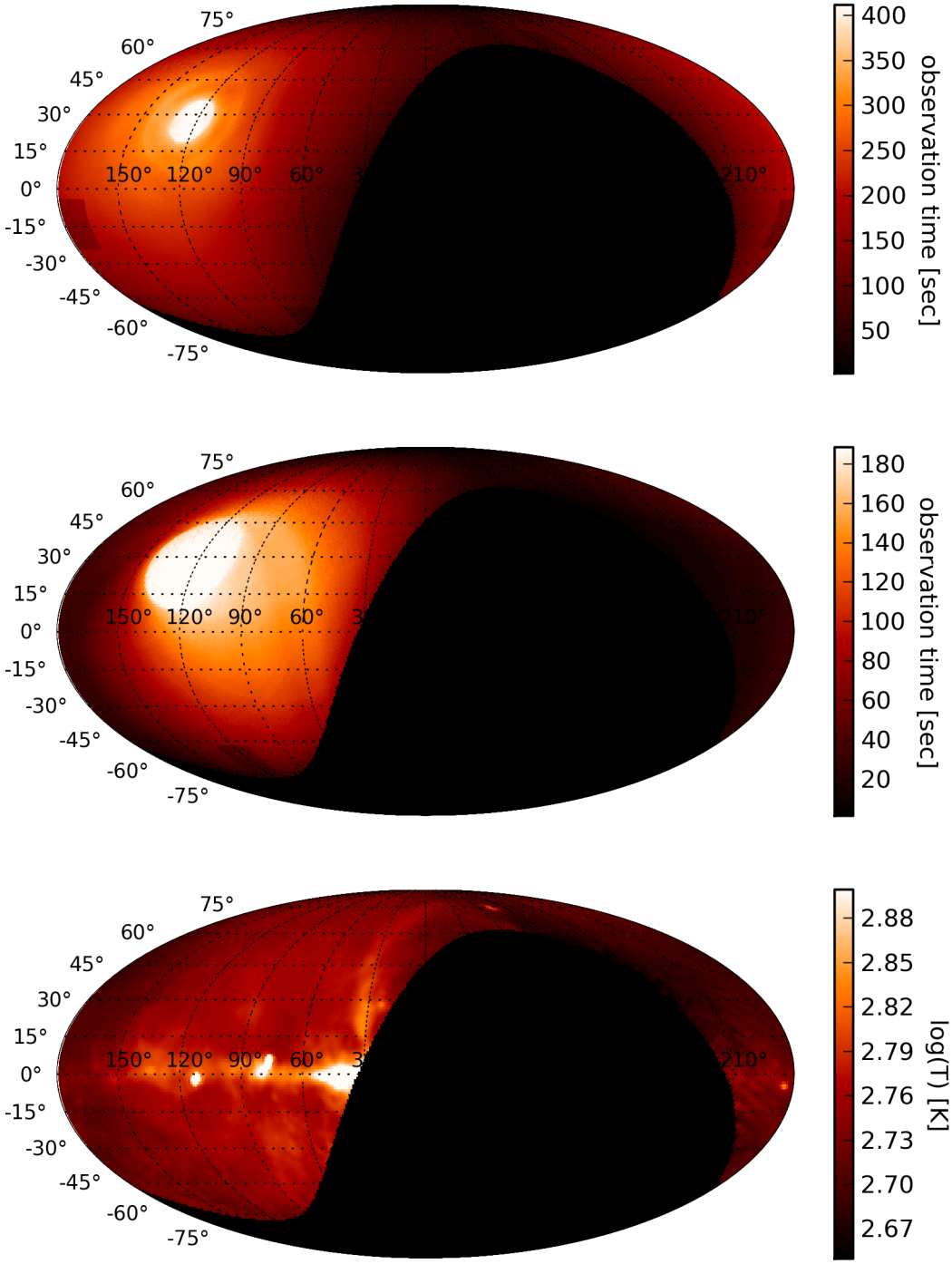

Figure 4.6: Top: Position dependent observation time of the survey at 45 MHz. Middle: Position dependent observation time of the survey at 130 MHz. Bottom: HBA survey at 130 MHz.

calculation of the corresponding regions is more difficult. But as the ghost structures appear in every observation at a different position relative to the real structure, by the combination of all maps these features should be mostly averaged out. Nevertheless, it should be noted that this effect can increase the noise in the final maps.

The HBA survey centered at 130 MHz averaged over 10 MHz bandwidth is shown in the bottom image of Fig. 4.6. The image in the middle of Fig. 4.6 shows the corresponding observation times with a maximum of 200 seconds around the NCP. At galactic longitudes above 160° less observations are available, as this region correspond to observation times where Cyg A was below and Cas A close to the horizon. Due to unsolved calibration problems for this special case most of the snapshot observations were not usable.

The beam resolution of the shown map is around 2.5° wherefore some weak sources and structures can be resolved. Now the strong radio sources Vir A, Tau A and Her A can be resolved from the extended emission. In the Cygnus region Cyg-X can now be separated from Cyg A, which was due to the low beam resolution just a single source in the LBA maps. In addition, small structures in the extended emission can be detected, e.g. the 'break' in the NPS at a galactic latitude of around 37° - 40° and the small filaments in the Galactic plane at l = 40° and l = 50°. All of these structures can be seen in other high resolution surveys as well. Unfortunately Loop III around the NCP can not be detected due to the short integration time, which leads to less sensitivity in this region. Furthermore, due to the low sensitivity by using just one antenna out of 16 and the low number of observations, the noise in the presented map is much higher than in the LBA maps.

Due to missing spacings in the uv-coverage weak sidelobes around Cas A and Cyg A appear. No cleaning was performed on these maps as existing software is not working for these datasets and the invention of an own cleaning algorithm would have been gone beyond the scope of this project. This leads to errors in the final maps and therefore they will not be used for any scientific results presented in this thesis.

4.6 Contour maps at various frequencies

For comparison and to identify weak and small scale structures in Figs. 4.10 - 4.16 (at the end of this chapter) the brightness temperatures overlaid with contours are imaged for the LOFAR surveys at 45 MHz and 130 MHz. Besides, the 22 MHz (Roger et al., 1999) and 408 MHz (Haslam et al., 1982) surveys are shown. The maps at 45 MHz are integrated over 2 MHz bandwidth, the maps at 130 MHz over 20 MHz bandwidth. The contours in the 22 MHz and 45 MHz maps are given in kK, whereas they are in K in the 130 MHz and 408 MHz maps. As the beam resolution is around 6.5° in the 45 MHz map, just large-scale features are seen. In the other surveys some small-scale structures can be resolved. Even as the HBA maps is strongly affected by noise, they are shown for comparison, to prove that the small-scale structures can be detected. Of course more observations would be needed to improve the quality of these maps.

By direct comparison it is seen that all of the large-scale structures visible at 45 MHz

are nicely corresponding to the large-scale structures in the other surveys. In contrast, the 130 MHz maps show discrepancies to the other surveys in regions with a short total observation time (Fig. 4.6 middle) wheer the noise is dominating. This effect becomes most obvious at high galactic latitudes like in the top image of Fig. 4.10, in regions close to the anticenter like in the bottom of Fig. 4.12 where Loop III cannot be detected, and in the region of the minimum zone (bottom of Fig. 4.13). At least in some regions with strong emission already a few weaker sources and small-scale structures can be resolved and are in good agreement with the surveys at 22 MHz and 408 MHz. Unlike in the 45 MHz map, the strong radio sources Vir A (Fig. 4.11 bottom), Her A (Fig. 4.13 top) and Tau A (Fig. 4.15 bottom) can be resolved. In the Cygnus region it is possible to detect Cyg-X near to Cyg A (Fig. 4.14 bottom). By comparing the HBA map with the higher frequency survey at 408 MHz it is seen that Cyg A is stronger at lower frequencies, whereas Cyg X (in the images left below Cyg A) becomes stronger at higher frequencies. The decreasing spectrum of Cyg X toward lower frequencies can be explained by thermal absorption in the HII region around this area.

The good agreement between the surveys indicates that the self-calibration method as used for the data reduction of the LOFAR observations give reliable results.

4.7 Comparison to other surveys

In the following section the LOFAR survey will be compared to other already existing surveys to look for similarities and possible differences. For the comparison five other surveys at 22 MHz (Roger et al, 1999), 45 MHz (Guzmán et al., 2010), 408 MHz (Haslam et al., 1982), 820 MHz (Berkhuijsen, 1972) and 1400 MHz (Reich et al., 1981) are used as electronically datasets are available (Table 1.1; Fig. 1.7). All surveys were convolved to the same resolution of 7°. For the LOFAR survey the frequency of 45 MHz (in the following labeled as L 45 MHz) is chosen for the following analysis as it provides the best combination of reasonable good beam resolution and low system temperature noise. Besides, it allows an accurate comparison to the 45 MHz survey by Guzmán et al. (in the following labeled as G 45 MHz). The presented maps at 30 MHz and 60 MHz are not used, as the first one has a worse beam resolution whereas the second on is dominated by the system temperature noise.

Already in the previous section the LOFAR survey at 45 MHz was directly compared to the surveys at 22 MHz and 408 MHz using contour maps. For the following comparison of the surveys brightness temperature profiles at various galactic longitudes and latitudes will were produced.

4.7.1 Temperature profiles at different latitudes

The brightness temperature profiles at galactic latitudes of 45°, 20°, 0° and -20° are shown in Fig. 4.7). A normalization of the surveys is done by using the highest brightness temperature within each survey appearing at the corresponding latitude. Note that due to different

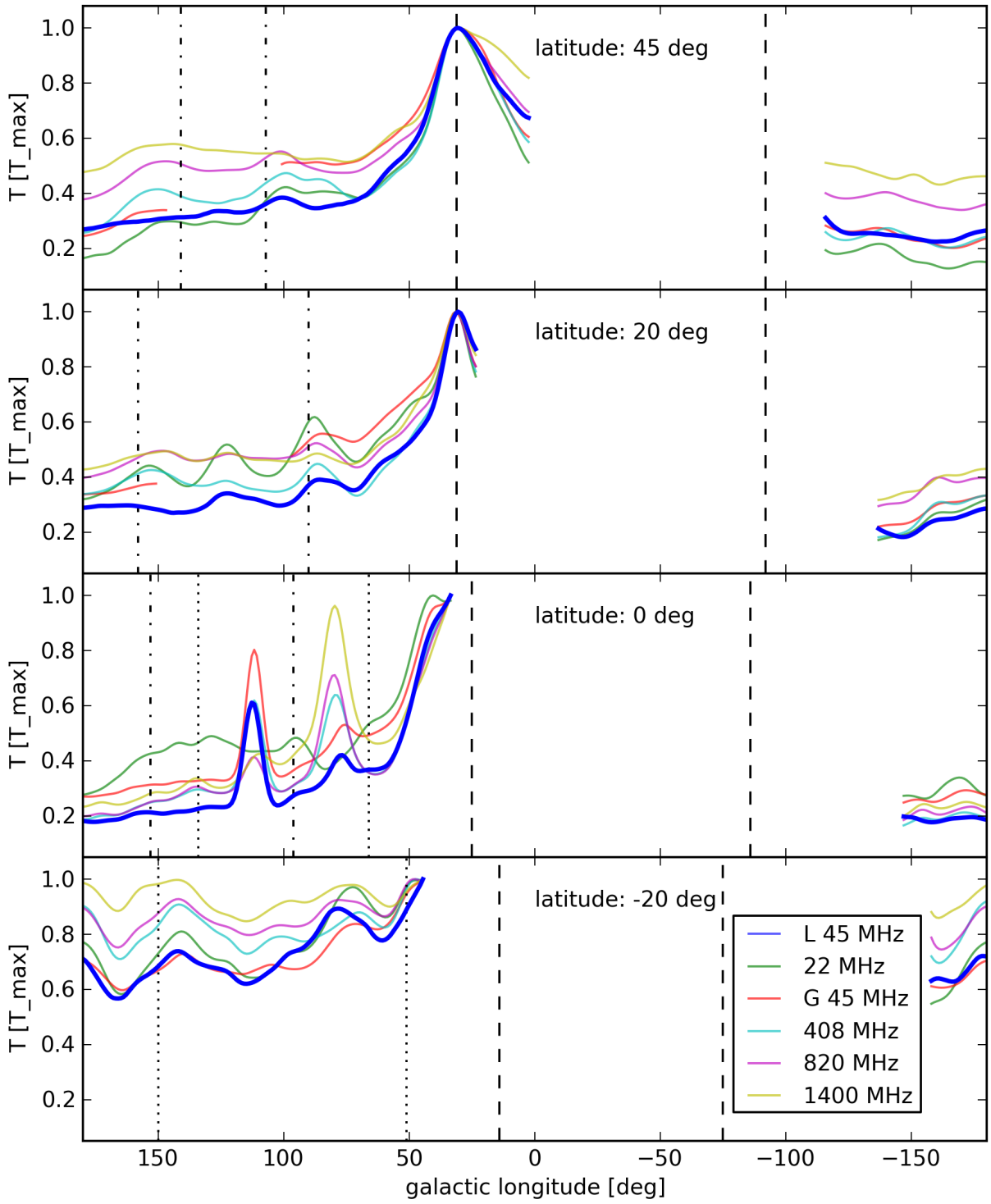

Figure 4.7: Profiles at different latitudes. The thick blue line shows the LOFAR profile at 45 MHz. The vertical lines show the position of the calculated loop circles, using the parameters summarized in Table 4.3. The brightness temperatures are normalized to the highest temperature value at the given latitude.

spectral index behaviors the relative brightness temperatures vary for the different surveys. Therefore the focus in the following discussion will be on the seen structures in the surveys. The location of the four prominent Loops (4.3) is given by the vertical lines within the plots.

Table 4.3: Center and radius of the loops (Berkhuijsen et al., 1971)

Loop	l [deg]	b [deg]	r [deg]
I	329	17.5	58
II	100	-32.5	45.5
III	124	15.5	65
IV	315	48.5	19.8

Profile at the galactic latitude b = 45°:
In all the surveys the maximum of the brightness temperature shows up at l = 30° and belongs to the North Polar Spur as part of Loop I. Loop III becomes visible at l = 100°and l = 150°. The peak at l = 150°, which is clearly visible in all of the other surveys, is not detected in the LOFAR survey at 45 MHz. In opposite to that, the peak at l = 100° is visible in all surveys beside of the one at 1400 MHz. Another small peak at l = 85° is detected in all surveys except in the LOFAR and 820 MHz survey. In this region the LOFAR and 820 MHz map are in good agreement with each other by showing a valley of weaker emission. It is not clear, what causes this difference. The direct comparison of the both surveys at 45 MHz shows that the survey by Guzmán et al. measures stronger emission for the region close the NPS compared to the LOFAR survey. It cannot be explained what causes the difference as for all other regions both surveys are in good agreement with each other.

Profile at the galactic latitude b = 20°:
In these profiles the maximum of the brightness temperature is again detected at l = 30° (Loop I). Loop III is detectable at l = 150° and l = 85° in all surveys. As seen before in the profile at b = 45° the survey from Guzmán et al. shows strong emission in the region next to NPS what cannot be confirmed by the LOFAR survey.

Profile at the galactic latitude b = 0°:
These profiles show the brightness temperatures along the Galactic plane. Outstanding are the strong intensities at the position of Cas A (l = 113°), near Cyg A (around l = 78°) and toward the Galactic center region. Another smaller peak is visible for all frequencies at l = -170° (Tau A) and one at l = 135°, which not appears in both 45 MHz surveys. The 22 MHz survey do not show any good agreement with the other surveys what could be due to thermal absorption in the Galactic plane toward 22 MHz. The disagreement in the relative values of the LOFAR and the Guzmán map is possibly due to the normalization, as the highest point in the LOFAR map is at a low declination, where the map is stronger occupied by noise effects. At least the structures as seen in both surveys are in a good agreement with each other. For the Cygnus region a strong frequency dependence is detected, with decreasing temperatures toward lower frequencies. Nothing like this can be seen for Cas A as its flux density decreases every year by 1% and all of the surveys were produced at different epochs. Furthermore, the position of Cyg A is shifting toward smaller galactic longitudes with decreasing frequencies. This is due to the fact that at higher frequencies Cyg X is the dominating source in this region, whereas the radio source Cyg A is dominating

at low frequencies. This can be explained by the thermal absorption of Cyg X toward low frequencies, as it is surrounded by strong HII emission.

Profile at the galactic latitude b = -20°:
At this latitude several loops and spurs become visible. The peak at l = 45° belongs to Loop II. An other spur shows up at l = 75° - 80°. Hereby the peak position seems to vary for the different surveys. The LOFAR data show the best agreement with the 820 MHz survey. Two other spurs can be detected at l = 142° and l = 180°. The region around l = 165° shows a deep minimum and appears in all surveys. In the HII map (WHAM; Haffner et al., 2003) strong emission can be found at this part of the sky, as well as in CO (Dame et al., 2001). In contrast to that this region also has a minimum in the HI emission (Dickey and Lockman, 1990).

4.7.2 Temperature profiles at different longitudes

The profiles at different longitudes (Fig. 4.8) allow to study the extent of the Galactic disk, which is centered at a latitude of b = 0°. After all surveys were convolved to the same resolution of 7° no frequency dependence of the disk extent is noticeable. Furthermore, even in the halo of the Galaxy all surveys show a similar behavior for the relative temperature values.

Profile at the galactic longitude l = 150°:
At this galactic longitude the maximum in the Galactic disc is slightly shifted toward negative galactic latitudes. Another smaller peak shows up at b = 35° and belongs to the emission of Loop III. At galactic latitudes below -25° the LOFAR survey is noise dominated what results in higher temperature values compared to the other surveys.

Profile at the galactic longitude l = 120°:
All of the shown surveys are in good agreement with each other and only the LOFAR survey is again noise dominated at high negative galactic latitudes. Nevertheless, there is one region at b = 20° where the 22 MHz survey shows stronger emission which cannot be explained.

Profile at the galactic longitude l = 90°:
In this profiles the maximum of the galactic disc is shifted to a galactic latitude of around 5°. Some emission related to Loop III is detected, which becomes visible at a b = 25°. Beside of the G 45 MHz and the 22 MHz survey all profiles are in good agreement with each other. Especially the Guzmán map shows much stronger emission than seen by the other surveys. Note that in their case this galactic longitude is already close to their observing horizon what may causes the increasing of the temperature. In the presented spectral index map by Guzmán et al. (2010) a high spectral index value of 2.7 is detected in this region. The LOFAR survey shows in the region a better agreement with the other high frequency surveys and therefore seems to be more trustful.

Profile at the galactic longitude l = 60°:
Once more the Guzmán survey shows stronger emission at positive galactic latitudes. And

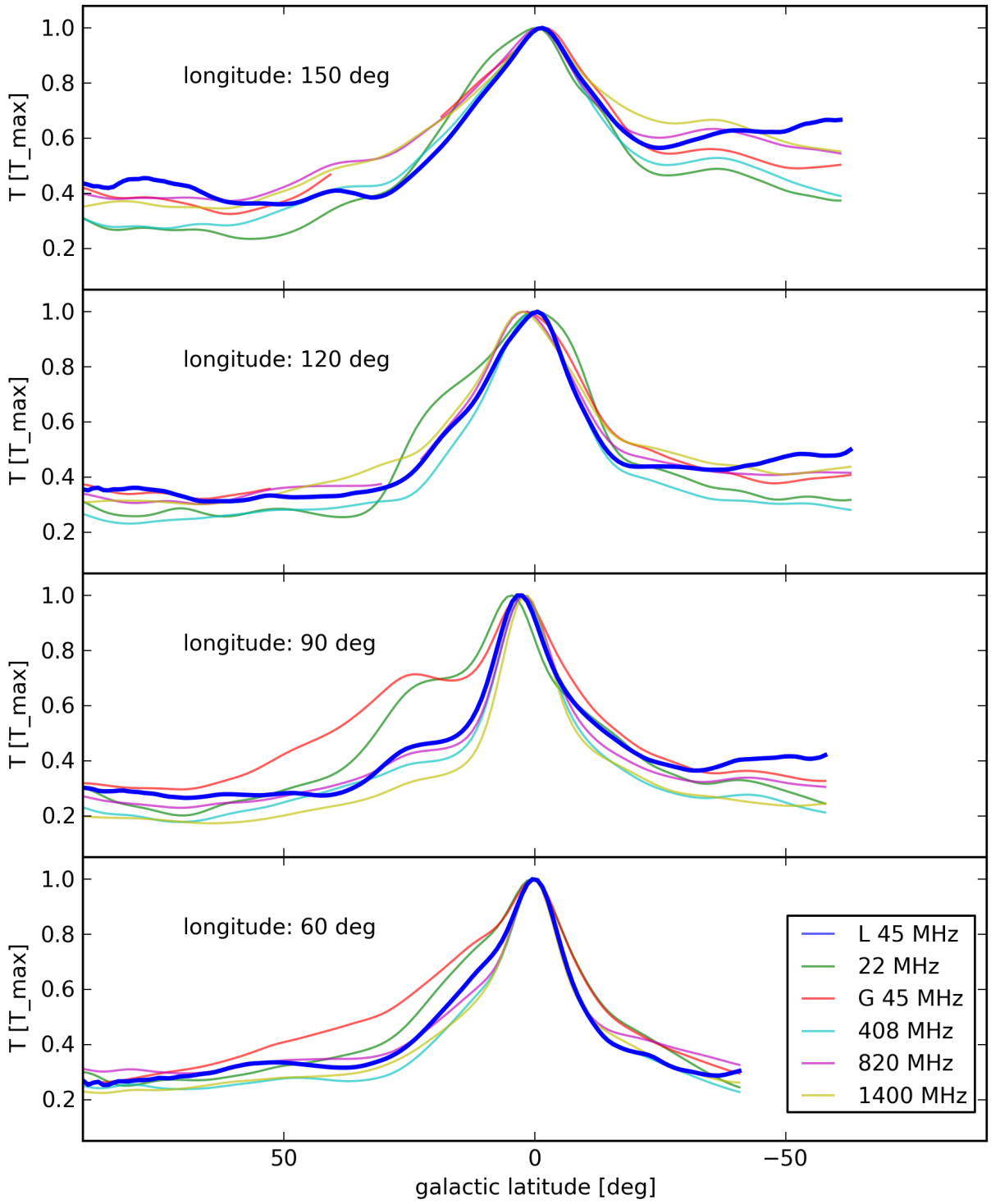

Figure 4.8: Profiles at different longitudes. The thick blue line shows the LOFAR profile at 40 MHz. The brightness temperatures are normalized to the highest temperature value at the given longitude.

again the LOFAR survey at the same frequency is in a better agreement with the other surveys. The extended structure at positive galactic latitudes next to the Galactic disc comes from a small spur in the region.

By comparing the profiles at different longitudes a decreasing extent of the Galactic disk emission is seen toward lower longitudes. This larger extent belongs to the emission from Loop III and an other small spur at l = 120° and is not related to a different behavior of the Galactic disc.

4.8 Error discussion

Errors in the skymaps can be due to systematic effects caused by the instrument or can be introduced during the calibration process of the snapshot observations.

The success of the gain calibration depends on the quality of the local sky model. As, mainly due to a bad RFI environment in Effelsberg, the self-calibration method is used it means that the quality of the calibration model depends on the quality of the uncalibrated skymap. Hereby strong RFI sources or phase errors due to strong ionospheric fluctuations are expected to have the biggest influence on the data quality. In particular, ionospheric fluctuations which are varying within the field of view are problematic as no direction dependent calibration is performed. Nevertheless, during the test performances of the software and while having a random look on the quality of the calibrated datasets, it turned out the calibration was in around 90% successful. Small errors in some of the snapshot observations can be assumed to be averaged out by combining a high number of observations. Datasets containing strong errors are removed before the combination of the data.

Another error source is the used antenna beam model by Hamaker which is known to be incorrect, especially at low elevations. In Sect. the Hamaker model was introduces, as well as a beam model generated by using the source tracking of Cas A and Cyg A. The difference of both models for the final survey

$$\frac{skymap(E_{mymodel}) - skymap(E_{Hamaker})}{skymap(E_{Hamaker})} \tag{4.5}$$

is shown in Fig. 4.9. At most parts of the map the difference due to the two different beam models is below 5%. The largest discrepancy of both models is found at negative galactic latitudes, where the beam model generated by the source tracking would lead to intensities up to 20% higher than seen by the Hamaker model. In comparison, by using the Hamaker model in average 10% higher intensities would be measured towards the Galactic center region and at galactic longitudes above 150°. Following this, the error caused by the beam model is assumed to be in the order of 5-10%.

Errors in the final brightness temperatures depend on the absolute calibration of the survey which is related to former sky surveys. Most of the used surveys are not absolute calibrated and bring in errors. This is already recognized by comparing the brightness

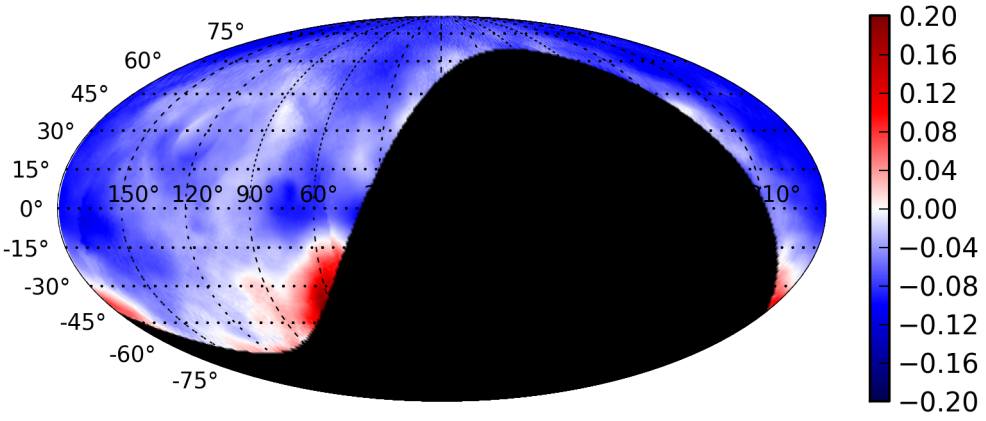

Figure 4.9: Fractional difference of the Galactic maps at 45 MHz as generated by source tracking and the Hamaker model (see Sect. 4.8).

temperatures measured by different surveys at the same frequencies. As it is impossible to judge which survey is giving the better results, a median value was used, if a larger number of surveys was available at one frequency. Of course some of these variations can be caused by a different beam resolution due to different instruments. As some surveys are just available as contour plots in the literature, errors can be introduced by reading the brightness temperatures from the papers. Papers which have tables for their measurements just have values at a few declinations and right ascensions available. Therefore assumptions have to be made for regions which are slightly off the given sky position. This is especially problematic for regions where the brightness temperatures are strongly changing. Unfortunately it is not possible to calibrate the amplitudes without using other observations, wherefore every available survey was used to keep the errors as small as possible by using a high number of observations. As in average the error as quoted by the other surveys is around 10%, the error of the absolute calibration of the LOFAR survey is expected to be around 10% as well.

The noise in the LOFAR survey is not constant and changing with position in the sky due to a variation of the antenna sensitivity with sky position and different integration times. For the single snapshot images the noise is, due to the antenna properties, higher toward low elevation. As a result, the noise in the final survey is highest at low declinations where only measurements at low elevations are available. As the final survey is combined by single snapshot observations, which are always observing the entire visible sky, the integration time depends on the position in the sky. Regions close to the zenith have longer integration times and therefore are expected to have a better signal to noise ratio. In consequence the errors are expected to be lower in this regions of the sky.

Furthermore the measured noise not only varies with position in the sky but also with frequency. As toward higher frequencies the sky noise is decreasing and the system noise is increasing, more noise and errors are expected to be seen at higher frequencies. From

measurements at high galactic latitudes noise temperatures of 1600 K at 30 MHz, 750 K at 45 MHz, and 1200 K at 60 MHz can be achieved. Note that this is at 30 MHz and 45 MHz one third of the minimum temperature (at l = 192°, b = 48°) and twice as much at 60 MHz. Therefore most of the following studies are done using the survey at frequencies below 50 MHz. In the LBA (below 100 MHz) the system temperature is dominating over the sky temperature for frequencies above 60 MHz. In the HBA (above 100 MHz) the system temperature is in every case dominating over the sky temperature. The situation is even worse as for the HBA observations only one antenna per tile can be used for the all-sky imaging. Therefore much more observations would be needed to get a reasonable good signal to noise ratio, which was not possible in the time period of this work.

4.9 Summary

In this chapter the first large-scale continuum survey produced with a LOFAR single station has been presented. As part of this sky maps at 30 MHz, 45 MHz and 60 MHz, observed with the LBAs, are shown. Even a first HBA map at 130 MHz is shown, although more observations would be needed to improve the quality of this map. Nevertheless it proves that it is possible to use HBA data from a single station to generate all-sky surveys. Due to a better beam resolution of the HBA data (2.5° instead of the 6.5° at 45 MHz) it is already possible to resolve some small scale structures and weaker point sources.

The observed large-scale structures as seen in the presented LOFAR maps are in good agreement with earlier surveys, even if they are produced in different ways. Whereas the older surveys are produced by scanning the sky in stripes, for the LOFAR survey all-sky observations were used. Even more the LOFAR survey was self-calibrated with the software introduced in Chapter 3. By recovering known structures in the sky, it is confirmed that the calibration software is working properly.

A direct comparison between the LOFAR survey at 45 MHz and the surveys at 22 MHz (Roger et al, 1999), 45 MHz (Guzmán et al., 2010), 408 MHz (Haslam et al., 1982), 820 MHz (Berkhuijsen, 1972) and 1400 MHz (Reich et al., 1981) is done by plotting the temperature profiles at various galactic latitudes and longitudes. In this way it was possible to have a direct look at similarities and differences between the surveys. The largest discrepancy is found for the 45 MHz survey by Guzmán et al. (2010) which shows strong emission next to the NPS, which is by a factor of 1.4 above the 45 MHz LOFAR temperatures in this region. It is unknown what causes this difference as both surveys are in good agreement everywhere else. Nevertheless, the LOFAR survey is in this region in good agreement with all the other presented surveys. Following this, it can be assumed that the LOFAR survey is in this region of the sky more trustful than the survey presented by Guzmán et al. (2010).

At the end of this chapter contour maps from the LOFAR survey at 45 MHz and 130 MHz are presented together with the surveys at 22 MHz (Roger et al, 1999) and 408 MHz (Haslam et al., 1982).

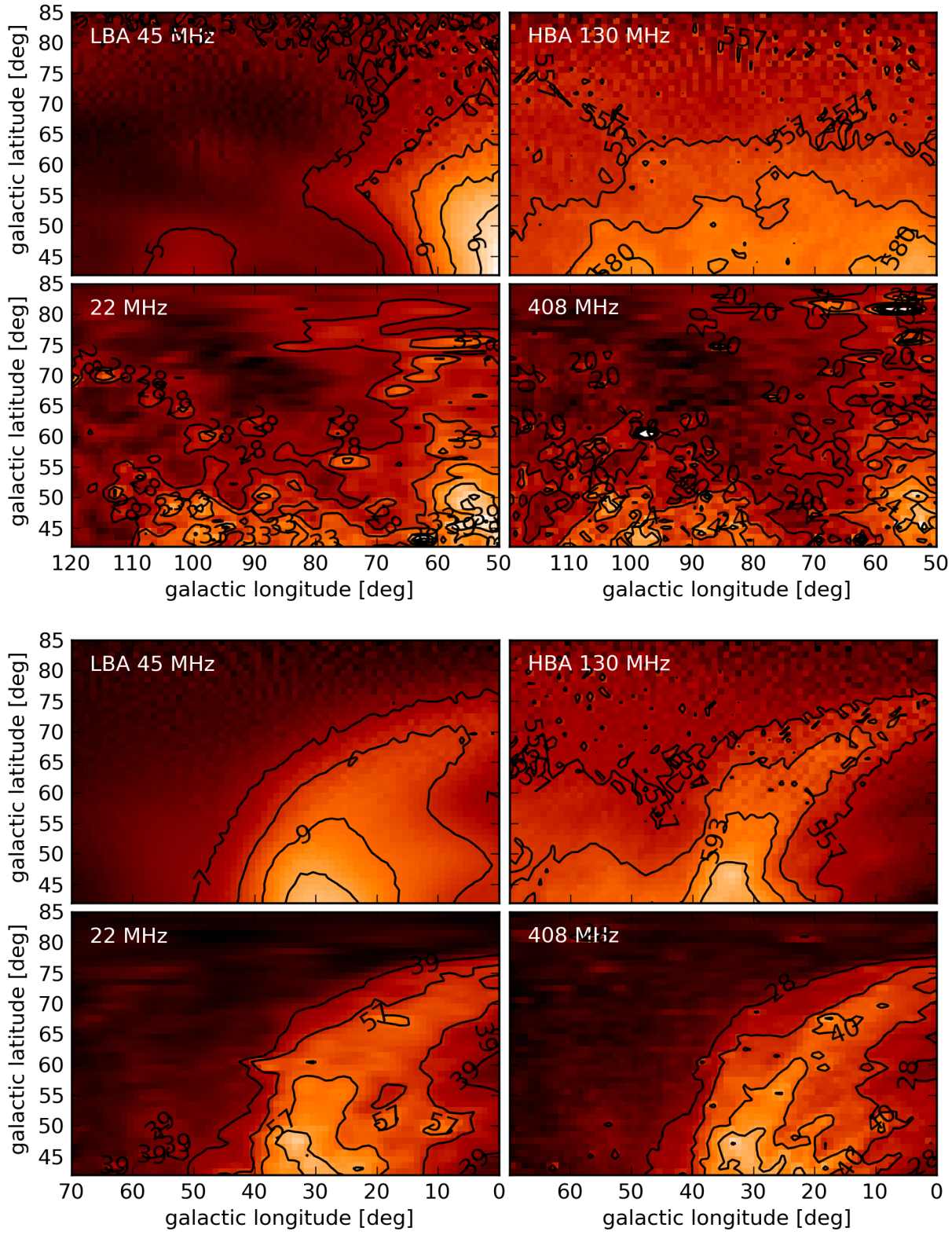

Figure 4.10: LOFAR maps at 45 and 130 MHz. For comparison the 22 MHz survey (Roger et al., 1998) and the 408 MHz survey (Haslam et al., 1982). Shown is the temperature brightness overlaid with the corresponding contours (at 22 and 45 MHz in kK, at 130 and 408 MHz in K.)

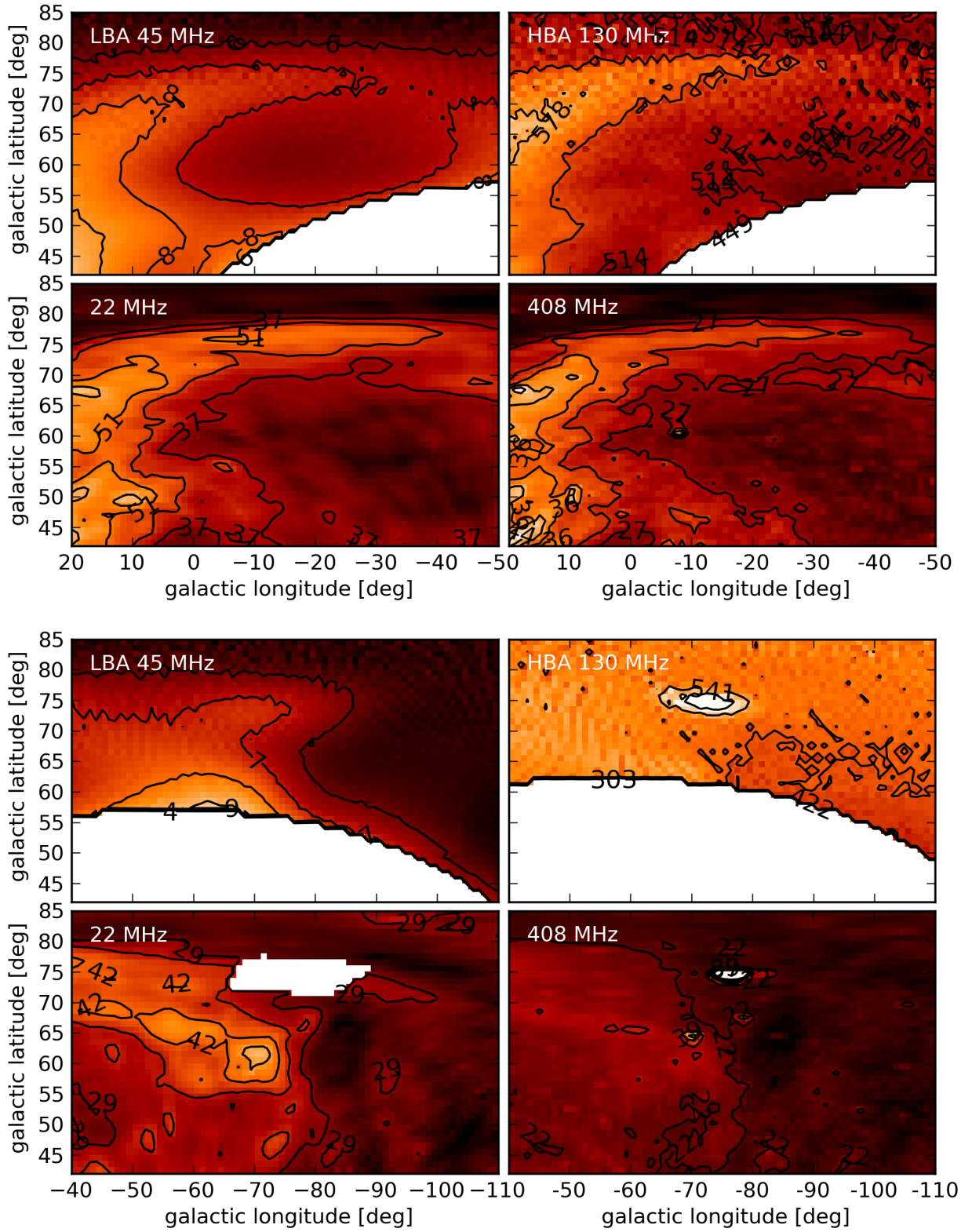

Figure 4.11: LOFAR maps at 45 and 130 MHz. For comparison the 22 MHz survey (Roger et al., 1998) and the 408 MHz survey (Haslam et al., 1982). Shown is the temperature brightness overlaid with the corresponding contours (at 22 and 45 MHz in kK, at 130 and 408 MHz in K.)

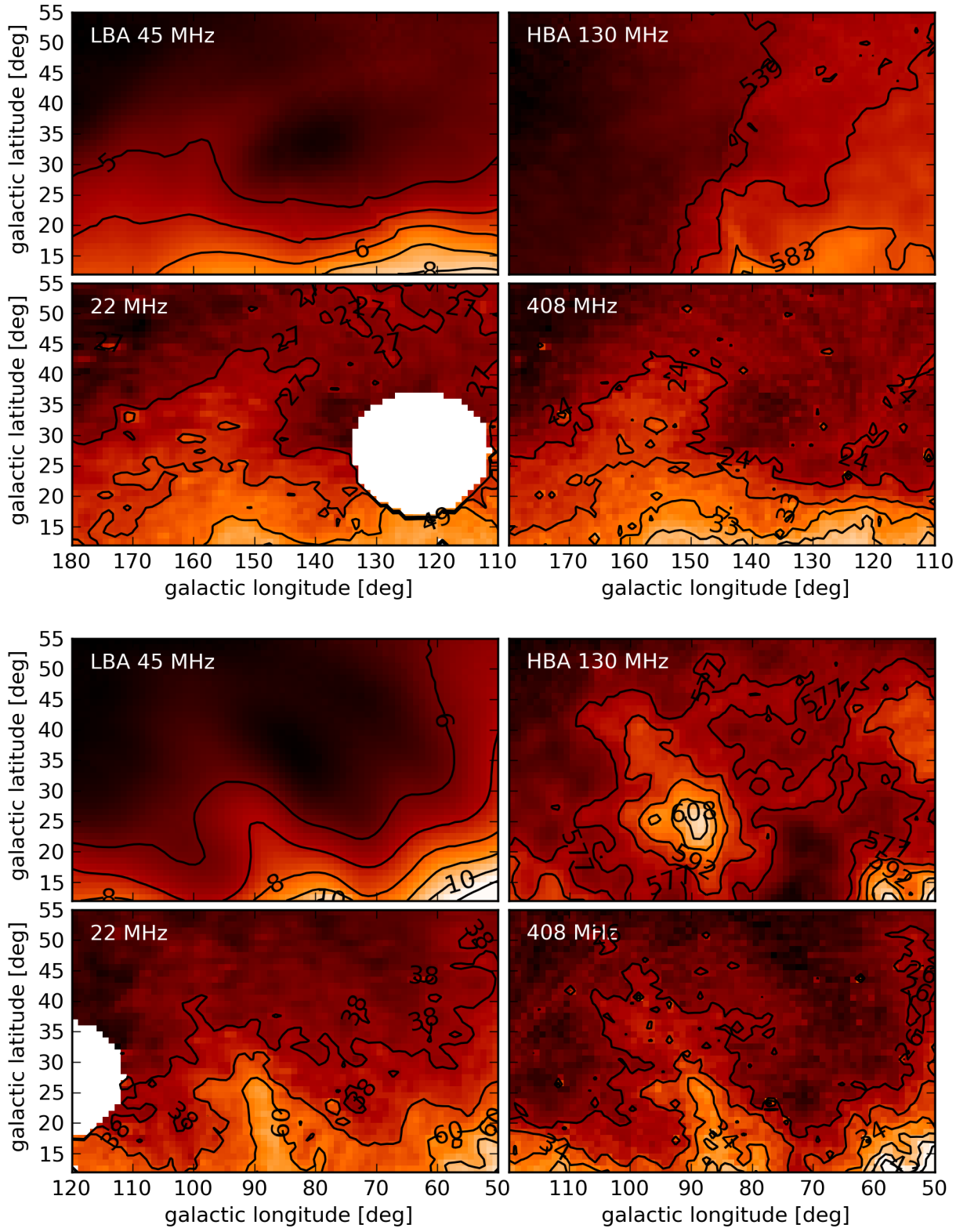

Figure 4.12: LOFAR maps at 45 and 130 MHz. For comparison the 22 MHz survey (Roger et al., 1998) and the 408 MHz survey (Haslam et al., 1982). Shown is the temperature brightness overlaid with the corresponding contours (at 22 and 45 MHz in kK, at 130 and 408 MHz in K.)

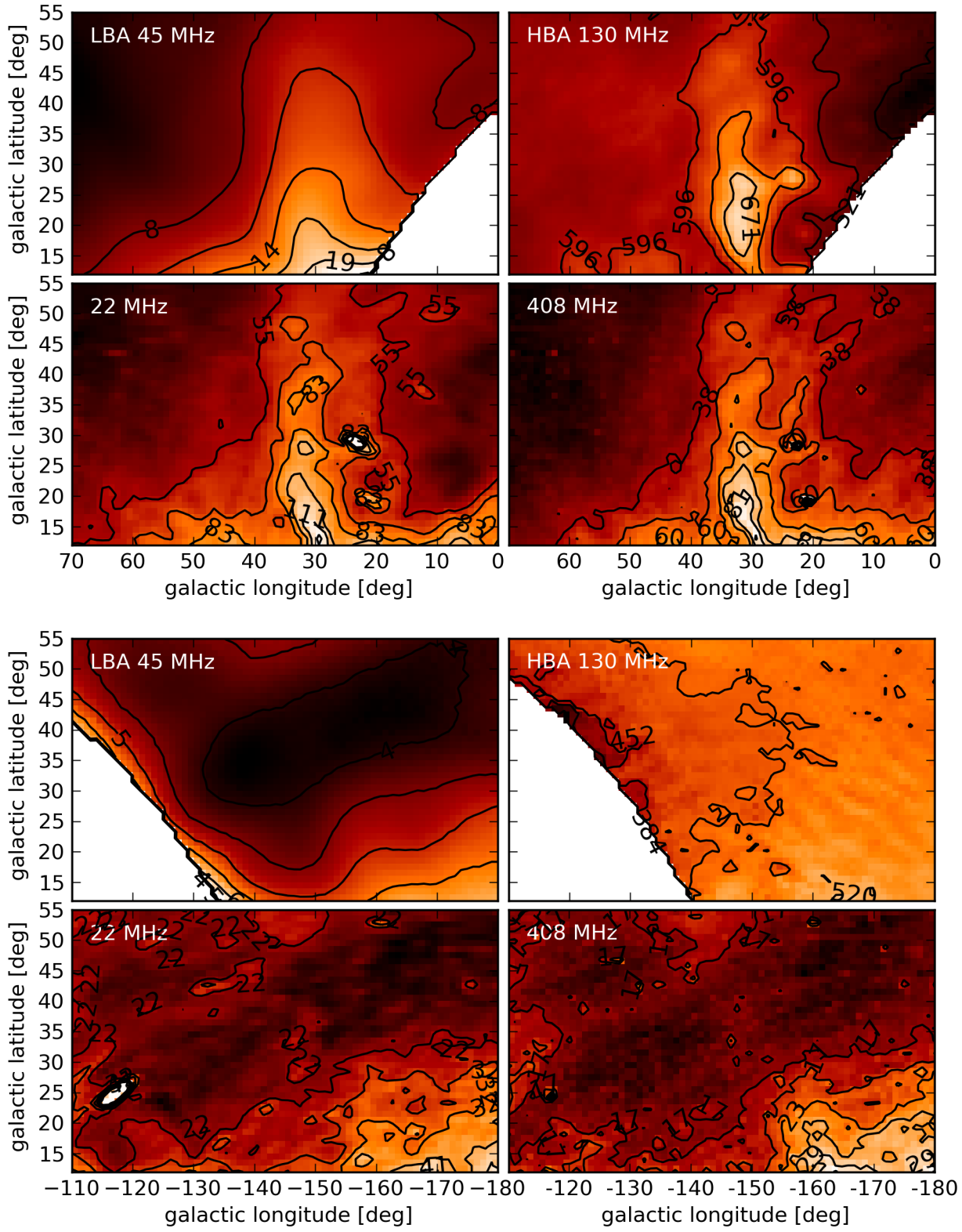

Figure 4.13: LOFAR maps at 45 and 130 MHz. For comparison the 22 MHz survey (Roger et al., 1998) and the 408 MHz survey (Haslam et al., 1982). Shown is the temperature brightness overlaid with the corresponding contours (at 22 and 45 MHz in kK, at 130 and 408 MHz in K.)

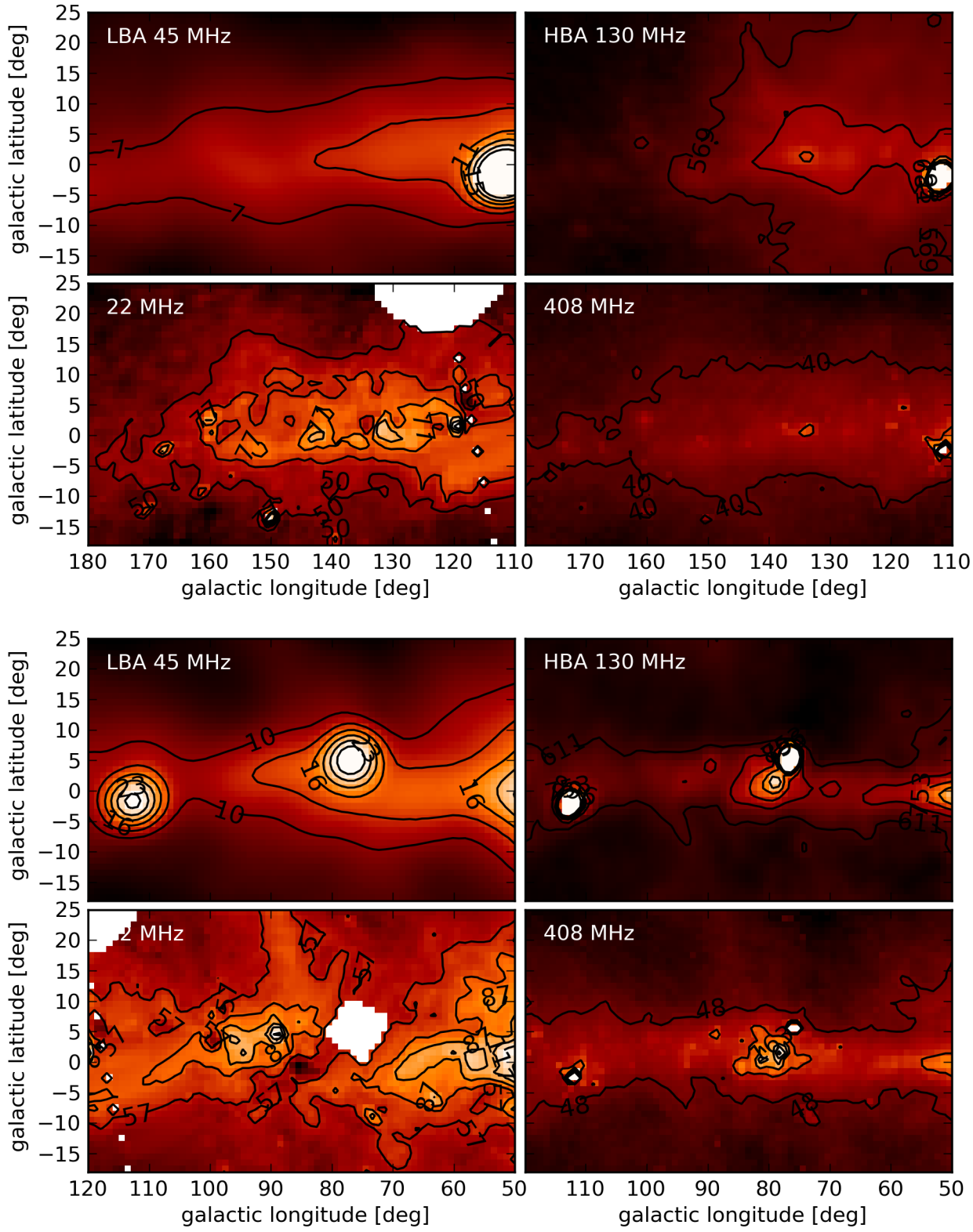

Figure 4.14: LOFAR maps at 45 and 130 MHz. For comparison the 22 MHz survey (Roger et al., 1998) and the 408 MHz survey (Haslam et al., 1982). Shown is the temperature brightness overlaid with the corresponding contours (at 22 and 45 MHz in kK, at 130 and 408 MHz in K.)

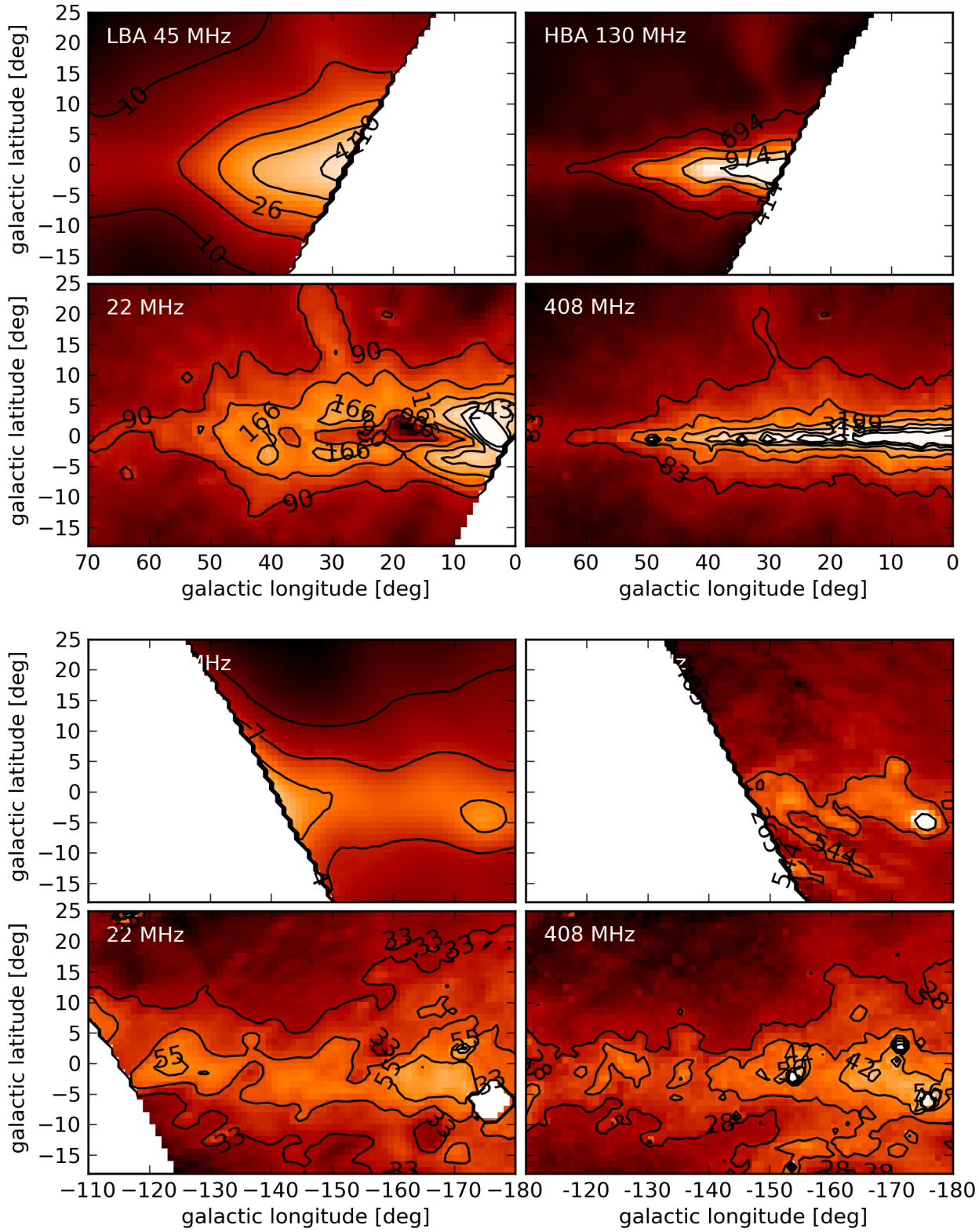

Figure 4.15: LOFAR maps at 45 and 130 MHz. For comparison the 22 MHz survey (Roger et al., 1998) and the 408 MHz survey (Haslam et al., 1982). Shown is the temperature brightness overlaid with the corresponding contours (at 22 and 45 MHz in kK, at 130 and 408 MHz in K.)

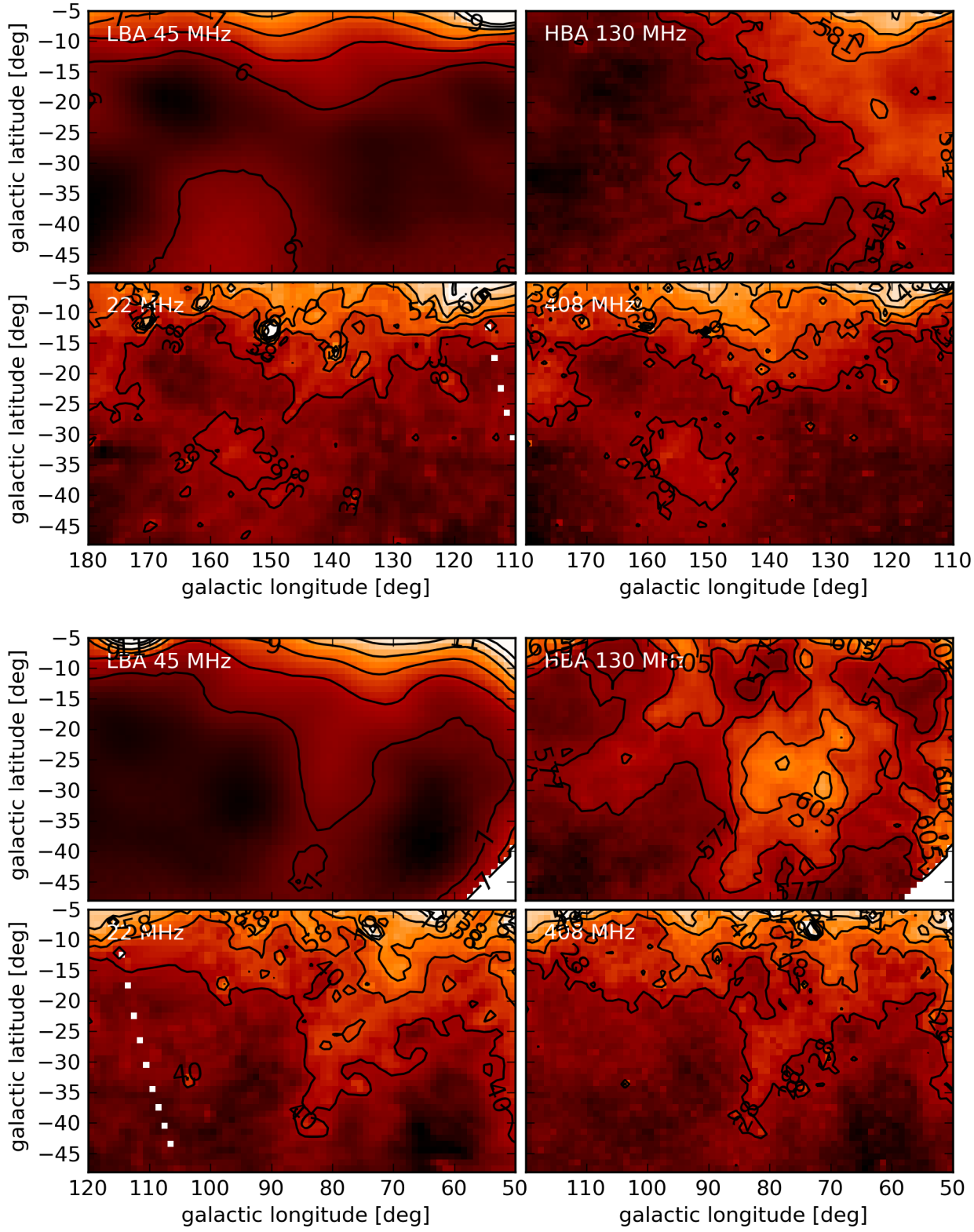

Figure 4.16: LOFAR maps at 45 and 130 MHz. For comparison the 22 MHz survey (Roger et al., 1998) and the 408 MHz survey (Haslam et al., 1982). Shown is the temperature brightness overlaid with the corresponding contours (at 22 and 45 MHz in kK, at 130 and 408 MHz in K.)

Chapter 5

Spectral Index Studies

The spectral index gives another possibility to study the properties of the observed emission. As introduced in Sect. 1.1 we expect a temperature spectral index of 2.7 for synchrotron emission and a value of 2.1 for thermal emission. Towards low frequencies a turn-over in the spectrum can be observed, especially in the case of strong HII regions. As some of the earlier surveys are electronically available, it is possible to study the spectral behavior of the sky including the LOFAR maps at frequencies below 100 MHz.

5.1 Calculating the temperature spectral index

By measuring the brightness temperatures at two frequencies ν_1 and ν_2, a temperature spectral index β can be obtained via:

$$\beta = -\frac{\log\left(\mathrm{T}_{\nu_1}/\mathrm{T}_{\nu_2}\right)}{\log\left(\nu_1/\nu_2\right)} \tag{5.1}$$

where T_{ν_1} and T_{ν_2} are the brightness temperatures at the given frequencies ν_1 and ν_2. Note that both surveys should have the same beam resolution to assure that the same amount of emission is measured. In the optimum case both surveys would have performed with the same uv-coverage. Unfortunately, this is not always possible since the use of different instruments. To solve this problem, a convolution of all surveys to the same beam resolution is performed. The measured brightness temperatures in the surveys are a sum of different components:

$$\mathrm{T} = \mathrm{T}_{\mathrm{Gal}} + \mathrm{T}_{\mathrm{Ex}} + \mathrm{T}_{\mathrm{CMB}} + \mathrm{T}_{\mathrm{Zero}} \tag{5.2}$$

with the following parameters
- $\mathrm{T}_{\mathrm{Gal}}$: Galactic brightness temperature
- T_{Ex}: non-thermal extragalactic backround
- $\mathrm{T}_{\mathrm{CMB}}$: cosmic microwave background (CMB) and
- $\mathrm{T}_{\mathrm{Zero}}$: zero-level correction.

Table 5.1: Left: Brightness temperatures of the CMB and extragalactic background at different frequencies. Right: Zero-level correction (ZLC) as obtained from the TT-plots, which have to be applied to the LOFAR survey at 30 and 45 MHz.

	T_{CMB}	T_{Ex}
30 MHz	2.7 K	3458 K
45 MHz	2.7 K	1116 K
125 MHz	2.7 K	65 K
408 MHz	2.7 K	2.38 K
820 MHz	2.7 K	0.76 K
1400 MHz	2.7 K	0.33 K

ZLC	30 MHz	45 MHz
408 MHz	275 K	90 K
820 MHz	-1900 K	-1100 K
1400 MHz	-500 K	-400 K

To get just the Galactic contribution the other values have to be subtracted from the measured temperatures. The CMB is 2.7 K at all frequencies (Mather et al., 1994). The correction of the extragalactic background is more complicated. It is an interpolation of all unresolved background sources, which means an averaged value for the entire sky is used. A detailed discussion on this is e.g. done by Guzmán et al. (2010), where they came up with a best fit solution from other observations:

$$\log T_{Ex} = 7.66 - 2.79 \log (\nu[\mathrm{MHz}]) \ . \tag{5.3}$$

This equation will be used for the following corrections of the extragalactic background. The results for a number of frequencies are given in Table 5.1. The zero-level is an offset in the brightness temperatures of the two surveys. It has the largest influence on the spectral index, as well as the largest uncertainty. For the calculation of the offset the method of TT-plots (temperature-temperature-plots) is used.

5.2 Zero-level corrections using TT-plots

For the spectral index maps a second order correction of the zero level of both surveys is performed by using TT-plots. By plotting the brightness temperatures of one survey against the brightness temperatures of the second survey (like done in Fig. 5.1) a slope can be obtained, which corresponds to a spectral index between the surveys. This slope is independent of the offset between the two surveys. Nevertheless, the offset becomes important by generating the spectral index maps. As the slope varies for different regions in the sky, caused by the different spectral behavior, it is essential for the determination of the offset that a region is chosen with no strong variation in the spectral index. The offset should be nearly constant for all regions in the sky (under the assumption that all former corrections of systematic effects were successful) and independent of the individual slopes.

In Fig. 5.1 the TT-plots from the LOFAR survey at 45 MHz toward the 408 MHz (Haslam et al., 1982), 820 MHz (Berkhuijsen, 1972) and 1400 MHz (Reich et al., 1981)

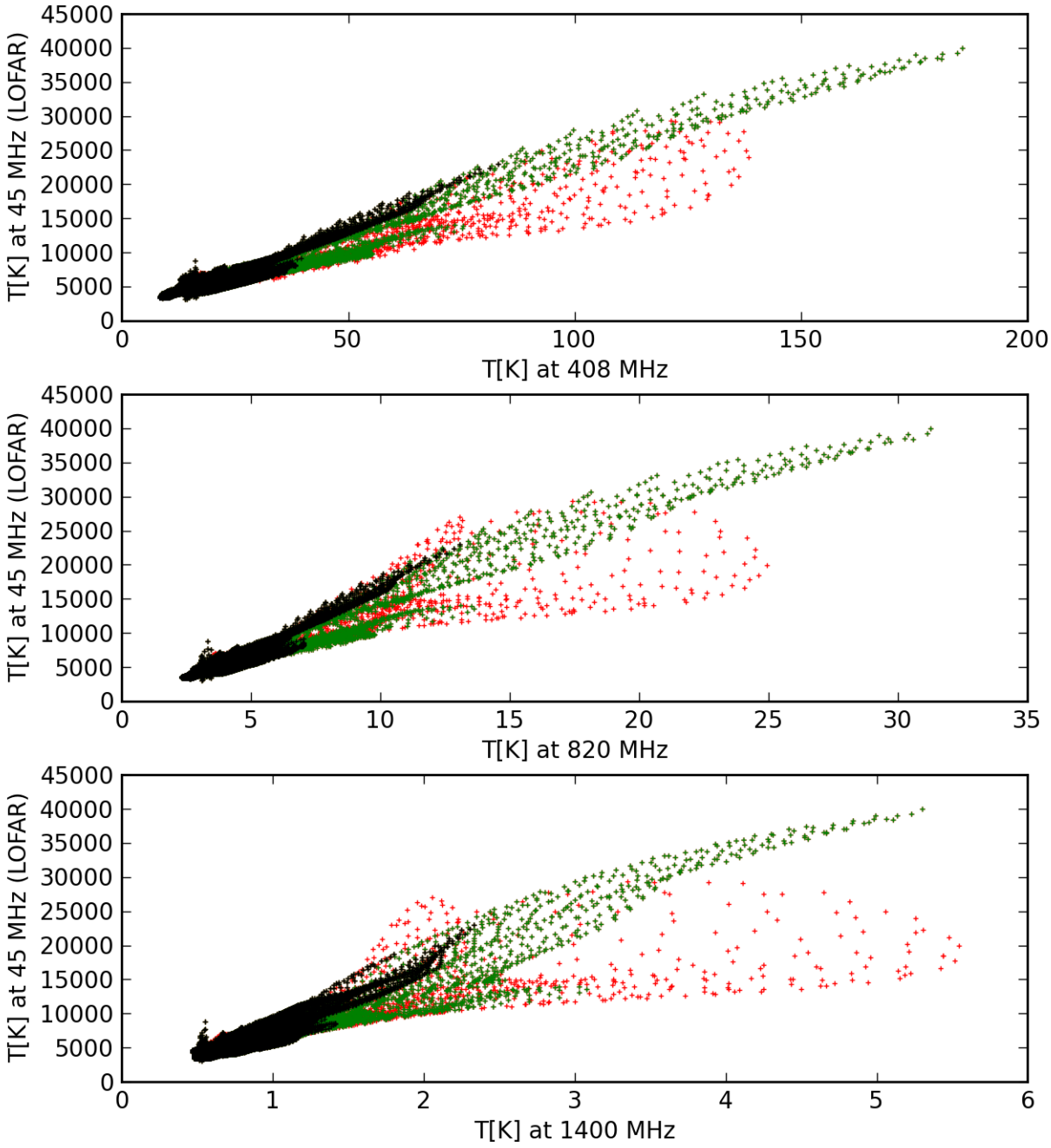

Figure 5.1: TT plots between the 45 MHz LOFAR survey and higher frequency surveys. Red points are belonging to the strong radio sources Cyg A, Cas A and Vir A and the green points represent data points from low latitudes values (b $< |10°|$).

survey are shown. The red points represent the strong point sources Cyg A, Cas A and Vir A. Variations from a straight line are caused by problems in the convolution of the surveys which is expected to be strongest for the point sources. The green points represent the brightness temperatures at low galactic latitudes b $< |10|$ (Galactic disk). Mainly two straight lines with different slopes are seen. One of them corresponds to the regions with low spectral indices due to thermal absorption, what will be discussed in more detail at a later stage in this chapter. The black points mark everything else and are used for the zero-level correction of the surveys. The obtained values from the TT-plots are summarized in Table 5.1. These points follow clearly a straight line. Only toward higher frequencies (mainly seen in the TT-plot between 45 MHz and 1400 MHz) curvatures in the data points become visible which can be explained by a flatting in the spectrum toward lower frequencies. These data points are part of the region close to the Galactic center, where strong absorption from HII regions is present.

5.3 Temperature spectral index maps

In Fig. 5.2 and Fig. 5.3 the spectral index maps from the LOFAR survey toward higher frequency surveys, after all corrections applied, are shown. The dashed lines represent the Galactic loops as introduced earlier (Table 4.3). In all cases the survey with the higher beam resolution is convolved to the resolution of the LOFAR map. For the frequency of 30 MHz this corresponds to a beam resolution of 9.7° and for 45 MHz it is 6.5°. The strongest point sources are not subtracted from the maps, what can result in weird structures around these regions. To obtain the spectral indices of the strong point sources, the integrated flux density has to be taken (like done for Cas A in Chapter 6) as they cannot be archived directly from the shown spectral index maps. The radio source Cas A is anyhow a special case, as it is loosing around 1% of its flux density every year (Vinyaikin, 2014). As the used surveys for the following studies are produced at different epochs, the values of Cas A in the spectral index maps not just depend on the frequency behavior, but also on the time variability of Cas A.

Spectral index maps between LOFAR and 408 MHz:
In the spectral index maps toward 408 MHz (top) low indices are measured in the inner disc caused by thermal absorption within HII regions, which is strongest at the Cygnus region around l = 80°. At this region the lowest temperature spectral index of 2.2 is found. Another HII region with strong absorption is detected at the area of l = 135° (W3, W4, W5). Low spectral indices are also detected along the Galactic loops, especially in Loop III at the galactic longitude of b = 150°. Even as this region is expected to have a flat spectrum, it is not clear how much it is affected by calibration errors, as it appears much flatter than seen in other surveys (compare with the spectrum of point 6 in Fig. 5.6). The region of l = 85° and b = 37° shows lower indices as well. The highest spectral indices are found next to the NPS as already measured by Guzmán et al. (2010), even though the high values of 2.7 as seen by Guzmán et al. cannot be confirmed. In the temperature spectral index map from 45 MHz

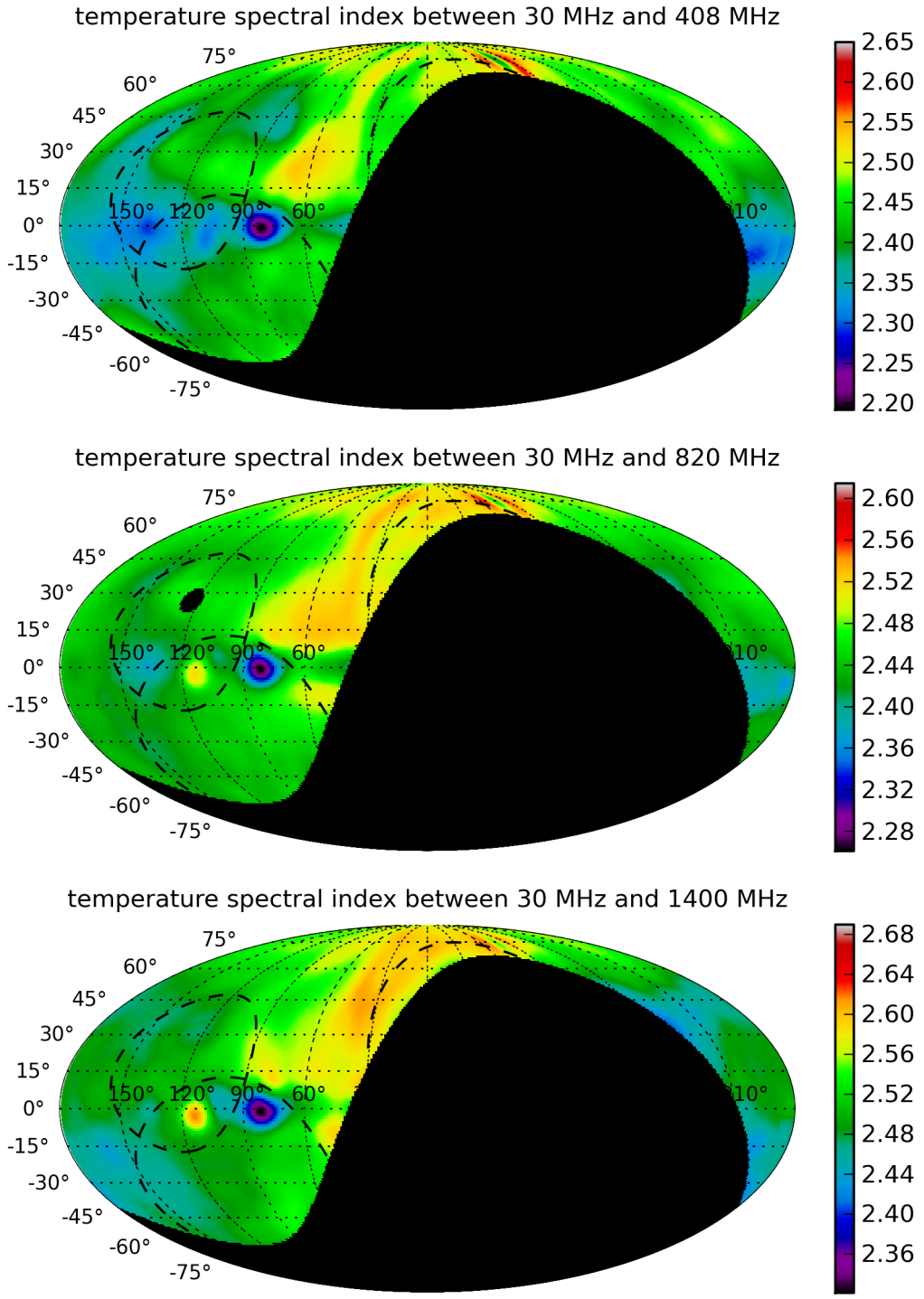

Figure 5.2: Temperature spectral index maps from 30 MHz (LOFAR) and higher frequency surveys.

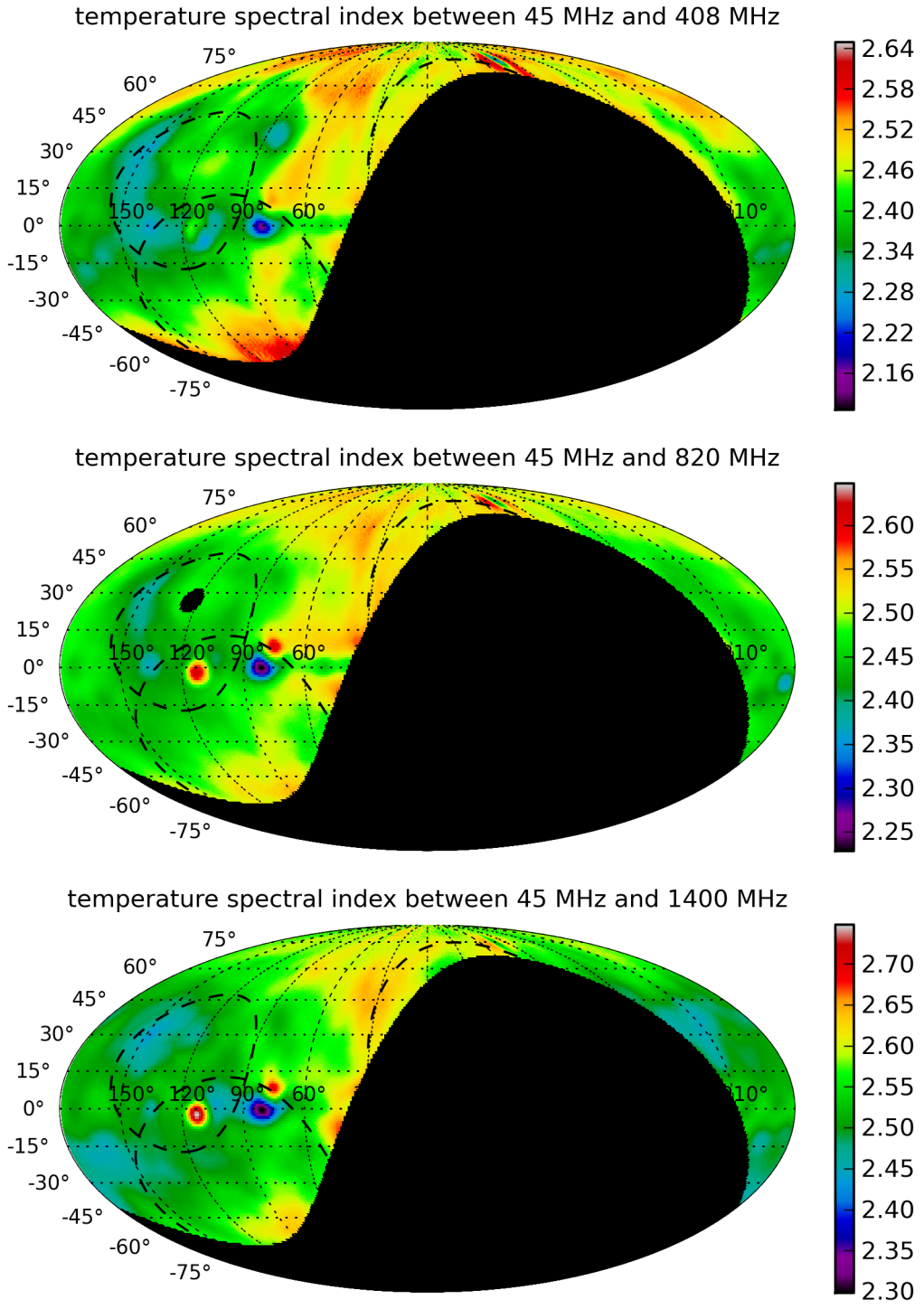

Figure 5.3: Temperature spectral index maps from 45 MHz (LOFAR) and higher frequency surveys.

to 408 MHz high spectral index values appear at low declinations, which are expected to be due to a higher noise level in this region. In the 30 MHz map the sky noise is strongly dominating over the system noise and therefore no declination depending effects are visible.

Spectral index maps between LOFAR and 820 MHz:
The images in the middle of Fig. 5.2 and Fig. 5.3 show the calculated temperature spectral index toward 820 MHz. Again the lowest spectral indices are found in the Cygnus region having a minimum of 2.25. Besides, low spectral indices are seen in the galactic plane around l = 140° (the W3/W4/W5 region). These two regions are known to have strong HII emission which causes thermal absorption at low frequencies. Furthermore low spectral indices of around 2.42 are found in Loop II and Loop III at a galactic latitude of l = 150°. The highest spectral indices are next to the NPS and reaching values up to 2.55. The high spectral index at l = 120° belongs to the radio source Cas A and is partly due to its decreasing flux density spectrum with time (Chapter 6). For the 45 MHz survey even Cyg A at l = 80° can be resolved and appears with a high spectral index. In the spectral index map produced with the 30 MHz survey Cyg A cannot be resolved from the large-scale emission.

Spectral index maps between LOFAR and 1400 MHz:
In the spectral index maps toward 1400 MHz (bottom images) no more low spectral indices appear along the Galactic disk. Only the Cygnus region still shows low spectral indices down to 2.3. Further regions with low spectral indices of around 2.45 are found in the temperature minimum zone, in the southern halo, and at some parts of Loop III. The spectral index of the minimum zone remains nearly constant in all spectral index maps. The same result can be obtained by looking at the spectrum plotted in Fig. 5.6. The highest spectral indices are measured for to the NPS with values around 2.6. In comparison to the low frequency spectral indices this time the NPS itself shows high spectral indices and not just the surrounding regions. Due to a larger difference between the frequencies the errors in the obtained spectral indices are lower and therefore no high spectral index values at low declinations are detected anymore.

In Fig. 5.4 the distributions of the spectral indices for the shown temperature spectral index maps are plotted. Two Gaussian distributions (dashed red lines) are plotted above with the given mean values and standard deviations. The distribution of the spectral indices are shifting toward lower indices for the lower part of the frequency spectrum. This can be explained by a flattening of the spectrum toward low frequencies. Toward 820 MHz and 1400 MHz the shape of the distribution is small compared to the one produced for the spectral indices toward 408 MHz. From LOFAR to the 408 MHz survey most of the indices are distributed from 2.3 to 2.6 with peaks around 2.4 and 2.48. Toward the 820 MHz survey spectral indices from around 2.4 to 2.6 can be detected with two peaks visible at around 2.46 and 2.51. Comparing the LOFAR data with the 1400 MHz survey shows a distribution from 2.4 to 2.7 with two mean values of around 2.5 and 2.57. In addition to this, for the spectral indices toward 408 MHz most values are below a temperature spectral index of 2.5 (marked with a dashed black line in all of the plots), whereas for the spectral indices toward

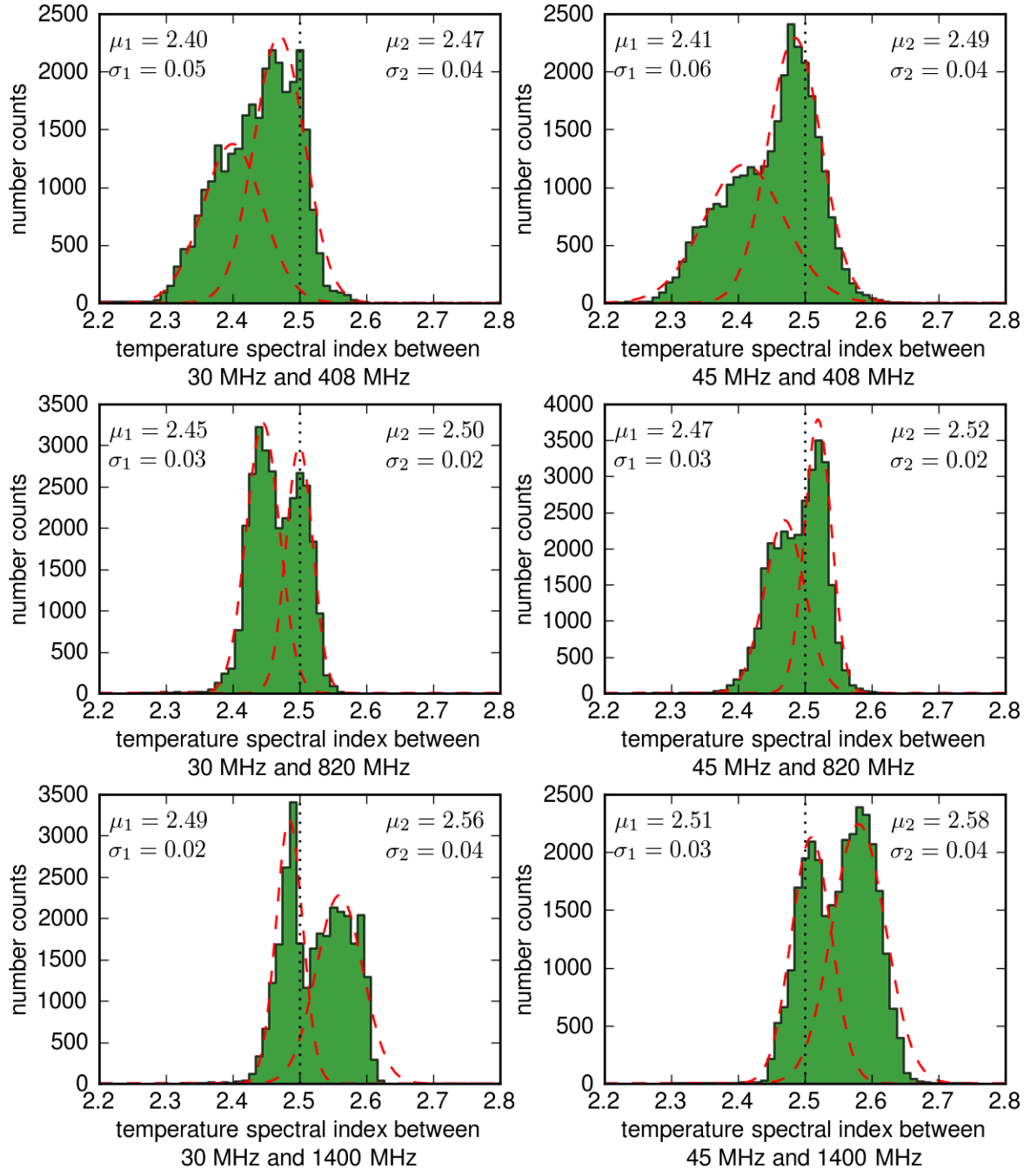

Figure 5.4: Temperature spectral index distribution from the LOFAR survey at 30 MHz (left side) and 45 MHz (right side) toward the 408 MHz (top), 820 MHz (middle) and 1400 MHz survey (bottom). The range of the spectral indices is in all plots the same to reveal the shift of the spectral indices depending on the frequency range. The red dotted lines belong to the Gaussian distributions. The black dotted line marks a temperature spectral index of 2.5.

Table 5.2: Summary of the chosen points. The first three (Minimum North, Anticenter and Calpoint) were used for the absolute calibration of the survey. β^1_{fit} is the fitted spectral index through the measured survey points, using frequencies up to 178 MHz. β^2_{fit} is the fitted spectral index including measurement points up to 1400 MHz. For comparison the spectra of all points are plotted in Fig. 5.6.

region	position lon lat	position RA DEC	β^1_{fit}	β^2_{fit}	β^{408}_{30}	β^{820}_{30}	β^{1400}_{30}	β^{408}_{45}	β^{820}_{45}	β^{1400}_{45}
Min. North	192°, 48°	9.6, 33°	2.41	2.40	2.48	2.46	2.46	2.53	2.51	2.50
Anticenter	180°, 0°	5.8, 29°	2.34	2.43	2.37	2.44	2.49	2.40	2.47	2.53
Calpoint	38°, -1°	18.8, -3°	2.11	2.45	2.34	2.40	2.53	2.43	2.48	2.61
P1 (HII)	85°, -5°	21.2, 41°	2.29	2.35	2.30	2.35	2.40	2.36	2.41	2.46
P2 (NPS)	30°, 45°	16.0, 17°	2.39	2.48	2.45	2.50	2.61	2.47	2.53	2.65
P3 (by NPS)	60°, 30°	17.6, 35°	2.51	2.58	2.53	2.51	2.56	2.51	2.51	2.56
P4 (halo)	90°, 60°	14.5, 50°	2.48	2.53	2.42	2.47	2.56	2.47	2.52	2.62
P5 (plane)	150°, 0°	4.1, 52°	2.24	2.36	2.32	2.40	2.48	2.32	2.42	2.51
P6 (Loop III)	150°, 30°	7.7, 66°	2.45	2.48	2.37	2.42	2.47	2.28	2.38	2.44
P7 (Loop II)	150°, -30°	2.6, 27°	2.39	2.45	2.38	2.41	2.46	2.39	2.44	2.49

1400 MHz most values are above 2.5. In the spectral index distribution from 45 MHz to 820 MHz the values are equally distributed around the value of 2.5. This clearly shows how the indices are shifted toward lower values for the low frequency spectrum and shifted toward higher values in the high frequency range of the spectrum.

The distribution of the spectral indices can be overlaid with two Gaussian functions. By comparing this with the shown spectral index maps, it can be seen that there are existing areas with mainly high spectral indices (around the NPS) and areas with low values (toward the anticenter.)

5.3.1 Multifrequency data of selected regions in the sky

To test the LOFAR survey for consistency with other surveys, different points were chosen to compare the LOFAR observations at different frequencies with existing surveys from the literature (Fig. 5.6). These points are chosen in a way that they have different temperature behaviors and appearing at various declinations. The positions in Galactic and Equatorial coordinates are summarized in Table 5.2 and plotted into a galactic map in Fig. 5.5. A first (straight line) and second order fit (dashed line) is used to model the given data points in Fig. 5.6. In case of the black points the data were not available electronically and therefore no convolution to the LOFAR beam resolution was performed. The values are directly taken from the given tables or contour plots in the according papers. In case of the LOFAR data (red and blue points) and the available electronically surveys (green points) a convolution to the resolution of 7.5° was performed. The summary of all obtained spectral indices is summarized in Table 5.2. Here β^1_{fit} is the slope of a fitted line trough all data points down to a frequency of 178 MHz. β^2_{fit} is the slope through all data points down to a frequency of 1400 MHz. All of the other temperature spectral indices are calculated by using the LOFAR survey and the given high frequency surveys.

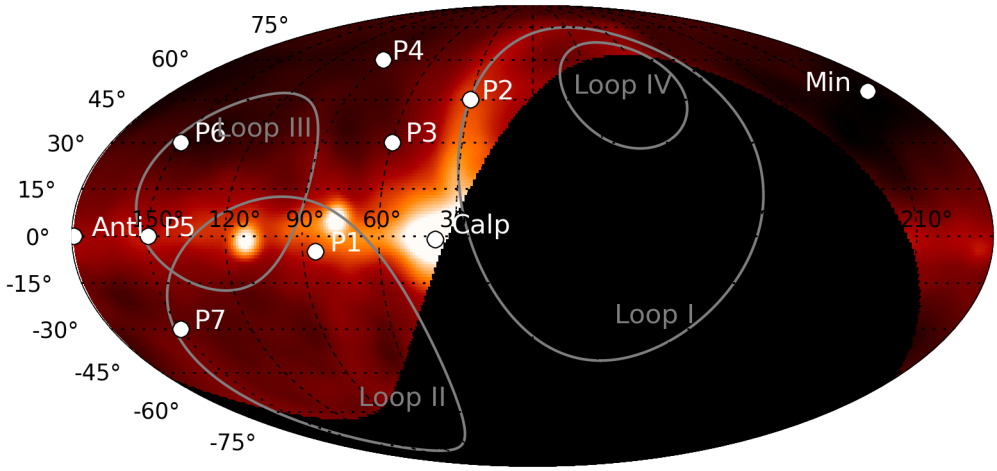

Figure 5.5: LOFAR 45 MHz map including the points for the calibration and single spectra.

Point 1:
This point is part of the HII region in the Cygnus complex. Due to thermal absorption a flat spectrum with a slope of around 2.3 is visible. Existing surveys follow the fitted model without deviations. Similarly, the LOFAR measurements in the LBA (red points) and HBA (blue points) are in a good agreement with the model fit as well. As a result the fitted spectral index β^{1}_{fit} give the same result as the value β^{408}_{30} using the LOFAR survey. There is a slight steepening of the spectrum toward higher frequencies resulting in a spectral index of $\beta^{1400}_{45} = 2.46$.

Point 2:
This point is part of the North Polar Spur. Measurements from various surveys are in good agreement with the fitted line, as well as the LOFAR observations. Toward high frequencies the spectrum appears steeper ($\beta^{1400}_{45} = 2.65$) than at low frequencies ($\beta^{480}_{30} = 2.45$). The spectral index calculated by the use of the LOFAR maps are steeper compared to the ones of the fitted lines.

Point 3:
In this case a point next to the NPS is chosen. All temperature surveys follow the fitted line, whereby small deviations can be found. The measurements from the LOFAR LBA survey are lower than expected from the fitted line. The value from the HBA survey is above the expected value. Nevertheless, the spectral indices from the LOFAR survey are in good agreement with the one from the fitted line through all surveys. Besides, it shows nearly no steepening toward high frequencies ($\beta^{480}_{30} = 2.53$ and $\beta^{1400}_{45} = 2.56$).

Point 4:
This point represent a region in the halo of the Milky Way. Due to the lower brightness

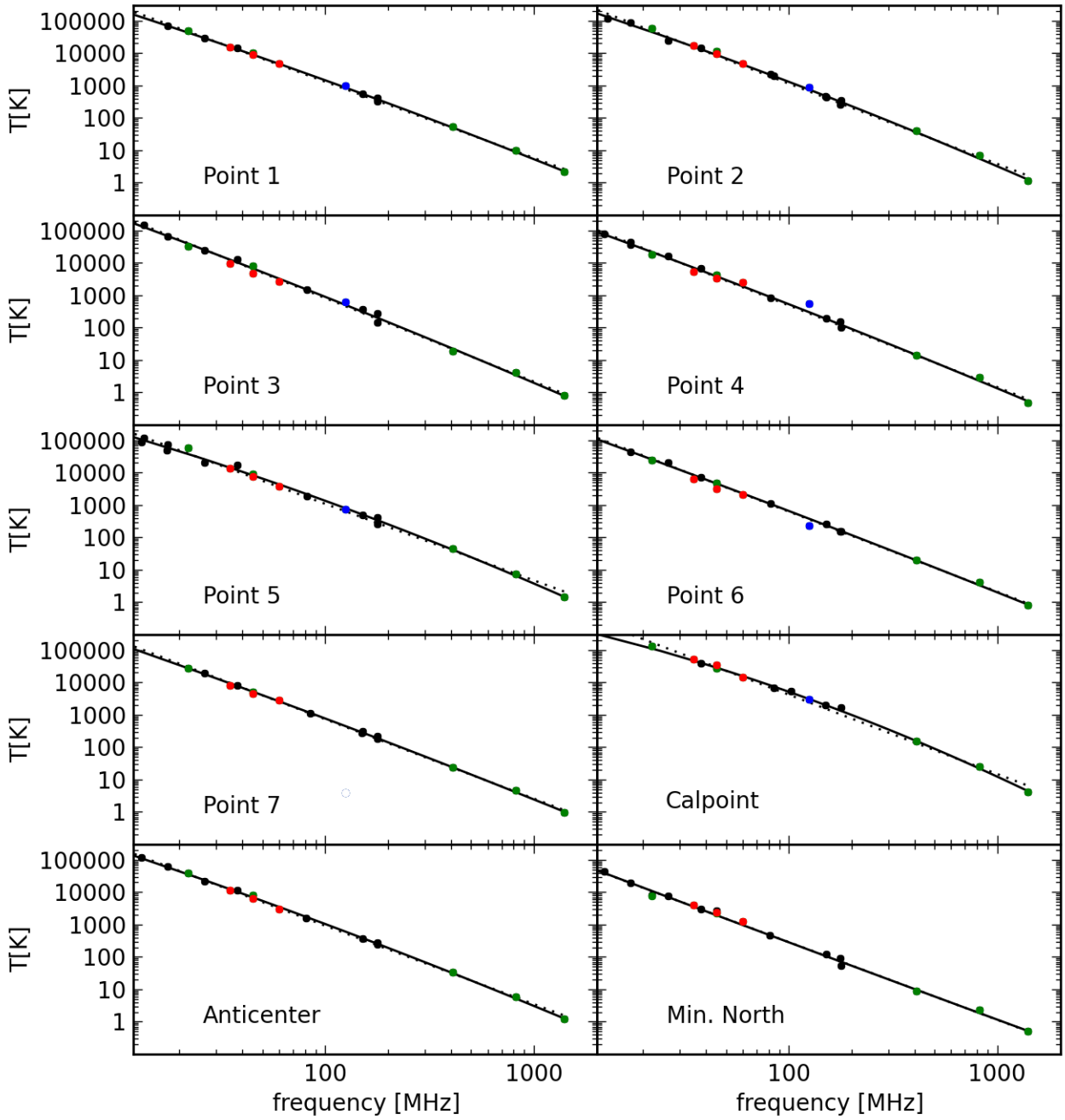

Figure 5.6: Brightness temperature spectra of various points as introduced in Table 5.2. Black points are values from the literature, green points are from surveys, where the data are electronically available (Table 1.1) wherefore a convolution of the data can be performed. The red points indicates the LOFAR measurements at 35 MHz, 45 MHz and 60 MHz, the blue point corresponds to the LOFAR HBA measurement at 125 MHz. The dashed line is a first order fit to the data and the straight line us a second order fit. In both cases the LOFAR data are not used for the fitting of the curve. In all cases the simplified assumption of a 10 percent error is made.

temperatures it is more affected by noise and therefore the brightness temperature at 60 MHz is above the multi frequency fit. In contrast to that, the measurements at 35 MHz and 45 MHz lie below the fitted line. Due to that, the spectral index obtained from the survey at 35 MHz is lower than the slope of the fitted line. Using the 45 MHz survey, the calculated values of $\beta_{45}^{480} = 2.47$ and $\beta_{45}^{1400} = 2.62$ indicate a flattening toward low frequencies.

Point 5:
This point in the Galactic plane shows a strong curvature toward low frequencies, as it lies within a strong HII region. Strong deviations between the surveys are due to possible errors while reading out the temperatures from the literatures and due to the low resolution of most surveys, as in the Galactic planes the temperatures are strongly changing even on small angular scales. Nevertheless the LOFAR points are in a good agreement with the fitted line. The curvature results in a changing of the spectral index from $\beta_{30}^{480} = 2.32$ to $\beta_{45}^{1400} = 2.51$.

Point 6:
The measurements of this point from Loop III follow a straight line without any visible curvature. Besides, no deviations between the various observations is seen. Only the LOFAR measurements at 35 MHz and 45 MHz appear with lower brightness temperatures than expected for the other observations. It is not clear what causes this strong deviation, but maybe is caused by errors in the beam pattern correction.

Point 7:
Here a point at negative latitudes as part of Loop II is chosen. No deviations are detectable and even the LOFAR data follow the expected values from the fitted line. No HBA point is plotted, as the integration time and corresponding sensitivity is too low at this direction in the sky. The spectral indices from the LOFAR surveys are in good agreement with the slope of the fitted line and range between $\beta_{30}^{480} = 2.38$ to $\beta_{45}^{1400} = 2.49$.

5.4 Modeling the spectral behavior

5.4.1 Overview of the models

Various models are existing to explain the characteristics in the frequency spectrum and even more to calculate a high frequency break due to aging of the electrons and a low frequency turn-over due to thermal absorption. For the following equations the spectral index is defined by:

$$S(\nu) \propto \nu^{-\alpha} \,. \tag{5.4}$$

In case of an injection, like from a Supernova (SN) explosion, an injection spectral index can be defined by

$$\alpha_{inj} = \frac{M^2 + 3}{2M^2 - 2} \,. \tag{5.5}$$

using the Mach number M. α_{inj} will always be above 0.5. In case of a smaller value no injection was introduced to the system. The Mach number itself depends on the sound speed $M = v/c_s$ and thereby on the gas density and temperature $M \propto \sqrt{\rho T}$.

After the injection, the cosmic ray electrons are loosing they energy with time due to various effects, which will be shortly summarized in the following. Synchrotron losses (electrons loosing they energy by radiating synchrotron emission) and Inverse Compton (IC) losses (electrons interacting with photons) are important for particles with energies $\gtrsim 2$ GeV and can lead to a cut-off at high frequencies. Depending on the age of the particles, the cut-off will shift more and more toward lower frequencies. Furthermore, this particle age is directly related to the magnetic field strength via

$$t_{syn} = 5.83 \cdot 10^8 \cdot B[\mu\mathrm{G}]^{-3/2} \cdot \nu[\mathrm{GHz}]^{-1/2}\, yr\,. \tag{5.6}$$

The cut-off at high frequencies due to the aging of the particles will in the following donated as ν_{break}.

For a continuous injection several SN would be needed, which provide always new particles. In this case the particles only lose energy due to the radiation of synchrotron emission:

$$\mathrm{SYN} = I_0 \left(\frac{\nu}{\nu_0}\right)^{\alpha_{inj}} \cdot \frac{1}{\sqrt{1+\nu/\nu_{break}}}\,. \tag{5.7}$$

At frequencies larger than the break frequency the spectrum follows a power-law with $\alpha = \alpha_{inj} + 0.5$.

In case of a single shot injection two other models are available. Jaffe and Perola (JP; 1973) assume in they model that the electrons are moving along the magnetic field with a non constant pitch angle. This leads to an exponential cutoff at high frequencies:

$$\mathrm{JP} = I_0 \left(\frac{\nu}{\nu_0}\right)^{\alpha_{inj}} \cdot \mathrm{e}^{-\nu/\nu_{break}} \tag{5.8}$$

.

As opposed to this Kardashev (1962) and Pacholczyk (1970) (KP) assume a constant pitch angle of the electrons, like for example observed in Relics. The particles are not loosing their energy as fast as in the case of the JP model:

$$\mathrm{KP} \approx I_0 \left(\frac{\nu}{\nu_0}\right)^{\alpha_{inj}} \cdot \frac{1}{(1+\nu/\nu_{break})^{1-1/3\alpha_{inj}}}\,. \tag{5.9}$$

For frequencies much higher than the break frequency the spectrum will follow a power law with $\alpha = 4\alpha_{inj}/3 + 1$.

For low energy cosmic rays $\lesssim 1$ GeV ionization (electrons are hitting neutral particles, which will be ionized afterwards) and free-free absorption (Sect. 1.1.2) will play an important role in dense gas clouds. The ionization causes a flattening of the spectrum toward lower frequencies:

$$\mathrm{ION} = I_0 \left(\frac{\nu}{\nu_0}\right)^{\alpha_{inj}} \cdot \frac{1}{\sqrt{1+\nu_{break2}/\nu}}\,. \tag{5.10}$$

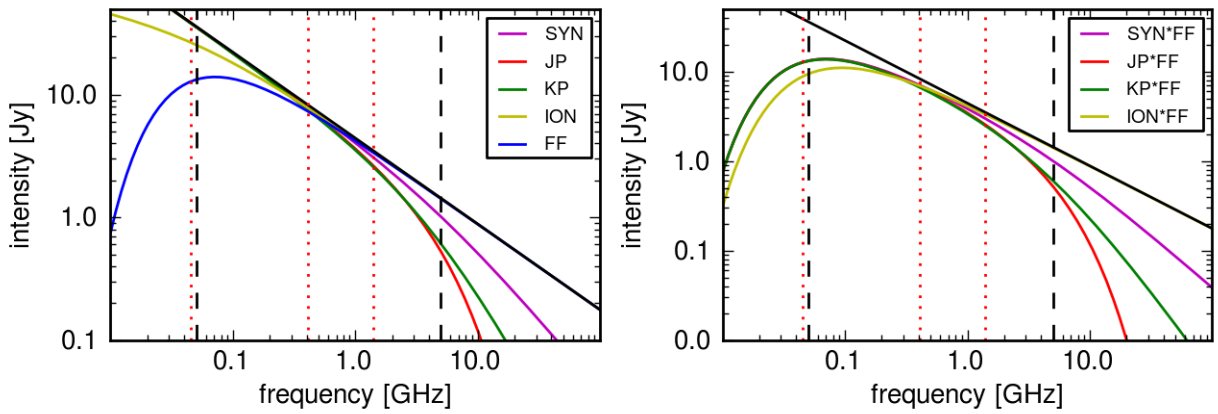

Figure 5.7: Comparison of the spectra for the various energy loss models. In the right plot the free-free absorption is multiplied with the other models.

Hereby the break frequency appears at low frequencies, wherefore it is named ν_{break2} to distinguish it from the high frequency break introduced above. The spectrum will become a power-law with $\alpha = \alpha_{inj} - 0.5$ for low frequencies.

In case of free-free absorption, as occurring in HII regions, even a turn-over ν_{crit} at low frequencies can be detected:

$$\mathrm{FF} = I_0 \left(\frac{\nu}{\nu_0}\right)^{\alpha_{inj}} \cdot \mathrm{e}^{-\nu_{crit}/\nu} \,. \tag{5.11}$$

This turn-over frequency is related to the emission measure as introduced in Eq. (1.19). Hereby high EM leads to a high turn-over frequency. Of cause it is also possible that the free-free absorption is combined with the other models. In this case the term for the free-free absorption is multiplied with the equations above.

Particles can lose energy due to Bremsstrahlung as well. In this case the electrons lose kinetic energy in form of photons while being reflected by protons. Nevertheless, this lose process has no influence on the spectral index and leads to a continuous spectrum.

In Fig. 5.7 all models are plotted together. The straight black line represents the injection spectral index $\alpha_{inj} = 0.7$. The vertical dashed black lines indicate the turn-over frequency at $\nu_{crit} = 50$ MHz and the break frequency at $\nu_{break} = 5$ GHz. The red dashed lines represent the frequencies of 45, 408 and 1400 MHz, as these surveys are chosen for the following analysis. The left hand image shows the spectral behavior of the various models following the equations as introduced above. Besides of the free-free absorption and the ionization all models follow at low frequencies the power-law as given by the injection spectral index of 0.7. In contrast to that, these both models follow the injection power law at the high frequencies, where all of the other models show a break in the spectrum. As in reality in most cases turn-over and break frequencies are observed within the same source, the right

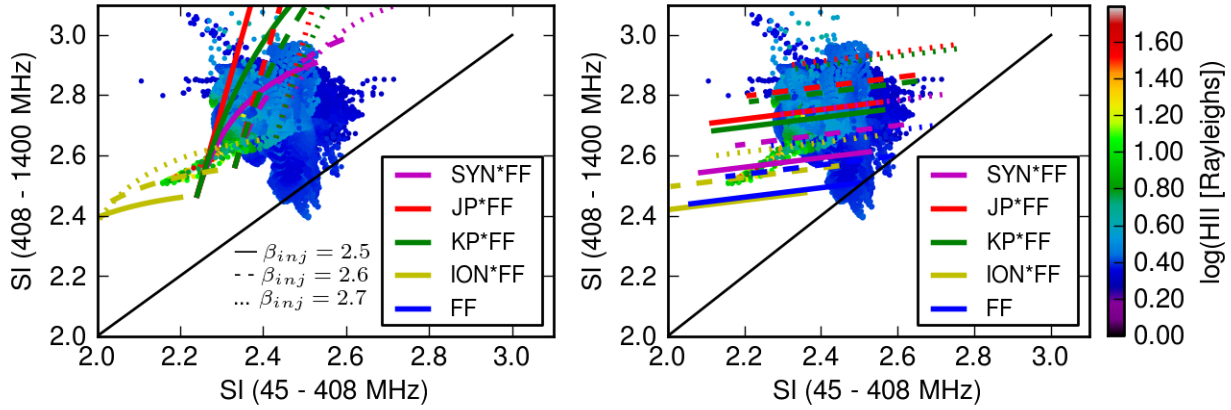

Figure 5.8: High frequency temperature indices plotted against low frequency temperature indices for all the entire skymap overlaid with the models. Left: The low frequency turn-over value is kept constant. Right: The high frequency break value is kept constant.

hand plot shows the free-free absorption term multiplied with the other models, to introduce a turn-over at low frequencies.

5.4.2 Estimating the turn-over and break frequencies by using spectral index maps

In the following the models introduced above will be used for the analysis of the Milky Way data. Therefore the high spectral indices between 408 MHz (Haslam et al., 1982) and 1400 MHz (Reich et al., 1987) are plotted against the low spectral indices between 45 MHz (LOFAR) and 408 MHz as presented in the subsections above (method from Basu et al, 2015). For the analysis all surveys were convolved to the same resolution of 6.5°. Besides, as brightness temperatures instead of flux densities are used for the Galactic data, in the following the brightness temperature spectral index as defined in Eq. (5.1) will be used. It is connected to the spectral index via:

$$\beta = \alpha + 2\,. \tag{5.12}$$

As consequence of that, the temperature injection spectral index $\beta_{inj} = \alpha_{inj} + 2$ is taken for the further discussions.

The plot of low frequencies spectral indices β_{low} against high frequencies spectral indices β_{high} for the Galactic data is shown in Fig. 5.8. The black line represents the case of $\beta_{high} = \beta_{low}$, while the colored lines stands for the models as labeled. The straight lines are for a temperature injection spectral index of 2.51, the dashed line for $\beta_{inj} = 2.6$ and the dotted lines are calculated using $\beta_{inj} = 2.7$. The color coding of the points indicates the HII emission (WHAM; Haffner et al., 2003) for the same direction in the sky and was as well convolved to the resolution of 6.5°.

For the models in the left hand plot the low frequency turn-over ν_{crit} is kept constant to a value of 30 MHz, while the high frequency break is varying. Points which are appearing in the bottom of the plot have lower break frequencies, than points appearing in the top of the plot. In this plot the free-free absorption appears just as a single point, as it is independent of a high frequency break. In the right hand plot the low frequency turn-off is varying, while the high-frequency break ν_{break} is kept constant to a value of 3 GHz. In this case the larger turn-over frequencies belong to the points at the left, whereas points at the right of the plot have lower turn-over frequencies. Changing both values (ν_{crit} and ν_{break}) at the same time would causes more curvatures in the plotted model.

By finding a good combination of the values for the low frequency cut-off, the high frequency break and the injection spectral index, different parts of the sky can be modeled by the presented models. Unfortunately this leads to a high number of combinations for modeling the observed spectra. Nevertheless, an analysis for some parts of the sky will be performed to give a rough estimate of the physics going on. For the calculations below, the equations for the models as introduced above are used, to solve them in a way that both frequencies are just depending on the injection spectral index. In this way the break frequencies for all models can be calculated by a given β_{inj}. For simplification a constant injection spectral index is assumed within the selected regions, even as this is not true in every case. Therefore it always will be discussed how much the changing of injection spectral index has an impact on the final results. The maximum and minimum values for the plotted regions are summarized in Table 5.3 for all the models and different injection indices. In any case a different injection spectral index only will have an influence on the absolute values of the break frequencies and not on the relative values. This allows a discussion of lower and higher break frequencies for different regions in the sky.

To compare the spectral behavior obtained from this method with a large number of observations, the models are plotted on top of the multi frequency measurements for various directions in the sky. In Fig. 5.16 the JP (red line) and KP model (green line) for $\beta_{inj} = 2.51$ with the obtained values for ν_{crit} and ν_{break} are plotted on top of the sky positions summarized in Table 5.2. For most of the directions, the model and measurements are in good agreement with each other. Mainly point 6 shows a strong disagreement. This point is part of Loop III and it was already discussed earlier that this part appears weaker in the LOFAR survey than predicted by other observation. Therefore the calculated spectral index toward 45 MHz is small, what leads to a higher obtained turn-over frequency. Some of the other points will be discussed in the following, as they are part of the selected regions.

5.9

5.4.2.1 The North Polar Spur (NPS)

For the North Polar Spur the temperature spectral indices for galactic latitudes from 20 to 70° and galactic longitudes from 15° to 45° are plotted in the upper left hand image of Fig. 5.9. The points follow nearly a straight line with the low frequency spectral indices ranging from 2.45 to 2.5. The spectral index between 408 and 1400 MHz changes over a larger

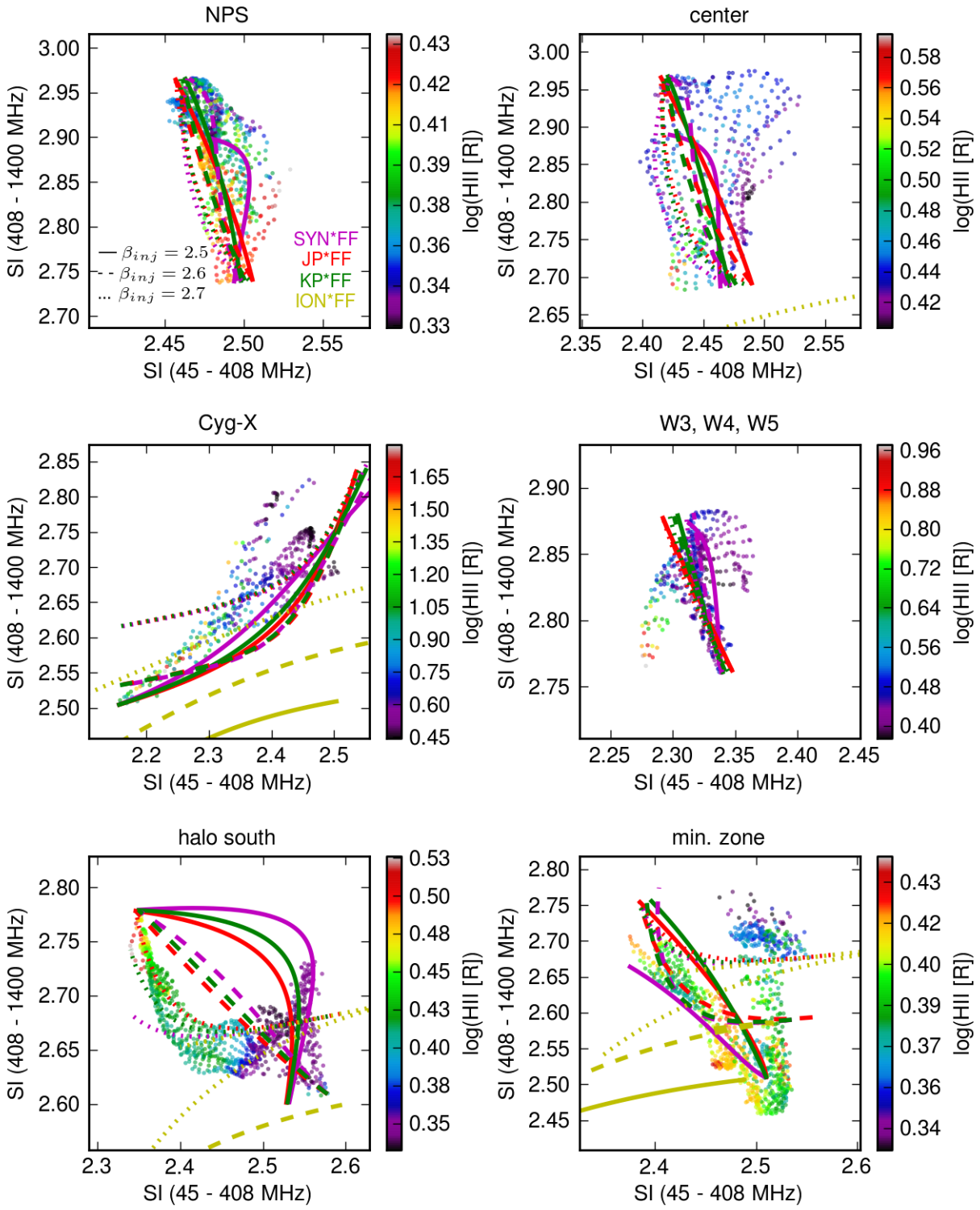

Figure 5.9: High frequency temperature indices plotted against low frequency temperature indices for various regions in the sky. Solid line: $\beta_{inj} = 2.51$. Dashed line: $\beta_{inj} = 2.6$. Dotted line: $\beta_{inj} = 2.7$.

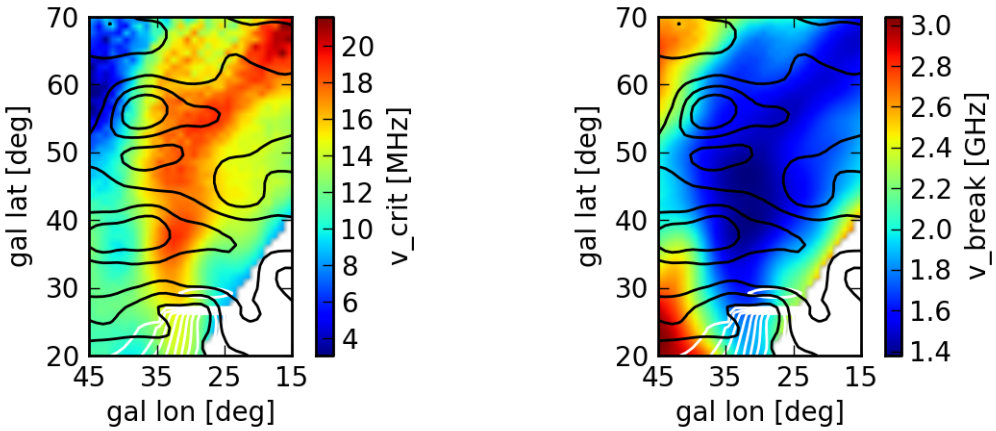

Figure 5.10: Analysis of the North Polar Spur. Left: Low frequency turn-over using the averaged values from the JP and KP model for $\beta_{inj} = 2.51$. Right: High frequency break for the same parameters. Black contours represent the HII intensities and the white contours the CO intensities.

range from around 2.7 to 3. The color coding represent the HII emission in the position of the measured spectral index, which appears strongest for lower spectral indices. As seen all three models give reasonable results, even as the JP and KP model with $\beta_{inj} = 2.51$ (straight lines) seem to fit the curvature of the data best. Nevertheless, using $\beta_{inj} = 2.6$ (dashed lines) or $\beta_{inj} = 2.7$ (dotted lines) for both models leads to similar results.

The images of Fig. 5.10 show the turn-over (left hand panel) and break frequencies (right hand panel) for all positions, overlaid with HII (black contours) and CO (Dame et al., 2000)(white contours). Note that measurements for the CO emission are only available for galactic latitudes below 30°. The frequencies are averaged values from the JP and KP model with an injection spectral index of 2.51. The frequencies obtained for other injection indices are found in Table 5.3. The shown structures will stay the same, just the absolute numbers will change. For the given parameters the low frequency turn-over is in the order of 18 MHz within the NPS above a galactic latitude of 30°. Below this latitude a slightly lower value of around 14 MHz is found. The higher values of ν_{crit} within the NPS compared to the surrounding medium can be explained by a higher EM within the NPS. For the high frequency break an averaged value of 1.5 GHz is found for the NPS and has its minimum around a galactic latitude of 45°. These relatively low frequencies indicates an aging of the electrons. As the NPS is expected to be an old but reheated SNR, this is a possible assumption. Furthermore, the low break frequencies within the NPS indicate the present of a strong magnetic field. Earlier studies by Heiles (1998) deduced a magnetic field strength up to 6 μG for Loop I.

The JP and KP model for $\beta_{inj} = 2.51$ and the obtained frequencies is plotted above the multi-frequency data of point 2 in Fig. 5.16. Its location at l = 30° and b = 45° is within

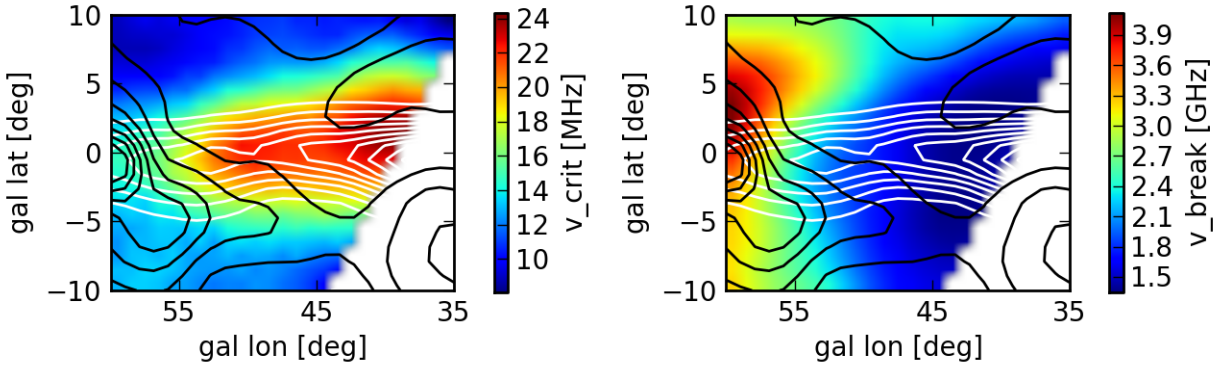

Figure 5.11: Analysis of the Galactic center. Middle: Low frequency turn-over using the averaged values from the JP and KP model for $\beta_{inj} = 2.51$. Right: High frequency break for the same parameters. Black contours represent the HII intensities and the white contours the CO intensities.

the NPS. Both models are in good agreement with the measurements even it seems that the JP model fits the data slightly better than the KP model.

5.4.2.2 Along the Galactic plane

The central region

For the central region of our Galaxy (upper right of Fig. 5.9) a spectral behavior similar to the NPS can be found. The low frequency temperature spectral indices ranging just over a small range from 2.4 to 2.5. In comparison the temperature spectral indices from the higher frequency surveys giving values from 2.72 to 2.97. Both, the JP and KP model, fit the given values, even for different injection spectral indices.

For the images in Fig. 5.11 again the averaged frequencies from the JP and KP model are used, taken an injection spectral index of 2.51 into account. For the low frequency turn-over the highest values up to 24 MHz are found within the Galactic disk. As expected, this value is higher than the one found in the NPS, due to a stronger HII emission in the disc. Furthermore, a strong correlation between CO and turn-over frequency is found. Both emissions lead to a high EM value and therefore to high turn-over frequencies.

For the high frequency break the minimum of around 1.5 GHz is found at low galactic longitudes. In comparison to the low frequency turn-over, which behavior follows the CO emission, no relation with CO or HII can be found. It just seems to depend on the galactic longitude with getting lower toward the Galactic center region what can be explained by an increasing magnetic field strength in this direction. For this region of our Galaxy a magnetic field strength of 5 - 10 μG is measured (Beuermann et al., 1985).

The JP and KP model with the obtained frequencies for $\beta_{inj} = 2.51$ are plotted together with multi-frequency data for the so-called Calpoint in Fig. 5.16. As its location is within

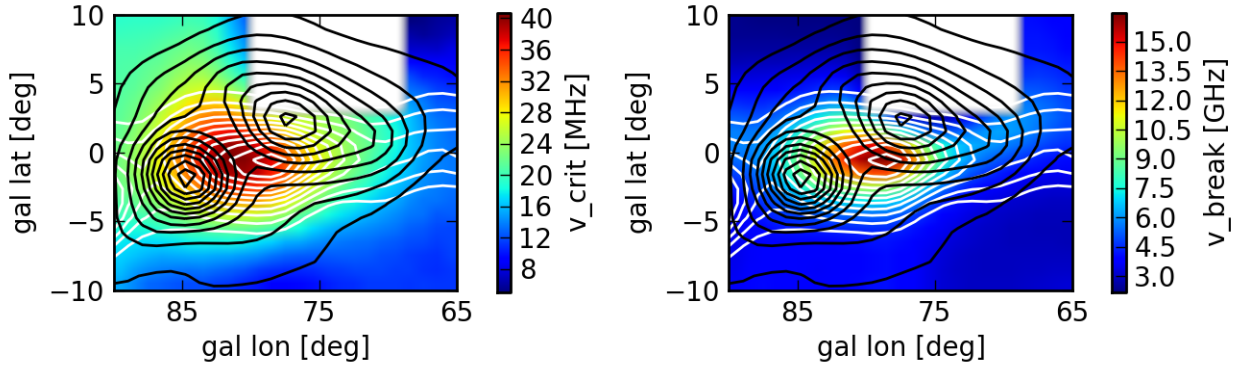

Figure 5.12: Analysis of the Cygnus complex. Left: Low frequency turn-over using the averaged values from the JP and KP model for $\beta_{inj} = 2.51$. Right: High frequency break for the same parameters. Black contours represent the HII intensities and the white contours the CO intensities.

the galactic disk near to the central region a strong curvature in the spectrum can be seen. Both models are in good agreement with the data points.

The Cygnus complex

The spectral indices for the Cygnus-X complex next to Cyg A (whereby the source Cyg A itself is blanked) is shown in the middle left hand plot of Fig. 5.9. This region is known to be one of the largest and richest star forming regions in our Galaxy and contains a massive molecular complex. The observed emission is coming from ionized interstellar gas clouds. All of that indicates a high intensity of HI, HII and CO.

The temperature spectral indices are this time strongly varying at the low and high frequencies and are getting down even to values of 2.15 in the low frequency part. For all studied and plotted regions the Cygnus complex shows the strongest HII emission (color coded). The spectral behavior can be modeled by the JP, KP and SYN model for low injection spectral indices. The ionization model fits some parts of the data for a injection spectral index of 2.7.

Using a injection spectral index of 2.51 for the average of the JP and KP model leads to the frequencies as shown in Fig. 5.12. The maximum turn-over frequencies (left hand panel) of around 40 MHz are detected at a galactic longitude of 82°. The shape of the turn-over frequencies mainly follows the CO emission, but the maximum at 82° is in a region, where the HII emission is becoming stronger. Something similar is seen for the high frequency breaks, whereas the maximum of 16 GHz is at a galactic latitude of 78°, where the CO has its maximum. These high values for the break frequencies are not due to physical effects in this region, but can be explained by a missing correction for the thermal contribution. For all of the presented survey no correction for the thermal component is done, as the main component of the observed radiation is expected to be nonthermal synchrotron radiation. Furthermore, toward lower frequencies the thermal component becomes more

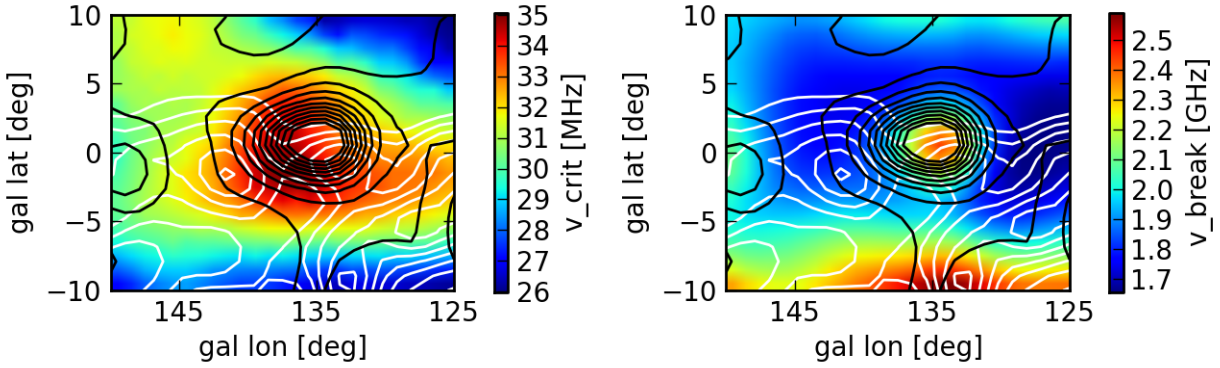

Figure 5.13: Analysis of the W3, W4, W5 region. Left: Middle: Low frequency turn-over using the averaged values from the JP and KP model for $\beta_{inj} = 2.51$. Right: High frequency break for the same parameters. Black contours represent the HII intensities and the white contours the CO intensities.

and more negligible. Nevertheless, in case of strong star forming region, like the Cygnus complex, the thermal component is strong and therefore a subtraction from the measured brightness temperature would be needed. After this subtraction the spectrum would appear much steeper at 1400 MHz than seen in the current data. This steepening would lead to smaller break frequencies in our analysis. Unfortunately, this correction is non-trivial and goes beyond the scope of this thesis.

Due to the present of a strong ionized medium, it is interesting to have a look at the ionization model as well. At least for an injection spectral index of 2.7 it is possible to get results for the regions with the strongest CO emission. The relative behavior is the same as seen by the KP and JP model as imaged in Fig. 5.12. The low frequency turn-over would in this case vary between 27 and 60 MHz.

Plotting the JP and KP model above the measurements of point 1 (which is located within the Cygnus region) in Fig. 5.16 shows again that the models with the obtained turn-over and break frequencies are able to model the spectral behavior. Both models are in good agreement with the data points and lead to similar results.

W3, W4, W5

Another region with strong ionized HII emission can be found in the region of W3/W4/W5. Even more this region is located in a molecular cloud. Gray et al. (1998) denoted an EM as low as 1 $\mathrm{cm}^{-6}\mathrm{pc}$.

The spectral behavior for this region is shown in the middle right panel of Fig. 5.9. In the low frequency domain the temperature spectral index is slightly varying between 2.28 and 2.35, whereas at the high frequency domain temperature spectral indices from 2.76 to 2.88 can be measured. The data can nicely be modeled by the JP, KP and synchrotron model and even for different injection spectral indices.

Using again the average of the JP and KP model with a constant injection spectral index

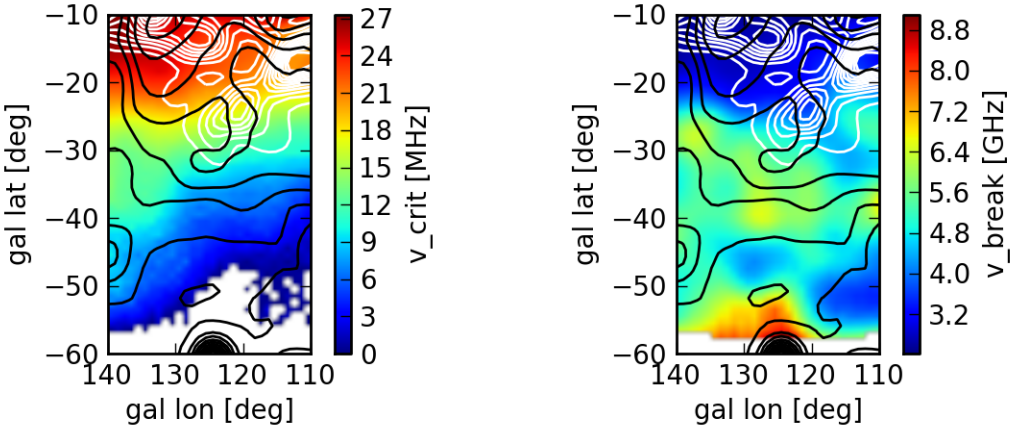

Figure 5.14: Analysis of the southern halo. Left: Middle: Low frequency turn-over using the averaged values from the JP and KP model for $\beta_{inj} = 2.51$. Right: High frequency break for the same parameters. Black contours represent the HII intensities and the white contours the CO intensities.

of 2.51, maps for the break frequencies were calculated (Fig. 5.13). The turn-over at low frequencies reaches its maximum with around 34 MHz at the region with the strongest HII emission. But even in the surrounding area where a strong CO emission is present most of the turn-over frequencies are found to be above 30 MHz. Again this can be explained by by thermal absorption caused by the HII emission. The maximum of the high frequency break (2.4 GHz) is found at a galactic latitude of 135°, exactly at the HII maximum. The break frequencies around are found to be lower, down to 1.7 GHz. As discussed above for the Cygnus complex, the missing correction for the thermal component will lead to errors in the obtained break frequencies. Due to the high HII emission the thermal component cannot be neglected in this region.

In Fig. 5.16 Point 5 represents a point at a galactic longitude of 150°, which is at the edge of the plotted area in Fig. 5.13. The JP and KP model show a good agreement with the data points down to a frequency of 26 MHz. For lower frequencies the models are diverging from the measured data by showing a stronger curvature.

5.4.2.3 Halo regions

After studying various regions with strong HII and CO (and partly even HI) emission, an analysis of the halo will follow. Here all of the named intensities are small, as well as the brightness temperatures. The spectral behavior for negative galactic latitudes along the galactic longitude of 120° is plotted in bottom left hand panel of Fig. 5.9. The temperature spectral indices for this region are strongly varying and the slope of the data points cannot be fitted by a single model, as the Galactic and halo emission have different behaviors. Nevertheless, a strong variation of the spectral index depending on the HII emission is

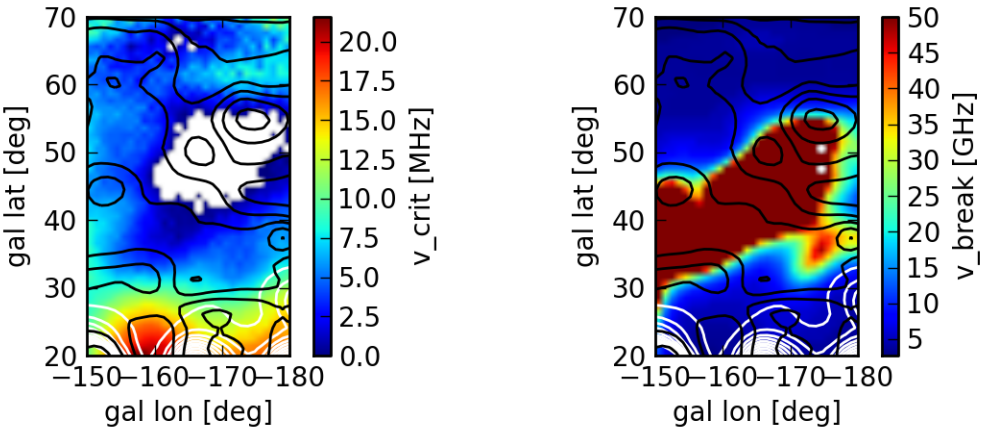

Figure 5.15: Analysis of the minimum zone. Left: Low frequency turn-over using the averaged values from the JP and KP model for $\beta_{inj} = 2.51$. Right: High frequency break for the same parameters. Black contours represent the HII intensities and the white contours the CO intensities.

found.

For the calculation of the turn-over and break frequencies as shown in Fig. 5.14 again an injection spectral index of 2.51 was used. At high galactic latitudes Galactic emission is detected, whereas at galactic latitudes below -30° mainly the halo emission is visible. At a galactic latitude of -60° an other strong HII emission can be detected. Due to this, the turn-over frequencies reach their maximum of 27 MHz in the Galactic disk. In the halo this value gets close to 0 MHz with decreasing galactic latitude. Some regions even reach negative values, which are blanked in the map. By using a higher injection spectral index it is possible to obtain positive values in this parts as well. But again they are close to 0 MHz (compare Table 5.3). This low or not existing turn-over frequency easily can be explained by a low EM in the halo.

For the high frequency breaks, low values of around 2.5 GHz are detected in the Galactic disc, whereas there are increasing toward lower latitudes. For a injection spectral index of 2.51 break frequencies in the order of 6 GHz are found for most parts of the halo. By using higher injection indices even much higher frequency breaks would be measured. The higher break frequencies in the halo, compared to the disk regions, are due to a weak magnetic field strength of around 1μG. Therefore less particle aging is observed.

The spectral indices in the halo around the minimum region are plotted in the bottom right panel of Fig. 5.9. For this region the data points are separated following two different lines. Part of that can be explained by the following discussion on the minimum zone itself.

In the images of the calculated frequencies as shown in Fig. 5.15 again some part of the Galactic disc is seen (up to a galactic latitude of 30°). This leads to higher turn-over frequencies (left hand panel) up to 20 MHz within the Galactic disk. Above the Galactic disk

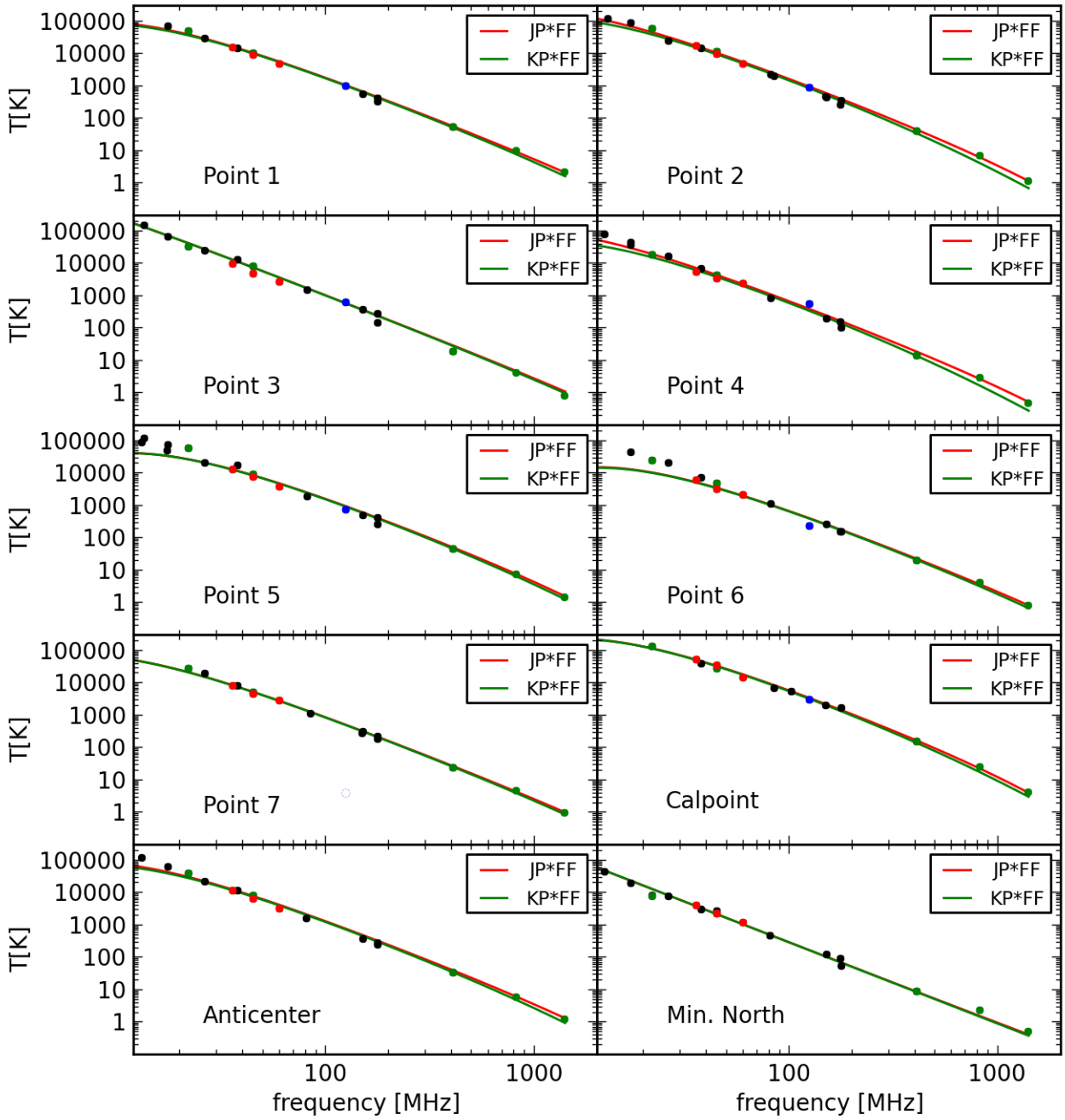

Figure 5.16: Brightness temperature spectra of various points as introduced in Table 5.2. Black points are values from the literature, green points are from surveys, where the data are electronically available (Table 1.1) wherefore a convolution of the data can be performed. The red points indicates the LOFAR measurements at 35 MHz, 45 MHz and 60 MHz, the blue point corresponds to the LOFAR HBA measurement at 125 MHz. The red line represents the JP model, whereas the green line represents the KP model. In all cases a temperature injection index of 2.51 is assumed. A 10% error is taken into account.

Table 5.3: Summary of turn-over and break frequencies for the different models.

β_{inj}	model		NPS		center		Cyg-X		W3,W4,W5		halo south		min. zone	
			min	max	min	max	min	max	min	max	min	max	min	max
2.51	JP*FF	ν_{crit} [MHz]	6	16	7	22	5	41	25	33	0	25	0	20
		ν_{break} [GHz]	1.7	3.4	1.7	4.2	2.4	15.6	1.9	2.8	2.7	8.8	3.0	-
	KP*FF	ν_{crit} [MHz]	8	22	9	27	5	41	27	36	0	27	0	20
		ν_{break} [GHz]	1.1	3.0	1.0	4.0	2.0	17.3	1.4	2.4	2.2	9.4	2.6	-
	SYN*FF	ν_{crit} [MHz]	11	35	12	41	7	40	32	53	0	32	0	21
		ν_{break} [GHz]	0.1	0.8	0.1	1.2	0.3	6.9	0.1	0.5	0.4	3.5	1.3	-
2.6	JP*FF	ν_{crit} [MHz]	14	25	15	30	13	49	33	42	3	33	5	28
		ν_{break} [GHz]	2.0	5.0	2.0	7.1	3.2	410	2.4	3.9	3.6	62	4.1	-
	KP*FF	ν_{crit} [MHz]	15	28	16	33	13	49	34	42	3	34	7	29
		ν_{break} [GHz]	1.5	5.1	1.5	7.7	3.0	616	2.0	3.7	3.4	73	3.7	-
	SYN*FF	ν_{crit} [MHz]	17	44	18	50	13	49	36	49	3	36	7	30
		ν_{break} [GHz]	0.1	1.6	0.1	2.7	0.7	616	0.3	1.0	0.9	30	1.0	-
2.7	JP*FF	ν_{crit} [MHz]	23	34	24	39	22	58	42	51	12	43	14	38
		ν_{break} [GHz]	2.6	10.9	2.51	31.5	4.8	656	3.2	6.6	5.8	-	7.5	-
	KP*FF	ν_{crit} [MHz]	24	36	25	41	22	60	43	52	14	43	16	38
		ν_{break} [GHz]	2.3	12.6	2.2	38.0	5.0	983	3.1	7.3	8.8	-	8.9	-
	SYN*FF	ν_{crit} [MHz]	24	41	26	47	22	60	44	53	14	41	16	38
		ν_{break} [GHz]	0.4	4.6	0.4	15	1.4	983	0.7	2.4	8.8	-	3.0	-

all plotted turn-over frequencies are below 8 MHz (for a injection spectral index of 2.51). In the region of the minimum zone, at a longitude of 192° and a latitude of 48°, the calculation gives negative values. For a higher injection spectral index, values slightly above 0 MHz are found. This low values are again due to a weak HII and CO emission resulting in a low EM. Nevertheless, at this part of the sky the entire calculation and analysis has to be done a bit more carefully. As the sky temperature reaches its minimum, the brightness temperature and temperature spectral indices are more affected by errors. Therefore it is possible that errors in the measurements causes problems in the solving of the equations (especially as the high frequency break also cannot be calculated for all directions).

The high frequency break (right hand panel) reaches values far beyond 50 GHz in the minimum temperature zone. In this region the Galactic contribution reaches is minimum as well as its magnetic field strength. Note that even the spectrum for the minimum zone plotted in Fig. 5.16 follows a straight power law with no visible curvature. This indicate that no turn-over and break frequencies are existing in this region.

5.4.3 Correlation between the spectral properties and the CO and HII emission

As seen in the previous subsecsections a relation between the spectral behavior and the CO and HII emission exists, which will be discussed in more detail. The low frequency turn-overs and the high frequency breaks are calculated by using the mean value from the JP and KP model with an injection index of 2.51. These parameters are chosen for all points in the Galactic map. The CO and HII data used for the following analysis were convolved to the same resolution as the spectral index data (6.5°). For the HII emission data are available for the entire sky, whereas CO data are just available at galactic latitudes from -30° to 30°.

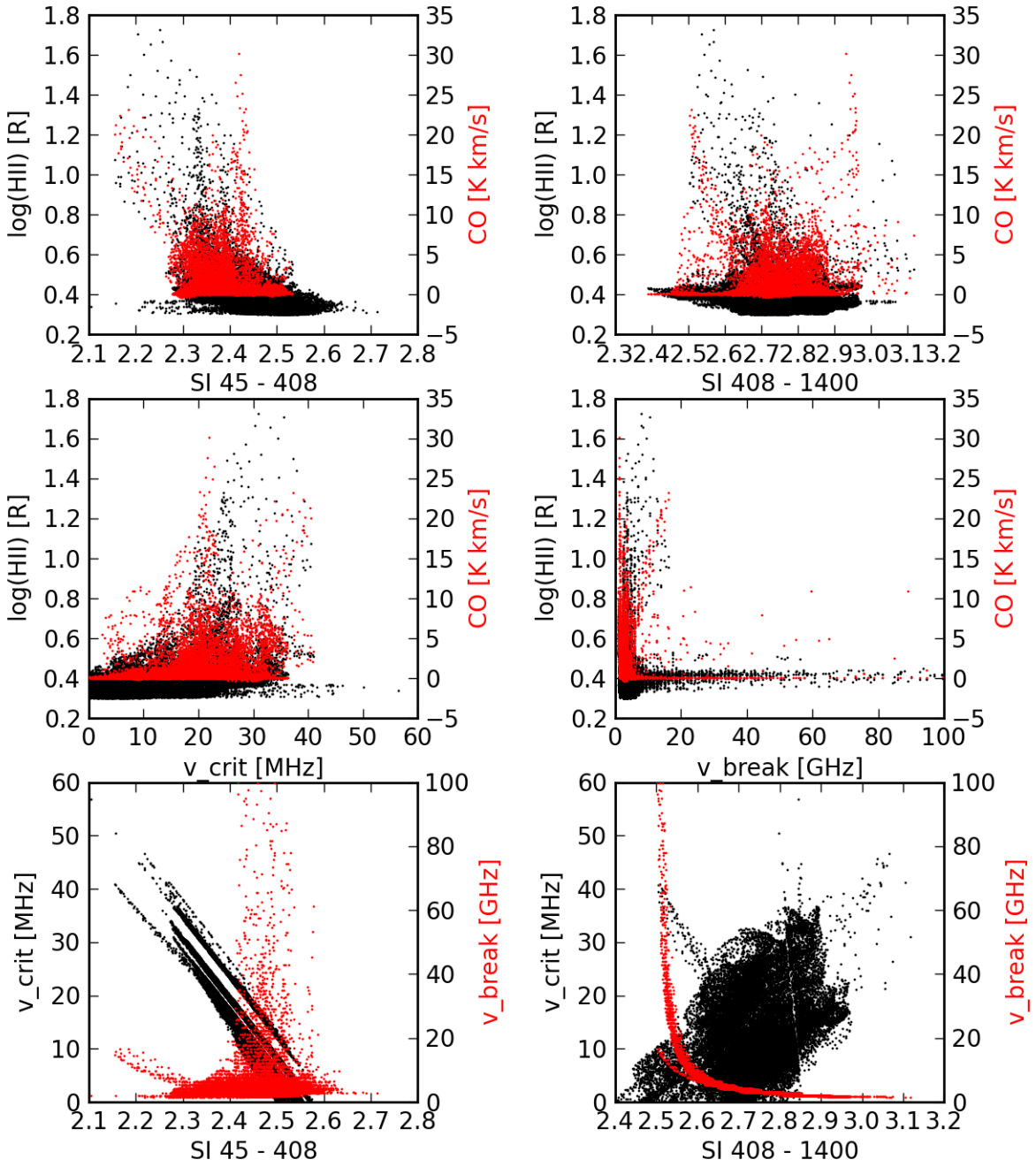

Figure 5.17: Correlation between SI, ν_{crit}, ν_{break}, CO (Dame et al., 2000) and HII (Haffner et al., 2003).

In the two upper plots of Fig. 5.17 the HII (black points) and CO (red points) emission is plotted over the temperature spectral index. In the left hand image the temperature spectral index between the LOFAR map at 45 MHz and the 408 MHz survey (Haslam et al., 1982) is used. For the right hand plot the 408 MHz and the 1400 MHz survey (Reich et al., 1981) are used instead. As already discussed for the temperature spectral index maps, low spectral indices appear in regions with strong HII emission. Related to that, high spectral indices are found in regions with low HII emission. A similar behavior is seen for the CO emission.

The plots in the middle of Fig. 5.17 show how CO and HII emission is correlated with to the low frequency turn-overs (left hand panel) and the high frequency breaks (right handed panel). The lowest turn-over frequencies are within regions with low HII and CO emission. For higher turn-over frequencies a stronger HII and CO emission is measured. The ionized gas of the HII is causing a free-free absorption at low frequencies (Sect. 5.4.1) what leads to a turn-over at higher frequencies. The more HII gas is present, the higher is the frequency at which the spectrum turns over. Most of the high frequency breaks is plotted in the middle right hand panel of Fig. 5.17 appear below 10 GHz. All values with higher break frequencies (here just values up to 100 GHz are plotted) appear at regions with low HII (around 0.4 R) and CO (around 0 K km/s) emission. Besides of the low particle density in this regions, the magnetic field strength is weak as well as both parameters are related to each other. Due to the weak magnetic fields less particle aging is present. No break frequencies above 20 GHz are detected for HII values above 0.6 R and for CO values above 10 K km/s.

In the bottom left hand panel of Fig. 5.17 the turn-over (black points) and break frequencies (red points) are plotted over the temperature spectral index between 45 and 408 MHz. The low frequency turn-overs show a linear correlation with the spectral indices, with low indices for high turn-over frequencies. This comes directly from the model introduced in Sect. 5.4.1 where $\beta_{low} \propto \nu_{crit}$. In comparison, by plotting the high frequency breaks over the spectral indices from 408 to 1400 MHz (bottom right hand panel of Fig. 5.17) a direct correlation is detected, whereas this time the low frequency turn-overs show a randomly behavior. Again by looking at the equations in Sect. 5.4.1 there is a relation of $\beta_{high} \propto 1/\nu_{break}$.

5.5 Error discussion

Errors in the temperature spectral index maps are caused by the brightness temperature noise, wrong scaling of the brightness temperatures as part of the absolute amplitude calibration, and errors of the zero-level.

In Fig. 5.18 the mean error of the spectral index maps is calculated by taking an error of 1000 K for the brightness temperature at 45 MHz and an error of 2000 K at 30 MHz. For the 408 MHz survey an error of 2 K is assumed, for the 820 MHz 0.5 K and for the 1400 MHz survey 0.1 K. Hereby a constant error over the entire brightness temperature map is taken into account, even as this not represent the true error behavior (see discussion Sect. 4.8). Note that for the LOFAR survey especially the increasing noise toward low declinations causes larger errors in this regions.

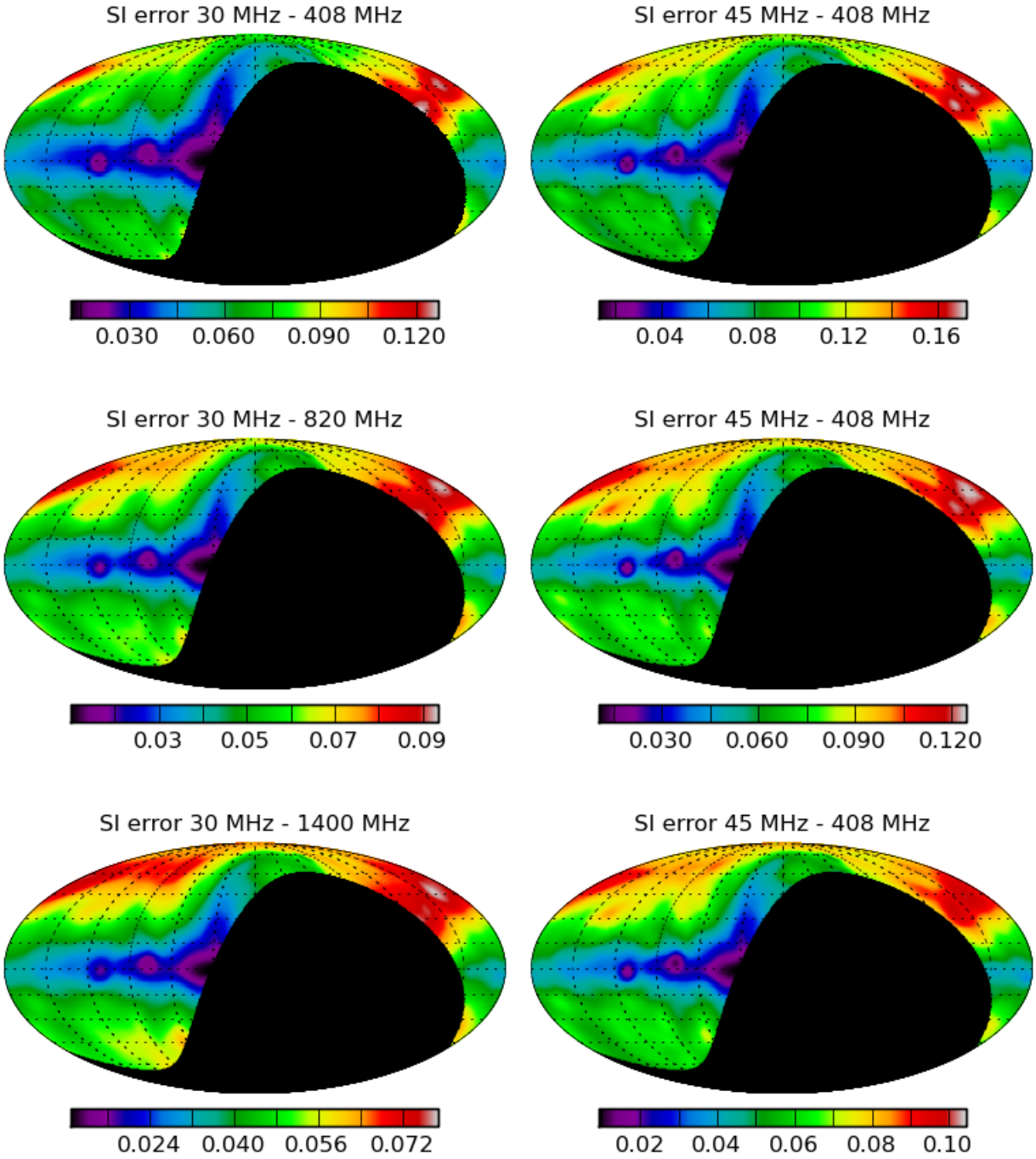

Figure 5.18: Errors in the spectral index maps.

Following the assumption of a constant temperature error over the entire map the largest errors in the spectral index maps appear in regions with low brightness temperatures, like in the halo and minimum zone. This leads to large uncertainties for the spectral indices measured in these regions. The lowest errors appear at high brightness temperatures, like along the galactic plane. Furthermore the errors are expected to be smaller for a larger frequency difference between the two surveys. This means the errors are highest in the spectral index maps using the 408 MHz survey and lowest by using the 1400 MHz survey. For the spectral index maps using the 408 MHz survey the calculated errors range between 0.012 in the galactic center region and 0.17 in the minimum zone. The resulting errors for for the spectral index using the 820 MHz survey range between 0.01 in the galactic center region and 0.1 in the minimum zone. Using the 1400 MHz survey the spectral index errors are between 0.01 and 0.08.

Uncertainties in the spectral index maps are also due to the low angular resolution of the LOFAR maps. As large-scale structures are observed only an averaged spectral index is measured for structures smaller than the beam resolution. This effect is strongest in the Galactic plane, where HII absorption regions with small angular diameters of 1-2° cannot be resolved. Therefore the measured spectral indices appear higher in this regions than seen by other observations using a higher beam resolution.

Errors in the spectral indices lead directly to errors in the calculated turn-over and break frequencies. Estimating an error of 0.1 for β_{low} leads to an uncertainty of 10 MHz for the low frequency turn-over and 0.5 GHz for the high frequency break. Using an error estimation of 0.1 for β_{high} leads to an uncertainty of 3 MHz for the low frequency turn-over and of several 10 GHz for the high frequency break.

5.6 Summary

With the existing surveys at 408 (Haslam et al., 1982), 820 (Berkhuijsen, 1972) and 1400 MHz (Reich et al., 1981), spectral index maps together with the LOFAR survey at 30 and 45 MHz were created. By the direct comparison a flattening of the spectrum toward lower frequencies is found. This flattening appears strongest in regions with a known strong HII emission, which allows to explain the flattening by the free-free absorption. A mean temperature spectral index of around 2.45 is found toward the 408 MHz survey, whereas the mean value toward the 1400 MHz survey is around 2.54. The highest spectral indices are found in the region near to the NPS (from 2.5 to 2.65). This was already seen by Guzmán et al. (2010), though the high value of 2.7 cannot be confirmed with the LOFAR data. The lowest values (down to 2.25) are found in the Cyg-X complex, which is known to be a strong HII region.

The obtained spectral index maps between 45 and 408 MHz and the spectral index map between 408 and 1400 MHz (Reich & Reich, 1987) are used to estimate turn-overs of the spectrum at low frequencies and breaks at the high frequency part due to particle aging. With a model of the free-free absorption and models from Jaffe and Perola (1973) and Kardashev (1962) and Pacholczyk (1970) for the particle aging, turn-over and break

frequencies for various regions in the sky were calculated. Even it is not possible to give absolute values, as some parameters stays uncertain, a relative behavior can be studied. The highest turn-over frequency of 40 MHz is found in the Cyg-X complex, whereas the minimum temperature zones in the halo do not show any turn-over at low frequencies. For clarification the obtained spectral indices, turn-over and break frequencies are plotted against the HII and CO emission of the Milky Way. A direct correlation is found for the low frequency spectral indices, which appear at regions with high HII and CO emission. Correlated to that, the highest values for the low frequency turn-over are found in this regions as well. Most of the obtained high frequency breaks are below 20 GHz. Higher values are just found in regions, where the CO and HII emission is low, meaning the particles aging is less within a thin environment with weak magnetic fields.

Chapter 6

Actual flux density of Cas A

The young supernova remnant Cas A is beside Cyg A the strongest visible radio source at low frequencies. Measurements during the last decades have been performed at various wavelength to predict the fractional flux density decrease per year at different frequencies. Following these studies the flux density of Cas A and Cyg A should be roughly the same at the current time.

In this chapter the combined LOFAR maps are used to obtain the flux densities of Cas A and Cyg A to study the actual flux density ratio of both sources, as well as the actual spectral index of Cas A and to compare it to known predictions.

6.1 Flux density ratio of Cas A and Cyg A

From the LOFAR all-sky survey as presented in Chapter 4 the fraction of the flux density of both sources can be calculated for a wide frequency range. In the analysis one has to be aware of the fact that low resolution observations are used, which means that both sources cannot be resolved and are disturbed by large-scale emission. Therefore one of the biggest problems in the measurements of the flux density of Cas A and Cyg A is the subtraction of the Milky Way contribution, which is of the order of 10000 to 15000 K at frequencies below 50 MHz. The environments of both sources are used to estimate the fraction of Galactic emission to the flux density, for which a correction is done afterwards.

The left image of Fig. 6.1 shows the ratio between Cas A and Cyg A for the LOFAR observations after the correction for the Milky Way emission. Each data point represents the measurement from the skymaps after an integration over 200 frequency channels. This corresponds to a bandwidth of 1 MHz below 50 MHZ and 2 MHz bandwidth above 50 MHz. A convolution to a resolution of 9.3° was performed on the skymaps for all frequencies. The flux density ratio of both sources is largest at low frequencies and decreases toward the higher frequencies. This is expected as Cas A has a steeper spectrum at this frequencies than Cyg A. The peak at around 55 MHz is most likely due to errors in the antenna beam model as it appears at the resonance frequency of the LOFAR low band antenna. This effect is already recognized by the LOFAR community and causes problems in all spectral index

analysis concerning the in-band spectrum. A solution for this problem is not available at the current state.

A detailed discussion of the flux density of Cas A and Cyg A has been done by Vinyaikin (2014), given an estimate for the flux density ratio at 38 MHz. Using the given formula

$$\frac{S_\nu^{CasA}(t)}{S_\nu^{CygA}(t)} = A(t - t_0)^{-\beta} \tag{6.1}$$

with log(A) = 5.991 and $\beta = 2.364$ for the year t = 2013 one gets a ratio of 1.066. The epoch of the supernova outburst, which was 1680, is taken as t_0. The ratio plotted in Fig. 6.1 gives a value of around 1.061 at 38 MHz which is in a good agreement with the prediction from Vinyaikin and leads to a flux density of Cas A of 26880 Jy for the year 2013. Following the formulae of Vinyaikin a flux density of 25330 Jy at 38 MHz can be calculated for Cyg A. Using the parameters of log(A) = 5.827 and $\beta = 2.320$, as quoted for 81 MHz, one gets a ratio of 0.94 for 2013. No parameters for the intermediate frequencies available.

Unfortunately the accuracy of the data is not good enough to study the yearly decrease of Cas A by analyzing the observation from January and September 2013 separately. From Vinyaikin the yearly decrease at 38 MHz is expected to be around 0.73% per year which is below the errors of the LOFAR maps.

6.2 Spectral Index of Cas A

As the decrease of the flux density of Cas A is frequency dependent, the spectral index of Cas A is changing with time, too. The variation with frequency, especially at low frequencies, can be explained by the HII region around Cas A, which causes a decrease in the optical depth with time due to recombination of hydrogen atoms.

For the spectral index study of Cas A with LOFAR, frequencies below 65 MHz are used, as at higher frequencies problems with the antenna model and signal to noise ratio appear, as already mentioned earlier. Especially in the ratio of Cas A and Cyg A as plotted in Fig. 6.1 the problems with the beam model around the frequency of 55 MHz become strongly visible.

For the following analysis the ratio of Cas A and Cyg A is used. By multiplication with the theoretical flux density of Cyg A, a corrected flux density for Cas A can be determined (as the absolute flux density calibration of the skymap is challenging). The theoretical values from Cyg A are again taken from Vinyaikin:

$$S_\nu^{CygA}[Jy] = 3.835 \cdot 10^5 \cdot (\nu[\mathrm{MHz}])^{-0.718} \cdot e^{-0.342(\frac{21.713}{\nu[\mathrm{MHz}]})^{2.1}} \tag{6.2}$$

and were used for the correction of Cas A:

$$S^{CasA} = \frac{S_{theo}^{CygA}}{S_{measured}^{CygA}} \cdot S_{measured}^{CasA}\,. \tag{6.3}$$

The theoretical flux densities for Cyg A and the flux density of Cas A as calculated with Eq. (6.3) are plotted in the right image of Fig. 6.1. For each data point an integration over

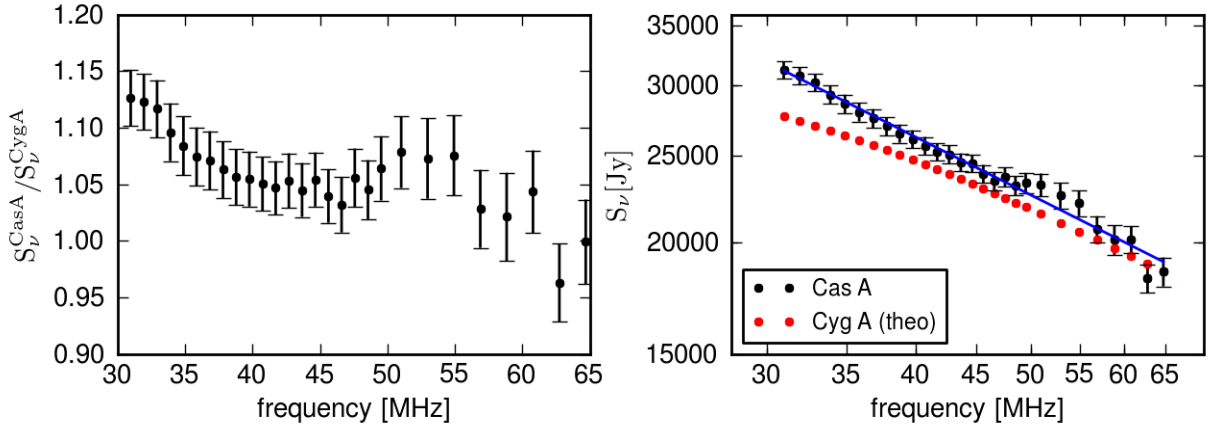

Figure 6.1: Left: Ratio of Cas A and Cyg A over the LOFAR low frequency range. Right: Spectra of Cas A as measured with LOFAR and Cyg A as calculated with Eq. (6.2) from Vinyaikin, 2014. The blue line gives the best fit to the Cas A data points with a slope of 0.67 as the spectral index of Cas A.

1 MHz bandwidth was done to increase the signal to noise ratio. Afterwards all maps were convolved to the same angular resolution of 9.3° and the flux density was measured over the same region.

The spectrum of Cyg A shows a curvature toward lower frequencies, whereas the spectrum of Cas A follows a straight line over the given frequency range. Fitting a line to all the frequency points of Cas A gives a slope of 0.67 which corresponds to the spectral index at these frequencies. Plotting the spectral index for the data points from 30 to 45 MHz leads to a spectral index of 0.70. Vinyaikin found an equation for the spectral index of Cas A depending on the frequency for the year 2015:

$$SI(\nu) = \alpha - 2\beta\log(\nu) - 2.1\tau_0\nu^{-2.1} \tag{6.4}$$

where $\alpha = 0.752$, $\beta = 0.0148$ and $\tau_0 = 6.162$ x 10^{-5}. At 40 MHz this leads to a spectral index of 0.68 for the year 2015 which is in good agreement with the values of 0.67 and 0.70 as calculated from the LOFAR measurements.

For the other strong radio sources, like Vir A and Tau A, the spectral study is not possible with the LOFAR data, as there are too weak compared to the surrounding medium and therefore it is not possible to distinguish them from the large scale emission.

Table 6.1: Summary of measured and predicted properties concerning Cas A.

	S_{38MHz}^{CasA}	$S_{38MHz}^{CasA}/S_{38MHz}^{CygA}$	SI^{CasA}(40 MHz)
LOFAR (2013)	26880 Jy	1.061	0.70
prediction (Vinyaikin, 2014)	26540 Jy	1.066	0.69

6.3 Summary

Even as the both strong radio sources Cas A and Cyg A cannot be resolved with the beam of a single LOFAR station, the predictions concerning the flux density of Cas A (summarized in Table 6.1) can be confirmed. By using Cyg A for the absolute flux density calibration a flux density of 26880 Jy for Cas A at a frequency of 38 MHz is calculated. The flux density ratio of both sources is found to be 1.061 at 38 MHz at the epoch of 2013.

Having a look at the spectrum of Cas A and Cyg A shows the difficulty of the bandpass correction within the LBA band. As already noticed earlier in Fig. 2.3 the bandpass of the low band antennas has a strong variation in amplitude, peaking at a frequency of 57 MHz. For the same frequency range, problems in the source spectra can be found. This is a known problem to the LOFAR community and not solved at this time. It is assumed that this is caused by errors of the antenna pattern, for which the modeling around the resonance frequency of 57 MHz seems to cause most problems. This effect not just cause problems for the point sources but for the entire galactic map and partly leads to errors in the final results of the data analysis.

Chapter 7

Obtaining pulsar RMs

For the calibration of the ionosphere simultaneous pulsar observation were done, like described in Sect. 4.1. As pulsars have no intrinsic RMs, the RMs that are measured for a pulsar contain information about the medium between us and the pulsar. Therefore they are an important tool to measure the Faraday rotation due to our Milky Way. Pulsars which are closer to the Galactic plane have higher values than sources at higher galactic latitudes. As the foreground is not changing or just on long timescales, the measured RMs should be constant and representing the intergalactic medium. The fluctuation in the measured RM values comes from Faraday rotation within the ionosphere, for which a correction is needed.

7.1 Selection of pulsars

The pulsars that were chosen for the correction of the theoretical RM values of the ionosphere had to full fill some criteria, like
- bright flux density
- high declination
- high RM value
- low Dispersion Measure (DM) value (see Eq. 7.2).

The first point is necessary to get a good signal to noise ratio, even for short observation times to reduce the errors of the measured values. High declination pulsars can be observed during a longer time period without getting too close to the horizon, where the data become more noisy. It is difficult to use pulsar observations when the elevation of the source is below 30°. The high RM values helps to distinguish better between the polarization of the pulsar and the instrumental polarization, which strongly shows up at a RM value of zero. The need for low DM values comes from the de-dispersion in the pulsar data reduction which becomes problematic for too high DM values. Taking these four points into account, three pulsars were chosen, which are J0332+5434, J0814+7429 and J2018+2839. The most important information about them were contained from the ATNF[1] catalog (Manchester et al., 2005)

[1]ATNF Pulsar Catalogue web address `http://www.atnf.csiro.au/people/pulsar/psrcat/`

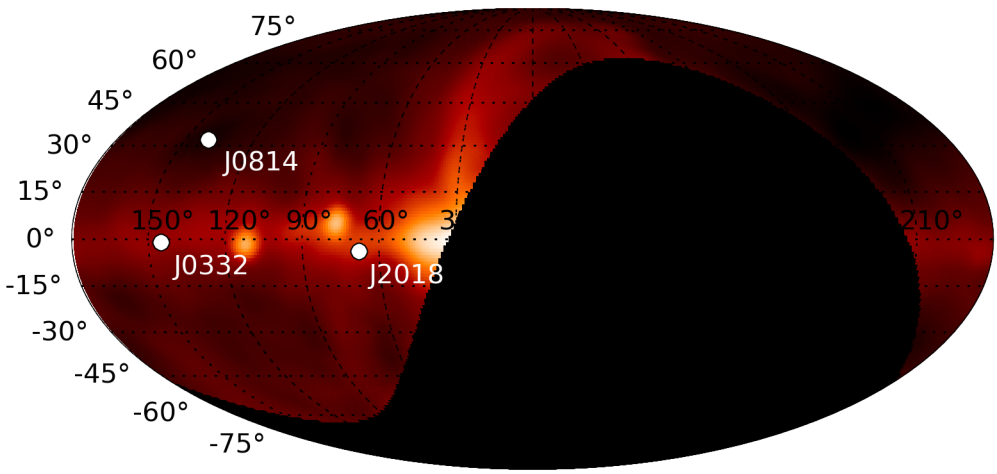

Figure 7.1: LOFAR 45 MHz map including the observed pulsars.

Table 7.1: Overview of the observed pulsars (ATNF)

pulsar	gal lon [deg]	gal lat [deg]	S_{400} [mJy]	spectral index	DM [pc/cm^3]	RM_{ATNF} [rad/m^2]	$RM_{thiswork}$ [rad/m^2]
J0332+5434	145.0	-1.22	1500	-1.6	26.83	-63.7	-64.55 ± 0.10
J0814+7429	140.0	31.62	41.1	-1.7	5.73	-14.00	-13.96 ± 0.15
J2018+2839	68.1	-3.98	314	-2.3	14.17	-34.6	-34.92 ± 0.20

and are summarized in Table 7.1. The position of these pulsars in Galactic coordinates are imaged in Fig. 7.1 using the 45 MHz LOFAR map. The pulsar with the highest elevation at the time of the observation was used for the RM correction of the galactic data.

7.2 Observations and data reduction

The pulsar observations were done with the HBAs in RCU mode 5 by using 244 channels in the frequency range from 120 MHz to 167 MHz. Every observation lasted 12 minutes with the beam-formed mode available at the Effelsberg LOFAR station. This means that all 16 antennas per tile were used and a delay correction to the observing direction was performed at the station correlator. The observations were done with HBAs, even if the all-sky observations were done using the LBAs. Just in January two observation runs were done using the LBAs for the pulsar observations. Due too the strong RFI in the LBA at the Effelsberg station it was not possible to obtain the RM values of the pulsars. Afterwards HBA observations were used instead.

For the de-dispersion and calibration of the pulsar data the DJLump software from

M. Kuniyoshi (priv. comm.) was used. The de-dispersion of the pulse is necessary, as the interstellar medium (ISM) causes a dispersion of the pulse. Lower frequency waves travel slower as waves with longer wavelength, which results in a delay of the travel time:

$$\Delta t = 4.149 \cdot 10^6 \cdot \mathrm{DM} \cdot \left(\frac{1}{\nu_1^2} - \frac{1}{\nu_2^2} \right) \tag{7.1}$$

where ν_1 and ν_2 are both ends of the observing frequency band in MHz and

$$\mathrm{DM} = \int n_e dl \tag{7.2}$$

is the dispersion measure (DM) of the pulsar in pc/cm^3. In case of observing the pulsar J0332+54 with LOFAR using the frequency band from 120 MHz to 167 MHz, this time delay corresponds to around 0.277 sec. By knowing the DM of the pulsar, a de-dispersion on the measured signal can be performed to correct for the frequency dependance of the signal.

Afterwards the flagging of bad data was done by hand using plots of the integrated pulse in the time and frequency domain. Finally RM Synthesis (Sect. 1.2.3) was used to obtain the RM value of the pulsar.

7.3 Obtaining pulsar RMs using ionospheric corrections

From the high number of pulsar observations and the theoretical predictions for the ionosphere, the corrected pulsar RM can be obtained. In theory the RM values as given by the ATNF could be used directly to obtain the RMs from the ionosphere. Nevertheless, as most of the earlier pulsar measurements were done without ionospheric correction or are maybe occupied by other errors, the LOFAR measurements were used to determine the pulsar RM. Besides, the comparison of the obtained RMs with values from the literature can be used, to prove that our instrument is working right and is given reasonable results.

The calculation is done by subtracting the RM value of the ionosphere from the measured RM value of the observed pulsar and getting the mean of all measured data afterwards:

$$\mathrm{RM} = \mathrm{mean}(\mathrm{RM}_i^{meas} - \mathrm{RM}_i^{ionosphere}) \tag{7.3}$$

where the ionospheric prediction was calculated using a code by Olaf Wucknitz (priv. comm.). For illustration Fig. 7.2 images this method for two observation runs in May 2013. The transparent points are the direct obtained RM values after the data reduction and RM Synthesis. The non-transparent points represent the values after the correction of the ionosphere prediction. Before this correction the measured points are varying with time, whereas they are mostly constant afterwards. The mean of all data points is shown by the black line.

In this way RM values for the three observed pulsar were achieved and are summarized in Table 7.1. For J0332+54 and J2018+28 these values differ from the ATNF catalog values. In the case of J0814+74 both values are similar, as the catalog value is obtained from other

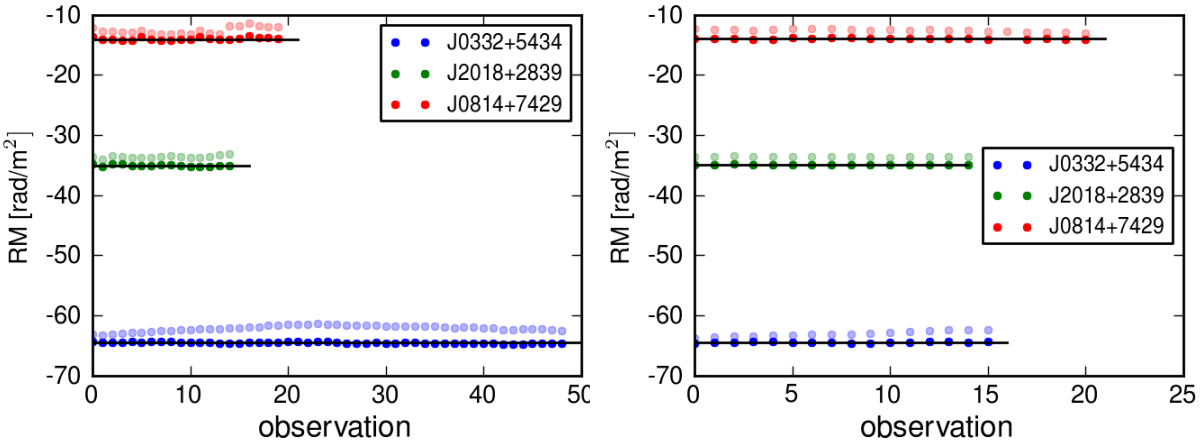

Figure 7.2: Obtained RM values of the pulsars for the observations on May 3th (left) and May 28th (right). The transparent points represent the direct measured values, before the correction of the ionosphere was applied. The black lines are the calculated median values for the ionospheric corrected RM values. Errors are of the order of the point sizes (0.2 rad/m^2).

LOFAR measurements by Noutsos et al. (2015), including a correction of the ionosphere. In earlier pulsar measurements the correction of the ionosphere was mostly ignored wherefore the RM values can vary from our measurement. Nevertheless my measurements and the values from the literature are in good agreement, with a difference of both values below 1 rad/m^2. In this way all obtained RM values prove that the data reduction is working properly and even more that the used software for the ionosphere prediction is given good results. Even as Noutsos et al. were using the entire LOFAR core instead of just one single international LOFAR station and another code for the ionosphere prediction (by Sotomayor-Beltran et al., 2013), the same result for J0814+74 was obtained.

7.4 Using pulsar RMs for the correction of ionospheric predictions

The calculated RM values are in the following used to compare the theoretical prediction of the ionospheric Faraday rotation with the measurements of the pulsars. As these predictions are done by using measurements of the TECs (Eq. 3.39) just every second hour with an interpolation of the intermediate times (see Sect. 3.10), variations of the ionosphere on smaller time scales are not detected. As a pulsar observation was done every 16 minutes during the observations of the LOFAR data (Sect. 4.1), a better correction for the fluctuations in the ionosphere can be performed.

Figure 7.3 shows pulsar measurements from two 24-hour runs made with the station in Effelsberg. The colored arrays indicate the predicted RM values as obtained from the TEC

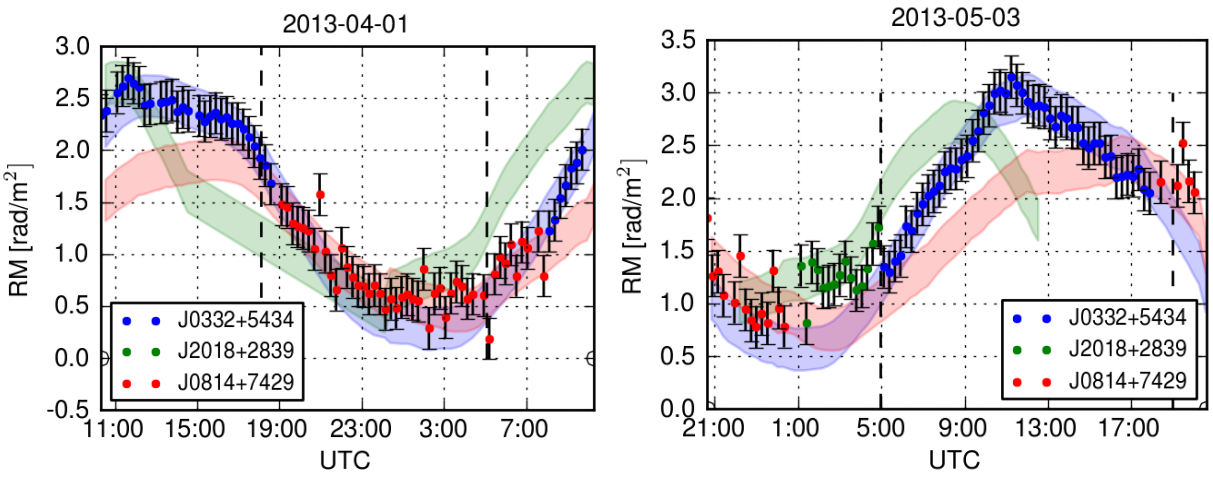

Figure 7.3: RM variation at two observations runs made in April and May 2013. The dotes indicate the pulsar RM measurements. The colored area are the predictions of the ionospheric RMs, calculated form GPS measurements of the TECs (code provided by Olaf Wucknitz (priv. comm.)), including errors of 0.2 rad/m^2. Sunset and sunrise are marked by the dashed lines.

measurements including an error of 0.2 rad/m^2. The points represent the measured values from the observations including an error of 0.2 rad/m^2 as well. The known RM values from the pulsars (as given in Table 7.1) were subtracted from the measured pulsar RM values, so that just the ionospheric RMs are left. The RM values from the pulsar observations are in good agreement with the theoretical models. On large time scales the observed values follow the slope of the theoretical predictions. Nevertheless, on short time scales the values can deviate by a few 0.1 rad/m^2. As expected the RMs of the ionosphere are strongest during day time peaking around noon. This is due to the high electron content in the ionosphere caused by the Sun. After sunset (marked with the dashed line) the electron content drops and has its minimum at the end of the night. After sunrise (marked with the dashed line) the electron content is rising again. The size of the RM value also depends on the direction on the sky by looking through a different path length of the ionosphere. Therefore the RM in the direction of the pulsar can vary between the pulsars.

Of course also the pulsar measurements contain errors occurred by RFI, less sensitivity of the signal, position on the sky and others. Therefore the fluctuations in J0814+74 and J2018+28 are stronger than for J0332+54, as J0332+54 is the strongest of these three pulsars and expected to be less affected by errors.

The Faraday rotation of the ionosphere just has an influence on the skymaps in Stokes Q and U, wherefore a correction is needed (Sect. 3.10). The ratio of the measured ionospheric RM and the predictions are used to scale the RM maps of the entire sky before they are applied to the Q and U maps.

All of the corrections are just helping to reduce the errors due to the low time resolution of the ionosphere predictions. There is still a direction dependent error left, for which no correction is available.

7.5 Summary

As part of this thesis, pulsar observations were done simultaneously with the all-sky observations. With the use of model predictions for the ionosphere, it was possible to determine the RM value of the three observed pulsars. The obtained RM values of -64.55 $\pm$ 0.10 rad/m^2 for J0332+54, -13.96 $\pm$ 0.15 rad/m^2 for J0814+74 and -34.92 $\pm$ 0.20 rad/m^2 for J2018+28 (summarized in Table 7.1) are in good agreement with earlier measurements by Noutsos et al. (2015) and Manchester (1972). These values are later used to correct for ionospheric fluctuations on time scales smaller than given by the predictions.

As the obtained RM values are in good agreement with other observations, it is shown that one international LOFAR station is sufficient to determine pulsar RMs. Of course this works better for bright pulsars, which have a good signal to noise ratio.

Having a look on the further analysis of this thesis, it has been proven that the code used for the model predictions of the ionosphere (as provided by Olaf Wucknitz) gives reasonable results and can therefore be used for the correction of the Faraday rotation. Besides it has been shown that the pulsar measurements can be used to model the Earth ionosphere. The changes of the RM values with time are well correlated with the changes predicted by the model.

Chapter 8

Polarization of Jupiter burst

As the bursts of Jupiter are strong and highly polarized, they can already be seen by using short observation snapshots with fractions of a second. In this chapter the properties of the linear and circular polarization of the Jupiter bursts are studies. Furthermore, RM Synthesis is used to obtain RM values which allow a detailed analysis of the corresponding radiation.

8.1 The bursts of Jupiter

In 1955 bursts from Jupiter were detected for the first time. It took some time for scientists to understand where this radiation is coming from. Although not everything is clear by now, studies of the bursts have shown that the decameter wavelength radiation is caused by an interaction of Jupiter with its moon Io. Io's size is just slightly bigger than our moon and mainly composed of silicate rock with an iron core. Beside of that, Io is one of the most volcanically active body in our solar system and is erupting nearly all of the time. In this way a lot of material is ejected into space, where it gets ionized and afterwards is trapped by Jupiter and its strong magnetic field. The ring of this material around Jupiter is called Io Plasma Torus and can reach an electron density up to 2000 cm^{-3}. Due to Io's properties and Jupiter's strong magnetic field, Io behaves like a conductor that is moving through a magnetic field in which way a current is induced. The accelerated electrons follow the magnetic field lines up the Jupiter's magnetosphere, where they are producing radiation at decameter wavelengths. This process will not be discussed here in detail, as it is not the main topic of this thesis. For more information one may have a look at the report of Voyager 1 (Stone, 1979).

Depending on the Central Meridian Longitude (CML), the Io phase ϕ_{Io} and the Jovicentric declination of the earth D_E, different sources of Io related Jupiter bursts can be observed. The CML contains information about the longitude of Jupiter facing the earth. For the description of the Io bursts the so-called System III is used, which uses the magnetic field as a reference for CML value. The magnetic field is tilted toward CML = 200.8°. The Io phase depends on the location of Io in relation to Jupiter. It is 0°, if Io is directly behind Jupiter as seen from Earth and 180° if Io is in front of Jupiter. An Io phase of 90° relates to

an Io position on the west side of Jupiter. The probability to detect one of the four sources of Jupiter bursts (named A, B, C and D) depends strongly on the CML and Io phase. A summary of CML and Io phase values for a high probability to detect the Jupiter events is given in Table 8.1.

Table 8.1: Locations for the highest probability to observe the individual Jupiter bursts.

source	CML [deg]	Io phase [deg]
Io-A	190 - 360	150 - 260
Io-B	0 - 210	20 - 120
Io-C	0 - 50	240 - 270
Io-D	0 - 180	90 - 120

Observations have shown that the bursts are up to 100% circular polarized. As already studied by Cyr (1985) the probability to detect whether the a right-handed or left-handed polarized depends on the Jovicentric declination. If D_E is positive there is a higher possibility to observe left-handed polarization as we are looking toward the southern hemisphere of Jupiter. For negative D_E we are looking toward the northern hemisphere and have a higher possibility to observe right-handed polarization events. In every cases it is always just a probability.

Furthermore one distinguishes between L bursts (long) and S bursts (short). L bursts are lasting between a few seconds up to several tens of seconds with a bandwidth a few MHz. In contrast S bursts lasting just for a fraction of a second and it is possible to observe around 100 bursts per second. There are just observed over a bandwidth of a few kHz. Observed Io-A events are mainly L bursts, whereas Io-B events are often S bursts. In case of Io-C events L and S bursts are observed equally frequent.

Of course Jupiter also is producing thermal and synchrotron radiation, but the intensities are much lower. Io related bursts from Jupiter have intensities up to several 10 kJy and can therefore be detected even with a single LOFAR station and short integration times.

8.2 Observing Jupiter with TBB data

Studying Jupiter bursts by using raw voltages of the LOFAR system has some advantages. The Io related Jupiter bursts at decameter wavelength can just be detected at frequencies below 38 MHz. Unfortunately the spectrum below 30 MHz is strongly occupied by RFI. With a frequency resolution of of 200 kHz as given by the station correltaor, most of the RFI peaks cannot be resolved, so that most of what is seen in the maps below 30 MHz is RFI. By correlating the raw voltages from the TBBs instead a higher frequency resolution can be reached. This gives the possibility to resolve most of the RFI peaks and to identify some channels with lower RFI where the Jupiter bursts can be detected. Two examples for the low frequency spectrum are given in Fig. 8.1. In the left hand plot, where the frequencies ranges from 15 to 35 MHz, still a large number of RFI free channels can be detected, especially toward the higher frequencies. In the frequency range from 10 to 20 MHz, as seen in the right hand plot, the situation looks different and mainly RFI is detected. Therefore it will be almost impossible to detect Jupiter bursts at frequencies below 18 MHz using the LOFAR

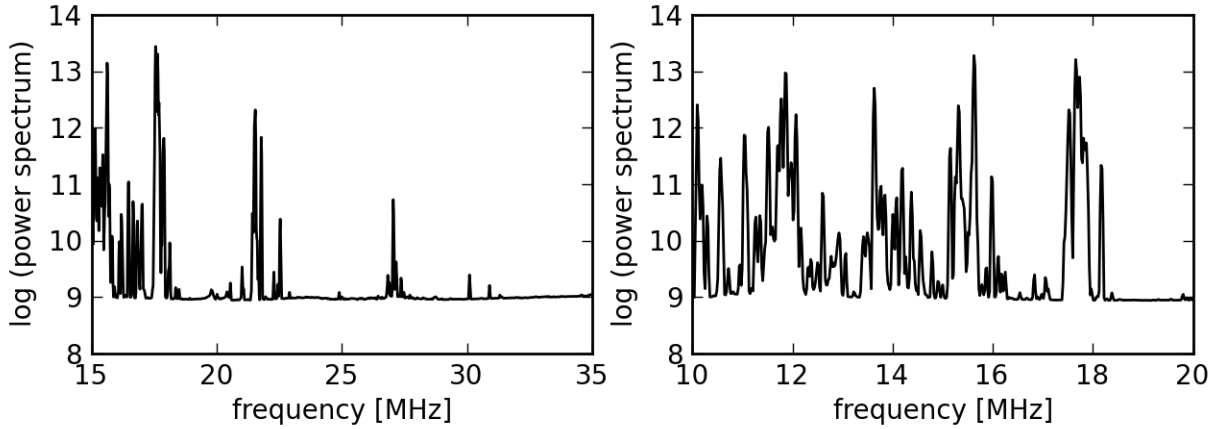

Figure 8.1: Observations using the TBBs from the Effelsberg station. Left: The averaged power spectrum of an 1.3 sec observation from 15 to 35 MHz as used for the analysis of the Io-A and Io-B events. In both cases a frequency resolution of 20 kHz is reached. Right: Averaged power spectrum of an 1.3 sec observation over the frequency band from 10 to 20 MHz as used for the analysis of the Io-C and Io-D events.

station in Effelsberg. The high frequency resolution is not just helpful to deal with the RFI, it is even more needed to perform RM Synthesis on the data. As explained in Sect. 1.2.2.1 at low frequencies bandwidth-depolarization becomes a problem, wherefore small frequency channels are needed.

With the beam resolution of a single station, which is at frequencies below 30 MHz more than 10°, it is not possible to resolve the structures of Jupiter. Nevertheless, a study of the polarization is still possible. At least the low beam resolution makes the calibration much easier, as the unresolved Jupiter appears as a simple point source. But no matter if a resolved or unresolved point source, there is no existing theoretical model for the intensity of Jupiter and the bursts are strongly time and frequency variable. Therefore the self-calibration as described earlier in Sect. 3.6 is used. Furthermore the self-calibration is needed for the calibration of the strong RFI appearing in the field of view. Without the self-calibration method the calibration of the data would be impossible.

The calibration is performed on the all-sky maps instead of doing a beam-forming in the direction of Jupiter. An observation of a type B Jupiter burst is shown in Fig. 8.2. Again the TBB data with 1.3 sec integration time are used and correlated with 20 kHz frequency resolution. This time just the self-calibrated images in Stokes Q and Stokes U are plotted for some nearby channels, so that the rotation of the Stokes Q and Stokes U vectors due to Faraday Rotation becomes visible. As seen the rotation from positive to negative values happens within 100 kHz at a center frequency of around 30 MHz. With the 200 kHz resolution from the station correlator this would not be detectable.

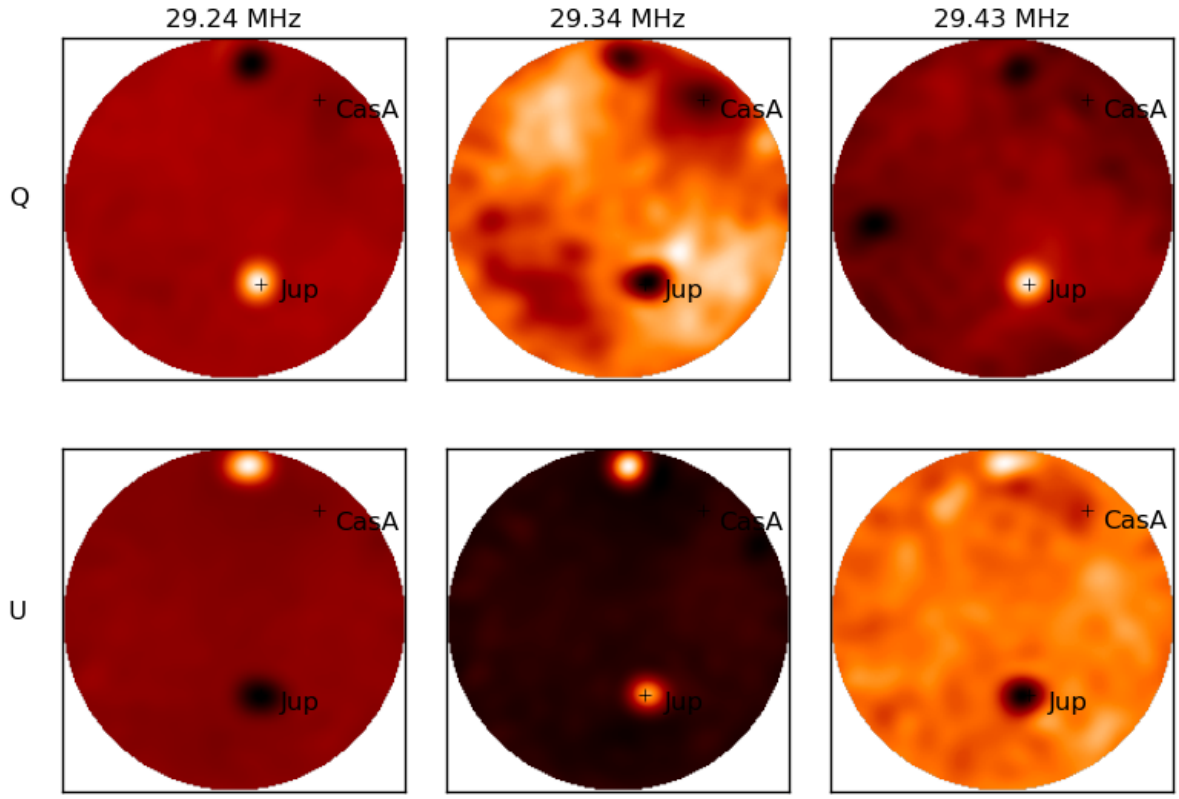

Figure 8.2: Jupiter observation from May 2013 done with the TBBs from Effelsberg. The integration time is 1.3 sec and the data were correlated with 20 kHz channel width. The self-calibrated images of Stokes Q and Stokes U for different frequency channels are plotted, so that the rotation of the Stokes Q and Stokes U vector due to the Faraday Rotation of the Jupiter emission becomes visible.

8.3 The observations

A number of observations have been performed during times with a high probability to detect the different Io related Jupiter bursts. A summary of the observations is given in Table 8.2 containing information about the burst type and source positions. Furthermore the CML vs Io-phase is plotted for all observations in Fig. 8.3. But even as times with high probabilities were chosen, there was no guaranteed for a positive detection. As already explained in Sect. 4.1 every 15 minutes an observation was performed by using raw voltages from the TBBs with 1.3 sec integration time. Depending on what kind of burst was observed, different correlations of the data were performed. The data for Io-A and Io-B events were correlated from 15 to 35 MHz, data for Io-C and Io-D events from 10 to 20 MHz. In all cases a frequency resolution of 20 kHz was chosen, which should be sufficient to avoid bandwidth

Table 8.2: Overview of my Jupiter observations. Hereby Δ_{JE} is the distance between Jupiter and the Earth. All of the other parameters are explained within the text.

date yyyy-mm-dd	time (UTC) start-end	RA h	DEC deg	source	CML deg	Io phase deg	Δ_{JS} deg	Δ_{JE} AU
2013-05-28	13:00 - 15:36	5.51	23.0	Io-B	130 - 225	96 - 118	17	6.1
2013-06-04	11:37 - 13:42	5.51	23.0	Io-B	53 - 128	70 - 88	12	6.1
2013-07-22	13:24 - 13:42	6.41	23.1	Io-D	123 - 132	119 - 125	21	6.0
2013-07-23	06:13 - 06:30	6.41	23.1	Io-C	22 - 32	261 - 265	21	6.0
2013-07-30	06:16 - 07:43	6.54	23.1	Io-C	356 - 50	248 - 259	30	6.0
2013-08-29	06:19 - 08:09	6.97	22.6	Io-A	190 - 256	228 - 240	52	5.7

depolarization. At frequencies below 20 MHz the RFI is expected to be the biggest problem in the analysis of the data.

During all of my observations in 2013 the Jovicentric declination of the Earth had a positive value ranging from 2.2° to 2.7°. This leads to a higher possibility to detect left-handed instead of right-handed circularly polarized events.

In the following, a detailed discussion of the observations of the different Io related Jupiter burst types is given. All of the obtained properties of the detected bursts for the individual observation dates and times are summarized in Table 8.3. The given frequency is the mean value from the frequency range at which the bursts is detected. Furthermore, the degree of linear polarization

$$m_{lin} = \frac{\sqrt{Q^2 + U^2}}{I}, \tag{8.1}$$

circular polarization

$$m_{circ} = \frac{V}{I} \tag{8.2}$$

and total polarization

$$m_{total} = \frac{\sqrt{Q^2 + U^2 + V^2}}{I} \tag{8.3}$$

is given.

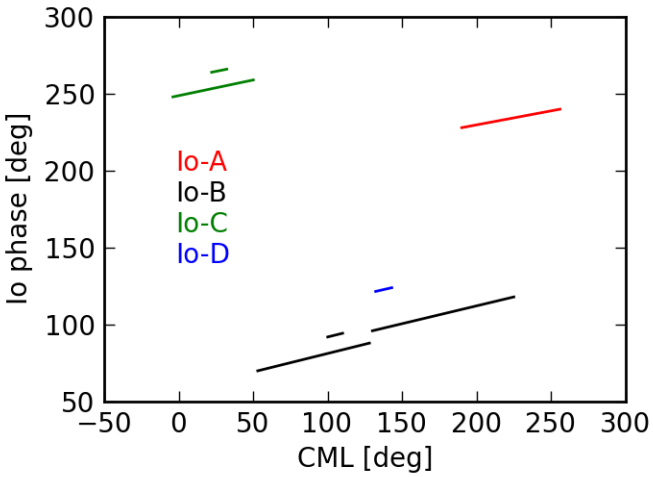

Figure 8.3: Location of the observed times in the CML-Io phase plot.

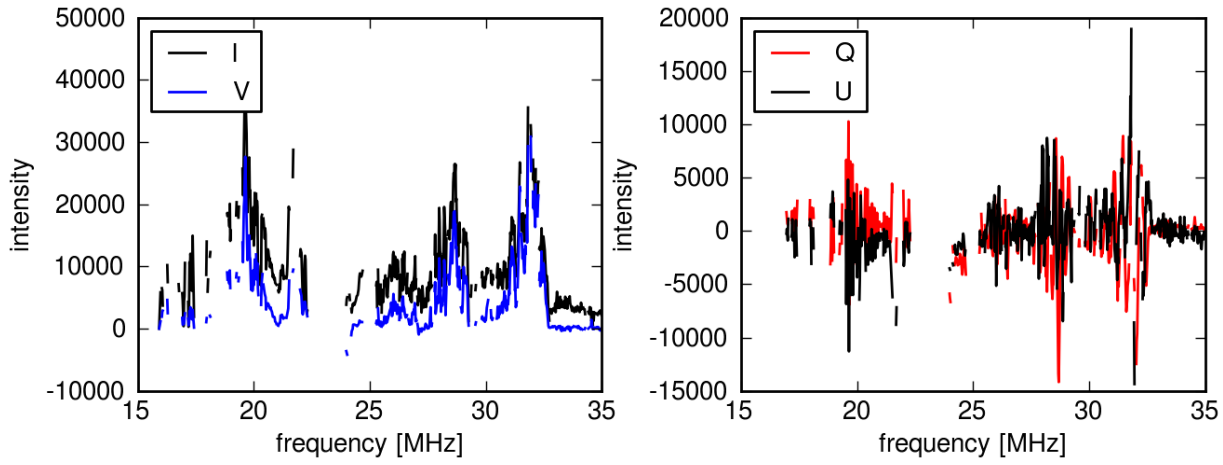

Figure 8.4: Spectra of a left-handed Io-A event observed at 07:22:54 on January 15th in 2013.

8.3.1 Observations of Io-A events

Eight observations with a high probability of detecting an A event were performed at the end of August in 2013. One observation was too much occupied and therefore not usable. In four of the observations Jupiter bursts were detected, up to frequencies of 34 MHz. All observed events were left-handed polarized and are therefore expected to come from the southern hemisphere of Jupiter. As summarized in Table 8.3 the fractional circular polarization (ranging from 53% to 80%) was in all observations higher than the fractional linear polarization (from 20% to 34%). The total fractional polarization ranges from around 60% to 84%. In two of the observations bursts appeared at various frequencies at the same time. In cases of a large separation between these peaks in the frequency spectrum, different properties of the bursts were obtained. This is due to the fact that the energy of the observed particles (which is proportional to the observed frequency) is originating from a different location in the Jupiter hemisphere. Radiation at around 40 MHz is emitted near the planetary surface, whereas the radiation at 10 MHz is emitted around 0.3 Jovian radii above the surface (Zarka, 2004). A more detailed discussion on this follows in Sect. 8.4. The measured total polarization is higher for events observed at higher frequencies. Even as the fractional circular polarizations seems to be higher for higher frequency peaks, there is no clear trend for the linear polarization. As time is passing by from one observation to the other, the observed bursts are shifting more and more toward the higher frequencies. This could be due to the changing of the emitting angle of the radiation caused by the changing of the CML and Io-phase with time.

In Fig. 8.4 the spectral behavior for one of the observations with bursts detected at around 20 MHz, 28 MHz and 32 MHz is shown. In the left hand plot the total intensity (Stokes I) and the circular polarization (Stokes V) is plotted. The positive sign of the circular polarization

indicates that left-handed polarization is observed. The linear polarization (Stokes Q and Stokes U) of the same event is plotted in the right image. The intensity of Stokes Q and Stokes U are strongest at frequencies with high intensities in Stokes I and Stokes V. Besides, a rotation from positive to negative values is detected.

8.3.2 Observations of Io-B events

For this type of bursts most of the observations are available, as most of them happen to be at the same time when the observations for the all-sky survey were performed. Therefore no extra observing time was needed.

During the observations at the end of May and beginning of June in 2013 the Sun was nearly in the line of sight between Jupiter and the Earth with a distance of around 15° apart from Jupiter as seen from Earth. The intensity of the quiet Sun is much lower at frequencies below 35 MHz and therefore should not causes trouble. Things just become complicated when the Sun is producing bursts at around the same time as the Jupiter bursts. This is especially complicated as the beam resolution is more than 10° below 30 MHz, wherefore a careful calibration is needed.

For the observation on May 28th, a lot of RFI appears at frequencies above 40 MHz as seen in the data for the all-sky survey. Nevertheless, it seems that below 40 MHz the quality of the data is fine and they can be used at least for studying the Jupiter bursts.

Seven detections of left-handed polarization events are made at different observation times mainly showing up at frequencies between 20 MHz and 30 MHz. In the observations of the right-handed polarized events it is harder to detect the bursts as there are showing up at frequencies below 20 MHz, where more RFI is present and just a low number of RFI free channels is available. Therefore, although it is possible to detect some of the right-handed events, it is not possible to study the properties of them, as the strong RFI appearance disturbs the measurements.

In all of the left-handed events the circular polarization is higher as the linear polarization, varying from 46% to 76%. The linear polarization is in the range from 15% to 37%. Already Dulk et al. (1994) measured a higher degree of circular polarization compared to the linear polarization.

The total and polarized intensity of a strong right-handed polarized B event is plotted in Fig. 8.5. The left image shows the total intensity Stokes I and circular polarized intensity Stokes V. The right image shows the corresponding intensities in Stokes Q and Stokes U at the frequency range from 24 MHz to 30 MHz. The circular polarization has a positive sign as the radiation is left-handed polarized. For a right-handed event the measured circular polarization would be negative. In Stokes Q and Stokes U the fast rotation of the vectors due to the Faraday Rotation can be detected. In two of the observed B events right-handed and left-handed circular polarization was observed at the same time. One of these observations is shown in Fig. 8.6 where the left-handed circular polarization is detected in the frequency range from 16 to 19 MHz, whereas the right-handed circular polarization is detected around 33 MHz. This effect was labeled by Gordon and Warwick (1967) as Y-one Faraday rotation

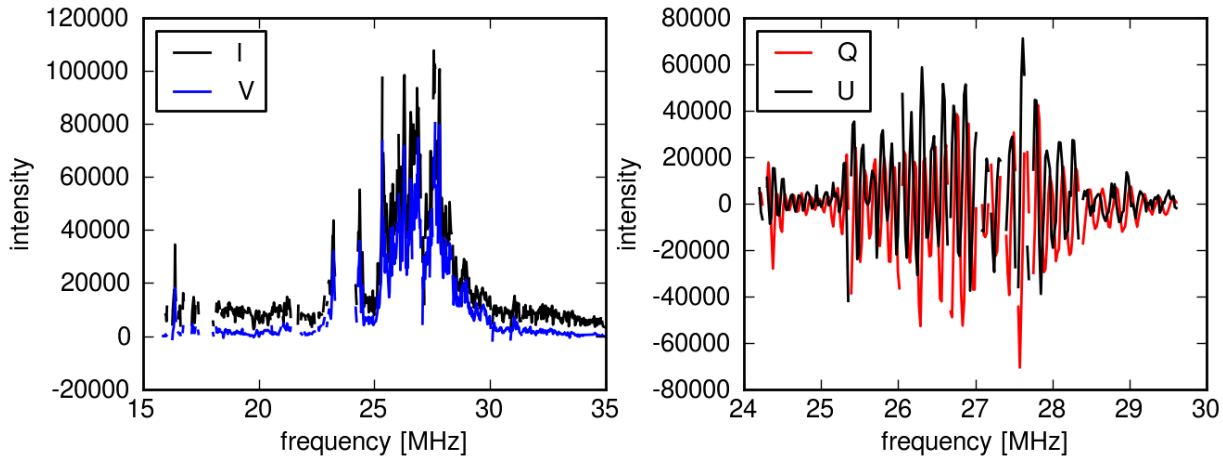

Figure 8.5: Spectra of a left-handed Io-B event observed at 13:00:40 on May 28th in 2013.

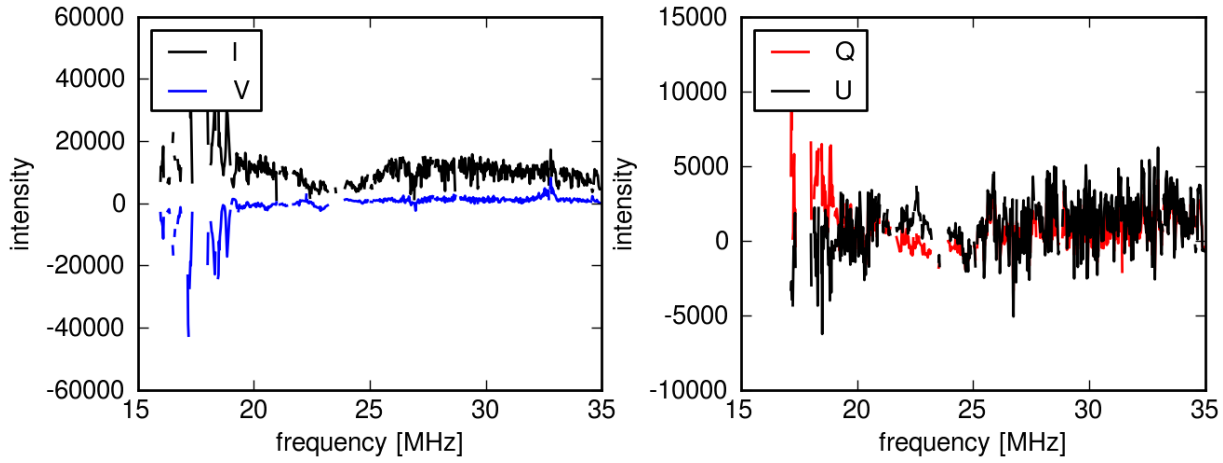

Figure 8.6: Spectra of an Io-B event observed at 14:18:26 on May 28th in 2013, showing strong right-handed circular polarization at around 18.4 MHz and weaker left-handed circular polarization at 33 MHz.

and is happening if the emitting frequency is similar to the gyrofrequency. These effects are rare and mostly seen in S-bursts. Due to the strong RFI situation in this observation a detailed analysis of this dataset is not possible.

8.3.3 Observations of Io-C and Io-D events

As these events appear at frequencies below 20 MHz, the spectrum is mainly dominated by RFI and it is difficult to find RFI free channels to look for the Jupiter bursts. Beside of that,

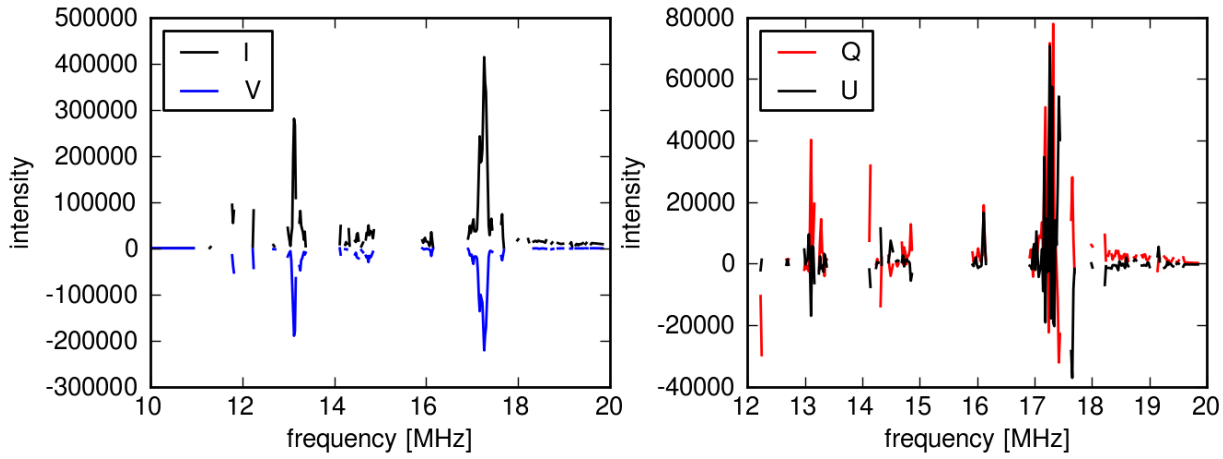

Figure 8.7: Spectra of an Io-C event observed at 6:32:10 on July 30th in 2013, showing strong right-handed circular polarization at around 13 MHz and 17.3 MHz.

the probability to observe this kind of bursts is lower than for type A and B what makes the situation even more complicated. Nevertheless, at least in two of the measurements a C event was detected, one of them is shown in Fig. 8.7. Both observed events were right-handed polarized and therefore expected to originate from the northern hemisphere. Due to the strong RFI, a detailed analysis of the data is impossible.

8.4 Faraday rotation of Jupiter bursts

After the successful calibration, RM Synthesis (Sect. 1.2.3) was performed on the single snapshot observations. This performance was done over a few MHz in the frequency range from 20 MHz to 30 MHz using a frequency resolution of 20 kHz. For the obtained Jupiter RM values an upper limit for the errors is calculated using the FWHM (Eq. 1.48) of the RM peak. Using the frequency range from 20 MHz to 30 MHz the FWHM is 0.03 rad/m^2. If several bursts appeared at different frequencies within one observation (like e.g. seen in the observation shown in Fig. 8.4), an RM value for each frequency range was calculated. The center of the used frequency range is given together with the obtained RM value (RM$_m$*eas*) in Table 8.3. An example of an RM spectrum for is plotted in the left image of Fig. 8.8, showing a strong peak at 2.36 $\pm$ 0.03 rad/m^2. This value corresponds to the Faraday rotation of the observed Jupiter burst. To prove that this peak really belongs to the Jupiter radiation, the polarization angle is plotted against the squared of the wavelength in the right hand image of Fig. 8.8, underlaid with the Stokes V intensity. A strong slope of the polarization angle shows up at frequencies where the Jupiter burst is detected. The calculated slope from this plot corresponds to the value obtained from the RM Synthesis. The peak at around 0 rad/m^2 in the Faraday spectrum corresponds to the instrumental polarization.

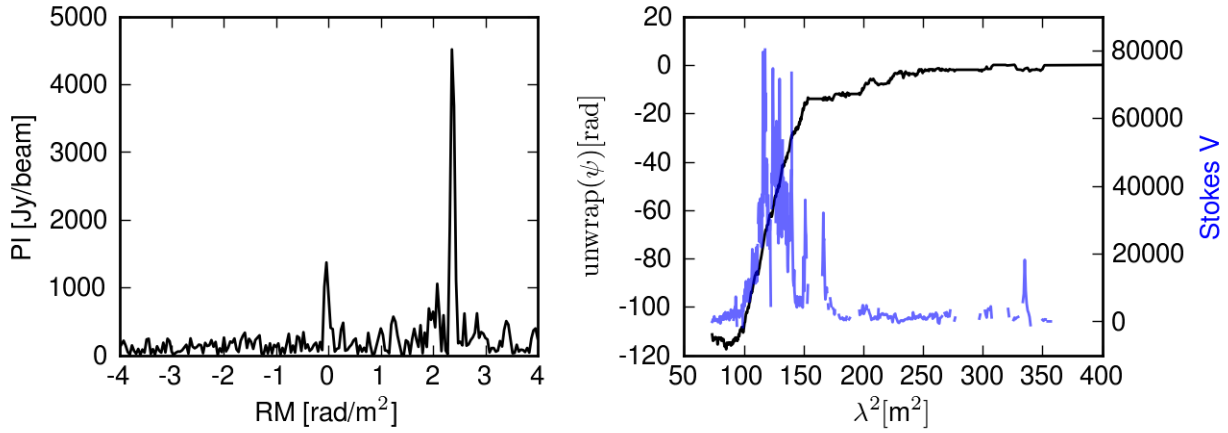

Figure 8.8: Left: Faraday spectrum performed by RM Synthesis on the observation from 13:00:40 on May 28th in 2013. The strong peak at 2.36 rad/m^2 belongs to the left-handed Jupiter event. The instrumental polarization shows up at 0. Right: Polarization angles are plotted versus the wavelength squared with Stokes V intensity underlaid.

The obtained RM value still contains the Faraday rotation due to the ionosphere (RM$_{ion}$), which has to be subtracted. The prediction for the ionosphere RM was again obtained from the code by Olaf Wucknitz (Sect. 3.10; priv. comm.). The error of the ionospheric RM values is expected to be at least 0.1 rad/m^2. Due to this the error of the final obtained Jupiter RM values is mainly influenced by the error of the ionospheric correction.

The summary of all detected Jupiter bursts is given in Table 8.3, including the obtained RM value, the predicted ionosphere RM toward the direction of Jupiter, and the difference of both values (RM$_{Jupiter}$). This difference still includes a small fraction of Faraday rotation caused by the interplanetary medium, which can be negligent. The main contribution originates at Jupiter itself.

As all of obtained RMs belong to left-handed events, there have a negative sign. This indicates that the magnetic field which causes the Faraday rotation is pointing away from us, as expected for the southern hemisphere of Jupiter. The size of the values indicates that they are real and not just an error from the ionospheric model. A clear detection is made for the Io-B events in the same way as for the Io-A events. Phillips et al. (1989), in an earlier observation of a single Io-A event, was not able to determine an Jupiter RM value away from around 0 rad/m^2. Nevertheless, my observations show RM values for Io-A events away from 0 rad/m^2 what indicates that Io-B and Io-A events are produced by the same mechanism.

8.4.1 Frequency dependence of the RMs

As shown in earlier observations the Jupiter emission originates close to the poles of Jupiter following its magnetic field lines (Calvert, 1983). If the cone of the moving electrons along

Table 8.3: Summary of polarization properties of the detected Jupiter bursts. The error of RM_{meas} is taken as 0.03 rad/m^2 using the FWHM of the RM peak. For RM_{ion} an error of 0.1 rad/m^2 is assumed. As result the error of $RM_{Jupiter}$ is taken as 0.1 rad/m^2.

date	time	source	ν [MHz]	m_{lin} %	m_{circ} %	m_{total} %	RM_{meas} [rad/m^2]	RM_{ion} [rad/m^2]	$RM_{Jupiter}$ [rad/m^2]
2013-05-28	130040	Io-B LH	27.0	54	+69	87	2.36	2.76	-0.40
	131613	Io-B LH	26.3	31	+60	71	2.36	2.75	-0.39
	133147	Io-B LH	20.3	15	+76	79	2.44	2.72	-0.28
		Io-B LH	34.1	21	+65	72	2.12	2.72	-0.60
	140251	Io-B RH	18.4	22	-47	48		2.65	
	141826	Io-B RH	18.4	26	-62	67		2.59	
		Io-B LH	33.0	20	+30	40		2.59	
2013-06-04	120859	Io-B LH	26.7	19	+19	28	2.24	2.77	-0.53
	122432	Io-B LH	30.3	29	+26	41	2.28	2.73	-0.45
	132643	Io-B LH	20.2	20	+62	66	2.28	2.53	-0.25
		Io-B LH	25.5	28	+40	49	2.24	2.53	-0.29
	134217	Io-B LH	19-29	35	+61	84	2.16	2.52	-0.36
2013-07-30	063210	Io-C RH		20	-55	59		2.06	
2013-08-29	063506	Io-A LH	20.4	30	+59	66	1.44	1.59	-0.15
	070721	Io-A LH	19.8	22	+53	59	1.52	1.71	-0.19
		Io-A LH	28.7	44	+62	66	1.48	1.71	-0.23
		Io-A LH	31.7	39	+71	80	1.40	1.71	-0.31
	072254	Io-A LH	31.8	31	+74	82	1.44	1.76	-0.32
		Io-A LH	33.5	27	+75	82	1.12	1.76	-0.64
	073828	Io-A LH	33.0	25	+80	84	1.40	1.80	-0.40

the field line is pointing toward our direction, a detection is made. The observed energy (and the corresponding frequency) of the radiation is directly related to the location of the origin. This means that radiation produced close to the Jupiter surface (where the magnetic field is stronger) will show up at higher frequencies, whereas radiation from further away from the surface will be detected at lower frequencies. The motion of a particle along the magnetic field causes a drift in the dynamic spectra (frequency vs time). Even as my observations are providing the integrated spectrum over 1.3 sec, detections of various bursts at different frequencies are made.

The measured RM values for the corresponding center frequencies are plotted in Fig. 8.9 using different colors for the individual observations dates. A frequency dependence becomes visible and is similar for all observation dates. Even more there is not a strong difference between the properties of Io-A and Io-B events. It just seems that all RM values obtained from the Io-A events are slightly shifted toward lower RM values. Nevertheless, the RM values of the Earth ionosphere (see Table 8.3)) are lower for the observing date of the Io-A event compared to the RM values of the Earth ionosphere obtained during the observation of the Io-B events. Following this, the Sun was more active in the middle of the year compared

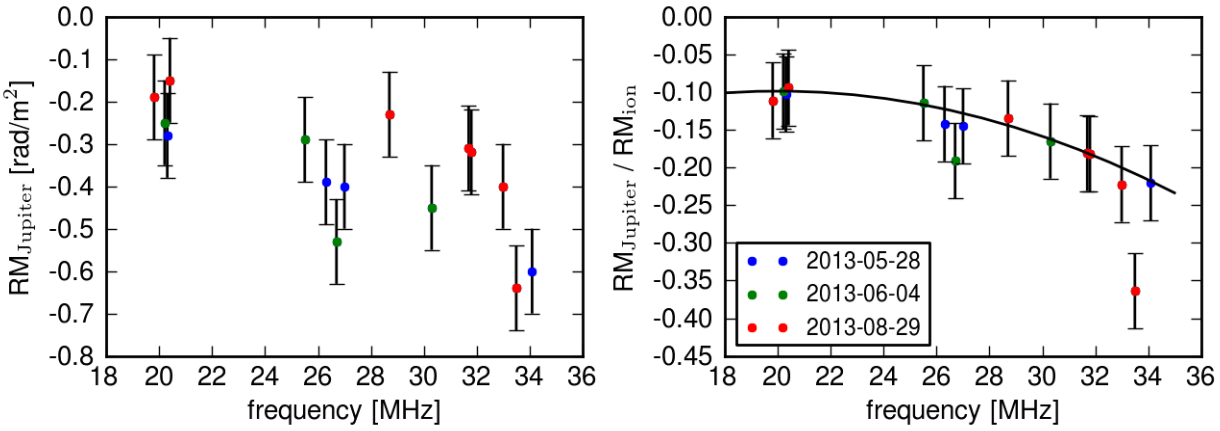

Figure 8.9: Left: Measured RMs vs frequencies. Right: Relation of Jupiter RM and ionosphere RM vs frequency. An error of 0.1 rad/m^2 is assumed.

to end of August. Even if Jupiter is more distant from the Sun it is likely that the Jupiter magnetosphere is affected by the Sun activity as well. In turn this would have an influence on the measured RM values as they are related to the electron density. For the following analysis a simple correction for the electron density in the Jupiter magnetosphere is done by using the ratio of $\mathrm{RM}_{Jupiter}$ and RM_{ion}. In reality this correction would be more complicated as the path length from the Sun to Jupiter is longer than the path length from the Sun to the Earth. Furthermore just one side of the Jupiter magnetosphere is facing the Sun and therefore is more affected by the Sun activity. In this case an information of the real origin of the measured Jupiter radiation is needed would be needed. As this detailed discussion would go beyond the scope of this thesis, just the simplified correction is used. In the right plot of Fig. 8.9 the ratio between the Jupiter RM and the Earth ionosphere RM is plotted against frequency. Except of two outliers, all measurements are following a clear trend which is fitted by the black line using a quadratic model. The strong frequency dependence proves that the measured RM values are not caused by errors in the ionosphere model or by Faraday rotation in the interplanetary medium, as both effects are frequency independent. The situation is different for the Faraday rotation in the Jupiter magnetosphere. Bursts detected at higher frequencies are originating close to the planetary surface. As the magnetic field strength and electron density gets stronger toward the planetary surface the observed radiation is stronger affected by Faraday rotation. Less Faraday rotation is expected for low frequency radiation originating further away from the planetary surface.

To obtain the origin point of the radiation at a given frequency, the cyclotron frequency

$$\nu_{ce}[\mathrm{MHz}] = \frac{eB}{2\pi m_e c} = 2.8B[\mathrm{G}] \tag{8.4}$$

is compared to the theoretical magnetic field strength at a given altitude. As Jupiter's

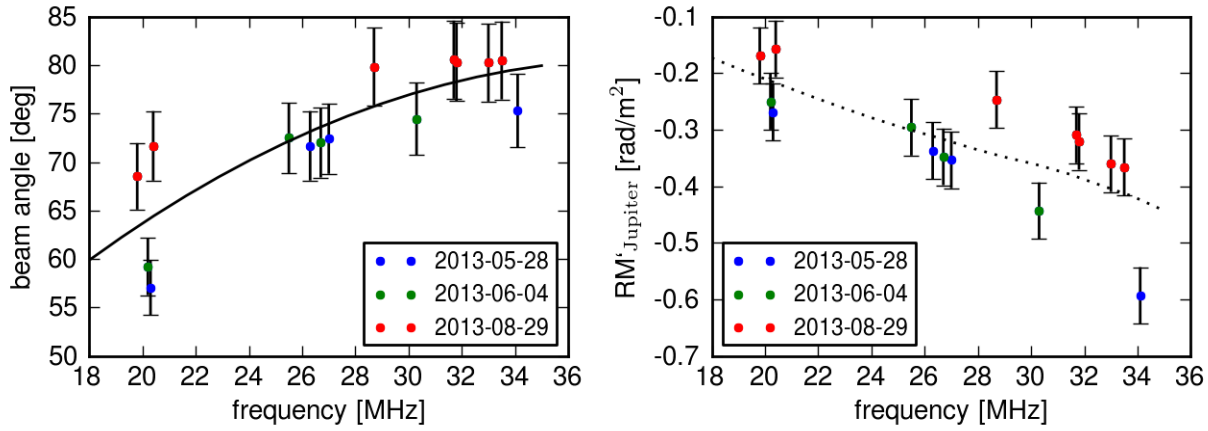

Figure 8.10: Left: Beam angle as function of frequency. Right: Measured RM values compared to theoretical predictions for the Jupiter magnetosphere.

magnetic field is complex and hard to model accurately, just a simple model is assumed:

$$B(r) = B_0 \frac{1}{r^3} \tag{8.5}$$

where B_0 is the magnetic field at r = 0 (Calvert, 1983). For the following calculations a value of 12 G at the planetary surface (r = r_j) around the southern pole is used (Connerney et al., 1998). In the same way an assumption for the electron density is made by

$$n_e(r) = n_{e_0} \frac{1}{r^2} \tag{8.6}$$

with $n_{e_0} = 200$ cm^{-3} one Jovian radii above the surface (r = 2r_j) as a typical value for the Jupiter plasma (Phillips et al., 1989). Using these relations a theoretical RM value depending on the altitude R, at which the radiation is originating, can be calculated:

$$RM = \frac{e^3}{8\pi^2 m_e^2 c^3 \epsilon_0} \int_R^{30 r_j} n_e \mathrm{B} \cos(\phi) \mathrm{d}l \,. \tag{8.7}$$

Hereby ϕ is the beam angle of the cone of the emitting radiation which also depends on the altitude of the origin point. The left hand plot of Fig. 8.10 shows the beam angle, as obtained from comparing observed and theoretical RM values, against the center frequency of the detected bursts. These calculated beam angles strongly depend on the chosen values of B_0 and n_{e_0}. Therefore the errors in the calculated beam angle are due to the uncertainties of the magnetic field strength and electron densities which are assumed to be constant for the performed calculations. To correct to some extent for the variation of the electron density the ratio of Jupiter RMs and RMs for the Earth ionosphere, as plotted earlier in Fig. 8.9, is used to generate the points in Fig. 8.10. The obtained beam angle is larger at higher frequencies,

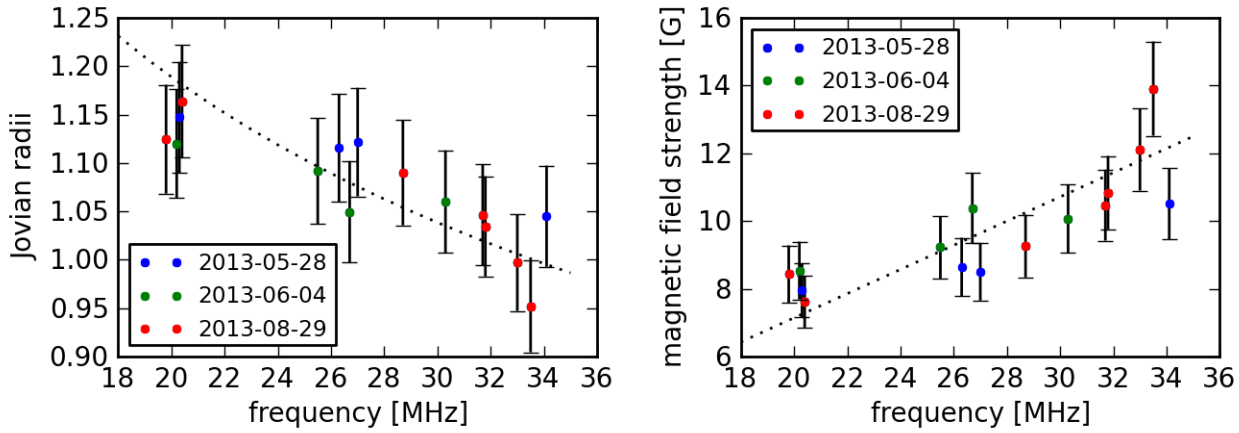

Figure 8.11: Origin of the radiation (left) and the magnetic field strength at the origin of the radiation (right) as function of frequency.

where the origin of the radiation is close to the planetary surface. There the magnetic field lines are nearly perpendicular to the planetary surface, whereas they are curved at high. As a result the beam angle of the detected emission is larger for radiation origin close to the planetary surface. In comparison the beam angle is smaller at lower frequencies, when the radiation originates at higher latitudes with a stronger curved magnetic field line. For my measurements the values of the beam angle ranging from 60° to 80° and are in good agreement with earlier measurements (e.g. Zarka, 2004).

For the right hand plot of Fig. 8.10 the obtained beam angle is applied to the electron density corrected RMs. The theoretical RM plotted as dotted line is described by the equations above. In average the theoretical model prediction is able to describe the measured Faraday rotation of the detected Jupiter bursts. Hereby the A events observed in August 2013 (red points) appear above the fitted line. The B events measured at the middle of the year (green and blue points) are below the fitted line and no difference between the both observation dates (May 28th and June 4th) are visible. Again it cannot be said, if the disparity between the A- and B-events is due to the difference in the origin of both events or due to a changing of the electron content in the magnetosphere, as the Sun was more active in May and June compared to August. For clarification more observations during a similar Sun activity would be needed. Apart from this disparity between both events, a clear trend within the A- and the B-event observations can be detected. Due to the good agreement with the prediction this proves that the observed Faraday rotation occurs within the Jupiter magnetosphere.

For a better understanding of the exact location of the origin of the radiation the left plot of Fig. 8.11 shows the altitude of the origin of the radiation measured in Jovian radii. The radius of 1 correspond to the planetary surface. The obtained position of the observed radiation, using model assumptions from above, ranges from around 1 to 1.2 Jovian radii.

This is in good agreement with Zarka (2004) who quoted that the radiation at 40 MHz is emitted just above the planetary surface, whereas radiation at 10 MHz is emitting at around 1.3 Jovian radii. The fitted line is calculated by using the cyclotron frequency (Eq. 8.4) with the magnetic field strength as introduced in Eq. 8.5. Using the same model parameters, the magnetic field strength at the origin of the radiation is plotted in the right image of Fig. 8.11, ranging from around 7 G to 14 G. Some of the emitting positions are too low, meaning below 1 Jovian radius. Corresponding to that some of the magnetic field strength are above 12 G, which was assumed as a maximum value at the planetary surface. This is due to the fact that all of the calculations strongly depend on B_0 and n_{e_0}, which are not known for sure and even more changing during the observations. Besides, the simple models as introduced above, are not reproducing the real properties of the magnetosphere. Nevertheless, even with these simple assumptions the measurements made with LOFAR can be modeled and explained and the obtained values are in good agreement with the literature.

8.5 Error discussion

Errors in the obtained RM values can be caused by different effects, which should be discussed in the following.

A first possible error for the measured RM values could be introduced during the calibration process, including errors from a problematic beam correction. As mentioned earlier the provided beam model for the LOFAR antennas is known to be not perfect. Furthermore, these errors are expected to be stronger at these low frequencies. Besides it is uncertain how the strong RFI sources, appearing in the field of view, cause errors in the calibration process of the data. Below 30 MHz the RFI situation is challenging, as strong RFI sources appear in nearly every frequency channel. The situation is even worse due to the low beam resolution of more than 10° below 30 MHz. Therefore the RFI sources coming from various direction occupy large parts of the skymaps and partly can get mixed with the Jupiter radiation.

For the performance of RM Synthesis all channels with too strong RFI were removed, as they would otherwise disturb the Faraday spectrum of the Jupiter radiation. Unfortunately, this leads to gaps in the frequency spectrum, which leads to stronger sidelobe effects in the Faraday spectrum. The same problem appears, if just a small part of the frequency spectrum is used for the performance of RM Synthesis, which was done for the analysis of the frequency dependence of the RM values. RM Synthesis was not successful on the bursts detected at frequencies below 18 MHz, due to the strong RFI environment.

After RM Synthesis a wrong correction for the Faraday correction due to the Earth ionosphere is expected to lead to the largest uncertainties in the obtained RM values. For the correction the code by Olaf Wucknitz (priv. comm.) was used to calculate a RM value for the Earth ionosphere in the direction of Jupiter, which was subtracted from the value obtained by the RM Synthesis method. The accuracy of this code was partly proven in Chapter. 7, where the predictions were compared to pulsar measurements. The good agreement of both showed that the ionosphere code gives reasonable results. Nevertheless,

even these model predictions are occupied by errors due to for example a time resolution of 2 hours, which enforced an interpolation for the inter median times. Besides, it needs a good model of the ionosphere geometry, which is expected to be more faulty at low elevations. At least an error of 0.1 rad/m^2 has to be assumed for the ionospheric corrections.

As the beam resolution of a single LOFAR station is more than 10° at the low frequencies of Jupiter bursts, it is unsure how much a possible beam depolarization influence the final results. The measured degree of linear polarization is partly lower than expected from earlier observations (Dulk et al., 1994). Also the total degree of polarization is below the expected 100%. Nevertheless Jupiter bursts are complicated events with changing polarization properties on short time scales, which are hard to model.

In case of observed S-bursts an other depolarization could be introduced due to the integration time of 1.3 sec. S-bursts events are expected to appear on time scale shorter than 1 ms and therefore an integration over several of them is performed by using 1.3 sec integration time. This problem could be solved by triggering directly on burst events and using a shorter integration time. For the observations performed for this work the timer for the observation was set manually.

8.6 Summary

Due to the strong emission of Io-related Jupiter bursts they can be observed with a single LOFAR station even on short integration times of a second or less. Although the events cannot be spatially resolved by the instrument, it is possible to study the polarization properties of the integrated flux density using all four Stokes values. Furthermore, using the raw TBB data, to get a high frequency resolution, allows to study the Faraday rotation of the bursts. The developed self-calibration code (Sect. 3.8) allows to calibrate the data, although no theoretical model for Jupiter is available. In Sect. 3.8 already Jupiter observations were used to prove the quality of the calibration code.

With the measurements, which were taken at times of high probabilities to observe Io-related events, it was possible to detect A, B and C events, which depend on the CML and Io-phase. Unfortunately, the detection of the C event was strongly occupied by RFI, which did not allow a detailed analysis of the event. In comparison a high number of good data of A and even more B events are available. Nearly all of my observed events were left-handed circular polarized, what indicates that the radiation originated from the southern hemisphere of Jupiter.

In my observations the fraction of linear polarization for the A events ranges from 22% to 44%, whereas the fraction of circular polarization ranges 53% to 80%. In the measurements by Dulk et al. (1994) the fraction of linear and circular polarization were in the range from 60% to 80%. For the fractional linear polarization of my observed B events values from 15% to 54% are obtained and fractional circular polarization values from 19% to 76%. Dulk et al. measured values from 44% to 60% for the fractional linear polarization and values from 80% to 90% for the fractional circular polarization of left handed Jupiter B events.

With the use of a high frequency resolution and the RM Synthesis method it was possible to calculate the Faraday rotation for most of the detected events. Just for four detections no RM value could be obtained, due to strong RFI and too small frequency ranges of the observed event. The summary of several RM measurements of Jupiter bursts show values reaching from -0.64 to -0.15 rad/m^2. These values are in the order of 10% to 20% of the Earth ionospheric Faraday rotation, which confirms earlier observations (e.g. Philips et al., 1989). Contrary to the positive RM values measured by Philips et al. for the B events, all of the LOFAR measurements give negative RM values. This is due to the fact that Philips was observing just right-handed circular polarization events (originated in the northern hemisphere), whereas all obtained RM values in this work are from left-handed circular polarization (originated in the southern hemisphere). This leads to a different sign in the measurements of the RM values.

In the past just few measurements of the Faraday rotation were done. Before the RM Synthesis method became available, a fitting of the polarization angles was needed, what was partly difficult due to the fast rotation of the polarization angle at these low frequencies. Nevertheless, the earlier measurements are of the same order of the values obtained for this work. Although it has to be mentioned that all RM values from recent work was obtained from B events, whereas in this work for the first time RM values for Io-A events were obtained.

On first sight the RM values for the A events seems to be slightly smaller than for the B events, although the Faraday rotation in the Earth ionosphere is weaker at the days of the A events, due to a smaller electron content in the atmosphere. By plotting the ratio of the Faraday rotation caused by Jupiter and in the Earth ionosphere, no strong separation between A and B events is visible anymore. In recent studies of Jupiter radiation the question came up, if the Sun activity has an influence on the Jupiter magnetosphere like it has on the Earth ionosphere, what could be confirmed by the measured ratio. Nevertheless, to be sure more observations of A and B events during times of same Sun activity are needed to clarify, if the observed difference is due to the Sun activity or due possible different properties of the events them self.

A distinction of the RM values with the frequency, where the observed emission is peaked, allows a detailed analysis to obtain the beam angle and origin of the radiation. Using data of the magnetic field strength and electron density in the Jupiter magnetosphere from the literature allows to compare a prediction for the Faraday rotation caused in the Jupiter environment with the observed values. The good agreement between both, even by just using a simple model for the field strength, proves that the observed Faraday rotation is caused in the Jupiter's atmosphere. Another evidence for this is given by the frequency dependence of RM values, due to the varying origin of the radiation, which would not appear for Faraday rotation caused by the Earth ionosphere or the interplanetary medium. The shown correlation of RM values and frequencies was done for the first time as part of this thesis.

Chapter 9

Measuring large-scale polarization

Finally, after it has been shown that the developed code allows to study large-scale emission in total intensity and for strong polarized sources like Jupiter bursts, large-scale Galactic polarization will be considered. For that the observations, which were already used to produced the LOFAR survey in Chapter 4, are taken. This chapter will present polarization maps, as well as an RM map for the LOFAR data. At the end of this chapter I will provide suggestions for improving the analysis.

9.1 Observations and data reduction

The polarization data were treated in the same way as the total intensity data. Each snapshot observation was calibrated individually, then the calibrated gains were used to calculate the weighted mean of all snapshot observations. Afterwards the combination of the Stokes Q and Stokes U datasets was performed in the same way as done for the total intensity maps (explained in Sect. 4.2). Therefore the gains, as obtained during the calibration process, were used to weight the individual snapshot images before they combination. To generate an all-sky map all data from a 24-hour run were combined first. Later the individual 24-hour runs were combined to increase the signal to noise ratio. In this case a scaling between the observation runs is performed as discussed earlier for the continuum survey.

For the maps presented in this chapter only the observations from March 11th and September 16th 2013 were used. All other observations were not performed over 24 hours due to various technical problems, or were badly affected by RFI. For the observation made on January 14th no pulsar measurements were available, because strong RFI made pulsar observations with the LBAs in Effelsberg impossible. 24-hour runs are preferred to averaged out some of the instrumental polarization and ionospheric effects during this period.

9.2 Linear polarization maps

For the map of the linear polarized intensity the single Stokes Q and U snapshot observations were combined. Maps of the circular polarization Stokes V were not produced, as they are expected to contain no astrophysical signal. Besides, it would had taken away to much computing time to produce these maps. The polarization bias is negligible due to the high values of the Stokes Q and U emission. A linear polarized intensity map at 40 MHz using a bandwidth of 0.5 MHz is shown in Fig. 9.1. For this map the 24 hour runs from March 11th and September 16th in 2013 were used. All the other datasets were not taken due to strong RFI or too less observation runs. From the snapshot images only elevations above 30° were used, since closer to the horizon instrumental polarization levels are too high to be usable. In the polarization map strong emission appears at low declinations and around the North Celestial Pole, as well as in regions with bright emission in total intensity (Galactic center region, Cas A, Cyg A, NPS). Weaker polarized emission is seen at declinations between 20° and 40° and in regions with weak emission in total intensities (halo, minimum zone). All of this indicates that the measured polarized emission is mainly due to instrumental effects and therefore not real. Already in the single snapshot images of Stokes Q and Stokes U most of the instrumental polarization is seen at low elevations and around the North Celestial Pole.

An example for an uncorrected and beam-corrected Stokes U snapshot at 40 MHz is shown in Fig. 9.3. In the uncorrected map the central region of the Milky Way (at the bottom of the map) and RFI in the north (top of the map) is clearly visible. After the beam model was applied to the data these structures disappeared and the point source Cas A becomes visible. Besides, strong intensities with a symmetric structure are seen close to the horizon. They are a result from the beam model, as introduced and discussed in Sect. 4.8. The center of this symmetric structures is the North Celestial Pole (NCP).

The uncorrected and beam-corrected Stokes Q snapshot image at 40 MHz show are shown in Fig. 9.4. Most of the instrumental polarization has disappeared after the correction. In the uncorrected map a symmetric structure with positive values from the north-east to the south-west and negative values for the perpendicular direction can be seen. Cas A shows a positive Stokes Q flux before the beam model is applied. After applying the beam correction these structures are completely gone. What is left is a strong positive flux at the bottom

Table 9.1: Galactic loops detected in polarization.

Loop	l [deg]	b [deg]	r [deg]	reference
I	332.6	20.7	54.3	Brown et al. (1960)
II	100.0	-32.5	45.5	Large et al. (1962)
III	118.8	13.2	31.6	Quigley & Haslam (1965)
IIIs	106.0	-22.0	25.0	Vidal et al. (2015)
VIIa	332.6	16.0	46.5	Wolleben (2007)
X	30.0	35.0	67.0	Vidal et al. (2015)

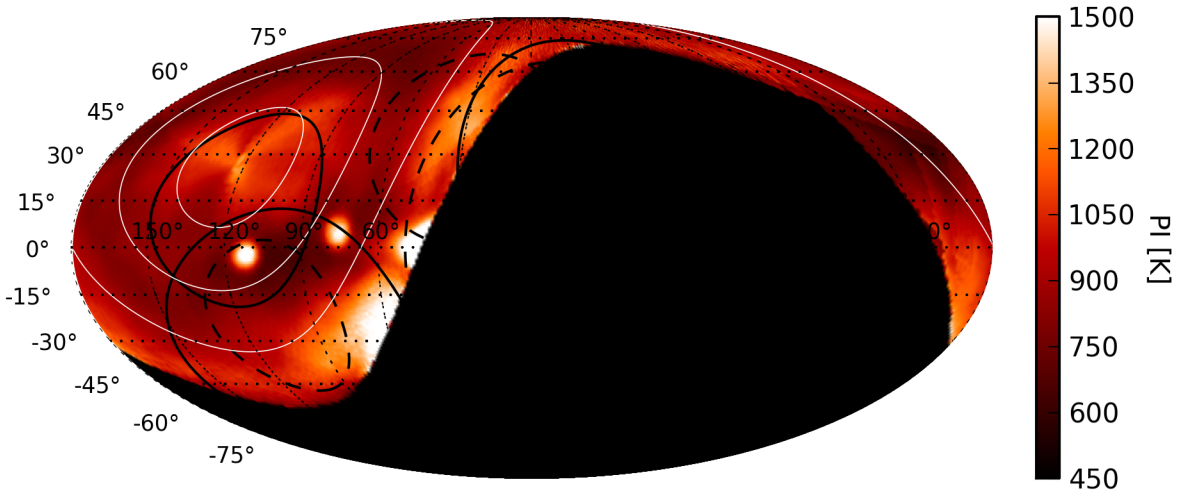

Figure 9.1: Polarized intensity at 40 MHz. Black lines are the defined loops (Table 9.1). The white lines indicate the declinations at 20°, 40° and 60°.

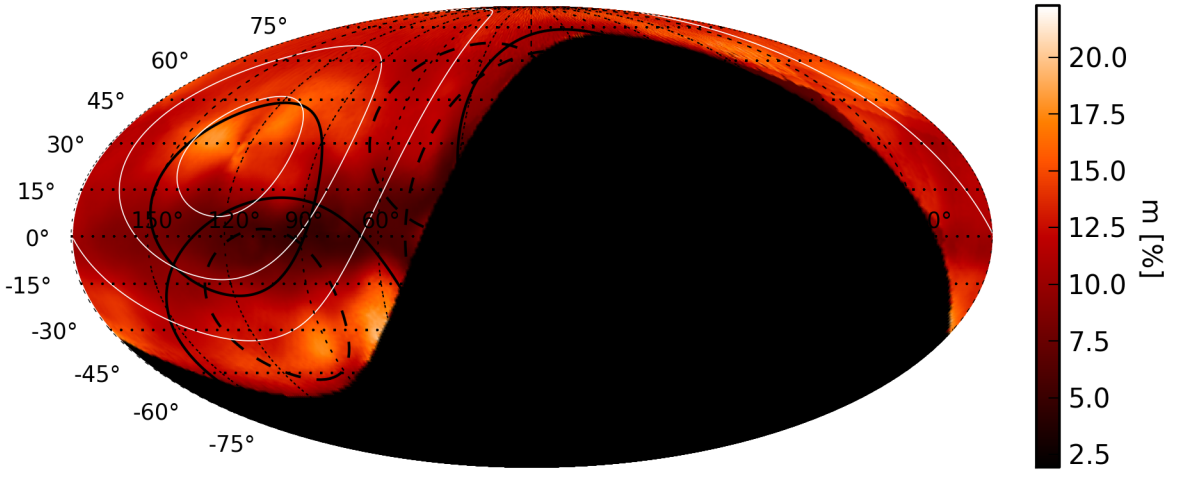

Figure 9.2: Fractional polarization at 40 MHz. Black lines are the defined loops (Table 9.1). The white lines indicate the declinations at 20°, 40° and 60°.

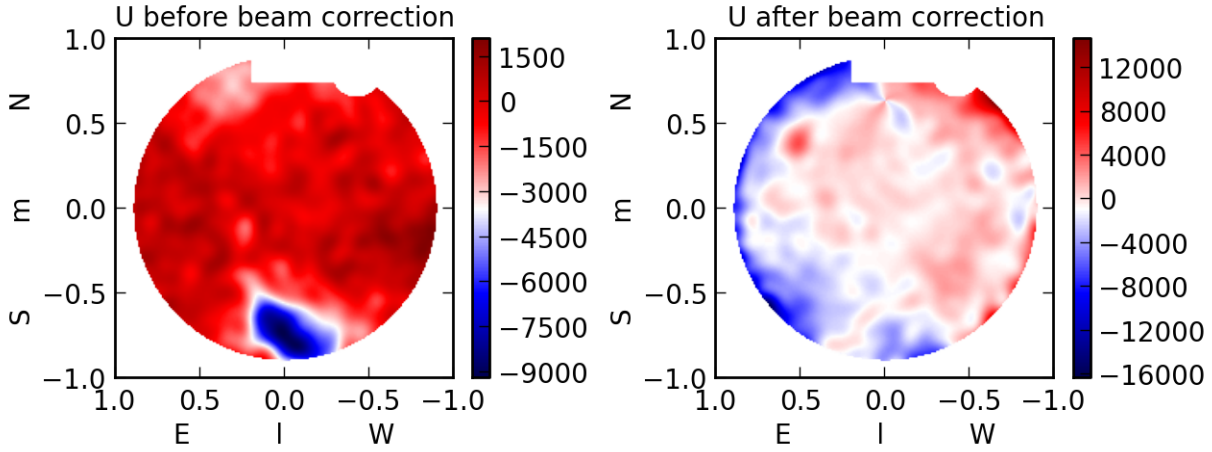

Figure 9.3: Stokes U snapshot image before and after the beam correction. No absolute amplitude calibration was performed.

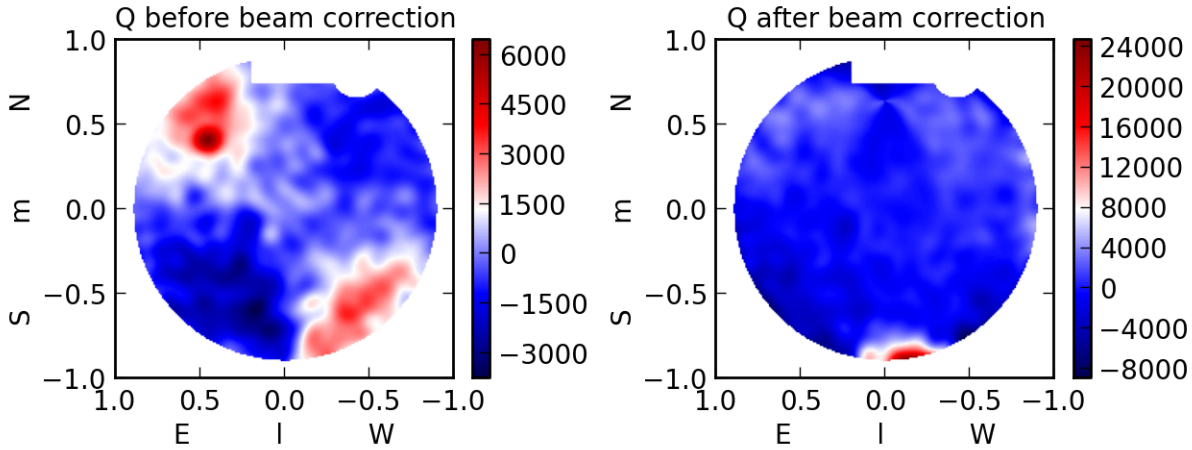

Figure 9.4: Stokes U snapshot image before and after the beam correction. No absolute amplitude calibration was performed.

of the map and the symmetric structure at the NCP due to the parallactic angle correction (compare to Fig. 3.16).

The fractional linear polarization at 40 MHz is shown in Fig. 9.2. The lowest fractional polarization of around 5% is found along the Galactic plane and within the NPS, were the total intensities are at their highest. The highest values of up to 20% are found near the NCP, in some parts of the southern halo, and in the minimum temperature zone. On average the fractional polarization is lowest in regions with bright Stokes I emission and highest in regions with faint Stokes I emission. Again this implies that the measured polarization

is mainly instrumental. Nevertheless, it is expected that depolarization at these low frequencies is strongest along the Galactic plane. This was already discussed in Sect. 1.3 where strong depolarization along the Galactic plane was visible in the 1400 MHz polarization map. Faraday depolarization at low frequencies and a low angular resolution is also detected in external galaxies like M31 (Gießübel, 2013) and M51 (Mulcahy et al., 2014). Unfortunately, at the current stage it is impossible to judge how much of the detected polarization is real and how much is due to instrumental polarization.

As the HBA maps already show a low signal to noise ratio in total intensity there will not be used for the polarization study.

9.3 RM Synthesis stacking

Instead of using the combined Stokes Q and Stokes U maps for RM Synthesis, a stacking of the individual RM maps was performed. This means that the RM Synthesis was performed using the single Stokes Q and U snapshots. After reducing the instrumental polarization, which is shows up at a Faraday depth of 0 rad/m^2, the ionosphere correction was applied and all observations were combined. Figure 9.5 shows two RMTF (Eq. (1.45)) functions containing a strong peak around 0 rad/m^2, including sidelobes at the surrounding RMs. In this examples RM Synthesis was performed using the frequency range from 30 MHz to 45 MHz with a 5 kHz frequency resolution. For the left handed plot the RM spectrum was calculated with a 1 rad/m^2 resolution, whereas in the right handed plot a resolution of 0.1 rad/m^2 was used. As the maximum resolution of the RM spectrum due to the given frequency range is in the order of 0.1 rad/m^2, smaller differences between RM values cannot be measured. For the following studies RM Synthesis was performed on the single snapshot observations from -10 rad/m^2 to 10 rad/m^2 with a 0.1 rad/m^2 resolution is shown in the right hand plot of Fig. 9.5. Different tests on the data have shown that this way of stacking the data gives better results than performing RM Synthesis on the combined Stokes Q and U maps.

Before running RM Synthesis strong RFI peaks from the frequency spectrum were removed, as these would otherwise dominate the entire RM spectrum. An example of this is shown in Fig. 9.6 where the amplitudes of the RM spectrum for an RFI source (left hand image) and a random point on the sky (right hand image) obtained from the same snapshot observation are plotted. Again RM Synthesis was performed from 30 MHz to 45 MHz with a frequency resolution of 5 kHz. The resolution in the RM spectrum is 0.1 rad/m^2. The polarized intensity at 0 rad/m^2 was set to zero. For the RFI source the measured intensities are by a factor 10 higher compared to the non RFI source and follows some periodic modulation, which not appears for the random sight line. This illustrates how import the removal of RFI is and how there can disturb the measurements.

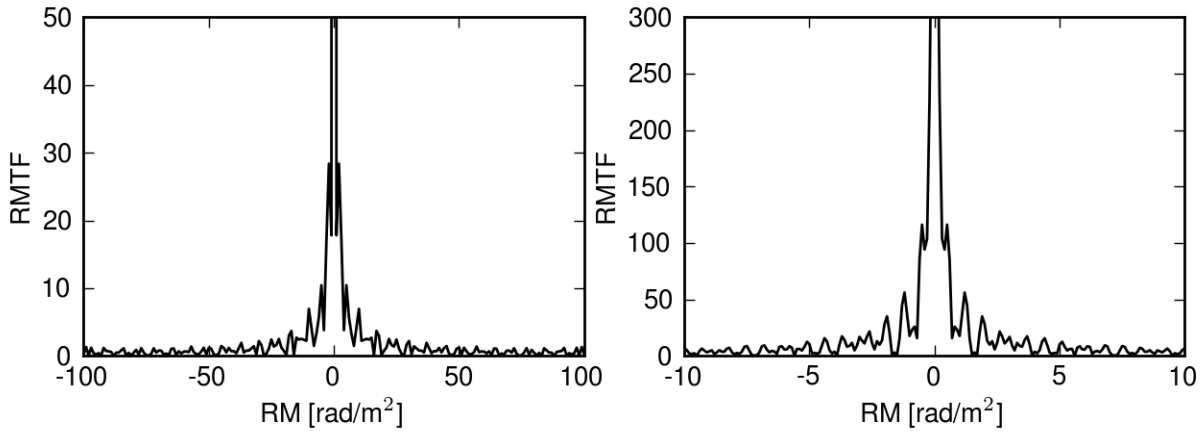

Figure 9.5: RMTFs for the frequency range from 30 MHz to 45 MHz. The peak at 0 rad/m^2 goes up to a value of 2500. Left: RMTF for Faraday depth from -100 to 100 rad/m^2 with a resolution of 1 rad/m^2. Right: RMTF for Faraday depth from -10 to 10 rad/m^2 with a resolution of 0.1 rad/m^2.

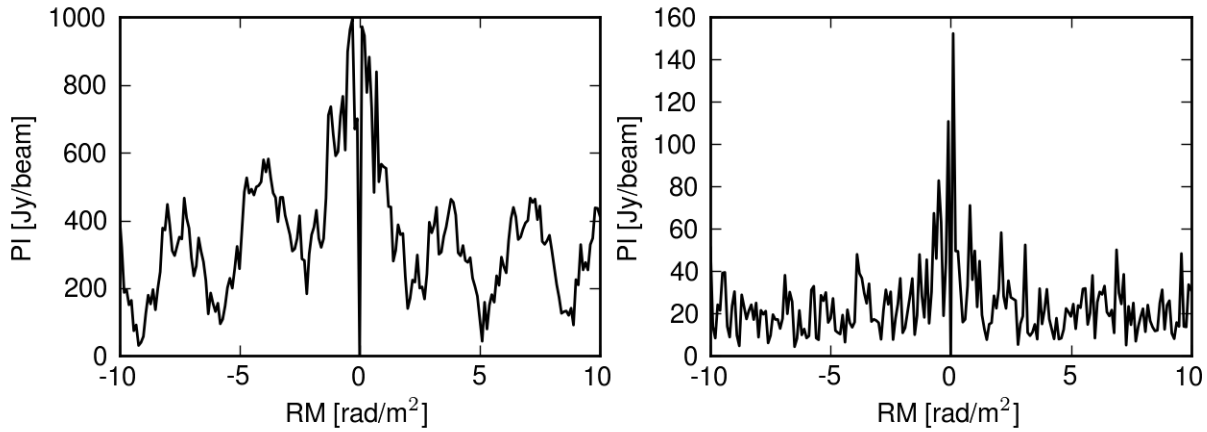

Figure 9.6: RM spectrum for a RFI source (left) and a random point in the sky (right) obtained from the same snapshot observation. The resolution is 0.1 rad/m^2.

9.4 RM map

To construct an RM map from the LOFAR data RM Synthesis was performed from -10 rad/m^2 to 10 rad/m^2 with a resolution of 0.1 rad/m^2 by using frequency channels from 30 to 45 MHz with a frequency resolution of 5 kHz. The relative small range from -10 rad/m^2 to 10 rad/m^2 was chosen as LOFAR is more sensitive to the low RM values. Furthermore, recent observations at 189 MHz (Bernardi et al., 2013) have shown that at this frequency most of the polarized emission occurs at $|\mathrm{RM}| < 10$ rad/m^2. Choosing a small RM range significantly also reduces the computing time, especially since individual snapshot images were used.

For the following results the observations from March 11th and September 16th 2013 were used. These were the only full 24-hour runs with not too much RFI present. As mentioned, the RM Synthesis was performed on the single snapshot images, before they were combined to a final map. This was done for both 24-hour runs independently, which allows a comparison between both of them afterwards.

The top image of Fig. 9.7 shows the mean RM map of the two datasets. Even though strong fluctuations between positive and negative values are visible, in some regions one sign is dominates. As it is hard to judge the accuracy of the data, in the following a comparison between both datasets is done. Similar RM values found in both datasets independently are more reliable. For around 50% of the data points RM values have the same sign in both datasets. Going one step further, the map in the middle of Fig. 9.7 only shows mean RM values for directions that differ by less than 2 rad/m^2 between the two 24-hour runs:

$$|\mathrm{RM}_i(20130311) - \mathrm{RM}_i(20130916)| < 2\,\mathrm{rad/m^2}\,. \tag{9.1}$$

This value was chosen to allow some error in both maps due to possible errors in the ionospheric correction and the fact that only weak emission is measured. A positive detection was obtained for around 20% of the data points. Decreasing the value to 1 rad/m^2 leads to 10% of positive detections (bottom map of Fig. 9.7).

As seen in the images, the RM values with a positive detection are spread randomly over the entire sky, without being concentrated in one direction. Nevertheless, it seems like some kind of structures can be found, where more positive or more negative RM values are detected. For comparison, the catalog data which were used to produce the map by Oppermann et al. (2012; see Fig. 1.10 in Sect. 1.3) are taken. As most of the measurements in the catalog data are much above the value of 10 rad/m^2, just a comparison on the sign of the RM value is performed. For this, I take my data (middle panel in Fig. 9.7) and compare them with the catalog data in the same direction, if available. If both RM values have the same sign the RM value from the LOFAR measurement was plotted. Using this method, 50% of positive detections were made. The result can be seen in the top panel of Fig. 9.8. The middle image of Fig. 9.8 shows all the detections where LOFAR measurements and catalog values have a different sign. As a result, a nearly equal distribution of data points is seen in both maps, with just a few small exceptions. For example, in the part of the Fan Region

(centered on l = 150° and b = 8°) mainly slightly negative RM values are detected, whereby the sign is in agreement with the data from Oppermann et al. in most directions. Detailed measurements for the Fan Region at 150 MHz by Iacobelli et al. (2012) indicate RM values from -13 to -1 rad/m^2 for most directions. Only a few positive values up to 5 rad/m^2 are found. At small positive galactic latitudes a high number of positive RM values are detected in the LOFAR data, which is in agreement with the catalog data. Just a small number of data points show a different sign for the RM values in the catalog data. The same can be seen for a small region with positive RM values at b = 160° and l = 20° and for a region with negative RM values at b = 140° and l = 40°. A strong discrepancy in the sign in RM between the LOFAR data and catalog data is found in the part with low negative galactic latitudes. With the LOFAR data mainly positive RM values are measured, whereas in the catalog negative values dominate.

Anyhow, a direction comparison between the LOFAR measurements and the presented catalog by Oppermann et al. (2012) is difficult. While the catalog RMs are mainly obtained from observations of extragalactic sources, the LOFAR measurements at low frequencies are detection radiation from nearby large-scale structures. By calculating the RM values from extragalactic sources the Faraday rotation due to a long path length through the Milky Way is measured. In contrast to this, for the nearby structures as observed by LOFAR only Faraday rotation within the nearby emission is measured. As a consequence the catalog values are up to a several hundred rad/m^2 whereas for the local foreground emission, due to a weak Faraday rotation, small RM values of several rad/m^2 are expected. In addition, in this way different signs for the obtained RM values can be explained. Nevertheless, in case of a thin foreground emission and weak magnetic field it is possible that both measurements lead to the same sign for the RM values. As mentioned above the largest structure with the same sign is found around the Fan region. Toward this observing direction the uniform magnetic field component which follows with spiral arms of our Galaxy is almost perpendicular to the line of sight. Therefore the measured RM values are expected to be nearly unaffected by the interstellar magnetic field component. Furthermore, former measurements by Wilkinson & Smith (1974) and Uyaniker et al. (2003) indicate that the Fan region is located at a distance less than 500 pc away from us with a mean parallel magnetic field of 1.2 μG in this direction (Iacobelli et al., 2012).

Even though it appears that results from previous authors are replicated, one needs to be caution when interpreting these results. Most of the peaks in the RM spectrum are detected below the 2σ level, which is too small to be a reliable detection. Furthermore, one has to be aware of the fact that only 10% of positive detections between both LOFAR datasets were made, by allowing a difference of 1 rad/m^2.

In the bottom panel of Fig. 9.8 the peak polarized intensity in the RM spectrum along each line of sight is plotted. The colors do not represent brightness temperatures, as no amplitude calibration was performed on the data. Nevertheless, by concentrating on the relative levels, strong emission is seen at low declinations and in regions with bright emission in total intensity (Cas A, Cyg A, Galactic center region, NPS), which also can be seen in Fig. 9.1. Polarized emission is detected along the Galactic plane, were also the strongest

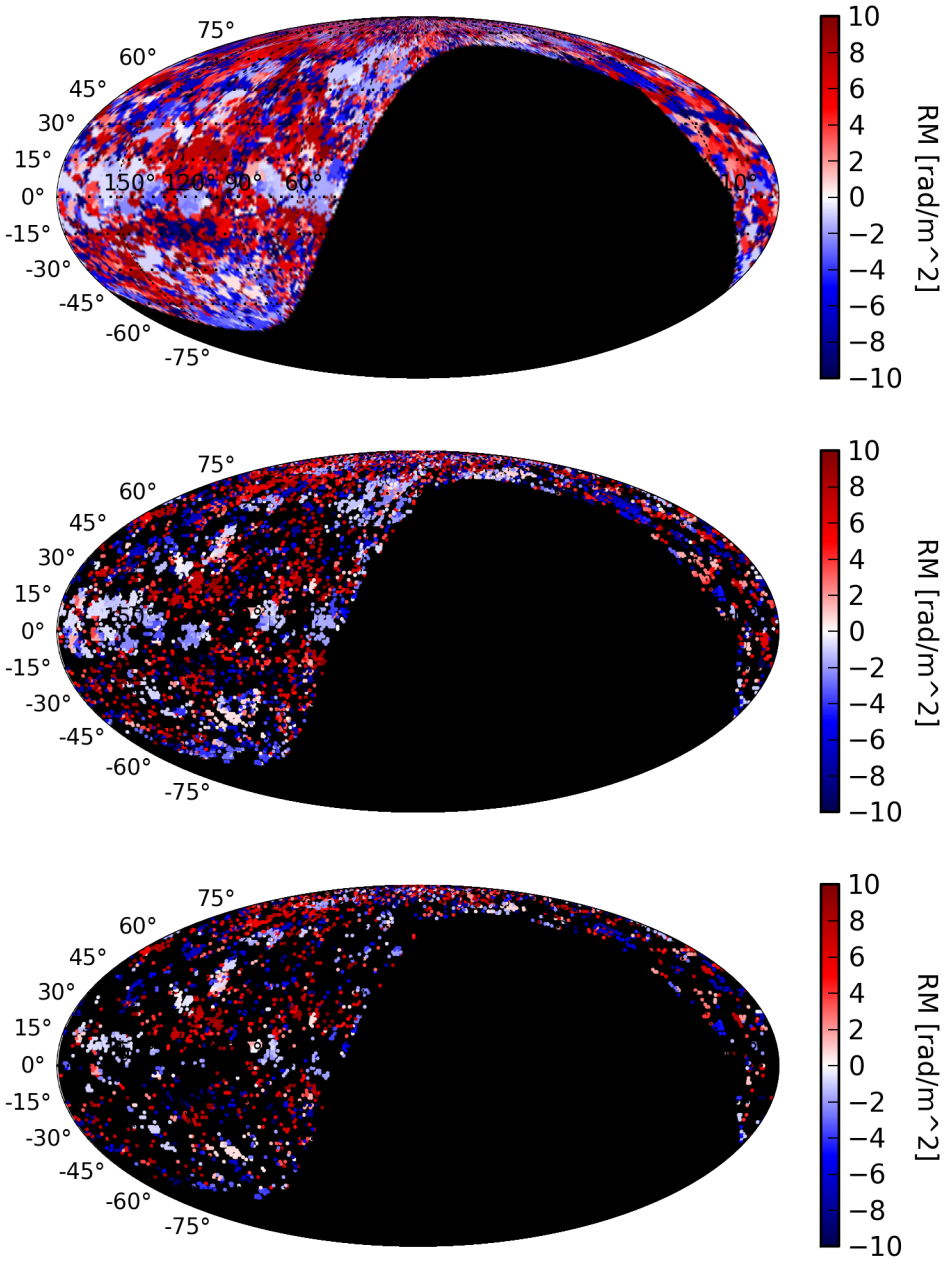

Figure 9.7: Top: Mean RM map from the measurements made at March 11 and September 16th. Middle: Mean RM values for peaks which were in both datasets not separated by more than 2 rad/m^2. Bottom: Mean RM values for peaks which were in both datasets not separated by more than 1 rad/m^2.

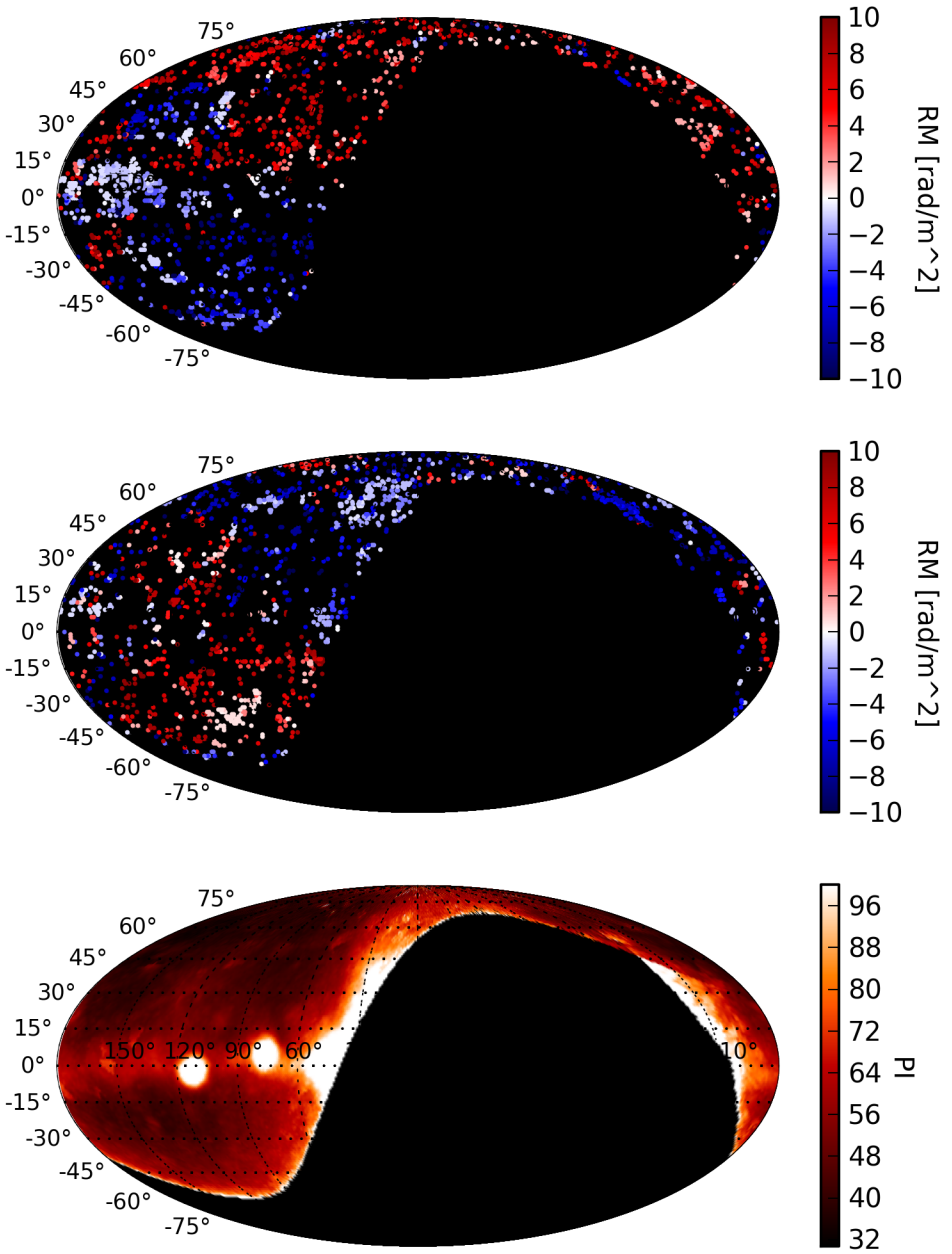

Figure 9.8: Top: Mean RM values for peaks which were in both datasets not separated by more than 2 rad/m^2 and have the same sign as the catalog data. Middle: Mean RM values for peaks which were in both datasets not separated by more than 2 rad/m^2 and have a different sign as the catalog data. Bottom: Polarized intensity measured by the intensity of the maximum RM peak.

emission in total intensity is present. Bright polarized emission is also seen toward the Fan Region. At this point this feature could be genuine, or it could be due to leakage from Stokes I.

9.5 Summary and suggestions for further improvements

Looking at the results in this chapter, the data are strongly affected by instrumental effects. Especially the correct removal of the instrumental leakage is a huge problem, which could not be solved in the end. Tests were performed to deal with the problems as good as possible, but no satisfying result was found. The presented maps are the best results that could be achieved at the current state. To improve the results in the future, some things should be considered.

As mentioned in previous chapters, the biggest problems are introduced by the current version of the antenna beam model. Possible leftovers after the beam correction cannot be corrected afterwards and produce problems in the data reduction and subsequent scientific analysis. for any future polarization study with a single station a better antenna beam model should be used.

Since the large beam size (10° at 30 MHz) can lead beam depolarization (compare Sect.1.2.2), a better resolution could be useful and partly necessary for the polarization detection. One option for doing polarization studies with a better beam resolution in the LBA, is be using the LOFAR core. As six small LOFAR stations are arranged within about 300 m, the resolution can be increased by a factor of five without loosing too much of the large-scale structures. To avoid the problem of missing zero-spacings the best way is to use the inner and outer antennas from the stations. At the moment observations with the Core stations can just be performed with either the inner OR the outer antennas of one station. All antennas can be used if only one dipole of each antenna is used. Since this makes it impossible to do radio polarimetry this is not an option. However an existing version of the TBB correlator and the calibration code (Chapter 3) is able to deal with all stations from the LOFAR Core. Of course larger data volume will require a longer processing time. Another option would be to use HBA data, which have an angular resolution on the order of 1° - 2°. Wilkinson (1973) was already able to detect polarized emission from the Fan Region at 240 MHz with an angular resolution of 1.5°.

In addition a LOFAR station in a low RFI environment would greatly benefit the analysis. Every RFI channel that has to be removed in the frequency spectrum increases the sidelobes in the RM spectrum. Besides, RFI is in most cases strongly polarized, which leads to image artefacts.

In the future more observations are needed to improve the signal to noise ratio of the polarization data. For a follow-up project observations could be spread over several days, instead of over just 24 hours. Within a few days time the system and Solar activity is expected to stay approximately constant. Comparing two three-day observing runs would help to identify problems with the telescope and ultimately produce better results.

However studying weak polarization with a single LOFAR station at frequencies below 200 MHz will always remain a challenge.

Chapter 10

Summary

For the first time TBB data from a LOFAR single station were used to produce all-sky maps. Combining these observation enabled us to generate a northern sky survey.

In order to use TBB data of a single LOFAR station various methods in data handling, reduction, calibration, and analysis had to be developed. The generated software tools allows to perform scientific studies on:

- the spectral behavior of large-scale emission in total intensity (Chapter 4 and 5)
- large-scale polarization at low frequencies (Chapter 9)
- polarization properties of Jupiter bursts (Chapter 8).

Instrumental properties of a single station can be estimated by

- obtaining an antenna beam model (Sect. 4.8)
- producing calibration tables of the individual dipole antennas of each station field (Sect. 3.5).

The scientific results of using TBB datasets of the Effelsberg LOFAR station can be summarized as (specific details of these results can be found in the summaries of the individual chapters):

- The first LOFAR large-scale survey of the brightness temperature of the Northern sky was produced using LBA and HBA observations. The instantaneous imaging allows for the first time a direct method of producing a Northern sky survey without artifacts due to the slewing method that has been used in earlier surveys.
- Spectral index maps, using the LOFAR observations at 30 and 45 MHz and previous all sky surveys at higher frequencies, were produced. A flattening of the spectrum toward low frequencies have been detected.

- The spectral properties of large scale structures have been theoretical investigated by comparing the spectral index maps and spectral shape of the measurements with various properties of the interstellar medium. In particular the spectral turn-over and breaks frequencies have be estimated for thus purpose.

- For the first time large-scale polarization properties have been studied at frequencies below 100 MHz. Strong depolarization effects have been detected. The first Northern sky RM map has been produced showing large-scale structures. The quality of the RM map need further improvement however the RM values obtained in the Fan region obtained are in good agreement with other measurements.

- It has been proofed that a single LOFAR station can be used to study polarization properties of Jupiter bursts at low frequencies. High-accuracy RM measurements show for the first time a frequency dependency of the RM values of Jupiter bursts. This new effect has been explain by introducing a model that is based on the current knowledge of radiation production at the surface of Jupiter. Hereby higher RM values are produced at higher frequencies as the corresponding radiation originate closer to the planetary surface.

LOFAR single station TBB datasets provide a unique way to investigate the Universe and has the potential to make a big impact in studying the polarized sky.
In the future the quality of the maps can be improved by

- Using the LOFAR core to archive a higher angular beam resolution. This would reduce the effect of beam depolarization at low frequencies.

- Using LOFAR station in a better RFI environment. With the new network set-up for the German LOFAR stations, the observing system in Effelsberg can be used to store the data of all the other German LOFAR stations.

- Performing more observations to increase the signal to noise ratio. This is especially needed for the HBA data and the polarization survey at these frequencies.

Future scientific applications of the single station observations can be:

- Clarify open questions of the polarization properties of the Jupiter bursts by performing observations on the different events during a time of a stable ionosphere.

- Search for fast transient sources in all-sky observations using the source finding algorithm as part of the self-calibration method.

- Correlate the obtained spectral and polarization properties of the LOFAR survey with measurements at other frequency requiems (e.g infra-red, X-ray).

- Cross-correlate the cosmic background images with the total intensity and polarized LOFAR sky.

Appendix - Developed software

CorrelatorTBB.py
Input: h5 files
Options: startblock, integration time, frequency range, frequency resolution
Output: Ascii File of visibilities (including: observation date, time, station, frequency range, number of channels)
Correlates raw voltages from a single station (stored in h5 files) to create visibilities.

LOSSCI.py (LOfar Single Station Calibration and Imaging)
Input: ascii files from CorrelatorTBB.py or acm files from the station correlator
Options: calibration strategy (non, self-cal, phase, amplitude-phase), frequency channel(s), frequency integration, imaging
Output: Ascii file with calibrated visibilities, gain files, images (for the Stokes parameters; also in Galactic coordinates)
Includes: data inspection and flagging, calibration, gain calculation, imaging
Calibrates the visibilities by the choice of using self-calibration or not. It is also possible to plot images of a single frequency channel, instead of calibrating the entire dataset for all frequencies (or a specified range). In this way also non-calibrated images can be watched. A transformation to Galactic coordinates is included.

fringefitting.py
Input: gain files
Options: frequency range, reference RCU
Output: Delay file
Uses the gain files from LOSSCI.py to calculate the delays for all RCUs compared to the chosen reference RCU. It can be chosen, if the calculations of the delays is done by a FFT or a least-square fit. The obtained delays can be used to produce station calibration files or for the phase calibration of the data (can be included in the LOSSCI.py code).

make_skymaps.py
Input: (calibrated) visibility files
Options: dipole (XX or YY), Stokes values
Output: Fits file with skymaps
Creates images from the visibilities and store them in fits files.

beam_correction.py
Input: Fits files of the skymaps
Output: Fits files of beam corrected skymaps
Applies a beam model to the skymaps.

dopple_sources.py
Input: Fits files of the skymaps
Output: Fits files of the skymaps
Blank areas in the HBA maps, where strong sources (Cas A, Cyg A, Sun, RFI) appear a second time in the map.

flag_skymaps.py
Input: Fits files of the skymaps
Options: range of frequency integration
Output: Fits file of flagged skymaps
Manual flagging of RFI sources in the skymaps, by using integrated images of a given frequency range.

flag_skymaps_auto.py
Input: Fits files of the skymaps
Options: range of frequency integration
Output: Fits file of flagged skymaps, frequency integrated skymap images
Automated flagging of the RFI region in the skymaps. Besides, it generates images of frequency integrated skymaps, which can be used to manually check the quality of the data and to produce control files.

flag_data.py
Input: Fits files of the skymaps, text control file
Output: Fits files with flagged skymaps
Takes a text file with information about the quality of all observations, to flag various parts of the spectrum.

combi_galac.py
Input: Fits files of the skymaps, gain files
Output: Fits files of the combined galactic map
Combines all skymaps from a observation to create a combined map in Galactic coordinates. Uses the gain file from LOSSCI.py to scale the individual observations.

combi_all.py
Input: Fits files of combined datasets
Options: Smooting, absolute amplitude calibration, spectral index maps
Output: Fits files of combined data

Combines various galactic maps, including a scaling between different observation runs. There is the option of smoothing all frequency maps to a common resolution, before performing the absolute amplitude calibration. Available surveys can be used to produce spectral index maps, including a ZLC with TT-plots.

get_source_Intens.py
Input: Fits files of the skymaps
Options: source
Output: Files containing intensities
Gets from a skymap the intensities for one source (e.g. Cas A, Cyg A, Sun, Jupiter) for all frequencies.

calc_beam.py
Input: Intensity files
Output: Beam model
Calculates a beam model from intensity files of various sources over a time range with the help of interpolation.

Acronyms

ADC	Analog to Digital Converter
AIPS	Astronomical Imaging Processing System
ASTRON	Netherlands Institute for Radio Astronomy
Cas A	Cassiopeia A
Cen A	Centaurus A
CMB	Cosmic Microwave Background
CML	Central Meridian Longitude
CS	Core Station
Cyg A	Cygnus A
DM	Dispersion Measure
DP	Depolarization
DRAO	Dominion Radio Astrophysical Observatory
FF	Free-Free (absorption)
FFT	Fast Fourier Transformation
For A	Fornax A
FWHM	Full Width at Half Maximum
GLOW	German Long Wavelength Consortium
GPS	Global Position System
Her A	Hercules A
HBA	High Band Antenna
IC	Inverse Compton
ISM	Interstellar Medium
JP	Jaffe-Perola
KP	Kardashev-Pacholczyk
LBA	Low Band Antenna
LOFAR	Low Frequency Array
MSSS	Multifrequency Snapshot Sky Survey
NCP	North Celestial Pole
NPS	North Polar Spur
NVSS	NRAO VLA Sky Survey
RCU	ReCeiver Unit
RFI	Radio Frequency Interference

RM	Rotation Measure
RMTF	Rotation Measure Transfer Function
RS	Remote Station
RSP	Remote Station Processing
SI	Spectral Index
SN	Supernova
Tau A	Taurus A
TBB	Transient Buffer Boards
TEC	Total Electron Content
TECU	TEC Unit
Vir A	Virgo A
WMAP	Wilkinson Microwave Anisotropy Probe
ZLC	Zero-level correction

List of Figures

List of Tables

Acknowledgements

First of all I want to thank my supervisor Prof. Dr. Michael Kramer for the opportunity to write this thesis. Furthermore I would like to thank Prof. Dr. Uli Klein, Dr. James Anderson, Dr. Hans Rainer Klöckner and Dr. Wolfgang Reich for helping and supporting me through my way of the thesis. A special thank goes to James for helping me with all the technical problems during the first years of my PhD and to Hans, who took over to take care of me and my work during the last part of my thesis. I also want to thank Prof. Dr. Pavel Kroupa for being available as my second referee.

My special gratitude goes to Dr. Andreas Horneffer for his help, like setting up my observations and for all the discussions about upcoming technical problems. Furthermore my gratitude goes to Dr. Olaf Wucknitz for discussions and providing me the ionosphere code, and to Dr. Tobia Carozzi for providing me the code for the beam model. I want to thank Dr. George Heald for discussions about polarization and the RM Synthesis. I want to thank Dr. Masaya Kuniyoshi, Dr. Joris Verbiest and Dr. Aris Noutsos for the help concerning the pulsar data reduction.

A big thank you also goes to my (ex-)colleagues and (ex-)room mate Dr. René Gießübel, Dr. David Mulcahy and Philip Schmidt for the great time we had together and all the fruitful discussions about our work. Other colleagues of the MPIfR, like Dr. Aritra Basu, Dr. Marita Krause, Ute Teuber, Dr. Dominik Schnitzeler, Maya Kierdorf, Dr. Björn Adebahr, Dr. Elly Berkhuijsen and Dr. Patricia Reich, contributed to this thesis as well by solving scientific problems, by having helpful discussions and by motivating me. A special thanks goes to Dr. Rainer Beck for discussions, corrections and his friendly support especially at the end of my thesis. Besides, I want to thank people from the LOFAR and the MKSP group, as well as the DFG 1254 group and they organization of workshops and female trainings, which I was allowed to attend. Furthermore I want to thank our secretaries Gabi Breuer, Kira Kühn and Elisabeth Kramer.

Many thanks go to Nadya for all her help, her support and for being a true friend even in hard times. And of course I have to thank you for all the fun we had together and for bringing light into dark moments (and for sharing dark moments with me ;-)).

Last but not least, my deepest gratitude goes to my family and friends, who supported me during the time of my thesis and who were there, whenever I needed them. And a final thanks goes to the voice in my head, telling me not give up and keep on going.

Bibliography

B.H. Andrew, The spectrum of low radio frequency background radiation, 1965, MNRAS, 132, 79

T.G. Arshakian, R. Beck, Optimum frequency band for radio polarization observations, 2011, MNRAS, 418, 2336

J.W.M. Baars et al., The Absolute Spectrum of Cas A, 1977, A&A, 61, 99

E.A. Basu et al., Synchrotron spectral index and interstellar medium densities of star-forming galaxies, 2015, MNRAS, 449, 3879

E.M. Berkhuijsen, Are the galactic loops supernova remnants?, 1971, A&A, 14, 252

E.M. Berkhuijsen et al., A Survey of the Continuum Radiation at 820 MHz between Declinations -7° and +85°, 1971, A&A, 14, 359

K. Beuermann et al., Radio structure of the Galaxy - Thick disk and thin disk at 408 MHz, 1985, A&A, 153, 17

G. Bernardi et al., A 189 MHz, 2400 deg^2 Polarization Survey with the Murchison Widefield Array 32-element Prototype, 2013, ApJ, 771, 105

J.H. Blythe, Results of a survey of galactic radiation at 38 Mc/s, 1957, MNRAS, 117, 625

M.A. Brentjens et al., 2005, Faraday rotation measure synthesis, A&A, 441, 1217

A.H. Bridle, The spectrum of the radio background between 13 and 404 MHz, 1966, MNRAS, 136, 219

H.R. Brown et al., A curious feature of the radio sky, 1960, Obs, 80, 191

B.J. Burn, On the depolarization of discrete radio sources by Faraday dispersion, 1966, MNRAS, 133, 67

J.L. Caswell, A map of the northern sky at 10 MHz, 1976, MNRAS, 177, 601

W. Calvert, The source location of certain Jovian decametric radio emissions, 1983, JGR, 88, 6165

J.N. Chengalur et al., Low Frequency Radio Astronomy, 2007

J.J. Condon et al., The NRAO VLA Sky Survey, 1998, AJ, 115, 1693

J.E.P Connerney et al., New models of Jupiter's magnetic field constrained by the Io flux tube footprint, 1998, JGR, 103, 11929

J.W. Cronin, Cosmic Rays at the Energy Frontier, 1997, SciAm, 276, 44

T.M. Dame et al.,The Milky Way in Molecular Clouds: A New Complete CO Survey, 2001, ApJ, 547, 792

J.M. Dickey, F.J. Lockman, H I in the Galaxy, 1990, A&A, 28, 215

G.A. Dulk et al., The complete polarization state of Io-related radio storms from Jupiter: a statistical study, 1994, A&A, 286, 683

S. Faint, W. Read, A Comparison of FFT and Polyphase Channelizers, 2003

J. Findlay et al., An Absolute Flux-Density Measurement of Cassiopeia a at 1440 MHz , 1965, ApJ, 141, 873

R. Gießübel et al., Polarized synchrotron radiation from the Andromeda galaxy M 31 and background sources at 350 MHz, 2013, A&A, 559, 27

M.A. Gordon et al., High Time-Resolution Studies of Jupiter's Radio Bursts, 1967, ApJ, 148, 511

J.F.R. Gower et al., A survey of radio sources in the declination ranges âĂŤ07° to 20° and 40° to 80°, 1967, MNRAS, 71, 49

A.D. Gray et al., Radio Polarimetric Imaging of the Interstellar Medium: Magnetic Field and Diffuse Ionized Gas Structure near the W3/W4/W5/HB 3 Complex, 1998, ApJ, 514, 231

A.E. Guzmán et al., All-sky Galactic radiation at 45 MHz and spectral index between 45 and 408 MHz, 2011, A&A, 525, 138

L.M. Haffner et al., The Wisconsin Hα Mapper Northern Sky Survey, 2003, ApJS, 149, 405

S.E.G Hales et al., A revised machine-readable source list for the Rees 38-MHz survey, 1995, MNRAS, 274, 447

J.P. Hamaker et al., Inventory of polarimetric transformations in the LOFAR signal path, 2011

J.L. Han et al., Antisymmetric rotation measures in our Galaxy: evidence for an A0 dynamo, 1997, A&A, 322, 98

C.G.T. Haslam et al., Rotation measure synthesis at the 2 m wavelength of the FAN region: Unveiling screens and bubbles., 2012, A&A, 549, 561

C. Heiles, The Magnetic Field Near the Local Bubble, 1998, LNP, 506, 229

M. Iacobelli et al., A radio continuum survey of the southern sky at 1420 MHz. The atlas of contour maps, 2001, A&A, 376, 861

W.J. Jaffe, G.C. Perola, Dynamical Models of Tailed Radio Sources in Clusters of Galaxies, 1973, A&A, 26, 423

N.S. Kardashev, Nonstationarity of Spectra of Young Sources of Nonthermal Radio Emission, 1962, SvA, 6, 317

K.I. Kellermann et al., The Spectra of Radio Sources in the Revised 3c Catalogue, 1969, ApJ, 157, 1

M.I. Large et al.,A new feature of the radio sky, 1962, MNRAS, 124, 405

Y. Leblanc et al., On Io's excitation and the origin of Jupiter's decametric radiation, 1994, A&A, 290, 660

K. Maeda et al., A 45 MHz continuum survey of the northern hemisphere, 1999, A&A, 140, 145

R.N. Manchester, Pulsar Rotation and Dispersion Measures and the Galactic Magnetic Field, 1972, ApJ, 172, 43

R.N. Manchester et al., VizieR Online Data Catalog: ATNF Pulsar Catalog, 2005, AJ, 129, 1993

J. Milogradov-Turin and F.G. Smith, A survey of the radio background at 38 MHz, 1972, MNRAS, 161, 269

D.D. Mulcahy et al., The nature of the low-frequency emission of M 51. First observations of a nearby galaxy with LOFAR, 2014, A&A, 568, 74

A.Nigl et al.,Jupiter Burst Observation with LOFAR/ITS, 2006, pre6.conf, 517

A. Noutsos et al., Pulsar polarisation below 200 MHz: Average profiles and propagation effects, 2015, A&A, 576, 62

N. Oppermann et al., An improved map of the Galactic Faraday sky, 2012, A&A, 542, 930

A.G. Pacholczyk, Radio astrophysics. Nonthermal processes in galactic and extragalactic sources, 1970, W.H.Freeman & Co Ltd

L. Page et al., Three-Year Wilkinson Microwave Anisotropy Probe (WMAP) Observations: Polarization Analysis, 2007, ApJS, 170, 335

I.I.K. Pauliny-Toth and J.R. Shakeshaft, A survey of the background radiation at a frequency of 404 Mc/s, 1961, MNRAS, 124, 61

J.A. Phillips et al., Earth-based observations of Faraday rotation in radio bursts from Jupiter, 1989, JGR, 94, 5457

J. Queinnec et al., Io-controlled decameter arcs and Io-Jupiter interaction, 1998, JGR, 103, 26649

M.J.S. Quigley and C.G.T. Haslam, Structure of the Radio Continuum Background at High Galactic Latitudes, 1965, Natur, 208, 741

P. Reich and W. Reich, A map of spectral indices of the Galactic radio continuum emission between 408 MHz and 1420 MHz for the entire northern sky, 1987, A&A, 74, 7

P. Reich et al., A radio continuum survey of the southern sky at 1420 MHz. The atlas of contour maps, 2001, A&A, 376, 861

W. Reich, A radio continuum survey of the northern sky at 1420 MHz. I, 1982, A&A, 48, 219

W. Reich and P. Reich, A radio continuum survey of the northern sky at 1420 MHz. II, 1986, A&A, 63, 205

R.S. Roger et al., The radio emission from the Galaxy at 22 MHz, 1999, A&A, 137, 7

G.B. Rybicki, A.P. Lightman, Radiative Processes in Astrophysics, 1985, WILEY-VCH Verlag GmbH & Co

P. Schellart et al., Detecting Cosmic Rays with the LOFAR Radio Telescope, A&A, 560, 98 2013

P. Schneider, Einführung in die Extragalaktische Astronomie und Kosmologie, 2006, Springer Verlag

G. Sironi, The spectrum of the galactic non-thermal background radiation - I, 1973, MNRAS, 166, 345

A.R. Taylor et al., A Rotation Measure Image of the Sky, 2009, ApJ, 702, 1230

J.C. Testori et al., A fully sampled λ21 cm linear polarization survey of the southern sky, 2008, A&A, 484, 733

A.R. Thompson, J.M. Moran, G.W. Swenson Jr., Interferometry and Synthesis in Radio Astronomy, 2001, WILEY-VCH Verlag GmbH & Co

A.J. Turtle et al., The spectrum of the galactic radio emission, 1962, MNRAS, 124, 297

A.J. Turtle and J.E. Baldwin, A survey of galactic radiation at 178 Mc/s, 1962, MNRAS, 124, 459

B. Uyaniker, 2003, Radio Polarization from the Galactic Plane in Cygnus, ApJ, 585, 785

M.P. van Haarlem et al., LOFAR: The LOw-Frequency ARray, 2013, A&A, 556, 2

M.V. Vidal et al., Polarised radio filaments outside the Galactic plane, 2015, MNRAS, 0, 1

E.N. Vinyaikin, Frequency Dependence of the Evolution of the Radio Emission of the Supernova Remnant Cas A, 2014, ARep, 58, 626

A.S. Webster, The spectrum of the galactic non-thermal background radiation - II, 1973, MNRAS, 166, 355

A. Wilkinson, 1973, Linear Polarization of the region round l=140deg, b=+8deg at 240.5 MHz, MNRAS, 163, 147

A. Wilkinson & F.G. Smith, 1974, Characteristics of the local galactic magnetic field determined from background polarization surveys, MNRAS, 167, 593

M. Wolleben et al., An absolutely calibrated survey of polarized emission from the northern sky at 1.4 GHz, 2006, A&A, 448, 411

M. Wolleben, A New Model for the Loop I (North Polar Spur) Region, 2007, ApJ, 664, 349

P. Zarka et al., A scenario for Jovian S-bursts, 1996, GeoRL, 23, 125

P. Zarka, Fast radio imaging of Jupiter's magnetosphere at low-frequencies with LOFAR, 2004, P&SS, 52, 1455